UNIVERSITY OF CALIFORNIA, SAN DIEGO

Cosmology from Quasar Spectra

A dissertation submitted in partial satisfaction of the
requirements for the degree Doctor of Philosophy
in Physics

by

Nao Suzuki

Committee in charge:

Professor David Tytler, Chair
Professor Kurt Marti
Professor Michael L. Norman
Professor Justin Roberts
Professor Arthur M. Wolfe

2005

The dissertation of Nao Suzuki is approved, and it is acceptable in quality and form for publication on microfilm:

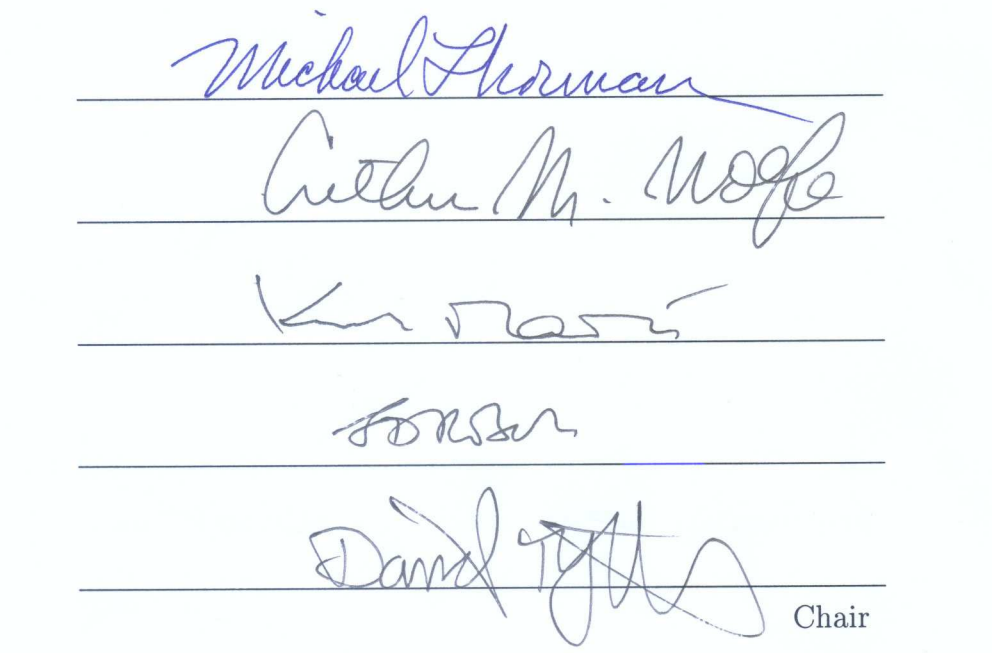

University of California, San Diego

2005

Dedicated to. My Mother, Father, Brothers and Sisters around the World

If we knew what it was we were doing, it would not be called research, would it?

–Albert Einstein

TABLE OF CONTENTS

LIST OF FIGURES

LIST OF TABLES

Acknowledgements

First of all, I would like to thank my adviser, David Tytler, for giving me this great opportunity. It was an honor and pleasure to work with you. I learned a lot from you not only on scientific insights and detail techniques but also on strategies, management of life itself. My life would not be spoken without you. My special thanks goes to the members of Tytler group: My practical skills of observation and data processing originated from David Kirkman, a.k.a. 'the programming artist', and his advices and support always helped me break the walls I faced. John O'Meara who always brings us laugh made my life so easy here. We shared a lot of fun, but we will need to work out our unfinished business, 'Jinrui Hokankeikaku' in the future. Dan Lubin helped me initiate observation at Lick and establish HST data set. We had an interesting crossover of ozone research at the end. It was a pleasure to work with undergraduate students who gave me new energy and stimulation: Carl Melis, Kory James, Geoffrey So, Susan Hollywood and Sarah Triples. Especially, Carl understood the details well and helped me a lot, and I enjoyed drinking beers with you on Fridays.

My life has been supported by many of CASS (Center for Astrophysics and Space Sciences) members. My life would not be the same without them. I would like to thank the director of CASS, Art Wolfe, for his leadership. I believe your excellent lectures are the world's bests, and I enjoyed every single one of them. Your deep insights in science always becomes my source of inspiration, and your advices showed me the paths and doors I should walk through. I owe a lot to Art's group members. Jason Prochaska, the man of perfect life, always amazes me for his brilliant ideas of solving problems. I thank his kind help and prompt support to our projects. I learned the basics of CMB from Eric Gawiser's organized lecture series. Chris Howk is my teacher of spectroscopic analysis.

I had a great time collaborating with Mike Norman's group. Although most of our work is truly experimental, I believe we established a brand new way of exploring the universe. I was always impressed by Mike's organization of the group

and heritage of supercomputer technology which is an ongoing evolution of science. We had a fun time together with Tridi Jena, Brian O'Shea, Wen-Chin Lin, Dan Whalen, Pascal Paschos, Alexei Kritsuk and Alex Razoumov. I wish to thank Tridi for hard work to explore the precision measurement. I have a lot in common with him and hope our collaboration continues to the future.

CASS faculties enriched my work and life here at UCSD. Kim Griest, I wish to thank for your scientific advices and guidance. It was such a great experience to work with you in teaching, and I believe we made a difference in our classes. It becomes my treasure to keep in touch with our students. I could not have gotten here without you. George Fuller, who I see in the mornings, evenings, on Saturdays and Sundays, is my hero. Your deep and wide range of physics knowledge and insights inspired me a lot. I wish to catch a big fish together in the future. Gene Smith showed me how to handle both teaching and research. It was such an extraordinary time for you to have the new Spitzer satellite and cosmology class, but you made 100% effort in both of them and amazed me. Barbara Jones and her dedication to the teaching made me think that teaching itself is a great experiment and we are all explorer. I witnessed that every year the lab teaching is making a progress and getting more sophisticated. Andreas Quirrenbach is an extraordinary person. How could you do so many things in such a high quality? Your lecture on ISM was excellent, and thank you for answering so many questions. It was a great honor to have a tea together with Margaret and Geoff Burbidge. Every episode you introduced to us was indeed the history of astronomy. Lu Sham at physics department inspired me to introduce PCA method to the quasar spectra. Without your lecture, I would not come up with the idea of this thesis and future projects. Computing was supported by Paul Yeatman and Pete James. Without Paul, I could not have survived. I am grateful for their timeless effort even on holidays when the computer went down. Thank you very much for your prompt help and tea services! CASS business office supported this work from the behind the scenes. Andi Stephens, Cheryl Matson, Susanna Pastell and Shirley Roy are the ones who

made our work possible. Debra Bomar is the one who helped me a lot in practice. She is the mother of the physics department.

This work is based on the data taken at the Keck and Lick observatories. It would not be possible without the great effort of the team of these observatories. Especially, I would like to thank Wayne Earthman, Keith Baker, Rem Stone, Elinor Gates, Bernie Walp and Tony Misch. I learned the basics of the observation from them. Although I could not include the data from the Subaru telescope, but I would like to thank the HDS team for their great effort to meet our requests: W. Aoki, H. Ando, K. Noguchi S. Kawanomoto, A. Tajitsu.

I wish to thank my colleagues and good friends who made my life much brighter. Regina Jorgenson always encouraged me and helped my writings. You are my shining starlight! and you have such a great family. Discussion with Neal Dalal is always fun and I will miss the days we spend together in La Jolla cove for snorkeling. Jeff Cooke and Brian Siana, what a fun to have you both work on the thesis at the same time. We will keep our connection in California, right? I had a great time with CASS folks at Journal Club, and having lunch, dinner, and beer parties. I would like to thank Emrah Kalemci, Wayne Coburn, Defne Ucer, Christian Thomas, Chad Kishimoto, Phil Amanik, Jun Hidaka, Dawn Galino, John Hays, and Ken Nagamine. My lunch buddies, Tom Gasaway, Ed Stephan and Ron Quillin made us internationalized every week.

I would not be here without people in Tokyo. I would like to thank their support. They are the ones who guided me to the studies of cosmology. S. Okamura and his group helped me a lot when I had a hard time. I am very grateful for his support and will to be loyal to them: M. Doi, K. Shimasaku, N. Yasuda, N. Kashikawa, M. Yagi, W. Kawasaki, Y. Komiyama, F. Nakata, H. Furusawa, and M. Ohuchi. M. Iye is the first who showed me the studies of quasars, and I would always find my origin at AGN seminar we had together. It becomes such a treasure to have T. Misawa, who we met in Tokyo, as our collaborator. His sincere efforts always impress and stimulate us. Computer support from Ichikawa's group was essential,

and I started studying HST quasar spectrum with them. I am a student of T. Kajino's school, and we always enjoy our discussions. M. Inoue saved my career in science and R. Kawabe is the one who enjoys cross over science. Discussions with N. Arimoto and Y. Yoshii are always fun.

I wish to have a few words to my best friends: J. Lien, C. Hwang, A. Fujihira, N. Fukai, N. Arakawa, T. Moriwaki, Y. Saito, Y. Watanabe, T. Machida, R. Takeuchi, Y. Ohbayashi, J. Ogikubo, and my surf buddy T. Katoh. Because you were always there standing beside me in good times and bad times, I could keep running. My hard working spirit is originated from a work experience at the Congressman Noda's office. Noda taught me there is no short cut to make dreams come true in life. Congressman Yamanoi showed me there are hard jobs people are reluctant to do but must be done by ourselves. I am sure I am missing many people I should thank. I would like to thank all of the people who helped and supported me. When my car got broken 2 years ago, I was taking a public bus to commute. I was surprised to see a full of people in the 5:20 am express bus from downtown to the UCSD campus. I wish to note and remember that our daily life is supported by these hard-working unsung hero and heroines.

Finally, I wish to thank my family. My parents, my sisters and my brothers for their unselfish support. The tears they shed for me are shining in my mind and they are much brighter than any stars in any galaxies in the universe.

VITA

1995	B.S. in Astrophysics and Applied Mathematics, University of California, Los Angeles
1998	M.S. in Astronomy, University of Tokyo
1999–2003	Research Assistant, University of California, San Diego
2001	M.S. in Physics, University of California, San Diego
2003–2005	Teaching Assistant, Department of Physics University of California, San Diego
2005	Doctor of Philosophy University of California, San Diego

PUBLICATIONS

"Quasar Spectrum Classification with PCA - II: Introduction of Five Classes, Artificial Quasar Spectrum, the Mean Flux Correction Factor dF,and the Identification of Emission Lines in the Ly alpha Forest", 2005 ApJ submitted, astro-ph/0503248

"Predicting QSO Continua in the Lyman Alpha Forest", Suzuki, N., Tytler, D., Kirkman, D., O'Meara, J. M., Lubin, D. 2005, ApJ, 618, 592

"Relative Flux Calibration of Keck HIRES Echelle Spectra", Suzuki, N., Tytler, D., Kirkman, D., O'Meara, J. M., and Lubin, D. 2003, PASP,115,1050

"The Cosmological Baryon Density from the Deuterium to Hydrogen Ratio in QSO Absorption Systems: D/H towards Q1243+3047", Kirkman, D., Tytler, D., Suzuki, N., O'Meara, J. M., and Lubin, D. 2003, ApJS, 149, 1

"The Deuterium to Hydrogen Ratio toward a fourth QSO:
HS0105+1619",O'Meara, J. M., Tytler, D., Kirkman, D., Suzuki, N., Prochaska, J. X., Lubin, D., and Wolfe, A. M. 2001, ApJ, 552, 718

"The Kast Ground Based UV Spectral Survey of 79 QSOs at Redshift 2 for Lyman Alpha Forest and Metal Absorption", Tytler, D., O'Meara, J.M., Suzuki, N., Kirkman, D., Lubin, D., and Orin, A. 2004, AJ, 128, 1058

"The HI opacity of the intergalactic medium at redshifts $1.6 < z < 3.2$", Kirkman, D., Tytler, D., Suzuki, N., Melis, C., Hollywood, S., James, K., So, G., Lubin, D., Jena, T., Norman, M. L., Paschos, P. MNRAS, 2005, 360, 1373

"Cosmological Parameters σ_8, the Baryon Density Ω_b, and the UV Background Intensity from a Calibrated Measurement of H I Lyman α absorption at $z = 1.9$", Tytler, D. Kirkman, D., O'Meara, J.M., Suzuki, N., Orin, A., Lubin, D., Paschos, P., Jena, T., Lin, W., and Norman, M. L. 2004, ApJ, 617, 1

"A concordance model of the Lyman forest at z= 1.95", Jena, T., Norman, M. L., Tytler, D., Kirkman, D., Suzuki, N., Chapman, A., Melis, C., Paschos, P., O'Shea, B., So, G., Lubin, D., Lin, W., Reimers, D., Janknecht, E., Fechner, C. MNRAS submitted, astro-ph/0412557

"Signature of Galactic Outflows as Absorption-Free Gaps in the Lyα Forest", Fang, T., Loeb, A., Tytler, D., Kirkman, D., Suzuki, N., ApJL submitted, astro-ph/0505182

"H I Gas in Higher Density Regions of the Intergalactic Medium", Misawa, T., Tytler, D., Iye, M., Paschos, P., Norman, M., Kirkman, D., O'Meara, J., Suzuki, N., Kashikawa, N. 2004, AJ, 128, 2954

"C IV and other Metal Absorption Line Systems in 18 z=4 Quasars", Misawa, T., Tytler, D., Iye, M., Storrie-Lombardi, L. J., Suzuki, N., Wolfe, A. M., 2002, AJ, 123, 1847

"The UCSD HIRES/Keck I Damped Lyman Alpha Abundance Database IV: Probing Galactic Enrichment Histories with Nitrogen", Prochaska, J. X., Henry, R. B. C., O'Meara, J. M., Tytler, D., Wolfe, A. M., Kirkman, D., Lubin, D., and Suzuki, N. 2002, PASP, 114, 933

"The UCSD HIRES/Keck I Damped Lyman Alpha Abundance Database III: Photoionization in the Damped Lyman Alpha System toward GB 1759+7539", Prochaska, J. X., Howk, J. C., O'Meara, J. M., Tytler, D., Wolfe, A. M., Kirkman, D., Lubin, D., and Suzuki, N. 2002, ApJ, 571, 693

"New Hubble Space Telescope Spectra of QSO PG 1718+4807: No Strong Evidence of Deuterium Absorption", Kirkman, D., Tytler, D., O'Meara, J. M., Burles, S., Lubin, D., Suzuki, N., Carswell, R., Turner, M. S., and Wampler, E. J. 2001, ApJ, 559, 23

"Review of Big Bang Nucleosynthesis and Primordial Abundances", Tytler, D., O'Meara, J. M., Suzuki, N., and Lubin, D. 2000, Physica Scripta, T85, 12

"Deuterium and the Baryonic Density of the Universe", Tytler, D., O'Meara, J. M., Suzuki, N., and Lubin, D. 2000, PhR, 333, 409

"Big Bang Nucleosynthesis", Tytler, D., O'Meara, J. M., Suzuki, N. and Lubin, D. 2000. NuPhysB, 87, 464

"A new Measurement of the Primordial D/H Ration in the Intergalactic Medium: HS 0105+1619", O'Meara, J. M., Tytler, D., Kirkman, D., Lubin, D., and Suzuki,

N. 2001, proceedings from the symposium "Cosmic Evolution" held at the Institut d'Astrophysique de Paris. 2001coev.conf, 57

"Measurements of the Primordial D/H Abundance Towards Quasars", Tytler, D., O'Meara, J.M., Suzuki, N., Lubin, D., Burles, S., and Kirkman, D. 2000, IAUS,198,125

FIELDS OF STUDY

Major Field: Physics and Astrophysics

Studies in Theoretical Mechanics:
Professor Vitali D. Shapiro

Studies in Mathematical Physics:
Professor Aneesh V. Manohar

Studies in Advanced Classical Electrodynamics:
Professor Aneesh V. Manohar

Studies in Quantum Mechanics:
Professors Lu J. Sham

Studies in Particles and Fields:
Professor Elizabeth Jenkins

Studies in General Relativity:
Professors Benjamin Grinstein & George M. Fuller

Studies in Computational Astrophysics:
Professor Michael L. Norman

Studies in Cosmology:
Professor Kim Griest

Studies in Hegh Energy Astrophysics and Compact Objects:
Professor George M. Fuller

Studies in Physics of the Interstellar Medium:
Professors Arthur M. Wolfe & Andreas Quirrenbach

Studies in Galaxies and Galactic Dynamics:
Professor Arthur M. Wolfe

Studies in Stellar Structure and Evolution:
Professor Arthur M. Wolfe

ABSTRACT OF THE DISSERTATION

Cosmology from Quasar Spectra

by

Nao Suzuki

Doctor of Philosophy in Physics

University of California, San Diego, 2005

Professor David Tytler, Chair

High resolution spectroscopy of high redshift quasar spectra enables us to investigate the properties of the intergalactic medium (IGM) and measure cosmological parameters from the Lyα forest. Toward high precision cosmology, this dissertation presents the following four topics. 1. Principal Component Analysis (PCA) on quasar spectrum: We introduce the PCA to describe quasar emission lines and continua quantitatively, and we attempt to make a prediction of the continuum shape in the Lyα forest using wavelengths redward of Lyα emission. 2. Flux calibration of Keck HIRES data: On our way to achieve high accuracy measurement, it was necessary to develop new calibration schemes and explore the origin of systematic errors. My contribution includes the following and is discussed throughout the thesis: (i) the development of the flux calibration scheme, (ii) the discovery of three emission lines in the Lyα forest, (iii) the establishment of high resolution standard star spectra, and (iv) the identification of ozone lines in the spectrum. 3. D/H measurement: We present precise measurements of the primordial deuterium to hydrogen ratio (D/H) toward two quasars, HS0105+1619 and Q1243+3047, which constrains the baryon to photon ratio $\eta = 5.9 \pm 0.5 \times 10^{-10}$ or the baryon density $\Omega_b h^2 = 0.0214 \pm 0.0020$ via the Big Bang Nucleosynthesis theory. 4. Studies of the Lyα forest at z $\sim$ 2 : We also present the measurements of the total amount of neutral hydrogen absorption in the IGM. We compare our observed data with hydrodynamic simulations and find good agreement when we use the following cosmological parameters:

$H_o = 71$ km $s^{-1}Mpc^{-1}$, $\Omega_\Lambda = 0.73$, $\Omega_m = 0.27$, $\Omega_b = 0.044$, the amplitude of the power spectrum $\sigma_8 = 0.9$, and the photoinization rate $\Gamma_{912} = (1.44 \pm 0.11) \times 10^{-12}\,s^{-1}$. We conclude that the measurements of the cosmological parameters from our primordial D/H measurements, recent WMAP satellite observation of the cosmic microwave background, and our the total amount of neutral hydrogen in the IGM at $z \sim 2$ are in a concordance with the ΛCDM model.

Chapter 1

Introduction

In the last 10 years, we have experienced a series of exciting discoveries in observational cosmology. The advent of the 10m Keck Telescope advanced the study of cosmology in an unprecedented manner. This dissertation attempts to perform precise measurements of a key cosmological parameter η , the baryon to photon ratio which is related to the baryon density Ω_b, and to test the ΛCDM model by comparing the observations of the Lyα forest with the cosmological simulations.

1.1 The Baryon Density Ω_b

In 1996, our group showed that baryons contribute only 4% of the critical density(Tytler et al., 1996) by measuring the primordial abundance of deuterium with the Keck telescope. "Big Bang Nucleosynthesis enters the precision era" (Schramm & Turner, 1998). This deuterium abundance measurement marked the beginning of the "precision cosmology".

The framework of the theory of the Standard Big Bang Nucleosynthesis (SBBN) was established in the 1950s (Alpher et al., 1948; Hayashi, 1950) and the precise calculation was performed in the 1960-70s (Peebles, 1966; Wagoner et al., 1967; Wagoner, 1973; Schramm & Wagoner, 1977). The theory predicts the abundance of the light elements – D, ^{3}He, ^{4}He and ^{7}Li – from η. Therefore, if we can

measure the light element's abundance, we can get to know η or the baryon density. However, the observation of these elements is extremely difficult and we had to wait until the Keck HIRES (High Resolution Echelle Spectrograph) enabled us to perform precise measurements of the deuterium abundance. Our strategy is simple: We survey the high redshift intergalactic medium to find a system which has a simple structure to analyze and which preserves the primordial deuterium abundance. Quasar spectra allowed us to do this measurement. However, the calibration of the Keck HIRES data is very difficult. The principle problem is that we did not know the continuum shape of the quasar spectrum in the UV region and it become a major source of uncertainty.

In the first half of this dissertation, I will present our deuterium abundance measurements. We established a method by which we can remove the systematic errors and could achieve the most secure and accurate measurements. I investigated and identified the possible origins of the systematic errors that arose when attempting to flux calibrate Keck HIRES spectra. The following list contains my unique contributions as described in this work:

1. Independently discovered or improved the identification of emission lines in the Lyα forest
2. Quantitative analysis of a variety of quasar emission lines
3. Identification of flux calibration error due to the currently available standard star data and Balmer γ line
4. Fixing HIRES wavelength calibration error
5. Recognition of ozone lines in our UV spectrum

Prior to this work, none of the above were well understood. I discuss the items 1 and 2 in Chapters 2 and 3 and the items 3 through 6 in Chapter 4. Then I will show the results of two deuterium abundance measurements to which I applied my calibration method, and I will report on the current status of the baryon density

measurement. This dissertation work laid the groundwork for achieving a more accurate measurement, by at least another factor of five in the near future.

1.2 The Concordance Model

The purpose of the second half of this dissertation is to test the currently favored cosmological model, ΛCDM, in the context of structure formation. During the last 10 years, a deeper understanding of the physics of the neutrino and evidence of the accelerating universe revolutionized the study of cosmology.

In 1998, neutrino experiments discovered that the neutrino must have a mass but cannot be a predominant part of dark matter (Fukuda et al., 1998). In 1999, the high redshift supernovae team found that the expansion of the universe is accelerating, making it necessary to revive Einstein's cosmological constant Λ (Perlmutter et al., 1999). In 2002, the satellite observation of the Cosmic Microwave Background (CMB) found that the age of the universe is 13.7 billion years, and measured the cosmological parameters to within 10% accuracy (Spergel et al., 2003).

These observations support the ΛCDM model, although we do not know the nature of Λ or Cold Dark Matter (CDM). Our Big Bang Nucleosynthesis study tests the epoch of the first three minutes of the universe, and the CMB tests the epoch of 300,000 years after the Big Bang. Now we wish to test if the ΛCDM model can describe the evolution of the universe. We use the Lyα forest at redshift 2 to 3 when the universe 6 to 8 billion years old. The opacity of the neutral hydrogen is sensitive to the ultraviolet background from quasars and star forming galaxies and the amplitude of the density fluctuation, σ_8. Collaborating with Prof. Michael Norman's group, we started a brand new type of research. It was also in the last 10 years when the numerical simulations became so precise that a comparison with the observed data can give us a precise measurement. We are testing both the cosmological model and the numerical simulations if we can describe the evolution of the universe and investigating the characteristics of the intergalactic medium. I

present the quasar survey we undertook over the past five years, and the measurements of the opacity of neutral hydrogen. I will report on the best fit cosmological parameters.

1.3 Overview of the Dissertation

The structure of this dissertation is as follows. In the next two chapters, Chapters 2 and 3, I introduce a method to describe and calibrate the quasar UV spectra and present the variety of quasar spectra. In the next four chapters, Chapters 4-7, I discuss the measurement of η and Ω_b. In chapters 5 and 6 I present the measurement of the deuterium abundance in two systems. I discuss the chemical evolution of the deuterium abundance, and the status of current measurement in Chapter 7. In the following three chapters, Chapters 9-11, I present a comparison of the observations of the Lyα forest with simulations in order to test the concordance model. I present the quasar survey in Chapter 9. I present the measurement of the amount of absorption in the Lyα forest from the Lick Kast survey in Chapter 10 and from the Keck HIRES data in Chapter 11. I discuss the cosmological parameters we derived from the comparison with simulation in Chapter 10.

Chapter 2

Predicting QSO Continua in the Lyα Forest

2.1 Abstract

We present a method to make predictions with sets of correlated data values, in this case QSO flux spectra. We predict the continuum in the Lyman-α forest of a QSO, from 1020 – 1216 Å, using the spectrum of that QSO from 1216 – 1600 Å. We find correlations between the unabsorbed flux in these two wavelengths regions in the HST spectra of 50 QSOs. We use principal component analysis (PCA) to summarize the variety of these spectra and we relate the weights of the principal components for 1020 – 1600 Å to the weights for 1216 – 1600 Å, and we apply this relation to make predictions. We test the method on the HST spectra, and we find an average absolute flux error of 9%, with a range 3 – 30%, where individual predictions are systematically too low or too high. We mention several ways in which the predictions might be improved. I believe that this is the first time to use PCA for making predictions in this area of astrophysics. We had hoped to use PCA to place continuum on the Lyα forest of QSOs. However, the systematic error is too large, and hence we manually fit the continuum to the observed QSOs to perform measurements in Chapters 9-11.

2.2 Introduction

We would like to have an accurate and objective way to find the continuum level in QSO spectra, because these levels are required to measure the amount of absorption. The uncertainty in the continuum level is often one of the largest uncertainties in the studies of intergalactic medium (IGM, e.g. Croft et al., 2002b), and the precise continuum shape is required for precision measurement of absorption lines, such as the measurement of D/H (Kirkman et al., 2003; Suzuki et al., 2005).

Standard methods of estimating the continua in the Lyα forest region of QSO spectra are frequently unsatisfactory. For redshifts $2 < z < 4$, the standard way to find a continuum level is to fit a smooth curve over the peaks of the flux in the Lyα forest. This method works well, giving $< 2\%$ errors in the continuum level in high resolution spectra (e.g. 8 km s^{-1} FWHM) with high S/N (e.g. 100 per 2 km s^{-1}, Kirkman et al., 2003). However, the method fails when there are few pixels that we can clearly identify as unabsorbed continuum, and this lack of continuum information is common in low S/N spectra, in low resolution spectra where lines blend together, and at higher redshifts where the Lyα forest absorbs more than a few percent at all wavelengths. In fact, by redshifts $z > 6$ the complete Gunn-Peterson trough (Becker et al., 2001; Djorgovski et al., 2001; Fan et al., 2001) makes it impossible to directly measure the continuum. Instead, at high redshifts, especially $z > 4$, it is common to approximate the continuum in the Lyα forest with a power-law extrapolation from wavelengths larger than Lyα (Telfer et al., 2002; White et al., 2003). But the continuum in the Lyα forest is not a power law, because the wings of the Ly-β-O VI emission line and especially the Lyα line, extend far into the Lyα forest and there exist weak emission lines especially near 1073 and 1123 Å (Zheng et al., 1997; Vanden Berk et al., 2001; Bernardi et al., 2003).

We might be able to predict the unabsorbed flux in the Lyα forest if it is correlated with the unabsorbed flux at other wavelengths. Here, the unabsorbed flux includes both continuum and emission lines, but not the random intervening

absorption. We measure correlations in a set of QSO spectra (hereafter the training set), that cover both 1020 Å $\leq \lambda \leq$ 1215 Å (hereafter the blue side) and 1216 Å $\leq \lambda \leq$ 1600 Å (hereafter the red side). We will use the red side spectra of individual QSOs to make predictions of their blue sides.

We use Principal Component Analysis (PCA) to summarize the information in the QSO spectra. PCA seeks to reduce the dimensionality of large data sets and is widely used in astronomy. (Whitney, 1983; Kanbur et al., 2002; Efstathiou, 2002). Francis et al. (1992) applied PCA to the LBQS (Hewett et al., 1995, 2001) optical spectra of QSOs to give an objective classification scheme, and they showed that any normalized QSO spectrum, $q_i(\lambda)$, is well represented by a reconstructed spectrum, $r_{i,m}(\lambda)$, that is a weighted sum of m principal components,

$$q_i(\lambda) \sim r_{i,m}(\lambda) = \mu(\lambda) + \sum_{j=1}^{m} c_{ij}\ \xi_j(\lambda), \tag{2.1}$$

where i refers to a QSO, $\mu(\lambda)$ is the mean of many QSO spectra, $\xi_j(\lambda)$ is the j th principal component, and c_{ij} is its weight. Instead of classifying QSO spectra, we use PCA to make predictions.

In §2.3 we describe HST spectra that we use for the training set. We show the correlations in the QSO spectra and results of the PCA in §2.4. In §2.5 we show how we make predictions and we discuss their accuracy.

2.3 QSO Spectra and their Correction

For the training set we use UV spectra of low redshift ($z < 1$) QSOs because they have little absorption and we can clearly see their continua levels. Here we describe these spectra, the criteria that we use to select them, and the corrections that we make.

We use a subset of the 334 high resolution *Hubble Space Telescope* (HST) *Faint Object Spectrograph* (FOS) spectra collected and calibrated by Bechtold et al. (2002). This sample includes all of the high resolution QSO spectra from the HST

QSO Absorption Line Key Project (Bahcall et al., 1993, 1996; Jannuzi et al., 1998). The gratings chosen are G130H, G190H, and G270H, and their spectral resolution is R $\sim$ 1300. Bechtold et al. (2002) identified both IGM and ISM lines in a uniform manner and they applied Galactic extinction corrections using the Galactic reddening map of Burstein & Heiles (1982) and the Milky Way reddening curve of Cardelli, Clayton, & Mathis (1989).

We select QSO spectra by wavelength coverage and S/N, and we remove a few QSOs with peculiar spectra. We reject QSOs that do not have complete coverage from 1020 Å to 1600 Å. This range covers from the Lyβ + O VI emission line blend to the C IV emission line. A larger range would help reveal the shapes of the QSO continua, but we would then have fewer QSOs in the sample.

We reject QSOs that did not have an average S/N $>$ 10 per binned pixel (0.5 Å in the rest frame) from 1050 Å to 1170 Å. We are interested in the intrinsic variation of the QSO spectra against the mean spectrum. Photon noise adds variation, masks the intrinsic variations, and alters the primary principal components. Before we removed the low S/N spectra, we found that some principal components were largely reproducing the photon noise of the spectra with unusually low S/N.

We remove QSOs with Broad Absorption Lines and Damped Lyα system because we are unsure where to place their continua. We also remove Q0219+4248 and Q0906+4305 whose emission line features are extremely weak. These removals make our sample not representative of all QSO spectra.

We end up using the spectra of 50 QSOs that we list in Table 2.1. The mean redshift is 0.58, with a standard deviation of 0.27 and a range from 0.14 to 1.04. The average S/N is 19.5 per 0.5 Å binned pixel.

We will represent the spectra of all 50 QSO by fitted smooth curves that reduce the effects of photon noise and interpolate over the absorption lines. To find the smooth curves, we mask the absorption lines which Bechtold et al. (2002) identified in both the blue and red sides. Then, for every 50 Å interval, with 20 Å overlaps, we fit Chebyshev polynomials and we choose the order of the polynomials

so that the reduced χ^2 becomes close to unity. The order is about $4 \sim 6$ if no strong emission line lies in that interval. In intervals which include strong emission lines such as Lyα and C IV, the order becomes $30 \sim 40$. For a few QSOs we made further adjustments using the software described in Kirkman et al. (2003) by fitting a smooth b-spline curve to the QSO continua.

In Table 2.1 we give emission redshifts that we measure from the peaks of the Lyα emission lines. In the rest frame the emission line peaks align, and the asymmetric profiles become a part of variance in the set of spectra. If we do not use the peak of the Lyα line, but instead we cross-correlate with a template of known redshift, we find that we need extra principal components to reconstruct the emission lines. Once we obtain the redshifts, we shift the spectra to the rest frame, and we rebin them into 0.5 Å pixels. We then have 1161 pixels of flux data values per QSO in the range 1020 Å – 1600 Å.

Since we are interested in the relative spectrum shape, we throw away absolute flux information. We find the average flux in 21 pixels around 1280 Å, and we normalize all spectra to unit flux at these wavelengths, far from any strong emission lines.

Table 2.1. Statistical Quantities for 50 Quasars

QSO	z	$\lvert\delta F_{10}\rvert$ Red Side	$\lvert\delta F_{10}\rvert$ Blue Side	δF_{10} Blue Side
Q0003+1553	0.450	3.3	5.2	4.1
Q0026+1259	0.145	5.2	6.7	5.4
Q0044+0303[a]	0.623	4.6	27.3	−27.1
Q0159−1147[a]	0.669	2.1	3.1	2.8
Q0349−1438	0.615	2.2	14.7	−14.5
Q0405−1219	0.572	2.3	4.4	−4.3
Q0414−0601	0.774	3.5	8.7	8.7
Q0439−4319	0.593	6.0	5.3	5.3
Q0454−2203[a]	0.532	3.0	31.4	−30.6
Q0624+6907[a]	0.367	4.7	29.1	−28.8
Q0637−7513	0.652	2.7	18.6	18.6
Q0923+3915	0.698	2.5	4.5	4.2
Q0947+3940	0.205	2.8	15.3	15.5
Q0953+4129[a]	0.233	5.0	16.8	17.4
Q0954+5537[a]	0.901	3.8	2.7	2.1
Q0959+6827	0.767	3.5	4.4	−2.3
Q1001+2910[a]	0.328	5.3	7.9	7.8
Q1007+4147	0.612	3.4	8.8	9.1
Q1100+7715[a]	0.312	3.9	31.0	31.0
Q1104+1644	0.630	3.1	2.7	−0.4
Q1115+4042[a]	0.154	5.6	14.5	14.7
Q1137+6604[a]	0.646	3.1	2.3	−2.3
Q1148+5454	0.970	3.0	12.3	12.5
Q1216+0655	0.332	9.4	4.7	−3.3
Q1229−0207[a]	1.041	3.1	7.0	6.9
Q1248+4007[a]	1.027	4.2	6.4	6.3
Q1252+1157[a]	0.868	3.5	6.8	6.8
Q1259+5918[a]	0.468	3.0	13.5	−13.4

Table 2.1—Continued

QSO	z	$\lvert\delta F_{10}\rvert$ Red Side	$\lvert\delta F_{10}\rvert$ Blue Side	δF_{10} Blue Side
Q1317+2743	1.009	1.5	10.8	10.8
Q1320+2925[a]	0.947	3.1	4.3	4.2
Q1322+6557	0.168	4.8	13.5	13.3
Q1354+1933	0.720	4.8	8.1	8.3
Q1402+2609[a]	0.165	3.6	10.6	10.9
Q1424−1150[a]	0.804	4.8	10.6	10.6
Q1427+4800[a]	0.222	4.1	25.9	26.1
Q1444+4047[a]	0.266	4.1	15.4	−15.1
Q1538+4745[a]	0.768	4.5	23.4	−23.2
Q1544+4855	0.400	7.4	13.3	−12.8
Q1622+2352[a]	0.926	4.5	2.7	0.5
Q1637+5726	0.750	2.5	3.6	3.6
Q1821+6419[a]	0.296	5.0	12.9	−13.2
Q1928+7351[a]	0.302	2.7	6.1	12.0
Q2145+0643	1.000	3.7	2.5	0.4
Q2201+3131[a]	0.296	3.1	3.2	3.3
Q2243−1222	0.626	3.6	2.6	2.2
Q2251+1120[a]	0.325	6.8	27.6	−27.1
Q2251+1552	0.856	2.7	4.1	2.2
Q2340−0339[a]	0.894	3.1	24.7	24.6
Q2344+0914[a]	0.671	7.8	5.5	4.9
Q2352−3414	0.707	3.6	3.9	1.0

Note. — We used 10 principal components for the error values, which we show multiplied by 100.

[a]The spectrum contains absorption or unusual photon noise in the region 1216 – 1240 Å that might have led to an inaccurate continuum level.

2.4 Principal Component Analysis of QSO Spectra

We calculate the correlation of the fluxes at different wavelengths to see how different parts of the typical QSO spectrum are related. In Figure 2.1, we see the 1161×1161 correlation matrix $\boldsymbol{R}$ with elements

$$\boldsymbol{R}(\lambda_m, \lambda_n) = \frac{1}{N-1} \sum_{i=1}^{N} \frac{(q_i(\lambda_m) - \mu(\lambda_m))\,(q_i(\lambda_n) - \mu(\lambda_n))}{\sigma(\lambda_m)\,\sigma(\lambda_n)}, \tag{2.2}$$

where $q_i(\lambda)$ is the continuum fitted and normalized spectrum for the i th QSO, N is the total number of QSO spectra, σ_m and σ_n are the standard deviations of the flux in the mth and nth wavelength bins, λ_m and λ_n respectively.

We find moderate correlation, about $0.2 \sim 0.6$, between the red and blue continua. The correlation between the emission lines, 0.8, is much stronger, and hence we expect that the emission lines in the red side will give good predictions for those in the blue side.

We can calculate the covariance matrix $\boldsymbol{V}$ for the 50 QSOs as:

$$\boldsymbol{V}(\lambda_m, \lambda_n) = \frac{1}{N-1} \sum_{i=1}^{N} (q_i(\lambda_m) - \mu(\lambda_m))\,(q_i(\lambda_n) - \mu(\lambda_n))\,. \tag{2.3}$$

In Figure 2.2 we see the covariance is relatively small in the continuum but large in the emission lines, meaning that the emission lines vary a lot from QSO to QSO. The peaks near 1073 and 1123 Å probably correspond to the weak emission lines in the Lyα forest that Bernardi et al. (2003) discuss.

We can find the principal components by decomposing the covariance matrix $\boldsymbol{V}$ into the product of the orthonormal matrix $\boldsymbol{P}$ which is composed of eigenvectors, and the diagonal matrix $\boldsymbol{\Lambda}$ containing the eigenvalues:

$$\boldsymbol{V} = \boldsymbol{P}^{-1} \boldsymbol{\Lambda} \boldsymbol{P}. \tag{2.4}$$

We call the eigenvectors, the columns of the matrix $\boldsymbol{P}$, the principal components. The principal components are ordered according to the amount of the variance in the training set that they can accommodate, such that the first principal component is the eigenvector which has the largest eigenvalue.

Let us quantitatively assess how well we can reconstruct the QSO spectra using a certain number of the components. We find the weight c_{ij} of the jth principal component for QSO spectrum $q_i(\lambda)$ from:

$$c_{ij} = \int_{1020\mathrm{A}^\circ}^{1600\mathrm{A}^\circ} (q_i(\lambda) - \mu(\lambda))\ \xi_j(\lambda)\ d\lambda. \tag{2.5}$$

When we use the first m components, we get the reconstructed spectrum $r_{i,m}$. The $\xi_j(\lambda)$ look similar to QSO spectra, but with more structure at the wavelengths of the emission lines. Examples of principal components and reconstructions, which are very similar to ours, are given by Francis et al. (1992).

We now introduce the accumulated residual variance fraction $\delta E_{i,m}$:

$$\delta E_{i,m} = \int_{1020\mathrm{A}^\circ}^{1600\mathrm{A}^\circ} (r_{i,m}(\lambda) - q_i(\lambda))^2 d\lambda \Big/ \int_{1020\mathrm{A}^\circ}^{1600\mathrm{A}^\circ} (q_i(\lambda) - \mu(\lambda))^2 d\lambda. \tag{2.6}$$

This quantity measures the square of the difference of a reconstructed spectrum from the continuum fitted QSO spectrum, in units of the square of the difference between that QSO and the mean. Hence $\delta E_{i,m}$ decreases from 1 to near zero as we add components to the reconstruction. The m in $\delta E_{i,m}$ tells us that we have used the first m components in the reconstruction $r_{i,m}(\lambda)$. In Table 2.2, we list the mean $< \delta E_m >= (1/N) \sum_{i=1}^{N} \delta E_{i,m}$, averaged over all 50 QSOs. The first three component takes 77% of the residual, and the first 10 components absorb about 96%. Francis et al. (1992, their Fig. 4) analyzed the LBQS set of QSO spectra (Hewett, Foltz, & Chaffee, 1995, 2001). Using a different statistic that accounts for photon noise, different wavelengths, and including BAL QSOs and all absorption lines, they found that the first three components accounted for 75% of the variance, and the first 10 components 95%. We also analyzed the LBQS spectra, kindly provided by Paul Francis and Paul Hewett, to confirm that our implementation of the PCA matched theirs given our wavelength range and selection criteria. The residual variance decreases in a different way for each QSO because the contributions of the components differ. However, on average, the rate of reduction slows after third component and saturates around the 10th component. The components greater than

about 10th look noisy and carry little information. In the following discussion, we use up to the first 10 principal components.

Figure 2.1: Visualization of the 1161 $\times$ 1161 correlation matrix (Equation (2)) created from the continua fitted to the 50 QSO spectra, normalized near 1280 Å. The numerical values, encoded in the lower bar, depend on the normalization wavelength, and the features near 1280 Å are artifacts of the normalization. The correlation is unity by definition on the diagonal, and the upper and lower triangles are identical reflections about this diagonal. Top and left panels show the wavelength range and the mean spectrum of the 50 QSOs. Emission lines are shown at effective wavelengths from Wills et al. (1995). We see that the correlation is strong between the emission lines, for example the horizontal row at the wavelength of C IV shows correlations 0.4 – 0.9 at the wavelengths of Lyβ and Lyα. The continuum between Lyβ and Lyα is moderately correlated (0.1 – 0.6) with that between Lyα and Si IV, and somewhat less correlated (0.0 – 0.5) with that from Si IV to C IV.

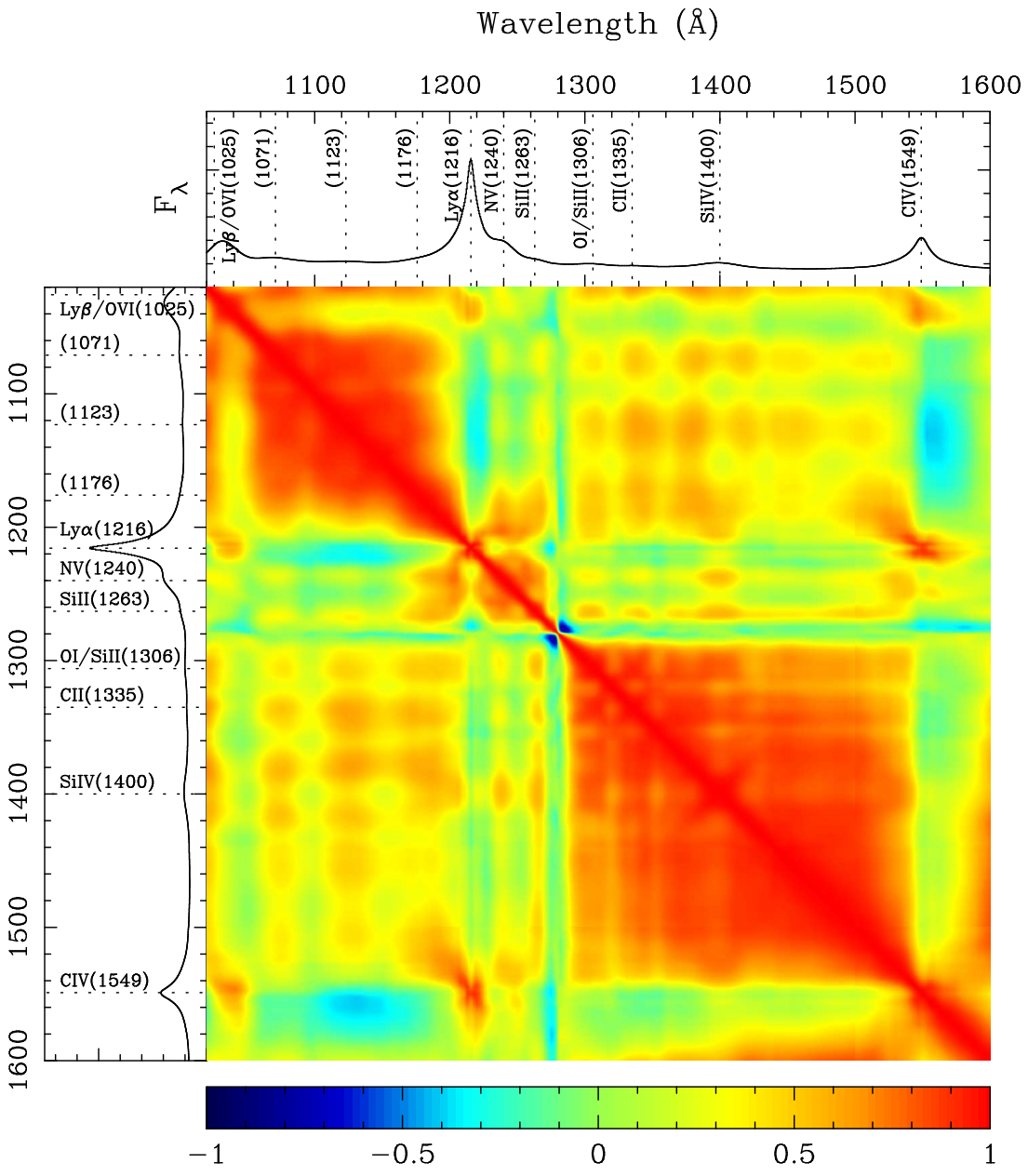
Wavelength (Å)
1100
1200
1300
1400
1500
1600
F_λ
Lyβ/OVI(1025)
(1071)
(1123)
(1176)
Lyα(1216)
NV(1240)
SiII(1263)
OI/SiII(1306)
CII(1335)
SiIV(1400)
CIV(1549)
−1
−0.5
0
0.5
1

Figure 2.2: As Figure 2.1, except showing the covariance matrix given by Equation (3). The variance is largest at the emission line wavelengths: Lyβ + O VI, 1073 Å, 1123 Å, Lyα, N V, Si II (1263), O I + Si II (1306), C II (1335), Si IV + O IV] and C IV. We see a grid of peaks in the variance at the intersections of these wavelengths. The variance is zero at 1280 Å where we normalized the spectra to the same flux. The variance is larger between Lyβ and Lyα than on the red side, perhaps because of errors in our continuum fits in the Lyα forest or because of intrinsic variations. We obtain the principal components by decomposing this covariance matrix into eigenvectors and eigenvalues.

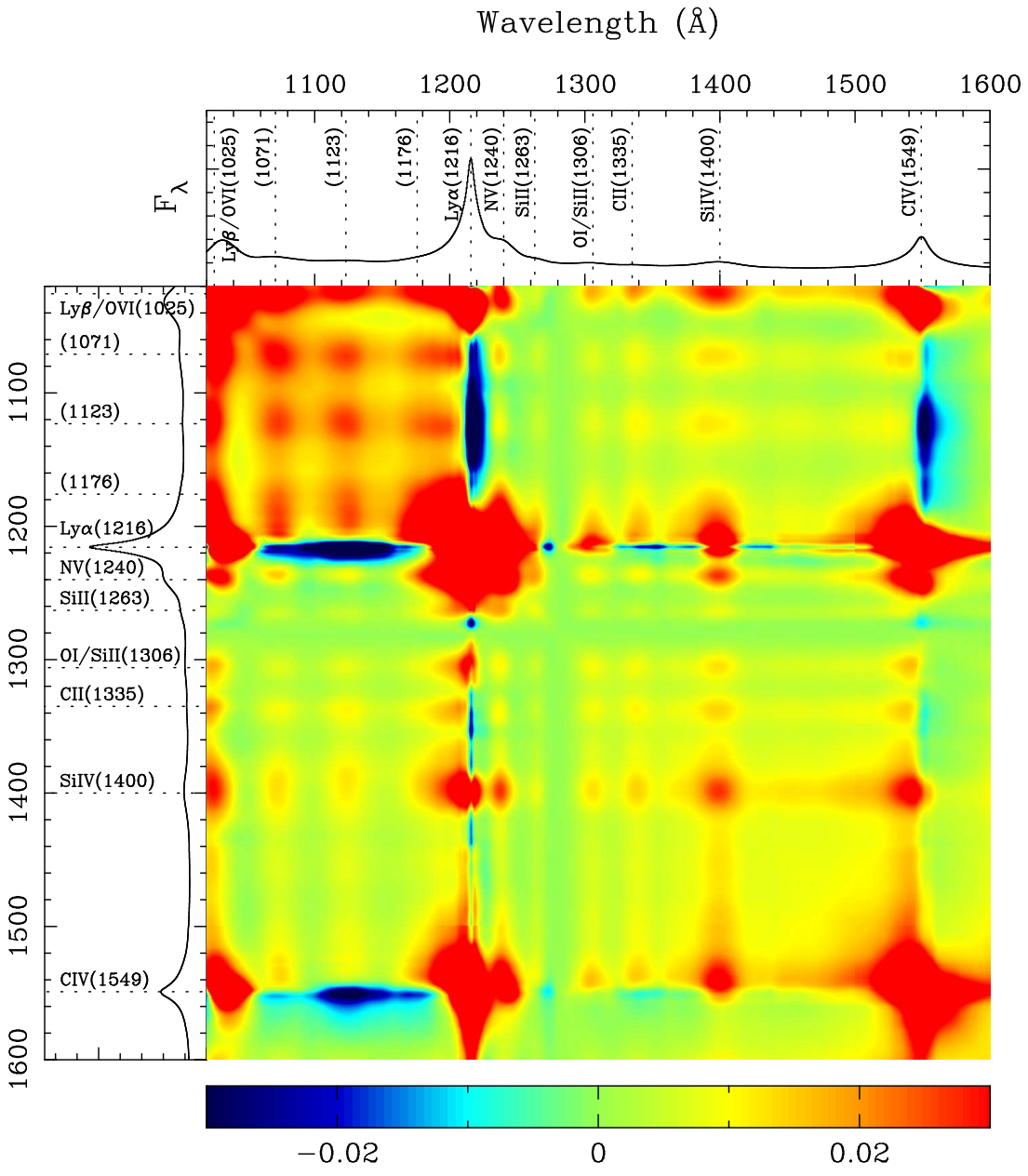
Wavelength (Å)
1100
1200
1300
1400
1500
1600
F_λ
Lyβ/OVI(1025)
(1071)
(1123)
(1176)
Lyα(1216)
NV(1240)
SiII(1263)
OI/SiII(1306)
CII(1335)
SiIV(1400)
CIV(1549)
−0.02
0
0.02

2.5 Predicting Spectra

Our goal is to predict the continuum of a QSO in the Lyα forest, the blue side, using a spectrum of wavelengths larger than Lyα emission, the red side. In §4.1 we describe how we relate the blue and red side continua, and in §4.2 we give a general recipe to make predictions.

2.5.1 Methods

Unfortunately, we do not have enough QSO spectra for both a training set and a separate set of spectra that we can use to test our predictions. Hence, we also use the training set for the tests. When we make a prediction for a QSO, we use a set of principal components which we generated without using any spectra of that QSO. We will call this the bootstrap method, and we will use it in most of the remainder of this paper. When we omit different QSOs, the first five principal components change by a few percent, most noticeably at the wavelengths of the emission lines. If we do not omit the QSO of interest, the complete set of principal components contains all the information on each QSO, including the continuum fitting and photon noise. We found the noise features could identify a QSO, giving weights with unrealistically high precision.

We chose three steps to quantify the relationship between the red and blue sides of the spectra in the training set.

- Step 1: Find the first m principal components $\xi_j(\lambda)$ and their weights, c_{ij}. We use all the blue and red side wavelengths, 1020 Å to 1600 Å, and we use the bootstrap method to give a slightly different set of $\xi_j(\lambda)$ for each QSO i.

- Step 2: Repeat step one, using only the red wavelengths 1216 Å to 1600 Å. We again keep the first m principal components, $\zeta_j(\lambda)$ and their weights, d_{ij}, which are similar to those from step one. We can write the weights in the $N \times m$ matrix form $\boldsymbol{C} = c_{ij}$ and similarly for $\boldsymbol{D} = d_{ij}$.

- Step 3: Find the $m \times m$ projection matrix $\boldsymbol{X} = x_{ij}$ which translates the weights found on the red side to the weights for the whole spectrum:

$$\boldsymbol{C} = \boldsymbol{D} \cdot \boldsymbol{X}. \tag{2.7}$$

We have $N = 50$ QSOs, and we keep $m = 10$ components. We then have more equations (N) than unknowns (m) and we wish to find the least-squares solution to this over-determined set of linear equations. The solution matrix $\boldsymbol{X}$ can be found via the Singular Value Decomposition technique (Press et al., 1992).

2.5.2 Making a Prediction

We are now ready to make a prediction of the Lyα forest continuum of any QSO spectrum, that need not be in the training set, provided we have the red side of its spectrum. We obtain predictions in three steps, that are similar to those presented above to find $\boldsymbol{X}$.

- Step A: Find the weights for the red spectrum,

$$b_{ij} = \int_{1216\text{Å}}^{1600\text{Å}} (q_i(\lambda) - \mu(\lambda))\ \zeta_j(\lambda)\ d\lambda. \tag{2.8}$$

The b_{ij} will be like the d_{ij} in step 2 above, except that the principal components could be different. If the QSO is not part of the training set, then the $\zeta_j(\lambda)$ can be derived using the entire training set.

- Step B: Translate the weights from the red side b_{ij}, to weights for whole spectrum, using

$$a_{ij} = \sum_{k=1}^{m} b_{ik}\ x_{kj}. \tag{2.9}$$

This resembles Equation (7), except that we now know $\boldsymbol{X}$ and we are deriving the a_{ij} that play the roles of the c_{ij} of step 1.

- Step C: Make a predicted spectrum,

$$p_{i,m}(\lambda) = \mu(\lambda) + \sum_{j=1}^{m} a_{ij}\ \xi_j(\lambda). \tag{2.10}$$

The predicted spectrum $p_{i,m}(\lambda)$ differs from the reconstruction $r_{i,m}(\lambda)$ because the reconstruction uses weights derived from the blue and red sides of the spectrum, using Equation (1), where as the predictions use weights derived from the red part of the spectrum alone, using Equations (8) and (9).

We provide the mean spectrum, the two sets of principal components, $\xi_j(\lambda)$ and $\zeta_j(\lambda)$, and the projection matrix $\boldsymbol{X}$, so the readers can make their own predictions. The numerical values of the projection matrix $\boldsymbol{X}$ are shown in the Appendix. The machine readable data are published in the electronic edition of the *Astrophysical Journal*.

2.5.3 Prediction Accuracy

In Figure 2.3, we show two relatively successful and two unsuccessful predictions, $p_{i,10}(\lambda)$, together with the corresponding continuum fitted QSO spectra, $q_i(\lambda)$. When the prediction fails, the predicted spectrum is systematically either too low or too high, but with no preference.

We assess the errors on our predictions using the absolute fractional flux error:

$$|\delta F_{i,m}| = \int_{\lambda_1}^{\lambda_2} \left| \frac{p_{i,m}(\lambda) - q_i(\lambda)}{q_i(\lambda)} \right| d\lambda \Big/ \int_{\lambda_1}^{\lambda_2} d\lambda. \tag{2.11}$$

For the blue side, $\lambda_1 = 1050$ Å and $\lambda_2 = 1170$ Å, avoiding the Lyβ and Lyα emission lines, and for the red side, $\lambda_1 = 1216$ Å and $\lambda_2 = 1600$ Å. In Table 2.1, we list the absolute fractional flux errors for each QSO, when we use $m = 10$ components. In Table 2.2, row (c) and (e), we list $< |\delta F_m| >= (1/N) \sum_{i=1}^{N} |\delta F_{i,m}|$, the mean of the absolute fractional flux error from all 50 QSOs, and we show how this mean changes with m. For comparison, in rows (b) and (d), we also list $< |\delta F_m| >$ obtained by reconstruction when we replace $p_{i,m}(\lambda)$ in Equation (11) by $r_{i,m}(\lambda)$ from Equation (1). These $r_{i,m}(\lambda)$ use principal components derived from the blue plus red sides. We find similar values if we use principal components from the red side alone.

The advantage of using more components is different for the reconstruction,

the red side prediction, and the blue side prediction. For the reconstruction and the red side prediction, more components always improve the fit (Table 2.2, row (b), (c), (d)), although the reduction of the error is small after about the 10th component, and we think the remaining 3% absolute fractional flux error is similar in size to the error of the continuum fitting (§2).

On the other hand, for the blue side prediction, adding more components does not reduce the mean error. We think the reason is related to the properties of the first few principal components. Only the third, fourth and fifth principal components have a significant slope. If we choose appropriate weights for these components, we are likely to make accurate predictions, and adding more components can reduce the residuals (Figure 2.3, panel (a), (b)). But if we choose inappropriate weights, there is no way to correct the slope (Figure 2.3, panel (c), (d)). Hence the main error in our predictions is a systematic slope error which makes the blue side prediction too high or too low.

Although our predictions give small errors for some QSOs, they give huge errors for others. With 10 components, the mode of the $|\delta F_{10}|$ distribution is 3%, the median is 8%, and the range is about 30%. We predict the blue continua of 28 QSOs out of 50 QSOs to $|\delta F_i| \leq 10\%$, but we do not know which QSOs will have these small errors. We find that many of the QSOs that give the largest errors have absorption or unusually low S/N on the red side of the Lyα line (1216 – 1240 Å, noted in Table 2.1) which makes the continuum level hard to estimate. This region is significant because it contains much of the variance and hence will have a large effect on the weights. However in others cases there is little or no absorption, and the slope of the spectrum appears to change as we cross the Lyα emission line. We do not in general see any correlation between the errors in the red and blue side predictions.

We introduce a third error statistic, the fractional flux error,

$$\delta F_{i,m} = \int_{\lambda_1}^{\lambda_2} \frac{p_{i,m}(\lambda) - q_i(\lambda)}{q_i(\lambda)} d\lambda \Big/ \int_{\lambda_1}^{\lambda_2} d\lambda, \tag{2.12}$$

to help us estimate the error in the integrated flux. This error is related to flux decrement statistic, D_a (Oke & Korycansky, 1982; Bernardi et al., 2003), which has been used to calibrate numerical simulations of the IGM (Croft et al., 2002b). In Table 2.1 we see that $\delta F_{i,10}$ has a similar magnitude to $|\delta F_{i,10}|$, also for the blue side, because the predictions tend to be too low or too high across the entire blue side. The mean of $\delta F_{i,m}$ for all 50 QSOs, $< \delta F_m >$, is zero by definition, at each wavelength, when we use $m = 0$, because $p_{i,0}(\lambda) = \mu(\lambda)$. When $m > 0$, the statistic $< \delta F_m >$ represents the bias in the predictions, and in Table 2.2 we see that it remains within a few percent of zero for all $m \leq 10$.

In Figure 2.4 we show an example of the prediction of the Lyα forest continuum of a higher redshift QSO from the Sloan Digital Sky Survey (York et al., 2000; Stoughton et al., 2002) for which the continuum is unobservable because of the large amount of absorption. To make this prediction, which looks acceptable, we use the red side of its spectrum.

Table 2.2. Mean Statistical Quantities for 50 Quasars

Component: m		1	2	3	4	5	6	7	8	9	10
Blue plus Red sides: 1020 Å $\leq \lambda \leq$ 1600 Å											
(a) Reconstruction	$< \delta E_m >$	50.1	31.5	22.8	15.9	11.8	8.7	6.7	5.7	4.6	3.7
Red Side: 1216 Å $\leq \lambda \leq$ 1600 Å											
(b) Reconstruction	$< \lvert\delta F_m\rvert >$	8.9	7.5	7.7	5.9	5.1	4.4	3.7	3.7	3.6	3.3
(c) Prediction	$< \lvert\delta F_m\rvert >$	8.7	6.7	6.5	5.4	5.6	4.4	4.3	3.9	4.1	3.1
Blue Side: 1050 Å $\leq \lambda \leq$ 1170 Å											
(d) Reconstruction	$< \lvert\delta F_m\rvert >$	10.5	6.9	5.5	4.1	4.0	3.9	4.1	3.3	3.7	3.2
(e) Prediction	$< \lvert\delta F_m\rvert >$	10.4	9.6	9.7	9.2	9.6	9.7	9.7	10.7	9.9	9.4
(f) Prediction	$< \delta F_m >$	−1.4	−1.0	−1.2	−1.0	−1.2	−1.2	−1.2	−2.2	−1.4	−1.3

Note. — We have multiplied the values, which are the means for all 50 QSOs, by 100.

Figure 2.3: Four examples of our predicted spectra and their accuracy. The top two gave relatively small errors, and the bottom two relatively large. Note that the vertical scales are not all the same. The panels on the left show in thick lines the original continuum fitted spectra, $q_i(\lambda)$. The thin lines show the spectra predicted using 10 components ($p_{i,10}(\lambda)$, Equation (10)). We do not show any reconstructions $r_{i,j}(\lambda)$, to either the red sides or the whole spectra. The panels on the right show the corresponding absolute fractional flux error (Equation (11)) averaged over the part of the blue (1050 – 1170 Å, thin lines) and the whole of the red (1216 – 1600 Å, thick) sides for each QSO. For both the blue and red we show the predictions (Equation (10)) and not reconstructions, which are usually better. For the top two QSOs the errors decrease when we use more components, reaching 2 – 6% on both the red and blue sides with 10 components. For the bottom two QSOs, the predictions reach 3 – 4% on the red side, because we use information from those parts of the spectrum, but they are too low or too high by 13 – 23 % on the blue side, primarily because the level is wrong, even though the emission line shapes seen excellent. These four QSOs represent the variety found in the sample of 50 QSOs. We were unable to predict which QSOs would behave like the top or bottom two.

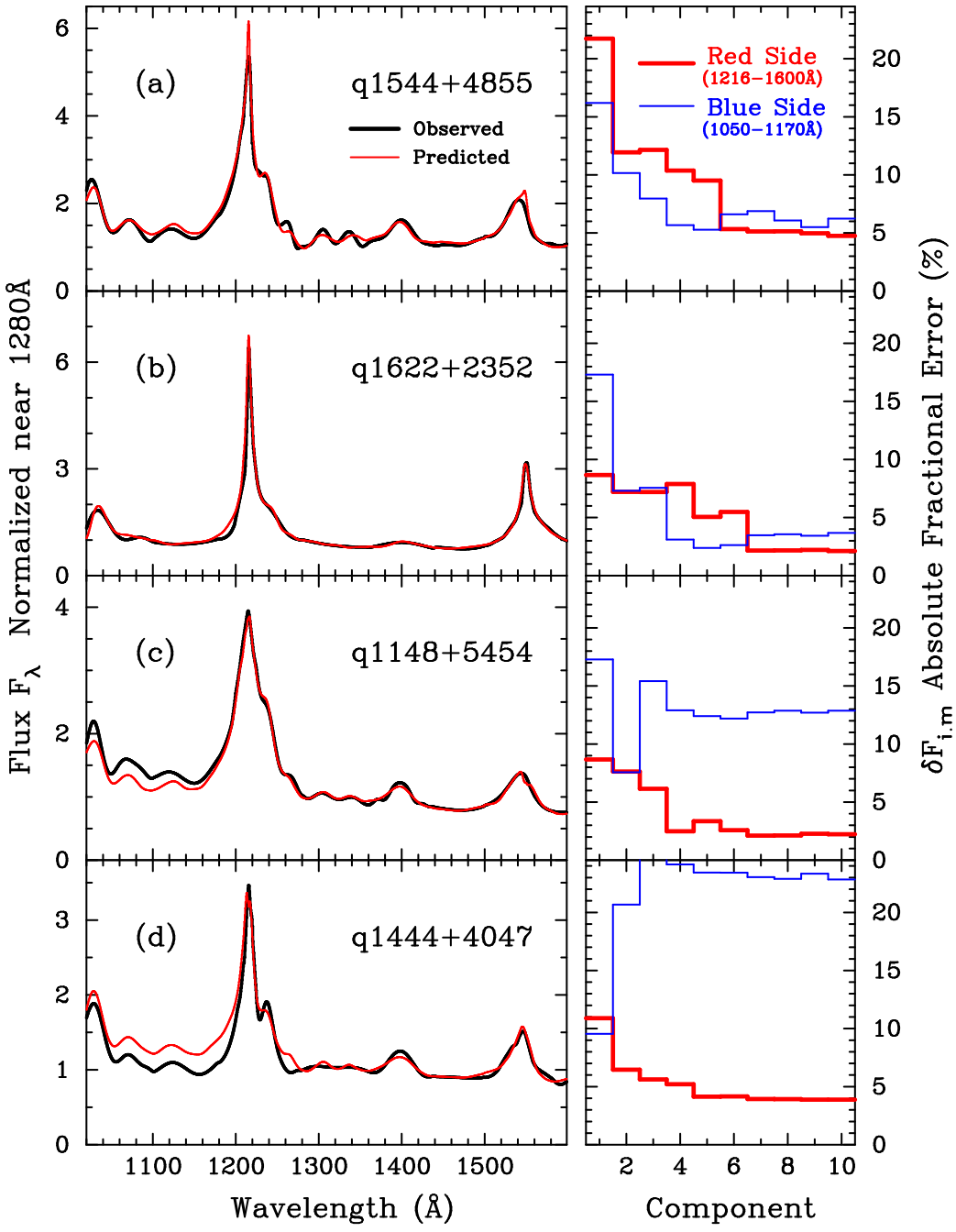
(a)
q1544+4855
Observed
Predicted
(b)
q1622+2352
(c)
q1148+5454
(d)
q1444+4047
Red Side
(1216–1600Å)
Blue Side
(1050–1170Å)
Flux F_λ Normalized near 1280Å
Wavelength (Å)
Component
$\delta F_{i,m}$ Absolute Fractional Error (%)

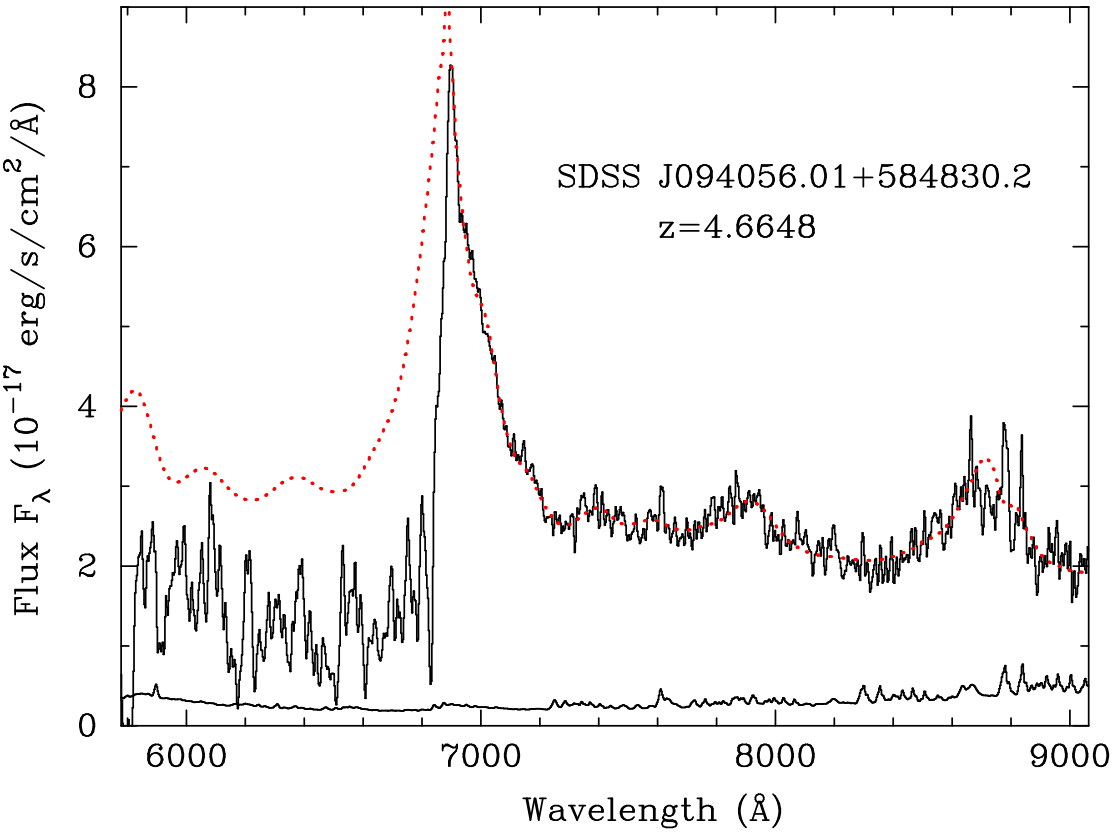

Figure 2.4: An example of a continuum predicted (dotted line) using Equations (8) – (10) for a high redshift QSO, SDSS J094056.01+584830.2 (solid lines). The only information that we use on this QSO is the red side of this spectrum, from 1216 – 1600 Å. The Lyα forest forest absorbs strongly and no pixels in this low resolution spectrum reach the predicted continuum level. We suspect the predicted blue continuum has the correct shape, including the two emission lines between Lyβ and Lyα, but we know that the overall level could be in error by 5 – 30%, as we saw in Figure 2.3.

2.5.4 Errors and Different Methods

Although the error in the levels of many of the predictions was unexpected, we can think of many possible explanations, including the intrinsic QSO spectra, calibration errors, and the method.

The intrinsic slope of the continuum may be changing at the UV wavelengths we consider (Zheng et al., 1997; Telfer et al., 2002). The UV flux from QSOs is black body radiation from the accretion disk around the central super massive black hole (Malkan, 1983; Sun & Malkan, 1989). If we pass over the peak of the black body continuum, the slope changes rapidly, and we will not have enough wavelength coverage to follow the change of the slope.

There are many possible errors in the calibration of the spectra, especially the Galactic extinction correction (Fitzpatrick, 1999). At our wavelengths, the extinction increases rapidly as the wavelength drops. If we underestimate color excess E(B-V) for a $z = 0$ QSO by 0.01 magnitudes, we decrease the flux at 1600 Å by 7%, and at 1020 Å by 14% .

We have presented only one of many ways of predicting spectra. We attempted some other less successful schemes before we arrived at this method. For instance, we fitted the red side by minimizing the χ^2 of $\xi_j(\lambda)$ against $q_i(\lambda)$ to get a_{ij}, but we found the blue side prediction is then unstable. Different combinations of the principal components give similar χ^2 on the red side, but their blue sides can have a large variety.

We also experimented with different ways of normalizing the spectra, both near 1450 Å and using the entire red side, and we obtain similar results. We tried attempting to remove the slopes from spectra, by fitting a straight line to the red sides, but these lines were not adequately determined.

The predictions given here could be improved in several ways. We should first seek improved methods, which might not involve PCA. If we had spectra of many more QSOs we would be less subject to the distortions and noise in individual

spectra, and we could test the predictions on spectra that were not in the training set. Higher resolution and higher S/N spectra would help to reveal the weak emission features, and reduce the errors in the initial continuum fit. Extending the wavelength range on the red side may help identify the slope of the continuum for some QSOs, but for others we found that a reduced wavelength range, from 1216 – 1400 Å gave better predictions, because this restricted range has a stronger correlation with the flux on the blue side. We have also made predictions with the red side restricted to 1280 – 1600 Å, to avoid the large flux errors that can occur when there are absorption lines in the Lyα and N V emission lines. We found that there was no significant change in $< |\delta F_m| >$.

2.6 Appendix : Projection Matrix $\boldsymbol{X}$

The following is the 10×10 projection matrix $\boldsymbol{X}$ discussed in §2.5:

$$\boldsymbol{X} = \begin{pmatrix}
-1.326 & -0.042 & -0.000 & -0.040 & -0.016 & -0.011 & -0.001 & -0.004 & 0.000 & 0.001 \\
0.023 & 1.158 & 0.054 & -0.488 & 0.078 & -0.120 & -0.016 & 0.013 & 0.003 & -0.006 \\
-0.143 & 0.457 & 0.883 & 0.528 & -0.251 & -0.224 & -0.115 & 0.001 & 0.014 & -0.016 \\
0.484 & -0.405 & 0.348 & -0.705 & -0.829 & 0.255 & 0.186 & -0.015 & -0.008 & -0.034 \\
-0.112 & 0.053 & -0.241 & 0.335 & -0.013 & -0.680 & 0.973 & 0.249 & 0.207 & -0.197 \\
-0.596 & 1.105 & 0.430 & 0.419 & 0.224 & 1.162 & 0.310 & 0.025 & 0.517 & 0.185 \\
-0.628 & 1.206 & -0.806 & 0.704 & -0.468 & 0.563 & -0.181 & 0.679 & -0.292 & -0.317 \\
0.414 & -0.301 & -1.021 & -0.112 & -0.552 & -0.529 & -0.665 & -0.141 & 0.840 & -0.249 \\
1.667 & 0.372 & -0.254 & 0.213 & -0.082 & -0.506 & 0.264 & 0.327 & -0.490 & 0.445 \\
3.039 & 0.344 & -0.426 & -0.321 & -0.515 & -0.585 & -0.139 & 0.118 & -0.080 & -0.144
\end{pmatrix}.$$

2.7 Acknowledgments

This Chapter 2, in full, is a reprint of the material as it appears in *Astrophysical Journal*, volume 618, page 592, 2005. The dissertation author did the bulk of the work and the first author of this paper.

Chapter 3

Quasar Spectrum Classification with PCA

3.1 Abstract

We investigate the variety in quasar UV spectra ($\lambda\lambda$1020-1600) with emphasis on the weak emission lines in the Lyα forest region using principal component analysis (PCA). This paper is a continuation of Suzuki et al. (2005, Paper I), but with a different approach. We use 50 smooth continuum fitted quasar spectra ($0.14 < z < 1.04$) taken by the *Hubble Space Telescope* (*HST*) Faint Object Spectrograph. There are no broad absorption line quasars included in these 50 spectra. The first, second and third principal component spectra (PCS) account for 63.4, 14.5 and 6.2% of the variance respectively, and the first seven PCS take 96.1% of the total variance. The first PCS carries Lyα, Lyβ and high ionization emission line features (O VI, N V, Si IV, C IV) that are sharp and strong. The second PCS has low ionization emission line features (Fe II, Fe III, Si II, C II) that are broad and rounded. Three weak emission lines in the Lyα forest are identified as Fe II λ1070.95, Fe II+Fe III λ1123.17, and C III* λ1175.88. Using the first two standardized PCS coefficients, we introduce five classifications: *Class Zero* and *Classes I-IV*. These classifications will guide us in finding the continuum level in the Lyα forest. We show that the

emission lines in the Lyα forest become prominent for *Classes III* and *IV*. By actively using PCS, we can generate artificial quasar spectra that are useful in testing the detection of quasars, DLAs, and the continuum calibration. We provide 10,000 artificially generated spectra. We show that the power-law extrapolated continuum is inadequate to perform precise measurements of the mean flux in the Lyα forest because of the weak emission lines and the extended tails of Lyα and Lyβ/O VI emission lines. We introduce a correction factor δF so that the true mean flux $\langle F \rangle$ can be related to $\langle F_{Power-Law} \rangle$ as measured using power-law continuum extrapolation by : $\langle F \rangle = \langle F_{Power-Law} \rangle \cdot \delta F$. The correction factor δF ranges from 0.84 to 1.05 with a mean of 0.947 and a standard deviation of 0.031 for our 50 quasars. This result means that using power-law extrapolation we miss 5.3% of flux on average and we show that there are cases where we would miss 16% of flux. These corrections are essential in the study of the intergalactic medium at high redshift in order to achieve precise measurements of physical properties, cosmological parameters, and the reionization epoch.

3.2 Introduction

It is important for the study of quasar absorption lines to understand the shape of the continua in the Lyα forest from which we study the physical properties of the intergalactic medium (IGM) and extract cosmological parameters (Kirkman et al., 2003; Tytler et al., 2004a). It is the uncertainty of continuum fitting to the Lyα forest that makes precise measurements difficult(Croft et al., 2002a; Suzuki et al., 2003; Jena et al., 2005). Thus, we wish to have a simple and objective quasar spectrum classification scheme that enables us to describe the global shape of the continuum as well as the individual emission line profiles. The principal component analysis (PCA), also known as Karhunen-Loève expansion (Karhunen, 1947; Loève, 1948), is one of the best methods to carry out such classification (Kendall, 1980).

PCA enables one to summarize the information contained in a large data

set, and it is widely used in many areas of astronomy (Connolly et al., 1995; Cabanac et al., 2002, and references therein). Francis et al. (1992) applied PCA to quasar spectra using 232 quasar spectra ($1.8 < z < 2.2$; $\lambda\lambda 1150 - 2000$) from the Large Bright Quasar Survey (LBQS; Hewett et al., 1995, 2001). They showed that the first three principal components account for 75% of the variance. Boroson & Green (1992) used 87 low redshift quasar spectra ($z < 0.5$) and showed the anticorrelation between the equivalent width of Fe II and [O III] and the correlation between the luminosity, the strength of He II $\lambda 4686$, and the slope index α_{ox}. Boroson (2002) investigated the relation between the first two principal components and the physical properties such as black hole mass, luminosity, and radio activity. Shang et al. (2003) studied 22 low redshift UV and optical quasar spectra ($z < 0.5$; $\lambda\lambda 1171 - 6607$) and showed the relation between the first principal component and the Baldwin effect, which is the anticorrelation between the luminosity and the equivalent width of the C IV emission line. Yip et al. (2004) applied PCA to the 16,707 Sloan Digital Sky Survey quasar spectra ($0.08 < z < 5.41$; $\lambda\lambda 900 - 8000$) and reported that the spectral classification depends on the redshift and luminosity, and that there is no compact set of eigenspectra that can describe the majority of variations. They also showed the relationship between eigencoefficients and the Baldwin effect.

In Suzuki et al. (2005, hereafter Paper I) we analyzed 50 continua fitted quasar spectra taken by the Hubble Space Telescope (*HST*) Faint Object Spectrograph. Since they are at low redshifts ($0.14 < z < 1.04$), and the Lyα forest lines are not so dense, we can see and correctly fit the continuum to the spectra. Using PCA we attempted to predict the continuum level in the Lyα forest where the continuum levels are hard to see because of the abundance of the IGM absorptions. Although we succeeded in predicting the shape of the weak emission lines in the Lyα forest region, our prediction suffers systematic errors of $3 - 30\%$.

The goal of this paper is to explore the variety of quasar UV spectra in the following manner: 1. we clarify the PCA formulation in order to describe quasar UV spectra quantitatively (§3.4) using eigenspectra or the principal component spectra

(PCS), 2. we introduce five classes of quasar UV spectra to help us understand the variety of quasar spectra qualitatively (§3.6), 3. we introduce the idea of artificial quasar spectra (§3.5) and 4. the mean flux correction factor δF (§3.7), and 5. we report the identities of three weak emission lines in the Lyα forest (Appendix).

3.3 Data

We use the same 50 *HST* FOS spectra from Paper I, and the detailed description is therein. Here we summarize the 50 *HST* spectra. These 50 quasar spectra are a subset of the 334 high resolution *HST* FOS spectra (R $\sim$ 1300) collected and calibrated by Bechtold et al. (2002) which include all of the *HST* QSO Absorption Line Key Project's data (Bahcall et al., 1993, 1996; Jannuzi et al., 1996). Bechtold et al. (2002) identified both intergalactic and interstellar medium lines and corrected for Galactic extinction.

For each spectrum, we combined the individual exposures and remeasured the redshift using the peak of the Lyα emission line. Then we brought the spectrum to the rest frame and rebinned it into 0.5 Å pixels. We masked the identified absorption lines and fitted a smooth Chebyshev polynomial curve. We normalized the flux by taking the average of 21 pixels around 1280 Å where no emission line is seen.

We chose the wavelength range from 1020 to 1600 Å so that we can cover the Lyα forest between the Lyβ and the Lyα emission lines while maximizing the number of spectra. We removed broad absorption line (BAL) quasars from the sample since we are interested in emission line profiles and the continuum shape. Lastly, we removed quasars with S/N < 10 per pixel because we cannot extract weak emission line features in low S/N spectra. The redshift range of the 50 spectra is from 0.14 to 1.04 with a mean of 0.58. The average S/N is 19.5 per 0.5 Å binned pixel.

3.4 PCA & Principal Component Spectrum

3.4.1 The PCA Formulation

We express a quasar spectrum in Dirac's "bra ket" form, $|q_i\rangle$, which is commonly used in quantum mechanics and simplifies our description (Sakurai, 1985). We claim that any quasar spectrum, $|q_i\rangle$, is well represented by a reconstructed spectrum, $|r_{im}\rangle$, which is a sum of the mean and the weighted m principal component spectra:

$$|q_i\rangle \sim |r_{i,m}\rangle = |\mu\rangle + \sum_{j=1}^{m} c_{ij}|\xi_j\rangle \tag{3.1}$$

where i refers to a quasar, $|\mu\rangle$ is the mean quasar spectrum, $|\xi_j\rangle$ is the jth principal component spectrum (PCS), and c_{ij} is its weight. Unlike quantum mechanics, the weight, c_{ij}, is not a complex number but a real number. We found the covariance and correlation matrix of the 50 quasar spectra in Paper I and by diagonalizing the covariance matrix, we can obtain the PCS. In practice, we found the PCS via a singular value decomposition (SVD) technique from the 50 quasar spectra. The recipes can be found in Francis et al. (1992) and Paper I. Since we defined PCS to be orthonormal:

$$\langle \xi_i | \xi_j \rangle = \delta_{ij}, \tag{3.2}$$

and we can obtain the weights c_{ij} by calculating the following inner product:

$$c_{ij} = \langle q_i - \mu | \xi_j \rangle. \tag{3.3}$$

We show the mean spectrum in Figure 3.1 and the first 10 PCS and the distribution of their weights in Figure 3.2 and 3.3. Although wavelength coverage, normalization, resolution, and the number of quasars are different, the general trend of PCS is similar to that of Francis et al. (1992) with the exception of the third PCS. The reason for the exception is that the third PCS of Francis et al. (1992) takes

into account BAL features, while we do not have such features since we removed BAL quasars. Our third PCS has sharp emission line features for Lyβ/O VI, the core of Lyα, and C IV emission lines, but broad negative features around the Lyα emission line. The continua of the third, fourth and fifth PCS have a slope, and the fifth PCS includes the asymmetric feature for the strong emission lines. The fifth PCS is similar to the second PCS in that P-Cygni profiles are seen but they are very broad, and there are no low ionization emission line features blueward of the Lyα emission line. The sixth and seventh PCS carry some information on low ionization weak emission lines, but the spectrum features are getting noisy. The eighth and higher order PCS have high frequency wiggles which no longer correspond to any physical emission lines and are probably due to fitting errors. We used continua fitted spectra which are free from photon noise, but still they are likely to suffer fitting errors of at least a few percent as we can see in Figures 3.7-3.11. The mean spectrum and the first 10 PCS are available on-line from the Paper I. Next, let us discuss the contribution from each PCS quantitatively.

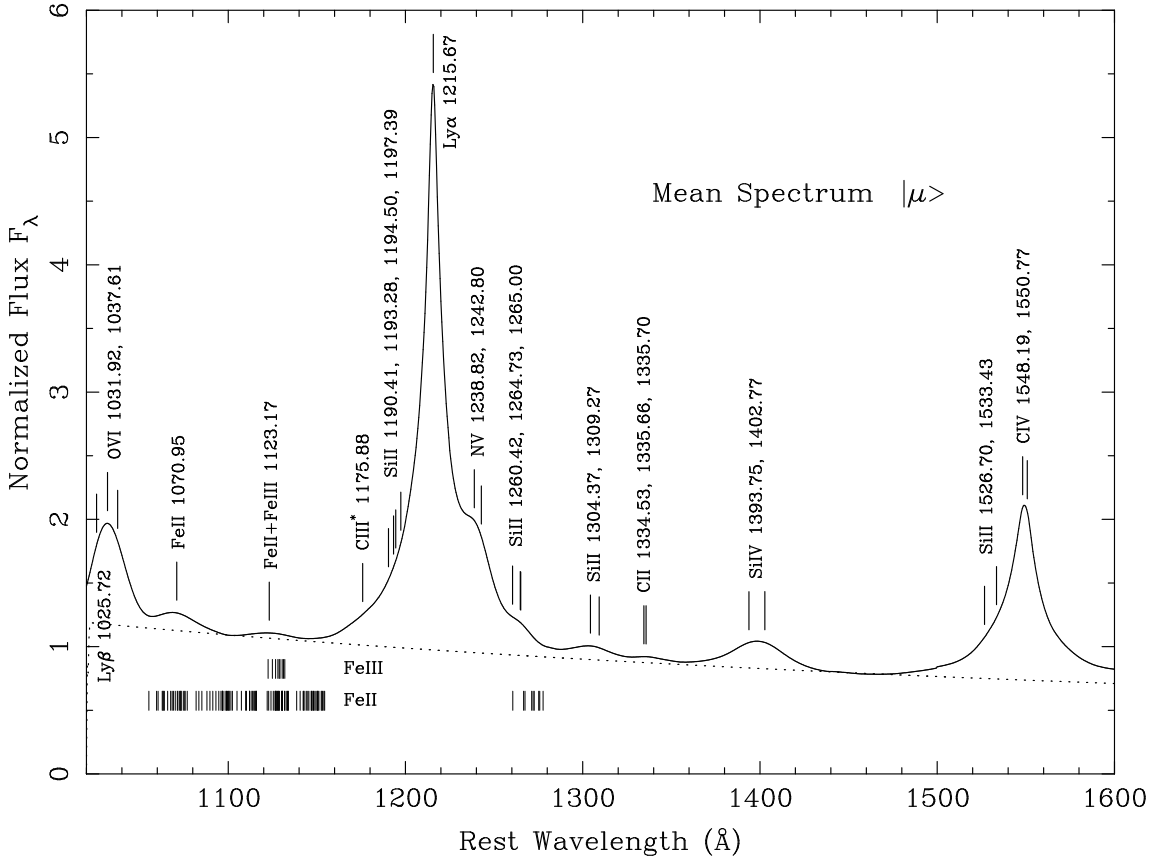

Figure 3.1: The mean spectrum of 50 *HST* quasar spectra: The spectrum is normalized near 1280 Å. The wavelengths are taken from Morton (1991) except Fe II, Fe III and CIII* lines that are observed wavelengths from Tytler et al. (2004b). The tick marks shown below the spectrum are the wavelengths of the Fe II and Fe III multiplet. The dotted line is the power-law continuum approximation. Note the emission lines do exist in the Lyα wavelength region, We also note the wavelength separation of Si IV doublet at λ1400 is relatively large, and makes the line profile broad.

Figure 3.2: The first five PCS 1-5 are shown in the left panels with the distribution of PCS coefficients c_{ij} on the right. The first PCS takes the Lyα, Lyβ and the high ionization line features (O VI, Si IV, C IV) while the second PCS account for the low ionization lines (Fe II, Fe III, Si II, C II). We expect to have the low ionization lines in the Lyα forest when a quasar has the negative second PCS coefficient. We note that PCS are designed to be orthonormal. The quasar spectra are normalized near 1280 Å and every PCS has zero value near 1280 Å.

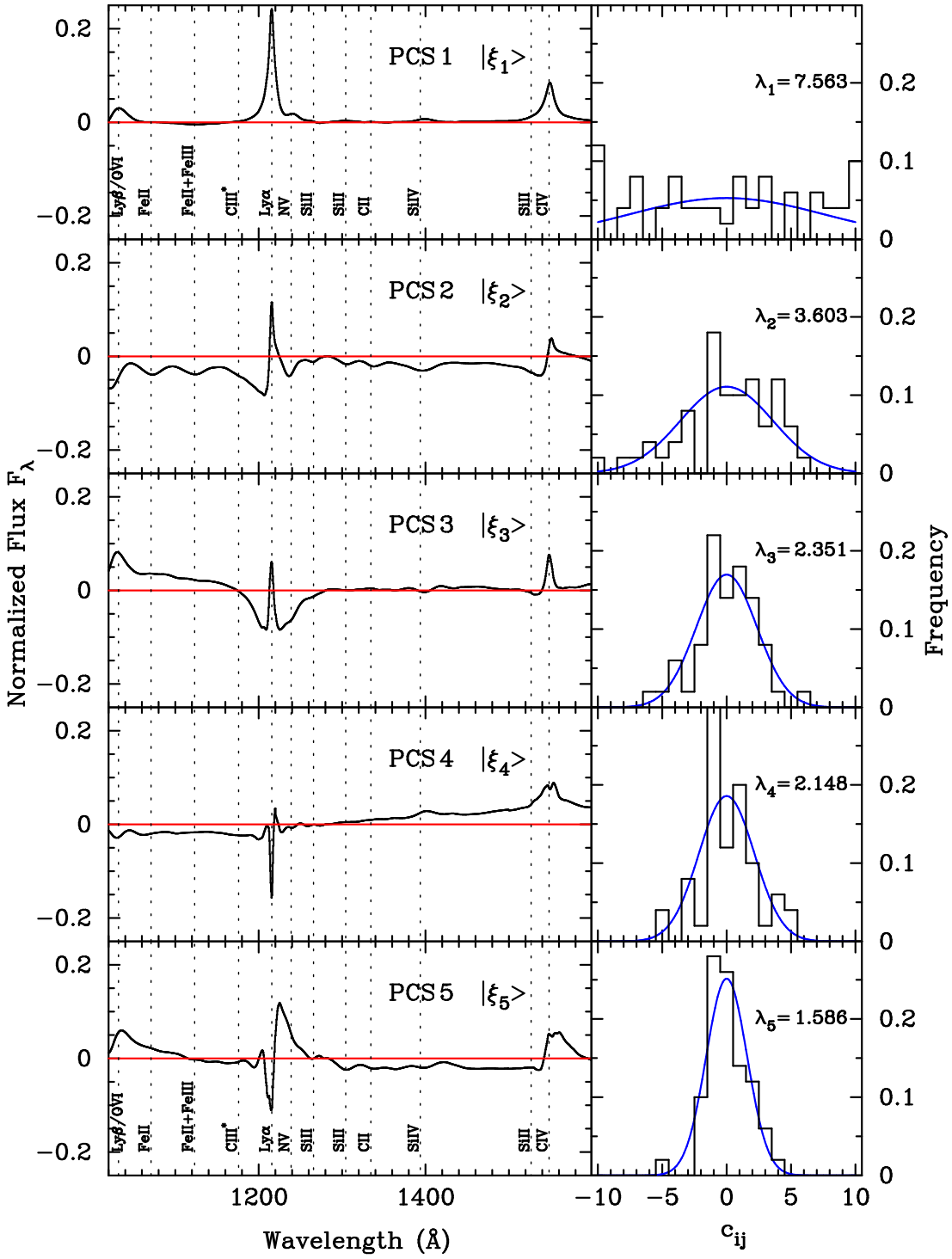
PCS 1 |ξ1>
PCS 2 |ξ2>
PCS 3 |ξ3>
PCS 4 |ξ4>
PCS 5 |ξ5>
λ1= 7.563
λ2= 3.603
λ3= 2.351
λ4= 2.148
λ5= 1.586
Lyβ/OVI
FeII
FeII+FeIII
CIII*
Lyα
NV
SiII
SiII
CII
SiIV
SiII
CIV
Normalized Flux Fλ
Wavelength (Å)
Frequency
cij

Figure 3.3: The same as Figure 3.2 but the second five PCS 6-10. From 8th and higher PCS, the features in PCS become noisy and no longer have physical correspondence. They are probably fitting errors.

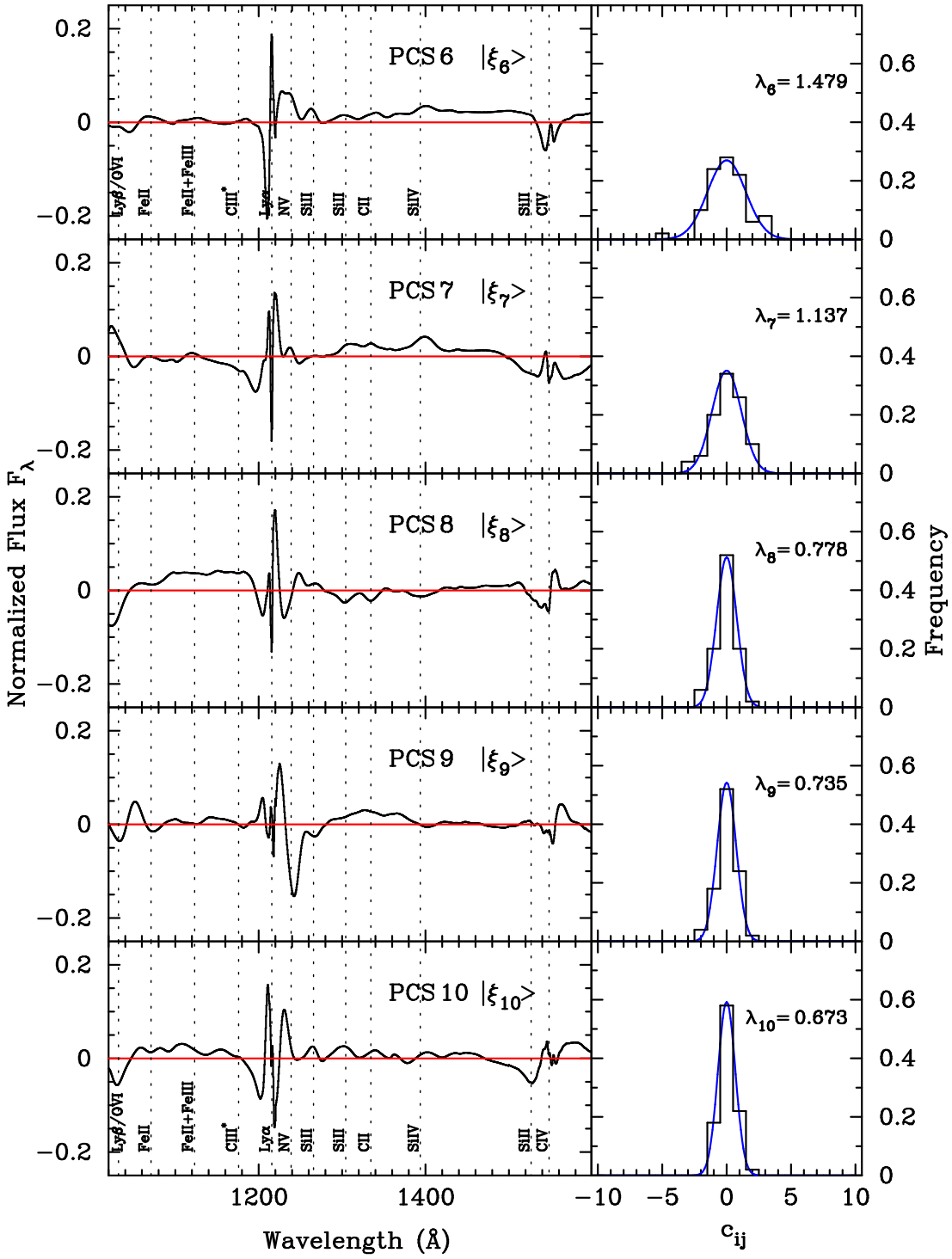
PCS 6 |ξ6>
PCS 7 |ξ7>
PCS 8 |ξ8>
PCS 9 |ξ9>
PCS 10 |ξ10>
λ6= 1.479
λ7= 1.137
λ8= 0.778
λ9= 0.735
λ10= 0.673
Lyβ/OVI
FeII
FeII+FeIII
CIII*
Lyα
NV
SiII
SiII
CII
SiIV
SiII
CIV
Normalized Flux Fλ
Wavelength (Å)
Frequency
cij

3.4.2 Quantitative Assessment of PCA Reconstruction

We make use of the residual variance to assess the goodness of PCA reconstruction. The residual variance of a reconstructed quasar spectrum with m components is a sum of the squares of the difference between the quasar spectrum, $|q_{i,}\rangle$, and the reconstructed spectrum, $|r_{i,m}\rangle$:

$$\langle q_i - r_{i,m} | q_i - r_{i,m} \rangle = \sum_{i=m+1}^{N} c_{ij}^2, \tag{3.4}$$

where N is the number of quasar spectra. For the overall contribution from mth PCS, we define the residual variance fraction, f(j), as follows:

$$f(j) = \frac{\sum_{i=1}^{N} c_{ij}^2}{\sum_{i,j=1}^{N} c_{ij}^2}. \tag{3.5}$$

We redefine the square root of the eigenvalue of the jth PCS as follows:

$$\lambda_j = \frac{1}{N-1} \sqrt{\sum_{i=1}^{N} c_{ij}^2}. \tag{3.6}$$

Then we wish to use λ_j to describe the probability distribution function (PDF) of the PCS coefficients. The PDF of the weights is not necessarily a Gaussian, but as shown in Figures 3.2 and 3.3, the PDF can be well represented by a Gaussian. We also note that by construction:

$$\sum_{i=1}^{N} c_{ij} = 0 \tag{3.7}$$

for any j. Thus, the PDF of weights is characterized by just one parameter, λ_j. The probability of having a weight, c_{ij}, in an interval, $-x_0 \leq c_{ij} \leq x_0$ can be expressed as:

$$P(-x_0 \leq c_{ij} \leq x_0) = \int_{-x_0}^{x_0} \frac{1}{\sqrt{2\pi}\lambda j} e^{-\frac{x^2}{2\lambda_j^2}} dx. \tag{3.8}$$

Naturally, it would be convenient if we standardize the weight, c_{ij}, by λ_j. We can then rewrite a quasar spectrum as:

$$|q_i\rangle \sim |r_{i,m}\rangle = |\mu\rangle + \sum_{j=1}^{m} \lambda_j \sigma_{ij} |\xi_j\rangle \tag{3.9}$$

where the σ_{ij} are the standardized PCS coefficients which represent the deviation from the mean spectrum of the jth PCS of quasar i. The PDF of the σ_{ij} is a normal distribution, so we can immediately tell how far and how different the quasar spectrum would be from the mean spectrum. This standardization of the weights simplifies the discussion of the variety of quasar spectra in §3.6.

Another advantage of using λ_j is that we can simplify the residual variance fraction f(j):

$$f(j) = \frac{\lambda_j^2}{\sum_{j=1}^{N} \lambda_j^2}. \tag{3.10}$$

The values of f(j) are listed in Table 3.1. The first, second and third PCS account for 63.4%, 14.5% and 6.2% of the variance respectively. In total, the first three PCS account for 84.3% of the variance of the 50 quasars in our sample. These fractions depend on the normalization and the wavelength coverage. In the literature, Francis et al. (1992) report that the first three PCS account for 75% ($\lambda\lambda 1150 - 2000$), and Shang et al. (2003) show that the first three PCS carry 80% ($\lambda\lambda 1171 - 2100$) of the variance. Both groups normalized flux by the mean flux, while this paper normalizes by a flux value near 1280 Å. Our value of 84.3% is slightly higher than the above numbers probably because we removed the BAL quasars, which are certainly a source of variance. In addition, we used fitted smooth continua to the Lyα forest, while they used the observed raw Lyα forest which obviously contains a large variance (Tytler et al., 2004a). As shown in Table 3.1, the contribution from each PCS component to the variance rapidly decreases with order m. It becomes less than 1% after the 8th PCS and then stays the same. With seven PCS components, 96% of the variance has already been accounted for. As is

seen in the PCS features in Figure 3.3, the remaining 4% of the variance is probably due to fitting errors.

Table 3.1. Eigenvalue and Residual Variance Fraction

Component : j	1	2	3	4	5	6	7	8	9	10
Eigenvalue λ_j^2	57.204	12.985	5.528	4.614	2.516	2.189	1.293	0.605	0.541	0.453
λ_j	7.563	3.604	2.351	2.148	1.586	1.479	1.137	0.778	0.735	0.673
Residual Variance Fraction f(j)	0.637	0.145	0.062	0.051	0.028	0.024	0.014	0.007	0.006	0.005
Cummulative Residual Variance Fraction	0.637	0.781	0.843	0.894	0.922	0.947	0.961	0.968	0.974	0.979

Note. — Cummulative residual variance fracion is a simple sum of residual variance fraction upto jth PCS.

3.5 Artificial Spectra

We can use PCS to generate artificial spectra. Artificial spectra can be useful in testing the detection of quasars and DLAs, in flux calibration, in intrinsic quasar flux level fitting, and in cosmological simulations. By assigning PCS coefficients randomly from known PDFs, we can generate artificial quasar spectra. As we have discussed in §3.4, the PDF of the jth PCS coefficient is well represented by a Gaussian with a mean of 0, and a standard deviation of λ_j. If we then sum up the PCS with these coefficients (equation 3.9), we can create a set of artificial quasar spectra.

Noiseless quasar spectra are of great use in IGM studies, since at high redshift, it is difficult to see the intrinsic flux level in the Lyα forest. Even at redshift 2, pixels in the Lyα forest hardly reach the flux level with FWHM=250km/s (Tytler et al., 2004b). Artificial quasar spectra can thus be useful to predict the shape of continuum in the Lyα forest (Paper I) and to calibrate continuum fitting to the Lyα forest (Tytler et al., 2004a,b). They would be also useful to test the detection limit of the high redshift quasar survey since the Lyα emission can possibly boost the brightness by 0.15 magnitude. We have generated 10,000 artificial quasar spectra using the first seven PCS for a more realistic representation of the quasar spectra. We concluded that the features seen in PCS greater than eighth are noise, and we did not include higher order PCS. We will provide artificially generated spectra to the community upon request.

3.6 PCA Classification

3.6.1 Introduction of Five Classes

This paper attempts to classify quasar spectra quantitatively using our standardized PCS coefficients, σ_{ij}. We note that there is no discrete classification of quasar spectra and that they vary continuously. However, this classification will

help us in fitting the continua to the Lyα forest spectrum. We use the first two PCS coefficients to demonstrate the variety of emission lines and continua. We divide the σ_{i1} vs. σ_{i2} diagram (Figure 3.4) into five zones and introduce five classes of spectral types that enable us to discuss the shape of continua qualitatively. As we have seen in §3.4 and Table 3.1, the first two PCS coefficients account for 77.9% of the variance and represent the overall shape of the quasar spectrum. We introduce polar coordinates as follows:

$$r_i = \sqrt{\sigma_{i1}^2 + \sigma_{i2}^2} \tag{3.11}$$

$$\tan\theta_i = \frac{\sigma_{i2}}{\sigma_{i1}} \tag{3.12}$$

where r_i represents the deviation from the mean spectrum, and the angle θ_i tells us about the profiles of the emission lines.

The main goal of this classification is to differentiate the families of quasar spectra. In practice, when we fit the intrinsic flux level to a quasar spectrum, it would be convenient for us if we could know from which family of the quasar spectrum we should start with. First, we define *Class Zero* for those close to the mean spectrum in shape. We define *Class I-IV* corresponding to the quadrant *I-IV* in the σ_{i1} vs. σ_{i2} diagram, shown in Figure 3.4. The probability of $r \leq r_0$ is:

$$P(r \leq r_0) = \int_0^{r_0} r e^{-\frac{r^2}{2}} dr \tag{3.13}$$

$$= 1 - e^{-\frac{r_0^2}{2}}. \tag{3.14}$$

Now, we wish to define the fraction of the five classes to be equal, namely 0.2 each. We find $r_0 = 0.668$ gives $P(r \leq r_0) = 0.2$, so we define *Class Zero* for a quasar spectrum that has $r \leq 0.668$. For quasar spectra with $r > 0.668$, we define the classes *I* through *IV* corresponding to the quadrants first through fourth on the σ_{i1} vs. σ_{i2} diagram (Figure 3.4).

Our standardized PCS coefficients are plotted on the σ_{i1} vs. σ_{i2} diagram in Figure 3.4 where the dotted circle is the circle with radius $r_0 = 0.668$. The small numbers noted beside the points are the quasar identification numbers i that are listed in Table 3.2.

3.6.2 Demonstration of Five Classes

We show the mean spectrum in Figure 3.1. By definition the mean spectrum $|\mu\rangle$ has r=0, and naturally it belongs to *Class Zero*. In Figure 3.5 we show the artificially generated four classes, *I-IV*, of the quasar spectra to illustrate their typical spectral shape. They are the sum of the mean and the first two PCS with $\sigma_{i1} = \pm 1$ and $\sigma_{i2} = \pm 1$. The generated four spectra of *Class I-IV* have angles θ: $45°, 135°, 225°$ and $315°$ respectively, and they all have $r = \sqrt{2}$. The four spectra are plotted on the same scale in Figure 3.5 so that we can see the contrast of the emission lines with the continuum in a uniform manner.

In Figure 3.7-3.11, we show three observed spectra from each class where we intentionally chose the extreme cases for *Class I-IV*. Quasars are plotted at rest frame wavelengths with the luminosities that are calculated by using the cosmological parameters from the first year WMAP observation (h=0.71, Ω_m=0.27, Ω_Λ=0.73 ; Spergel et al., 2003), and a flat universe is assumed. The smoothed line on the spectrum is the fitted intrinsic flux level, and the solid straight line is the power-law continuum fit. The vertical dotted lines show the wavelengths of emission lines in the Lyα forest and the low ionization lines redward of the Lyα emission line. The quasar numbering in Figure 3.7-3.11 is the same as in Figure 3.4 so that we can visualize where the quasar spectrum is in the σ_{i1} vs. σ_{i2} diagram. In Table 3.2, quasars are sorted by classes, and the equivalent width of the emission lines are listed.

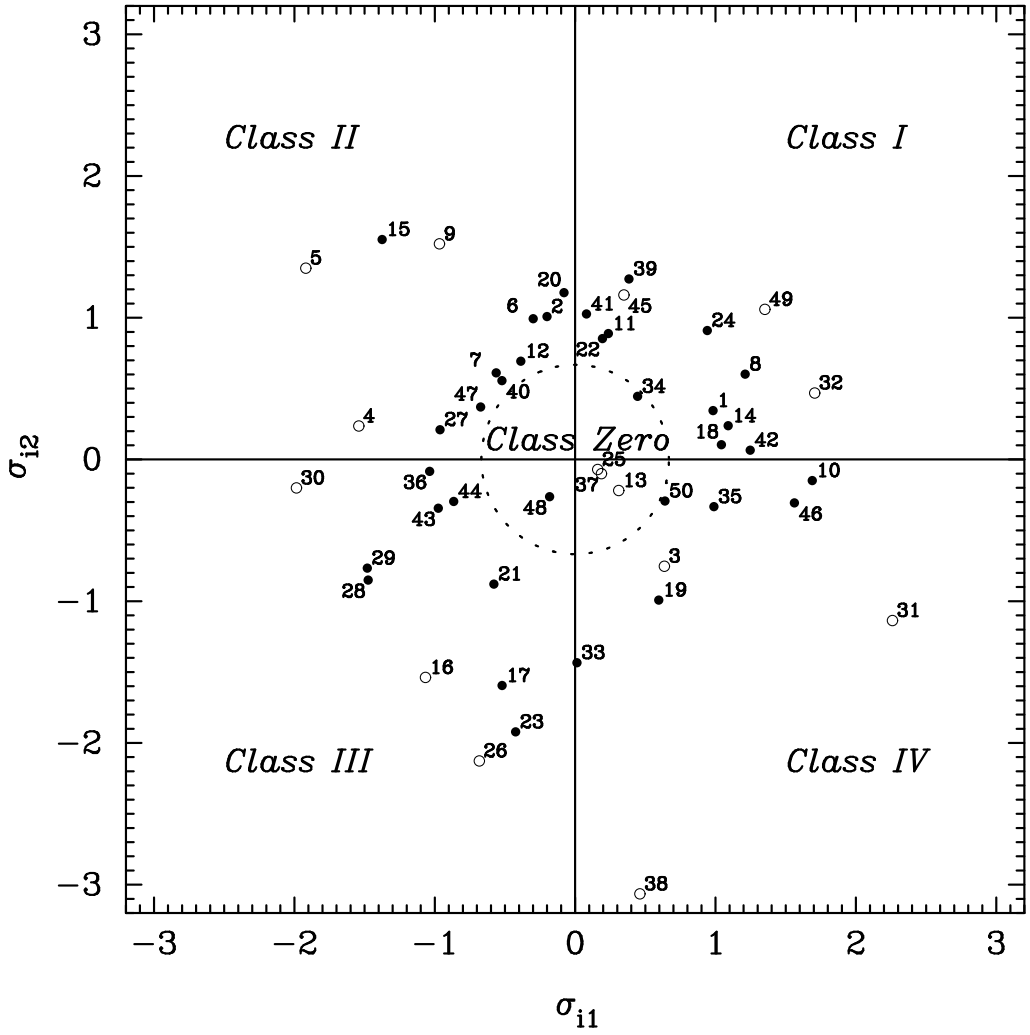

Figure 3.4: The distribution of standardized first two PCS coefficients for 50 quasars. The small number besides each point is quasar number i which is listed in Table 3.2. For quasars with open circles, we have quasar spectra shown in Figure 3.7-3.11. We intentionally chose extreme cases to show a wide variety of quasar spectra. The dotted circle has the radius of 0.668. We divide this plane into the five zones and define the five classes. We define *Class Zero* as the quasars which have radius less than or equal to 0.668 and *Class I-IV* as the ones which have radius greater than 0.668 and are in quadrants *I-IV* respectively.

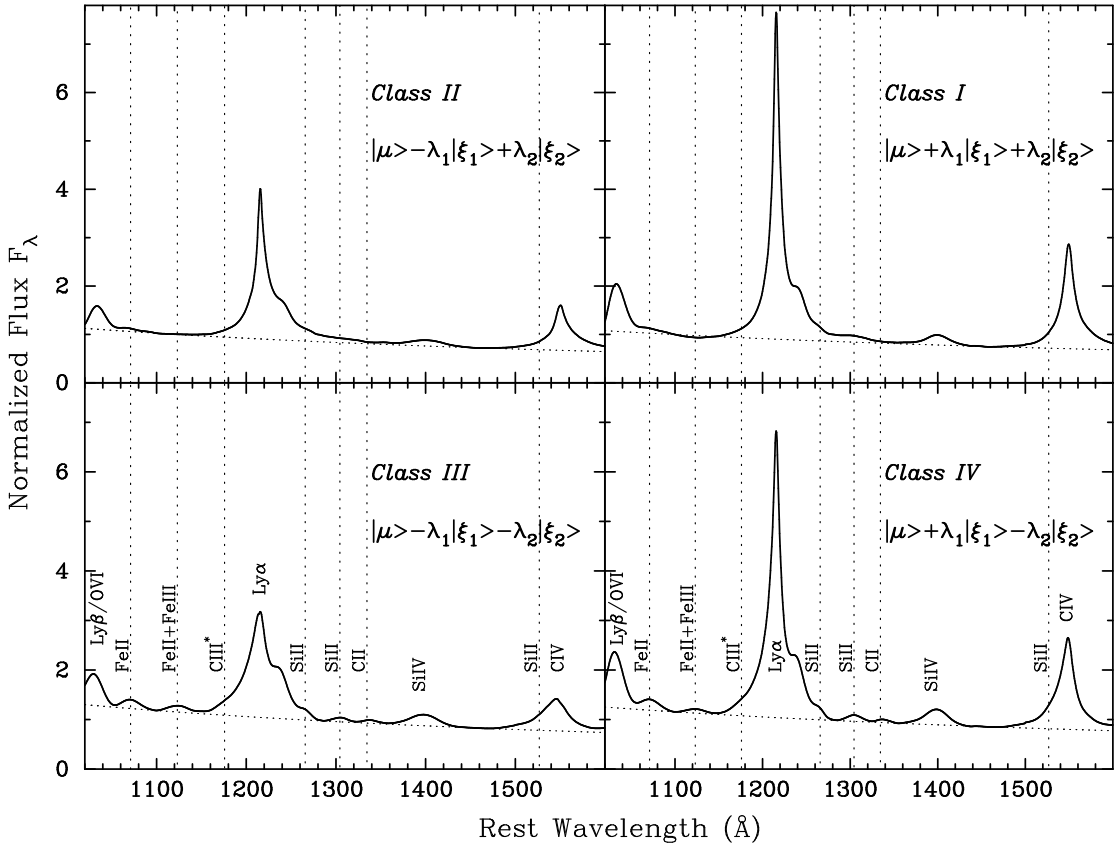

Figure 3.5: The illustration of four classes. We artificially generated these four spectra using the first two PCS. We chose $\pm\sigma_{i1}$ and $\pm\sigma_{i2}$ to generate the four spectra, and equation is given in the legend where $|\mu\rangle$ is the mean spectrum, λ_1 and λ_2 are the square root of the first two eigenvalues, and $|\xi_1\rangle$ and $|\xi_2\rangle$ are the first two PCS. The wavelengths of low ionization lines are shown as vertical dotted lines. Note that the four spectra are plotted in the same scale, and the emission line peak contrast with the continuum characterizes the classification. *Class I* and *II* do not have any weak emission lines and the power-law continuum fit (smooth dotted line) is a good approximation of the continuum in the Lyα forest while *Class III* and *IV* show prominent low emission lines.

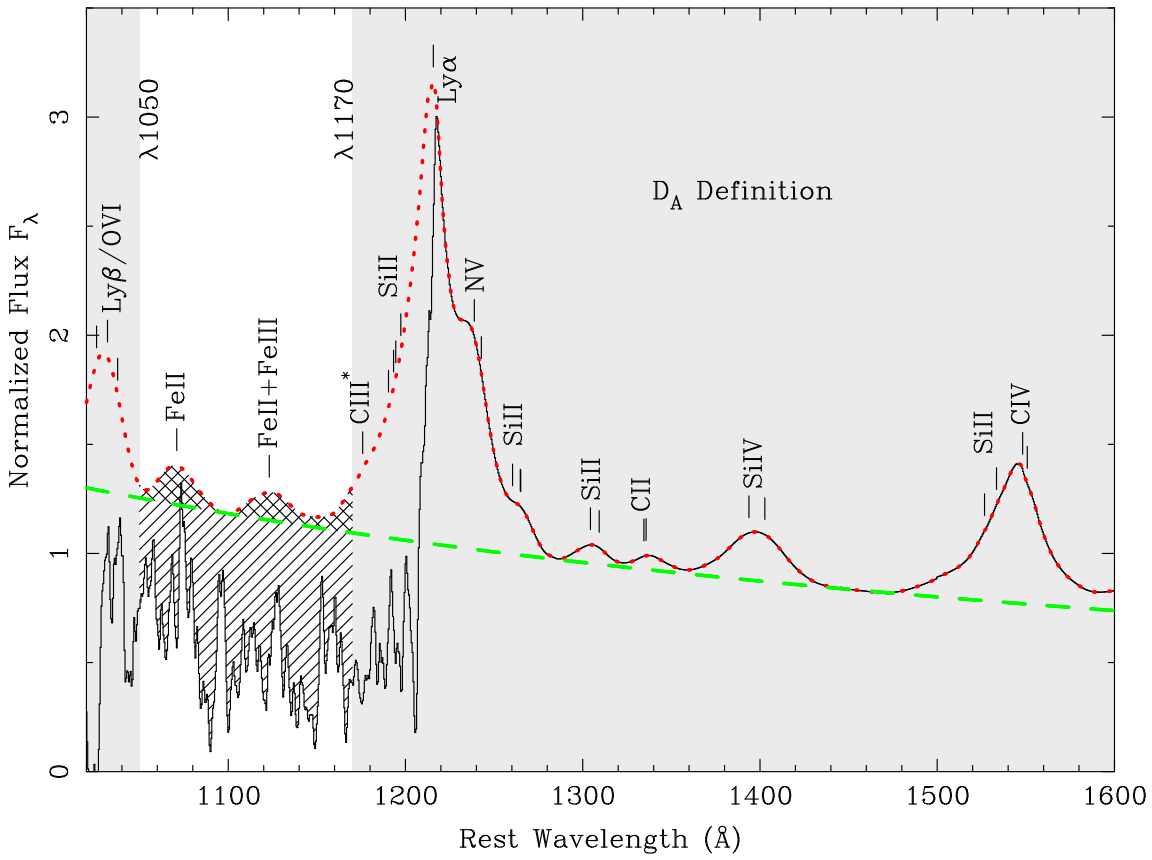

Figure 3.6: The illustration of the D_A definition. The solid line is the observed Lyα forest at z$\sim$ 4.0 and we artificially imposed on a *Class III* quasar spectrum. The dotted line is the intrinsic quasar flux level. The dashed curve is the power-law extrapolation from redward of the Lyα emission line. The flux decrement D_A is the fraction of the sum of the hatched and cross-hatched area over the intrinsic flux area in $\lambda\lambda 1050 - 1170$. If we use the power-law extrapolated line, we would miss the cross-hatched area which is not negligible for the precise measurement.

Figure 3.7: *Class Zero* (r $\leq$ 0.668) : The smooth line on the spectrum is the fitted continuum, and the straight solid line is the power-law continuum fit. The line at the bottom is 1-σ error of the spectrum. The vertical dotted lines show the wavelengths of emission lines in the Lyα forest and low ionization lines redward of the Lyα emission line. The luminosity, L_λ, is measured at λ1280 where we normalized the spectra. The emission lines in the Lyα forest are barely seen in the three spectra. A discontinuity of the spectrum is seen in the middle of the spectrum in Q0947+3940 and Q1538+4745. These are due to the different gratings used in the observations to cover the wide range of wavelength. We joined them together by taking the weighted mean, but it does not always give a smooth solution. This discontinuity could be another source of fitting errors.

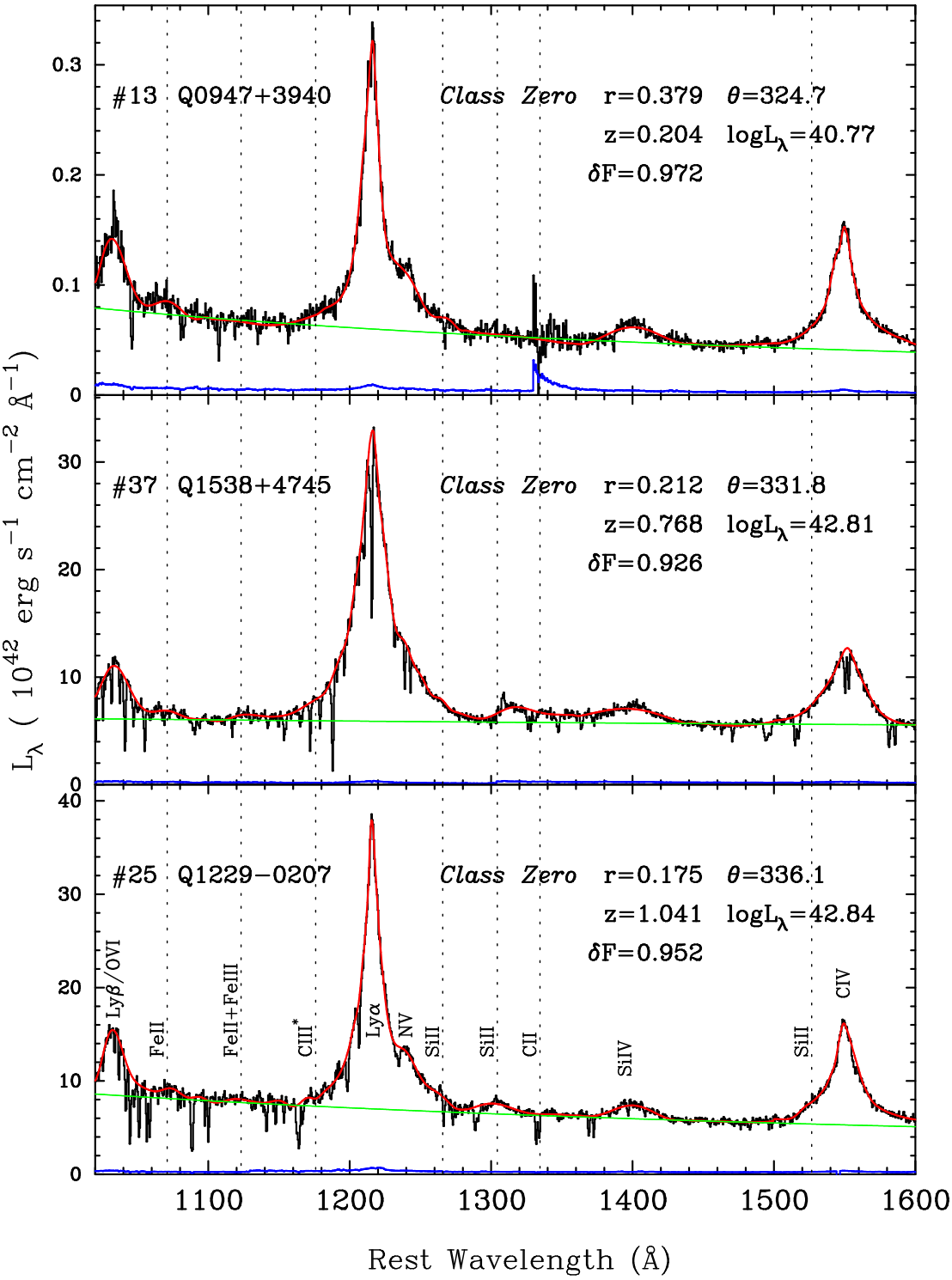
#13 Q0947+3940
Class Zero
r=0.379 θ=324.7
z=0.204 logL$_\lambda$=40.77
δF=0.972
#37 Q1538+4745
Class Zero
r=0.212 θ=331.8
z=0.768 logL$_\lambda$=42.81
δF=0.926
#25 Q1229−0207
Class Zero
r=0.175 θ=336.1
z=1.041 logL$_\lambda$=42.84
δF=0.952
Lyβ/OVI
FeII
FeII+FeIII
CIII*
Lyα
NV
SiII
SiII
CII
SiIV
SiII
CIV
L$_\lambda$ (10^{42} erg s^{-1} cm^{-2} Å^{-1})
Rest Wavelength (Å)

Figure 3.8: *Class I* (r > 0.668, $0 \leq \theta < 90°$): The Lyα, Lyβ and high ionization emission lines are all very sharp and high contrast with the continuum. The low ionization lines, Si II at $\lambda\lambda 1260, 1304$, are barely seen. We see no clear sign of emission lines in the Lyα forest, and the power-law continuum is a good approximation. The contrast of Lyα emission peak with the continuum is the highest among the five classes. In Q2344+0914, there is a huge spike at 1030 Å. It is due to an emission line caused by the Earth's atmosphere. We removed these spikes when we fitted the continuum.

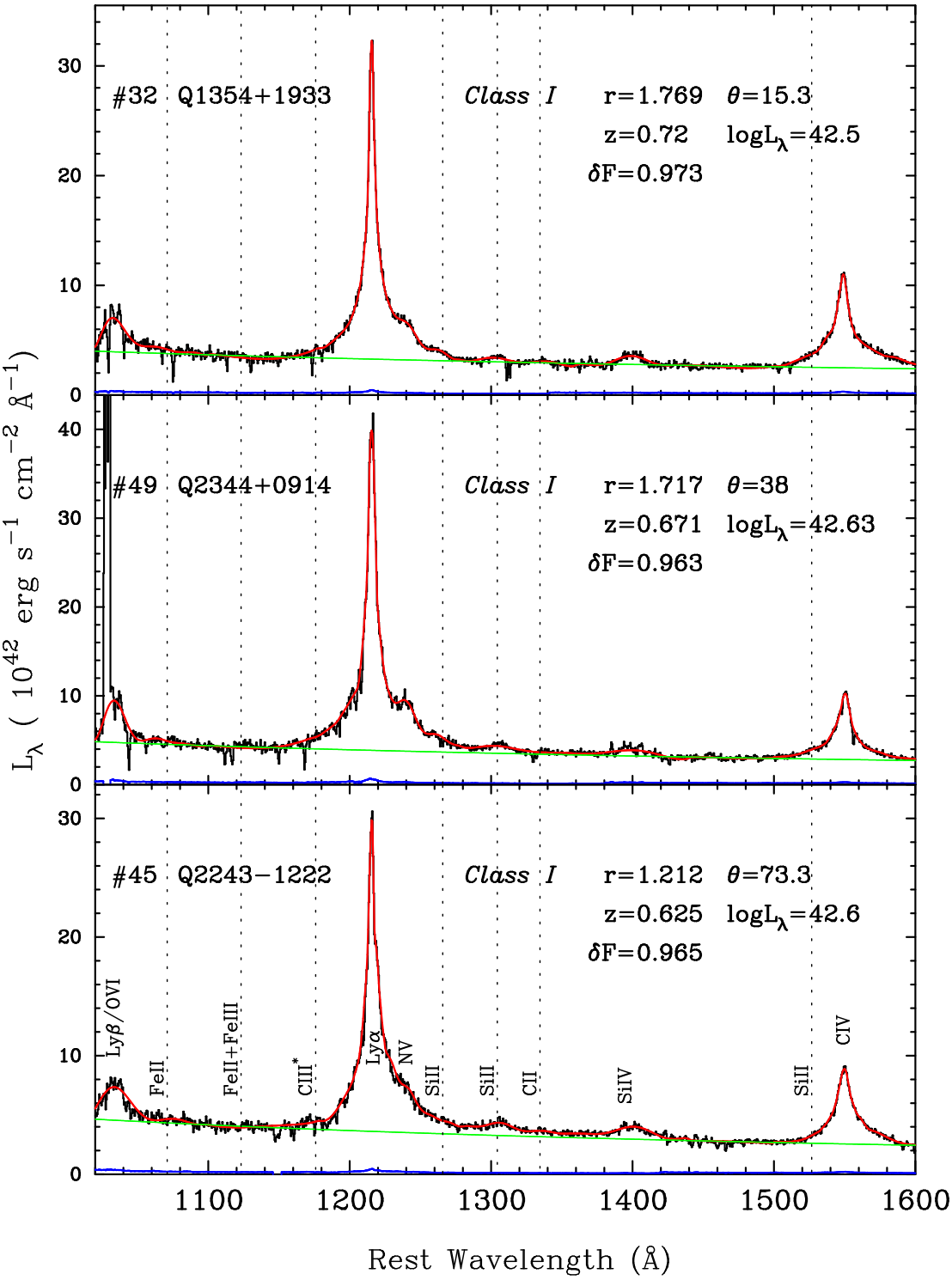
#32 Q1354+1933
Class I
r=1.769 θ=15.3
z=0.72 logL$_\lambda$=42.5
δF=0.973
#49 Q2344+0914
Class I
r=1.717 θ=38
z=0.671 logL$_\lambda$=42.63
δF=0.963
#45 Q2243−1222
Class I
r=1.212 θ=73.3
z=0.625 logL$_\lambda$=42.6
δF=0.965
Lyβ/OVI
FeII
FeII+FeIII
CIII*
Lyα
NV
SiII
SiII
CII
SiIV
SiII
CIV
L$_\lambda$ (10^{42} erg s^{-1} cm^{-2} Å^{-1})
Rest Wavelength (Å)

Figure 3.9: *Class II* ($r > 0.668$, $90° \leq \theta < 180°$): The Lyα emission peak has a moderate contrast, 4-6, with the continuum, and the emission peak ratio of Lyα and N V is 2-3. The Lyα emission has long tails, and the blueward tail of the fitted continuum does not meet with the power-law continuum until 1120 Å, which is 50 Å below the D_A wavelength definition, 1170 Å. In an extreme case, Q0349-1438 ($r = 2.345$), the tail of Lyα emission wings last about 100 Å. Lyβ/O VI, Lyα, and C IV emission profiles are triangular, and Si IV λ1393 is very broad and rounded. There is no clear separation between Lyα and N V emission lines and no sign of low ionization emission lines.

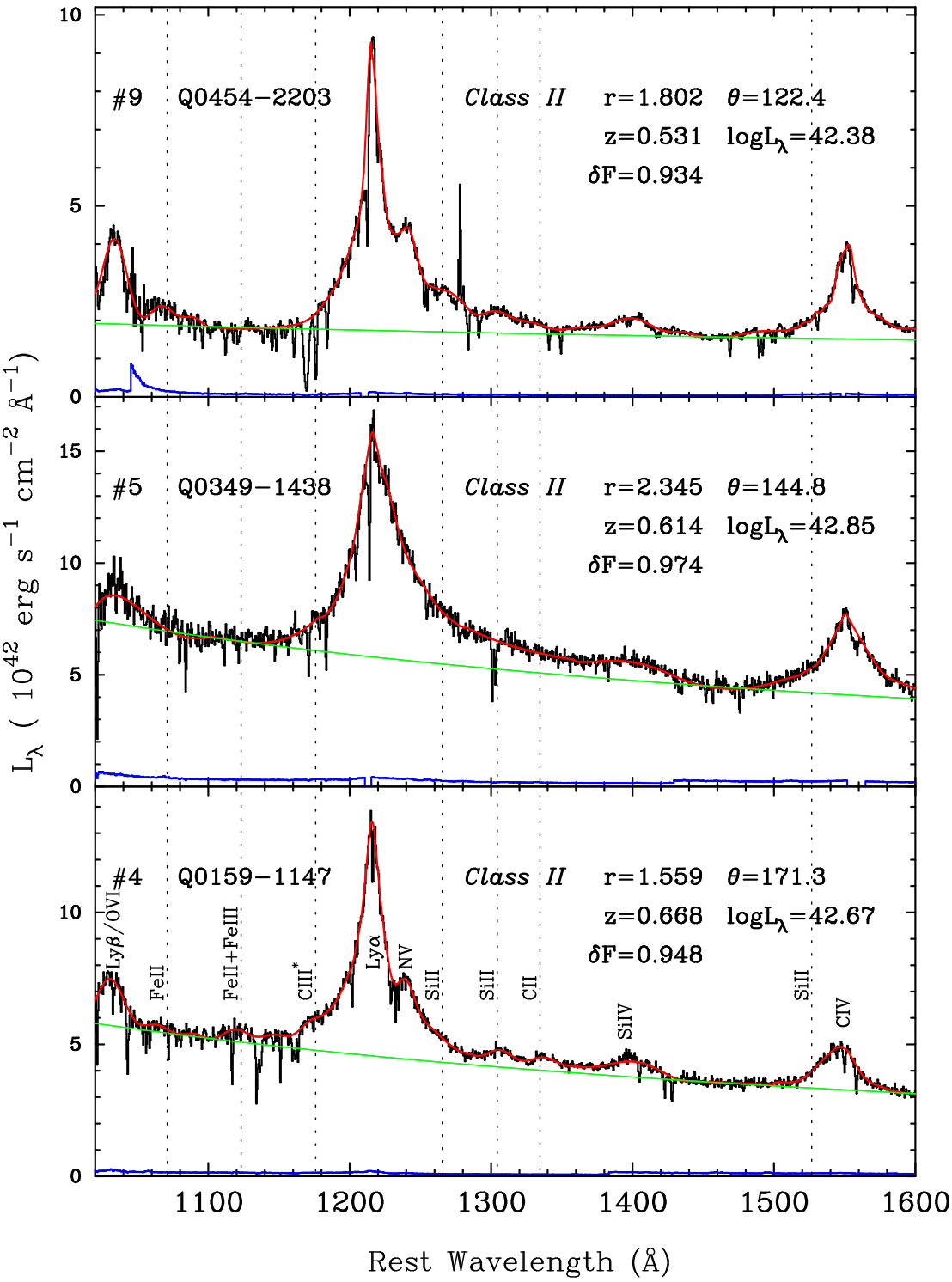
#9 Q0454−2203 Class II r=1.802 θ=122.4
z=0.531 logL$_\lambda$=42.38
δF=0.934
#5 Q0349−1438 Class II r=2.345 θ=144.8
z=0.614 logL$_\lambda$=42.85
δF=0.974
#4 Q0159−1147 Class II r=1.559 θ=171.3
z=0.668 logL$_\lambda$=42.67
δF=0.948
Lyβ/OVI
FeII
FeII+FeIII
CIII*
Lyα
NV
SiII
SiII
CII
SiIV
SiII
CIV
L$_\lambda$ (10^{42} erg s^{-1} cm^{-2} Å^{-1})
Rest Wavelength (Å)

Figure 3.10: *Class III* ($r > 0.668$, $180^\circ \leq \theta < 270^\circ$): The emission line profiles are all broad and rounded. Fe II and Fe III lines are clearly seen in the Lyα forest. The contrast of the Lyα emission line peak with the continuum is the lowest, 2-4, among the five classes. The ratio of Lyα emission peak to N V is also the lowest: 1-2. The C IV profile is asymmetric probably because of the contribution from the Si II λ1526 hidden inside the blueward tail of the C IV line.

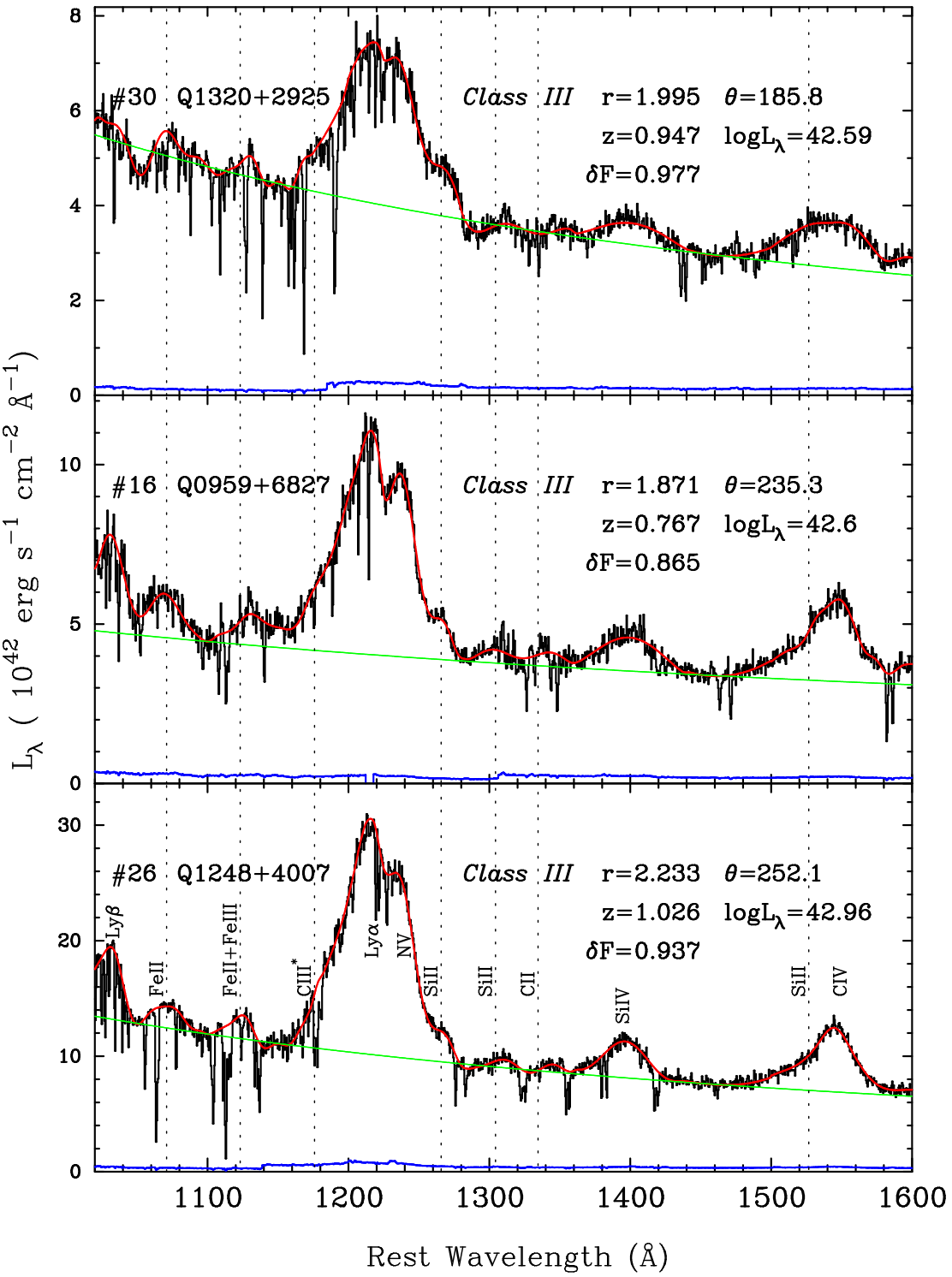
#30 Q1320+2925
Class III
r=1.995 θ=185.8
z=0.947 logL$_\lambda$=42.59
δF=0.977
#16 Q0959+6827
Class III
r=1.871 θ=235.3
z=0.767 logL$_\lambda$=42.6
δF=0.865
#26 Q1248+4007
Class III
r=2.233 θ=252.1
z=1.026 logL$_\lambda$=42.96
δF=0.937
Lyβ
FeII
FeII+FeIII
CIII*
Lyα
NV
SiII
SiII
CII
SiIV
SiII
CIV
L$_\lambda$ (10^{42} erg s^{-1} cm^{-2} Å^{-1})
Rest Wavelength (Å)

Figure 3.11: *Class IV* ($r > 0.668$, $270° \leq \theta < 360°$): The high contrast with the continuum and sharp emission profile are the characteristics of this class. Q1544+4855 is an extreme case that has r=3.099. Since it has $\theta = 278.5$, it is very close to *Class III*, but it has the characteristics of *Class IV*: high Lyα emission line peak contrast and the very sharp line profiles. Unlike a *Class III* quasar, the peaks of low ionization line profile are very sharp and not rounded. Q1322+6557 has a spike at λ1040 that is due to an atmospheric emission line. The fitted spectrum removed the spike for analysis.

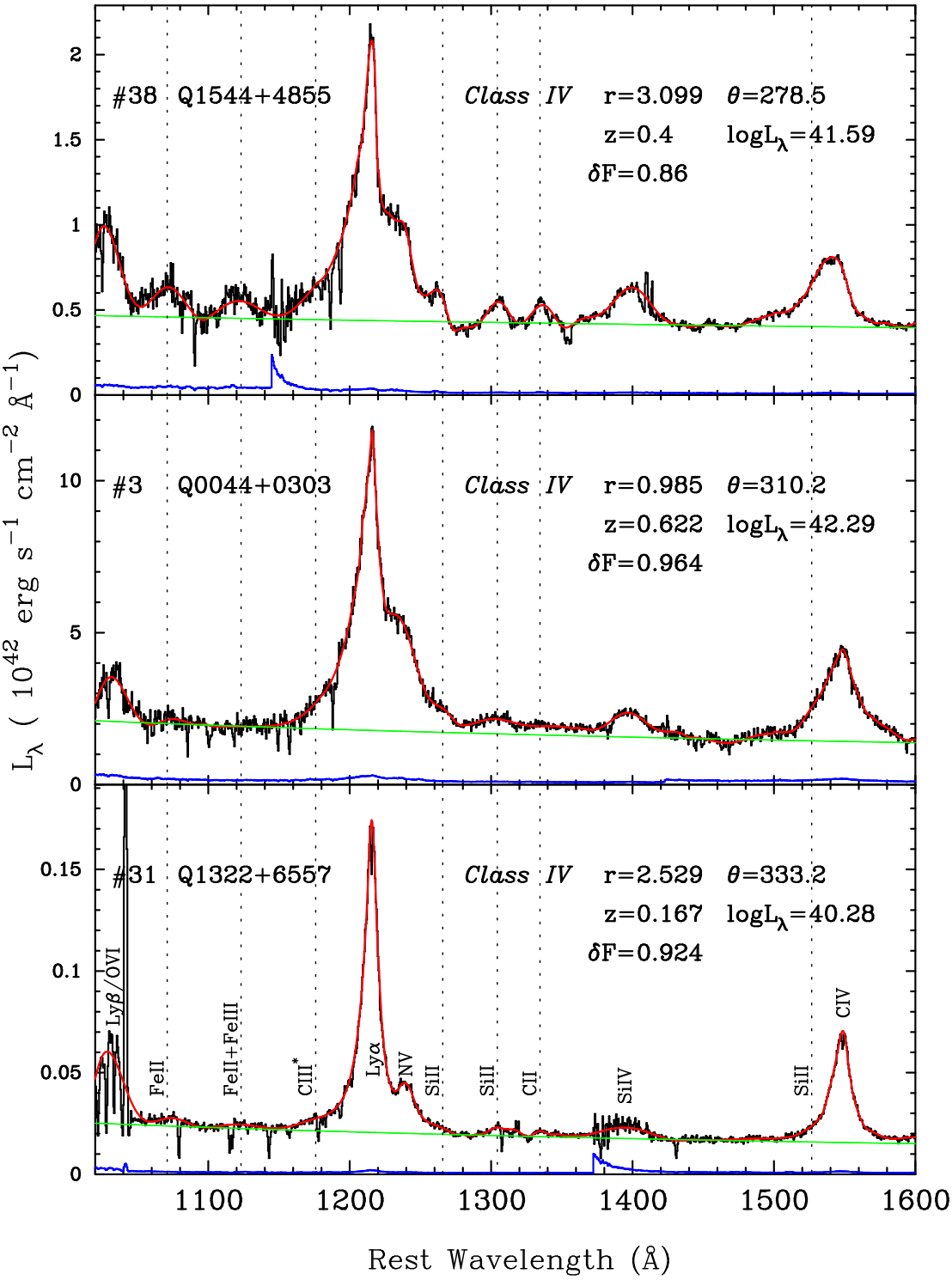
#38 Q1544+4855
Class IV
r=3.099 θ=278.5
z=0.4 logL$_\lambda$=41.59
δF=0.86
#3 Q0044+0303
Class IV
r=0.985 θ=310.2
z=0.622 logL$_\lambda$=42.29
δF=0.964
#31 Q1322+6557
Class IV
r=2.529 θ=333.2
z=0.167 logL$_\lambda$=40.28
δF=0.924
Lyβ/OVI
FeII
FeII+FeIII
CIII*
Lyα
NV
SiII
SiII
CII
SiIV
SiII
CIV
L$_\lambda$ (10^{42} erg s^{-1} cm^{-2} Å^{-1})
Rest Wavelength (Å)

3.6.3 The Characteristics of the Five Classes

The characteristics of the first two PCS directly reflect on the five classifications, thus let us take a close look at the first two PCS in Figure 3.2. The first PCS carries the sharp and strong lines – Lyα, Lyβ and high ionization emission line features (O VI, N V, Si IV, C IV). The second PCS has low ionization emission line features: Fe II and Fe III in blueward of the Lyα emission line, Si II and C II redward. Their profiles are broad and rounded. In the second PCS, the flux values of low ionization emission lines and the strong Lyα, C IV emission lines have opposite sign, meaning they are anticorrelated. In addition to that, Lyα and C IV emission lines have P-Cygni profiles which introduces asymmetric profiles to these emission lines.

By definition, the first two PCS engage the correlation between emission lines. Since we are particularly interested in the profiles of emission lines in the Lyα forest, let us look at low ionization lines first. If a quasar shows prominent low ionization lines redward of the Lyα emission line (Si II $\lambda\lambda 1260, 1304$, C II $\lambda 1334$), it should have a negative second PCS coefficient, and we should expect to have prominent Fe II $\lambda 1070$ and Fe III $\lambda 1123$ in the Lyα forest. Thus such a quasar should belong to either *Class III* or *IV*. As a consequence, these two classes have the largest equivalent widths of these low ionization lines among the five classes as seen in Table 3.2.

If another quasar has sharp and strong Lyα, Lyβ and high ionization lines (N V, Si IV, C IV), it should have a positive first PCS coefficient and belong to *Class I* or *IV*. The normalized flux of the Lyα emission peak and the ratio of the Lyα and N V peak flux are the highest for *Class I* among the five classes. We can differentiate *Class I* and *II*, or *Class III* and *IV* by combining the above characteristics. As we expect, the diagonal classes have the opposite characteristics. For example, *Class I* has sharp and high ionization lines while *Class III* has broad and rounded low emission lines.

In practice, the key point of finding the intrinsic flux level in the Lyα forest is to seek the low ionization lines (Si II $\lambda\lambda 1260, 1304$, C II $\lambda 1334$) and their profiles redward of the Lyα emission. If we see them, we should expect to have similar profiles of Fe II $\lambda 1070$ and Fe II $\lambda 1123$ lines in the Lyα forest. If we do not see them, we can expect the intrinsic flux level to be flat in the Lyα forest, and the power-law extrapolation from the redward of the Lyα emission to be a good approximation. We will discuss the accuracy of the power-law extrapolation in the next section.

Table 3.2. δF and the Equivalent Widths of the Emission Lines

i	Quasar	δF	Lyβ/OVI 1025 (Å)	Fe II 1071 (Å)	Fe III 1123 (Å)	C III* 1176 (Å)	Lyα 1216 (Å)	N V 1240 (Å)	Si II 1263 (Å)	Si II 1307 (Å)	C II 1335 (Å)	Si IV 1397 (Å)	C IV 1549 (Å)
	Class Zero												
13	Q0947+3940	0.972	8.8	1.4	0.0	0.0	102.9	0.7	0.5	0.0	0.0	13.2	59.8
25	Q1229-0207	0.953	9.5	0.9	0.2	0.0	87.7	0.4	0.1	1.8	0.0	6.9	47.4
34	Q1424-1150	0.903	9.5	1.1	0.0	0.0	131.9	0.6	0.0	0.0	0.0	8.1	50.4
37	Q1538+4745	0.926	8.2	0.4	0.9	0.0	132.9	0.0	0.0	0.4	0.0	6.8	43.4
48	Q2340-0339	0.963	5.1	0.3	0.0	0.0	83.5	0.7	0.0	0.0	0.0	5.7	41.5
	Average	0.944	8.2	0.8	0.2	0.0	107.8	0.5	0.1	0.4	0.0	8.1	48.5
	STD	0.028	1.8	0.5	0.4	0.0	23.6	0.3	0.2	0.8	0.0	2.9	7.2

Table 3.2—Continued

i	Quasar	δF	Lyβ/OVI 1025 (Å)	Fe II 1071 (Å)	Fe III 1123 (Å)	C III* 1176 (Å)	Lyα 1216 (Å)	N V 1240 (Å)	Si II 1263 (Å)	Si II 1307 (Å)	C II 1335 (Å)	Si IV 1397 (Å)	C IV 1549 (Å)
	Class I												
1	Q0003+1553	0.940	8.6	0.1	0.0	0.0	115.7	0.0	0.0	2.2	0.0	6.5	55.2
8	Q0439-4319	0.970	13.3	0.0	0.0	0.0	119.2	1.1	0.0	1.2	0.0	7.3	58.0
11	Q0637-7513	0.980	15.6	2.5	0.0	0.0	87.2	2.2	0.3	0.0	0.0	8.6	38.9
14	Q0953+4129	0.937	12.1	1.9	0.3	0.0	124.2	1.4	0.3	0.0	0.0	10.6	63.6
18	Q1007+4147	0.943	11.6	2.0	0.1	0.1	145.4	1.9	0.0	2.0	0.3	10.4	65.5
22	Q1137+6604	0.939	10.8	1.8	0.2	0.0	99.2	0.6	0.2	0.6	0.0	7.3	45.1
24	Q1216+0655	0.959	9.9	0.9	0.0	0.0	124.7	0.0	0.0	0.6	0.0	8.8	52.4
32	Q1354+1933	0.974	10.3	0.2	0.1	0.1	134.6	0.5	0.5	2.0	1.1	7.9	65.5
39	Q1622+2352	0.971	9.3	0.7	0.0	0.1	111.3	0.2	0.0	0.0	0.0	7.7	65.2
41	Q1821+6419	0.986	13.6	0.3	0.0	0.0	115.3	0.2	0.0	0.0	0.0	7.8	50.6
42	Q1928+7351	0.982	10.2	0.0	0.0	0.0	149.4	1.9	0.0	0.0	0.0	12.4	74.3
45	Q2243-1222	0.966	8.1	0.3	0.0	0.1	103.2	0.0	0.0	2.2	0.2	8.1	51.6
49	Q2344+0914	0.963	13.9	0.8	0.0	0.0	143.1	1.8	0.5	1.6	0.0	5.3	50.9
	Average	0.962	11.3	0.9	0.1	0.0	121.0	0.9	0.1	1.0	0.1	8.4	56.7
	STD	0.017	2.3	0.9	0.1	0.0	18.7	0.8	0.2	0.9	0.3	1.9	9.8

Table 3.2—Continued

i	Quasar	δF	Lyβ/OVI 1025 (Å)	Fe II 1071 (Å)	Fe III 1123 (Å)	C III* 1176 (Å)	Lyα 1216 (Å)	N V 1240 (Å)	Si II 1263 (Å)	Si II 1307 (Å)	C II 1335 (Å)	Si IV 1397 (Å)	C IV 1549 (Å)
	Class II												
2	Q0026+1259	0.950	9.6	2.4	0.1	0.0	92.1	3.6	0.1	0.0	0.0	9.2	19.4
4	Q0159-1147	0.948	2.8	0.3	0.9	0.0	52.8	1.0	0.0	1.1	0.8	4.2	16.8
5	Q0349-1438	0.974	1.8	0.0	0.0	0.1	54.9	0.0	0.0	0.0	0.0	4.0	28.0
6	Q0405-1219	0.950	6.9	0.7	1.1	0.0	92.5	0.4	0.0	1.1	0.0	6.5	35.0
7	Q0414-0601	0.958	6.1	0.0	0.1	0.0	114.0	0.9	0.0	0.0	0.0	5.1	40.1
9	Q0454-2203	0.935	11.6	4.2	0.0	0.0	105.7	2.2	0.3	1.1	0.0	7.2	33.9
12	Q0923+3915	0.973	7.2	0.0	0.1	0.0	95.1	0.1	0.0	1.2	0.0	5.1	46.4
15	Q0954+5537	0.983	3.3	0.0	0.4	0.1	42.6	0.3	1.1	0.0	0.0	1.9	17.9
20	Q1104+1644	0.958	5.7	0.7	0.0	0.0	104.5	0.0	0.0	0.5	0.0	7.8	54.1
27	Q1252+1157	0.939	6.1	2.7	2.4	0.0	72.7	1.0	0.2	0.0	0.5	6.0	25.5
40	Q1637+5726	0.945	4.5	0.9	0.2	0.0	77.6	0.7	0.0	0.3	0.0	5.4	33.2
47	Q2251+1552	1.015	7.1	2.3	0.0	0.0	60.1	1.0	0.0	0.0	0.0	2.6	23.2
	Average	0.960	6.1	1.2	0.4	0.0	80.4	0.9	0.1	0.4	0.1	5.4	31.1
	STD	0.022	2.8	1.4	0.7	0.0	23.7	1.0	0.3	0.5	0.2	2.1	11.6

Table 3.2—Continued

i	Quasar	δF	Lyβ/OVI 1025 (Å)	Fe II 1071 (Å)	Fe III 1123 (Å)	C III* 1176 (Å)	Lyα 1216 (Å)	N V 1240 (Å)	Si II 1263 (Å)	Si II 1307 (Å)	C II 1335 (Å)	Si IV 1397 (Å)	C IV 1549 (Å)
	Class III												
16	Q0959+6827	0.865	3.6	4.0	2.9	0.1	81.0	3.1	0.7	1.3	1.3	12.1	25.2
17	Q1001+2910	0.949	3.4	3.4	2.4	0.0	68.7	2.0	0.7	2.9	2.1	9.3	26.2
21	Q1115+4042	0.957	7.3	4.3	3.2	0.0	82.3	1.8	0.3	2.5	1.5	8.6	29.7
23	Q1148+5454	0.928	3.4	3.9	2.8	0.0	108.4	1.1	0.9	1.8	1.5	14.1	30.8
26	Q1248+4007	0.937	2.9	3.0	3.2	0.1	111.6	2.1	0.6	1.6	0.6	12.2	28.6
28	Q1259+5918	0.954	2.8	2.5	1.8	0.0	63.5	1.0	1.7	2.7	0.7	10.1	19.8
29	Q1317+2743	0.963	3.2	0.8	1.3	0.0	57.2	1.5	0.4	0.5	0.1	7.1	17.9
30	Q1320+2925	0.977	1.1	3.9	1.2	0.0	58.6	1.0	0.6	0.4	0.1	5.7	14.4
36	Q1444+4047	0.925	4.0	3.0	3.8	0.1	65.0	3.6	0.0	0.3	0.7	9.9	24.0
43	Q2145+0643	0.943	1.6	0.0	0.0	0.0	71.3	0.6	0.0	0.0	0.3	1.6	35.9
44	Q2201+3131	0.928	4.8	0.6	1.2	0.0	69.9	0.0	0.0	0.0	0.0	7.6	28.8
	Average	0.939	3.5	2.7	2.2	0.0	76.1	1.6	0.5	1.3	0.8	8.9	25.6
	STD	0.029	1.6	1.5	1.1	0.0	18.5	1.1	0.5	1.1	0.7	3.5	6.2

Table 3.2—Continued

i	Quasar	δF	Lyβ/OVI 1025 (Å)	Fe II 1071 (Å)	Fe III 1123 (Å)	C III* 1176 (Å)	Lyα 1216 (Å)	N V 1240 (Å)	Si II 1263 (Å)	Si II 1307 (Å)	C II 1335 (Å)	Si IV 1397 (Å)	C IV 1549 (Å)
	Class IV												
3	Q0044+0303	0.965	8.6	1.3	0.0	0.0	146.0	1.5	0.1	1.7	0.1	11.3	71.2
10	Q0624+6907	0.888	8.2	5.1	3.0	0.0	174.5	3.9	0.6	2.5	1.3	11.3	51.7
19	Q1100+7715	0.948	9.7	1.7	0.0	0.0	101.8	1.0	0.0	0.0	0.0	8.5	72.1
31	Q1322+6557	0.925	8.3	1.8	1.7	0.0	138.5	2.7	0.0	3.3	0.8	9.3	55.5
33	Q1402+2609	0.865	6.3	3.1	4.7	0.0	82.0	1.8	0.8	2.3	1.8	5.1	31.7
35	Q1427+4800	0.944	13.9	1.8	0.1	0.0	96.9	0.7	0.0	0.6	0.2	16.9	57.3
38	Q1544+4855	0.860	2.9	5.7	5.5	0.0	119.5	1.0	1.6	5.1	3.6	16.5	33.5
46	Q2251+1120	0.937	10.5	0.8	0.0	0.1	141.6	4.5	0.0	2.1	0.0	7.8	69.8
50	Q2352-3414	0.937	9.0	0.8	1.3	0.0	129.4	0.4	0.0	0.7	0.2	6.6	61.8
	Average	0.919	8.6	2.4	1.8	0.0	125.6	1.9	0.3	2.0	0.9	10.4	56.1
	STD	0.038	3.0	1.8	2.1	0.0	28.7	1.5	0.6	1.6	1.2	4.1	15.1
	Total												
	Average	0.947	7.5	1.6	0.9	0.0	100.9	1.2	0.3	1.0	0.4	8.1	42.8
	STD	0.031	3.7	1.5	1.4	0.0	30.4	1.1	0.4	1.1	0.7	3.3	17.0

3.7 Mean Flux $\langle F \rangle$ and Flux Decrement D_A

3.7.1 A Brief History of the Flux Decrement D_A

Gunn & Peterson (1965) predicted a flux decrement due to foreground neutral hydrogen in the IGM, namely the Lyα forest. Oke & Korycansky (1982) first defined and measured the flux decrement, D_A. Schneider et al. (1991) introduced the Lyα forest wavelength interval for D_A as $\lambda\lambda 1050 - 1170$, and it has been widely used since (Zuo & Lu, 1993; Kennefick et al., 1995; Spinrad et al., 1998). Madau (1995) and McDonald & Miralda-Escudé (2001) have used D_A to estimate the UV background. The flux decrement of the high redshift IGM probes the reionization epoch of the universe (Loeb & Barkana, 2001). The current estimate of the reionization epoch from the IGM is around $z \sim 6 - 7$ (Becker et al., 2001; Djorgovski et al., 2001; Fan et al., 2003), while the first year WMAP satellite estimates $z \sim 20$ (Spergel et al., 2003). The discrepancy is yet to be resolved or explained (Cen, 2003).

A precise measurement of the flux decrement, D_A, is of great importance for studies of the IGM (Rauch, 1998) because it is very sensitive to the cosmological parameters, σ_8 (the amplitude of the mass power spectrum) and Ω_Λ, as well as to the UV background intensity (Tytler et al., 2004b; Jena et al., 2005). However, it is this sensitivity that makes the D_A measurement a major source of error (Hui et al., 1999; Croft et al., 2002b).

3.7.2 The Mean Flux Correction Factor δF

The concept of the following flux decrement D_A and the power-law extrapolation is illustrated in Figure 3.6. The flux decrement is defined as:

$$D_A = 1 - \int_{1050\text{Å}}^{1170\text{Å}} f_\lambda(\lambda; Observed) d\lambda \Big/ \int_{1050\text{Å}}^{1170\text{Å}} f_\lambda(\lambda; Quasar) d\lambda. \tag{3.15}$$

Thus, what we are measuring is the mean flux:

$$\langle F \rangle = \int_{1050\text{Å}}^{1170\text{Å}} f_\lambda(\lambda; Observed) \Big/ \int_{1050\text{Å}}^{1170\text{Å}} f_\lambda(\lambda; Quasar) d\lambda. \tag{3.16}$$

However, the unabsorbed-intrinsic quasar flux level is not seen in the Lyα forest and the power-law extrapolation from redward of Lyα emission has been used as a background flux level. In fact, what is reported in the literature as the mean flux is:

$$\langle F_{Power-Law} \rangle = \int_{1050\text{A}}^{1170\text{A}} f_\lambda(\lambda; Observed) d\lambda \Big/ \int_{1050\text{A}}^{1170\text{A}} f_\lambda(\lambda; Power-Law) d\lambda \quad (3.17)$$

which is not exactly the same as $\langle F \rangle$ since the power-law is a crude approximation of the continuum in the Lyα forest as we have seen in §3.6, Appendix A, and Figures 3.7-3.11. We wish to introduce a correction factor δF :

$$\delta F = \int_{1050\text{A}}^{1170\text{A}} f_\lambda(\lambda; Power-Law) d\lambda \Big/ \int_{1050\text{A}}^{1170\text{A}} f_\lambda(\lambda; Quasar) d\lambda \quad (3.18)$$

so that we can estimate the true mean flux $\langle F \rangle$ from the reported mean flux $\langle F_{Power-Law} \rangle$:

$$\langle F \rangle = \langle F_{Power-Law} \rangle \cdot \delta F. \quad (3.19)$$

To calculate δF, we need to find the power-law extrapolation from the redward Lyα emission. Since our wavelength range is limited and not as large as other survey data, it is not easy to extrapolate. Moreover, we have a series of emission lines, and it is hard to define an intrinsic flux level with no emission lines. For example, as shown in Figure 3.10, *Class III* quasars have emission lines throughout this wavelength range. However, we have a fitted intrinsic flux level in the Lyα forest, and we take advantage of it. We choose two points and find a power-law fit which runs through these two points. We choose one from blueward (λ1100) and the other from redward (λ1450) of the Lyα emission. Then, we can have an inter- and extra-polated power-law continuum and its exponent α_ν, for $f_\nu \propto \nu^{\alpha_\nu}$. The average of α_ν is -0.854 with the standard deviation of 0.507. The power-law continua show that they are all sensible first order approximations which well represent the intrinsic flux levels in the Lyα forest. The power-law continua are shown in Figure 3.7-3.11.

The calculated δF is listed in Table 3.2 and the average of δF is 0.947, with a standard deviation of 0.031. This result means that the power-law approximation

misses 5.3% of flux from the quasar in the D_A wavelength range, and proves that the power-law approximation is inadequate to perform a D_A measurement that attempts 1% accuracy (Tytler et al., 2004a; Jena et al., 2005). The distribution of δF is shown in Figure 3.12, and it is not a Gaussian. The PDF of δF is asymmetric and has long tail toward small δF value.

There are two major reasons for the missing flux. The first reason is that the D_A wavelength range is still in the tail of the prominent Lyβ/O VI and Lyα emission lines. For example, the blueward tail of the Lyα emission starts near λ1160 which is 10Å below the λ1170 upper limit of D_A wavelength range. The effect from the tails of Lyβ and Lyα emission is common for all of the quasars as we can see in Figure 3.7-3.11. This contribution is about 4-5%, and we always miss this fraction of the flux, meaning δF is always less than unity.

The second reason is the contribution from the weak emission lines in the Lyα forest. The intrinsic flux level at the emission lines is naturally above the power-law extrapolation, therefore, we would always expect to miss flux from the emission lines, making δF always less than unity. The low ionization emission lines in the Lyα forest are prominent for *Class III* & *Class IV* quasars. Four quasars in *Class III* & *Class IV* have δF less than 0.9, meaning we miss more than 10% of the flux if we use power-law extrapolation. The quasar which has the smallest δF, 0.86, is Q1544+4855. This quasar is shown on the top panel of Figure 3.11 and the power-law continuum fit looks sensible. Together with the tails of Lyβ and Lyα emissions, the low ionization emission lines in the Lyα forest (Fe II, Fe III) contribute 14% of flux which is significant and should not be neglected.

There is another possible origin for the missing flux. We might have a global change of an intrinsic quasar flux level. Shang et al. (2005) showed that there exists a variety of UV spectrum shape in a global scale, known as the big blue bump. We think that this big blue bump is due to the thermal radiation of the accretion disk near the supermassive black hole (Malkan, 1983), and spectral shape varies quasar by quasar (Sun & Malkan, 1989). However, we found a moderate correlation

between the intrinsic flux levels and the emission profiles in Paper I, and we expect that the global trend is imprinted in the PCS. In addition to that, the wavelength range of the D_A measurement is relatively small compared to the global change of the slope, we expect the effect is minimal. But we need to have a quantitative study, and we note that this slope change could be the source of systematic errors.

We expect that we need to apply at least a $\delta F = 0.947$ correction to the D_A measurements in the literature. The discrepancy between the past D_A measurements and Bernardi et al. (2003) using the weak emission profile fitting method is shown in Tytler et al. (2004a, Figure 22). The disagreement is approximately 5% at redshift $2 < z < 3$, and in terms of the mean flux, the power-law fitted values (Press et al., 1993; Steidel & Sargent, 1987) are always above that of profile fitted ones (Bernardi et al., 2003). The correction factor, $\delta F = 0.947$, explains this disagreement well.

However, we expect that δF changes with redshift, and it is crucial to include the effect from the weak emission lines to investigate the reionization epoch. Known as the Baldwin effect (Baldwin, 1977), the emission profile of lines, such as C IV, and the luminosity of the quasar are correlated. Because of the anticorrelation between equivalent width of C IV and the luminosity, we expect that *Class III* quasars to be the brightest since they have the smallest C IV equivalent width. Due to the selection effect, we would expect to observe the brightest quasars at high redshifts. Therefore, the fraction of classes for the observed quasars should change with redshift. In fact, the highest redshift quasars reported by Fan et al. (2001), Becker et al. (2001) and Djorgovski et al. (2001) probably belong to *Class III*, because they all show the weak Si II λ1304 emission line implying they have weak emission lines in the Lyα forest regain. J104433.04-012502.2 (z=5.80) and J08643.85+005453.3 (z=5.82) definitely belong to *Class III* since they have broad Lyα, N V, and Si II emission lines and low Lyα/N V emission intensity ratio. The mean flux correction δF of *Class III* quasars are in the range of 0.91-0.97, meaning the power-law extrapolation misses 3-9% of the flux for *Class III* quasars. We note that the reported 1-σ error of the residual mean flux at redshift z=5.75 by Becker

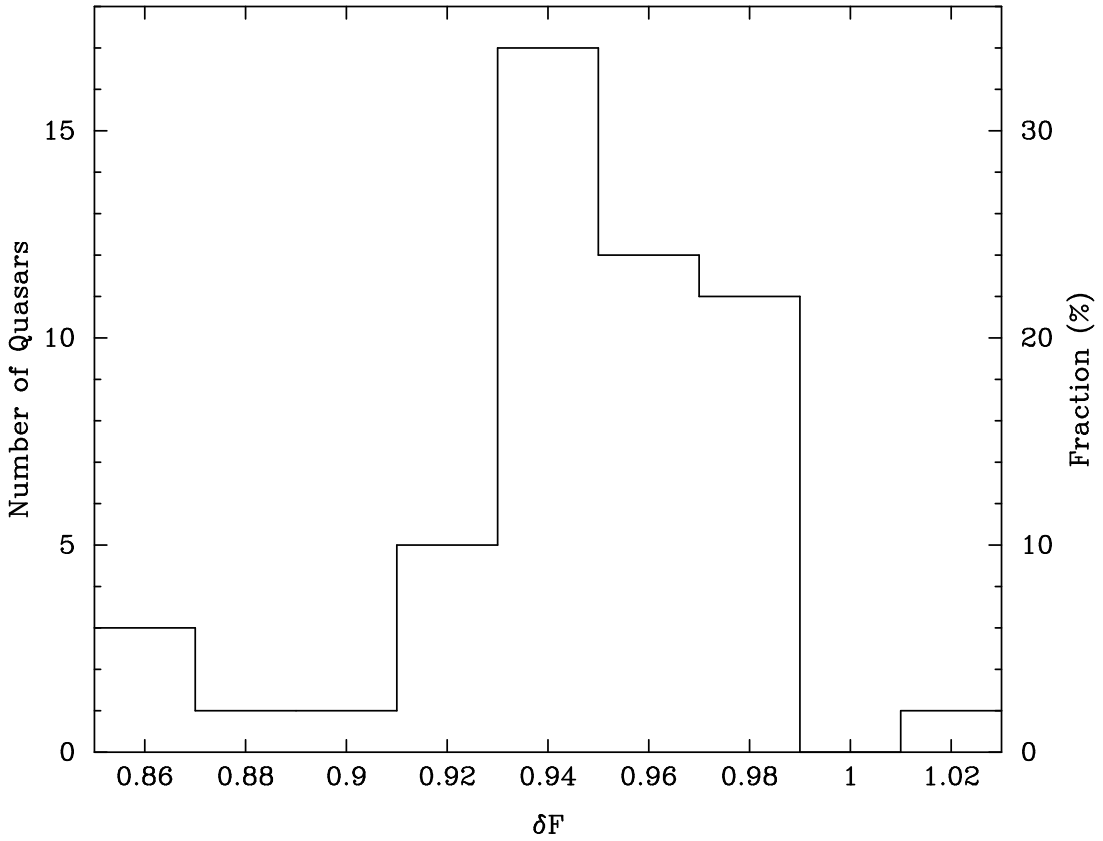

Figure 3.12: The distribution of the mean flux correction factor δF. The mean is 0.947 with the standard deviation of 0.031. The distribution is asymmetric with long tail toward small δF values. *Class III* and *IV* quasars have prominent emission lines in the Lyα forest, and tend to have small δF values. Two extreme spectra for low δF are shown in Figure 3.10 for Q0959+6927 and Figure 3.11 for Q1544+4855.

et al. (2001) is 0.03. The contribution from δF is bigger than their claimed error, and it is systematic. This correction would bring the observed mean flux down by 3-9% percent and would bring D_A up by the same fraction. Therefore, it is crucial to take into account the δF correction in order to investigate the reionization epoch.

3.8 Summary

We analyzed the wide variety of the emission line profiles in the Lyα forest both in a quantitative and qualitative way. We used PCA to describe the variety of

quasar spectra, and we found that 1161 pixels of data ($\lambda\lambda 1020 - 1600$ with 0.5 Å binning) can be summarized by the primary seven PCS coefficients because the pixels are not independent but are strongly correlated with each other. We presented, for the first time, the idea of generating artificial quasar spectra. Our artificial quasar spectra should be useful in testing the detections, in calibrations, and in simulations. We introduced five classes to differentiate the families of quasar spectra, and showed how the classification can guide us to find the intrinsic flux level in the Lyα forest. It is essential to account for emission line features in the Lyα forest to perform a precise measurement of the mean flux in order to probe cosmological parameters, the UV background, and the reionization epoch, otherwise, on average, the commonly used power-law extrapolation continuum misses 5.3% of the flux, and we have cases when it misses up to 14% of the flux.

To investigate the high redshift Lyα forest, we showed the need to account for the emission lines in the Lyα forest. An emission line profile oriented continuum fitting method by Bernardi et al. (2003), or improvement of the PCA method in Paper I would be useful for a large data set such as the Sloan Digital Sky Survey. If we can study the redshift evolution of the quasar spectra and if we can estimate the constituents of classes at a certain redshift, we would be able to estimate the mean flux statistically using the mean flux correction factor δF. For precision cosmology, the formalisms we presented here should play an important role.

3.9 Appendix A : Weak Emission Lines in the Lyα Forest

It has been suggested that there exist weak emission lines in the Lyα forest (Zheng et al., 1997; Telfer et al., 2002; Bernardi et al., 2003; Scott et al., 2004), however, their identities, strengths, and line profiles are not well understood. More importantly, we wish to know how they are correlated with other emission lines so that we can predict the strength and profiles of the emission lines in the Lyα forest. We attempt to find the identities of the three weak emission lines in the Lyα forest

reported by Tytler et al. (2004b). In this paper, we use their measured wavelengths : $\lambda = 1070.95, \lambda = 1123.17, \lambda = 1175.88$ Å.

3.9.1 Line at $\lambda = 1070.95$ Å : Fe II

Zheng et al. (1997) and Vanden Berk et al. (2001) identified this line as Ar I λ1066.66, but the contribution from Ar I cannot be this large. The Ar I line has another transition at λ1048.22 whose transition probability ($A_{ik} = 4.94 \times 10^8 s^{-1}$) is stronger than that of λ1066.66 ($A_{ik} = 1.30 \times 10^8 s^{-1}$). However, there is no clear sign of the λ1048.22 line feature in 50 *HST* spectra or 79 quasar spectra in Tytler et al. (2004a). In addition, the λ1070 line has a broad and asymmetric profile which suggests that this line is a blend of multiple lines. Thus, λ1070 is not likely to be a single Ar I line.

Telfer et al. (2002) labeled this λ1070 as N II + He II line, and mentioned S IV as a possible candidate. Scott et al. (2004) identify four lines in the proximity of this wavelength : S IV doublet ($\lambda\lambda$1062, 1073) and N II+He II+Ar I (λ1084). As we have seen in §3.6, the λ1070 line correlates with low ionization lines such as Si II and C II. S IV does not fit into this category. N II seems to be a good candidate, but the N II lines peaks around 1085 Å which is 15 Å away from what we see. It is unlikely that we have 15 Å of wavelength error. For the same reason, He II (1085Å), a high ionization line, is not likely to be the dominant contributor. However, it is reasonable to expect to have an He II line since He II λ1640 is often seen in quasar spectra. This λ1070 line is seen in the Q1009+2956 and Q1243+3047 spectra for which we have high S/N Keck HIRES spectra with a FWHM=0.0285 Å resolution at this wavelength (Burles & Tytler, 1998b; Kirkman et al., 2003). If λ1070 is comprised of the lines suggested by Scott et al. (2004), we would be able to resolve the individual lines. However, none of the individual emission line are resolved. This fact implies that this emission line is comprised of numerous weak lines and that they are probably low ionization lines because of the good correlation with other low ionization lines.

Fe II suits such a description, and in fact, Fe II has a series of UV transitions around this wavelength range: $\lambda\lambda$1060-1080. However, we do not see other expected Fe II emission lines. If this λ1070 is Fe II, we would expect to see the Fe II UV10 multiplet around λ1144 , which is supposed to be stronger than the λ1070 line. But no sign of an emission line is seen at that wavelength. Therefore, Fe II identification may be wrong or there may be a mechanism that we are not aware of that prevents the expected λ1144 emission line.

3.9.2 $\lambda = 1123.17$ Å : Fe II + Fe III

Telfer et al. (2002); Vanden Berk et al. (2001) identify λ1123 as Fe III. The f-value weighted Fe III UV1 multiplet has a wavelength at 1126.39 Å which is very close to what is observed by Tytler et al. (2004a). The distribution of the multiplet lines matches the broad λ1123 feature found in quasars. There are no other major resonance lines in this wavelength range except C I. In the wavelength range $\lambda\lambda 1114-1200$, C I has a series of lines, and there exists stronger lines redward of the Lyα emission line: $\lambda\lambda 1115-1193, \lambda\lambda 1277-1280$. However, we do not see these redward C I emission lines, and there is no sign of correlation between λ1123 and these possible lines (Paper I). Thus, λ1123 is probably Fe III. In addition to Fe III, Fe II also has UV11-14 multiplets around this wavelength: $\lambda\lambda 1121-1133$. Given the fact that this λ1123 line is well correlated with λ1070 line, it is reasonable to expect to see Fe II lines here as well, if the identification of λ1070 is Fe II.

3.9.3 $\lambda = 1175.88$ Å : CIII*

Telfer et al. (2002); Vanden Berk et al. (2001) identified λ1175 as C III*, although as shown in Table 3.2, we do not have a clear detection of this line because of it being a weak and narrow feature. We can see the λ1175 line in the *HST* composite spectrum (Telfer et al., 2002), the SDSS composite spectrum (Vanden Berk et al., 2001), and in 11 out of 79 quasar spectra in Tytler et al. (2004a). Therefore, we are confident that this λ1175 is a real emission line. The $f-$value

weighted wavelength of the C III* line is λ1175.5289 which matches well the observed wavelength. There is no major resonance line at this wavelength.

3.9.4 Other Possible Emission Lines in the Lyα Forest

Tytler et al. (2004b) and Telfer et al. (2002) reported observing the Si II λ1195 line in their spectra. We do not have any clear detection of the Si II λ1195 line in the 50 quasar spectra. Since other Si II lines, $\lambda\lambda$1265, 1304, are clearly seen redward of the Lyα emission line, it is plausible to expect the Si II λ1195 line.

Si III has a transition at λ1206.50. Since we see both Si II and Si IV redward of Lyα emission, it is natural to expect to see Si III. However, no detection is reported in the literature, and we do not have any positive detection in the 50 quasar spectra. The Si III λ1206 emission line is probably too weak or possibly overwhelmed by broad Lyα emission, only 10 Å away, whose equivalent width is often greater than 100Å.

3.10 Appendix B : 50 *HST* FOS Quasar Spectra

In Figure 3.7-3.11, we showed 15 *HST* FOS quasar spectra to illustrate 5 *classes*. Here we present the rest of 35 *HST* quasar spectra used in §2 and §3 in Figure 3.13. The quasars are sorted by their classification angle θ, and ordered from *Class Zero* to *Class IV*.

3.11 Acknowledgments

This Chapter 3, in full, is a reprint of the material as it has been submitted to *Astrophysical Journal* for publication. The dissertation author was the primary investigator and single author of this paper.

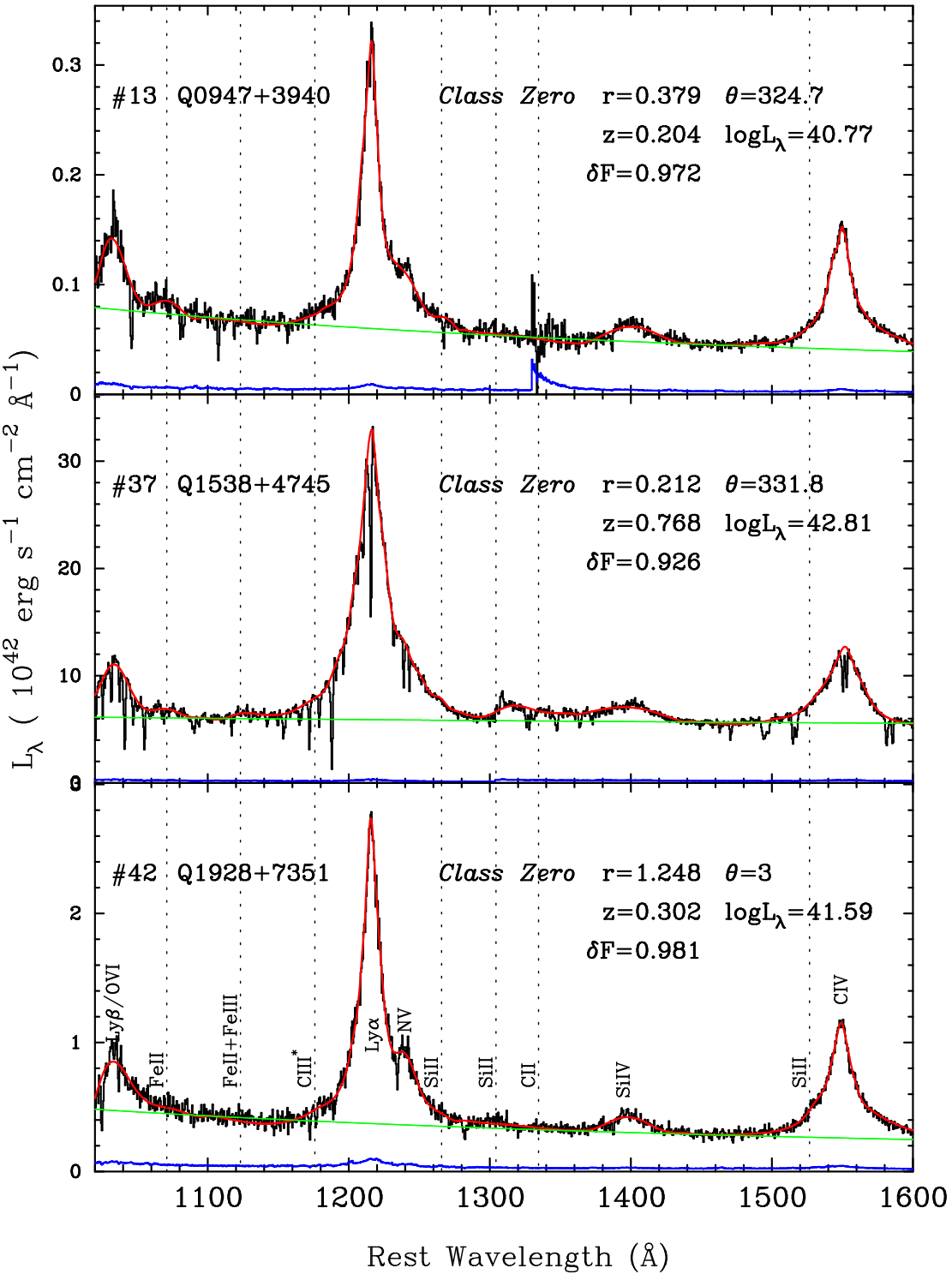

Figure 3.13: We show the rest of 35 *HST* FOS quasar spectra used in §?? and §3. The quasars are sorted by their classification angle θ. Lines are drawn in the same way as in Figures 3.7-3.11.

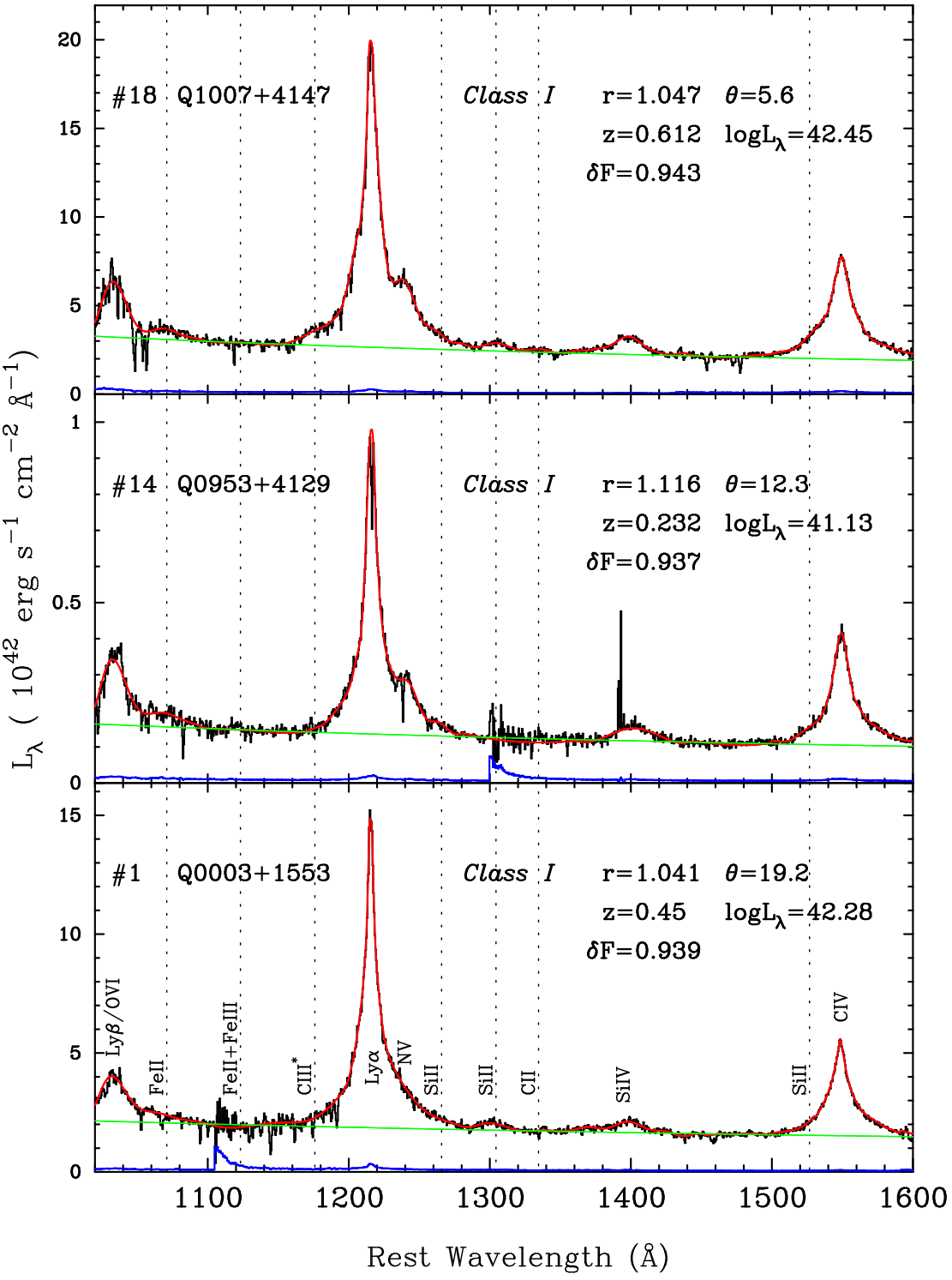

Figure 3.13: (continued)

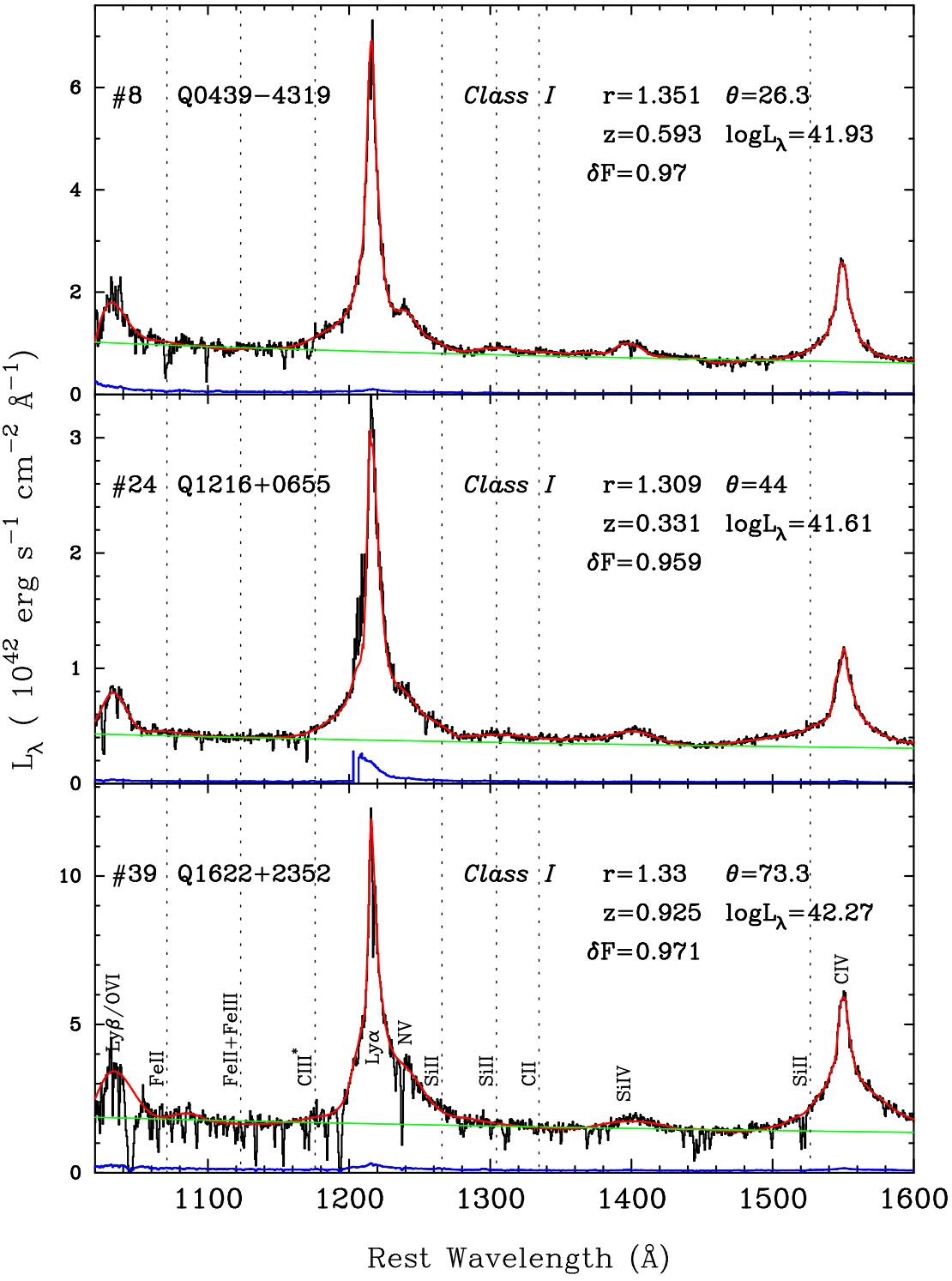

Figure 3.13: (continued)

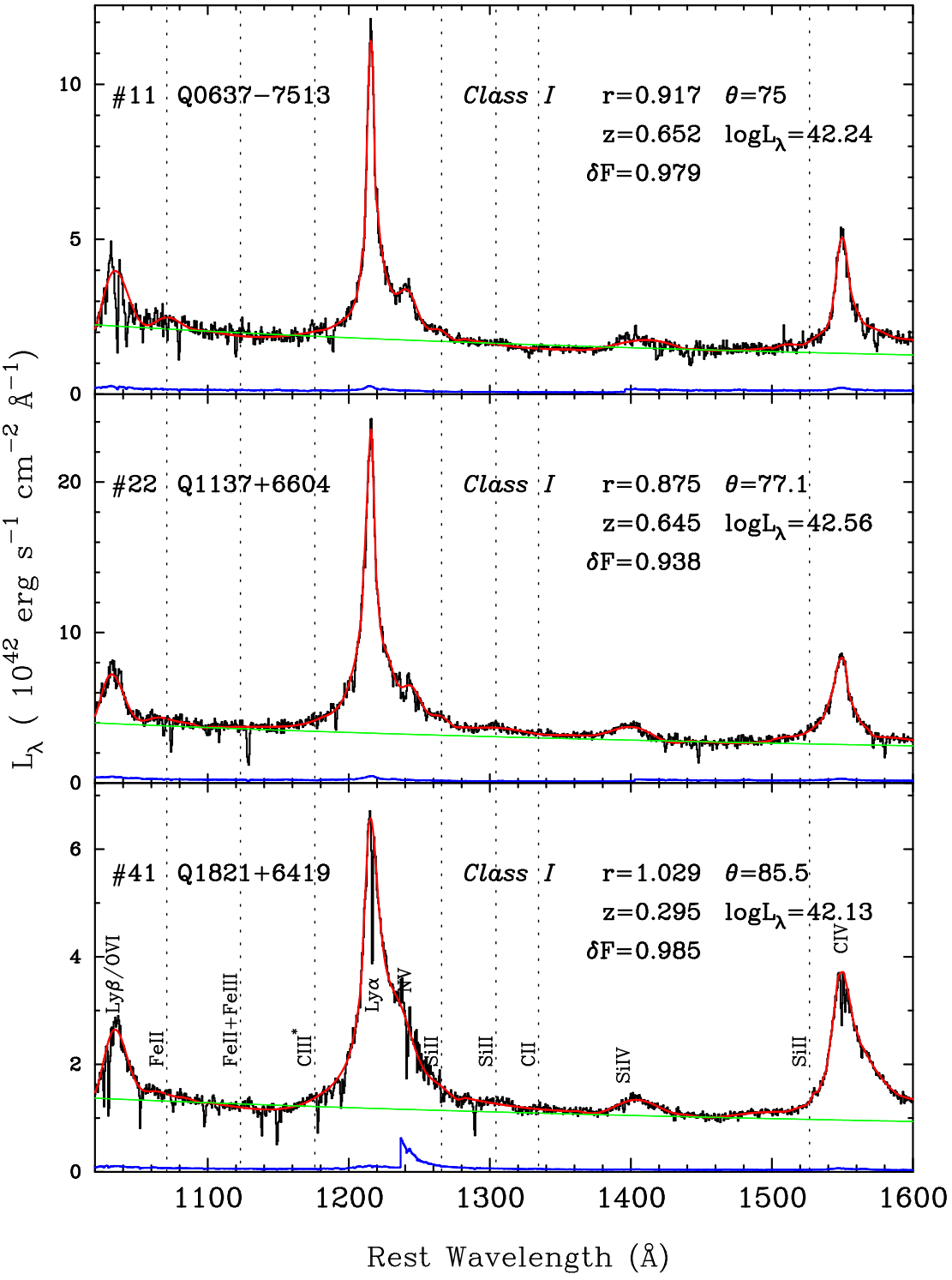

Figure 3.13: (continued)

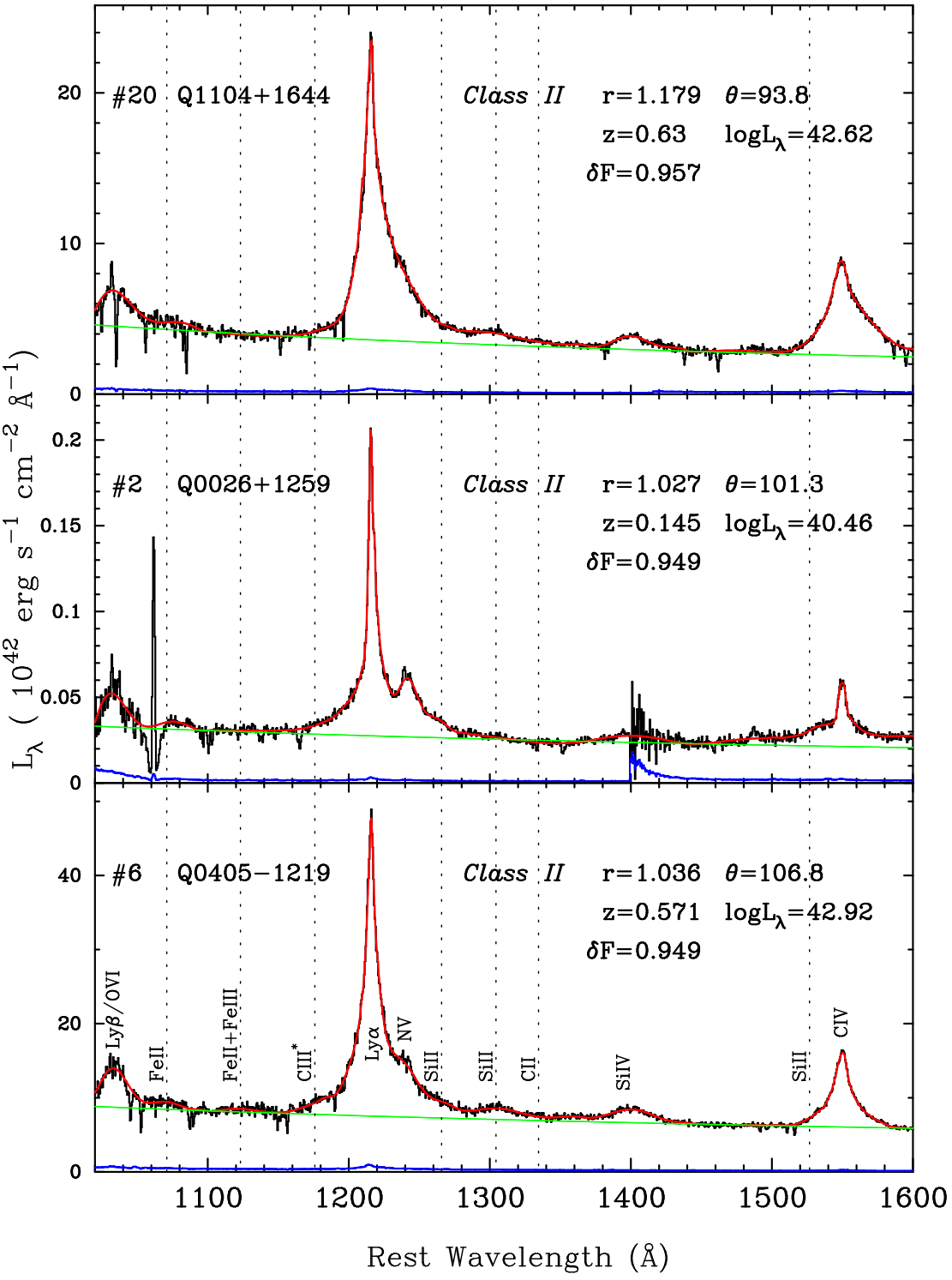

Figure 3.13: (continued)

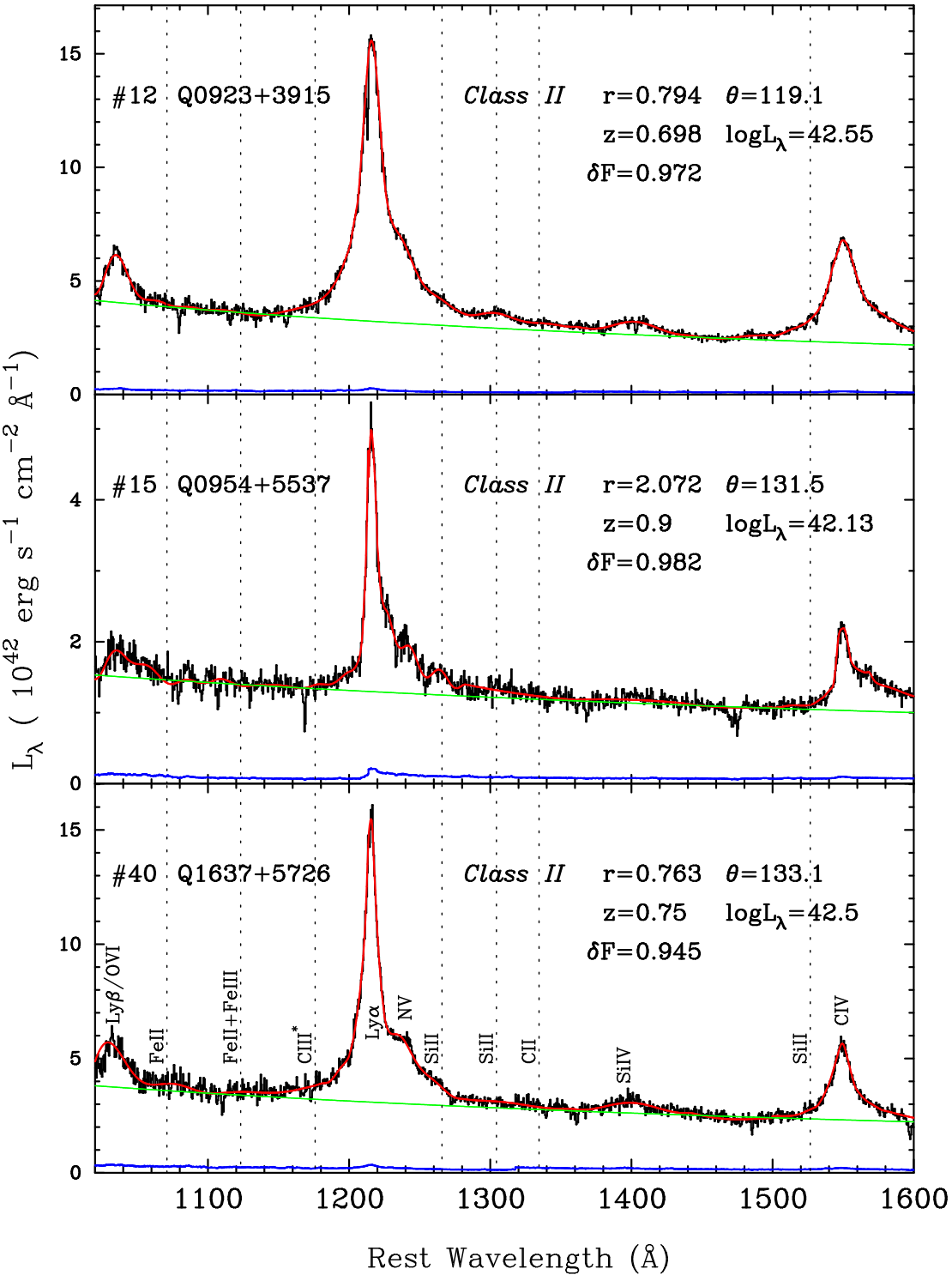

Figure 3.13: (continued)

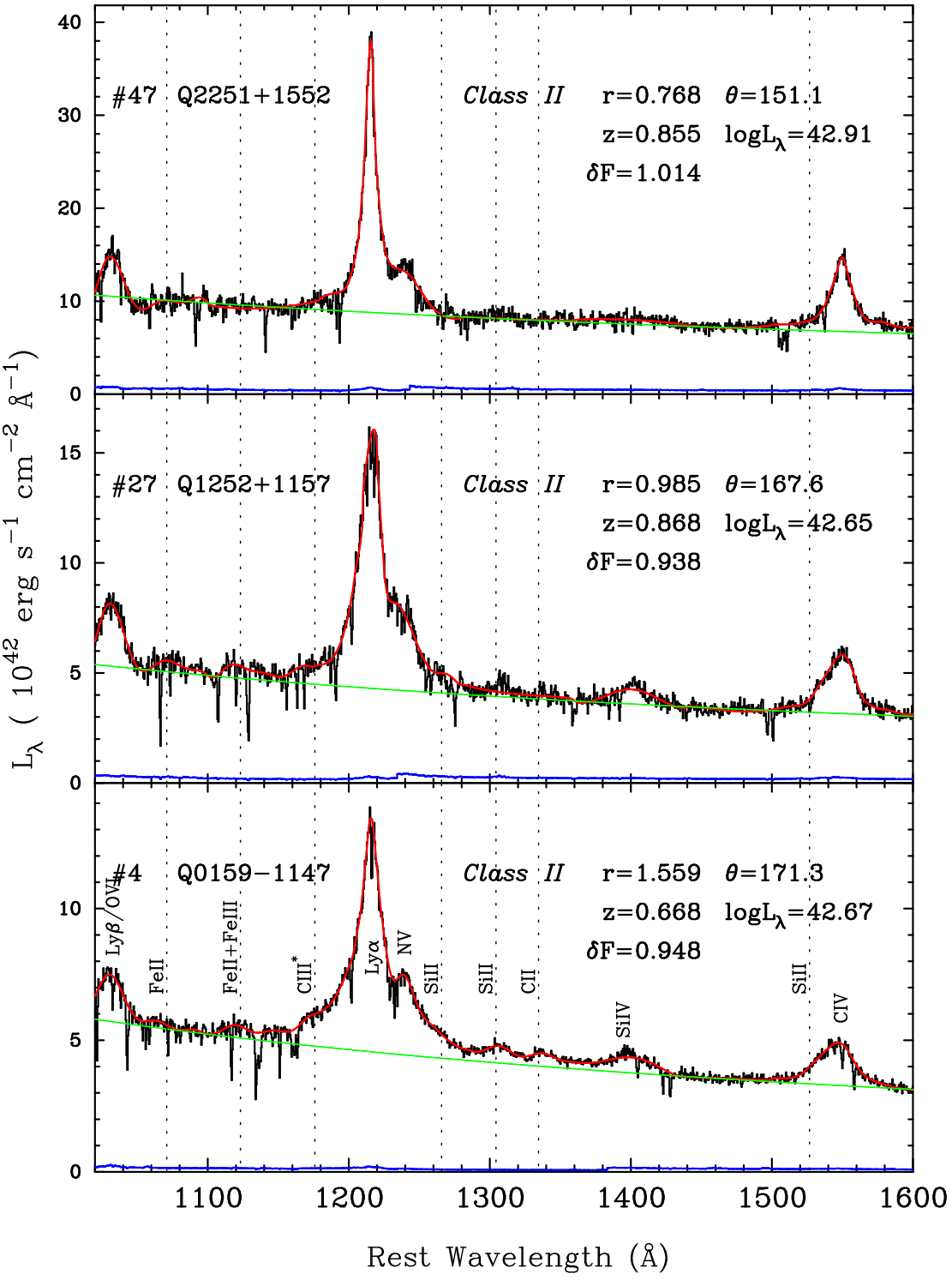

Figure 3.13: (continued)

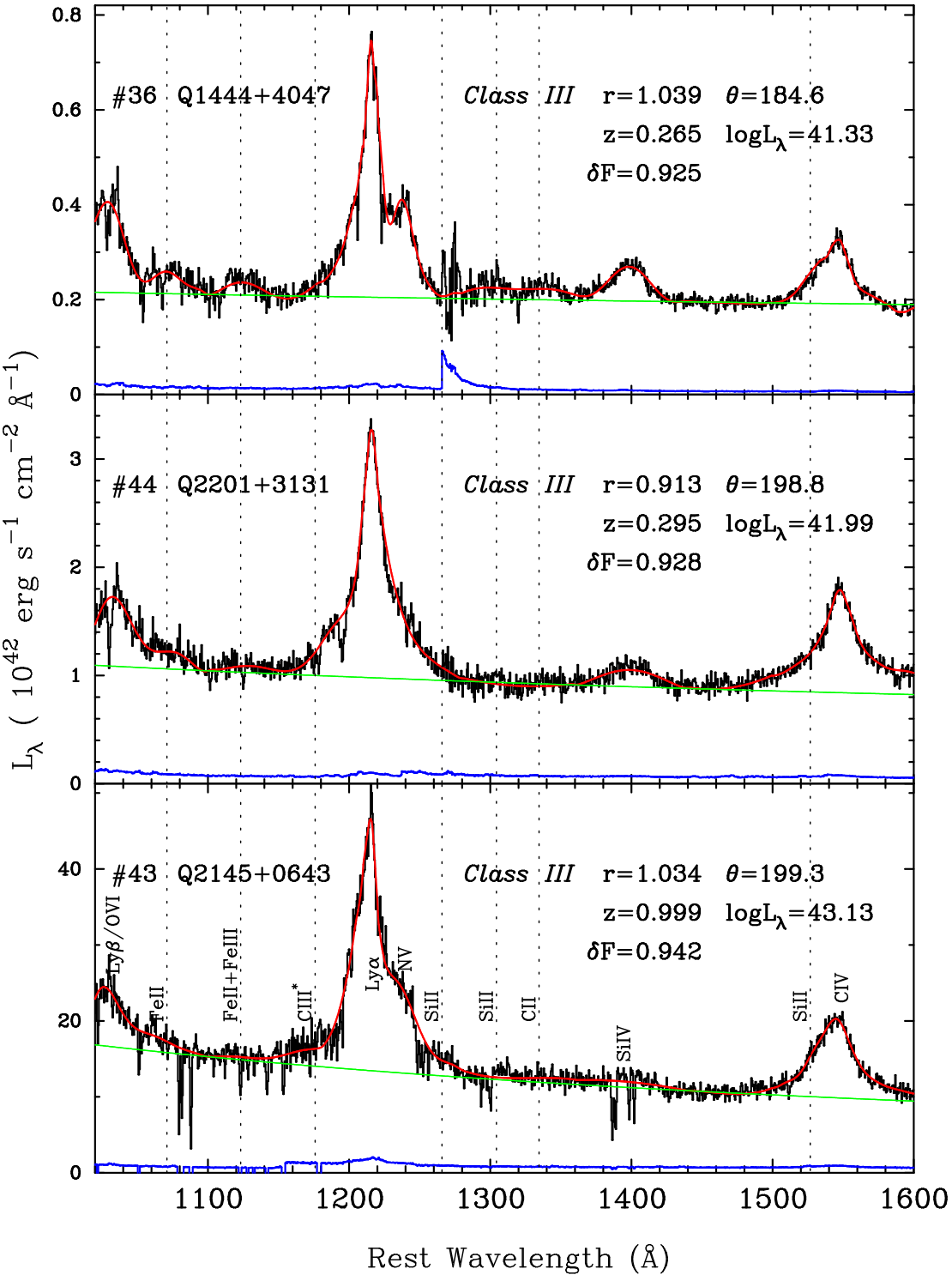

Figure 3.13: (continued)

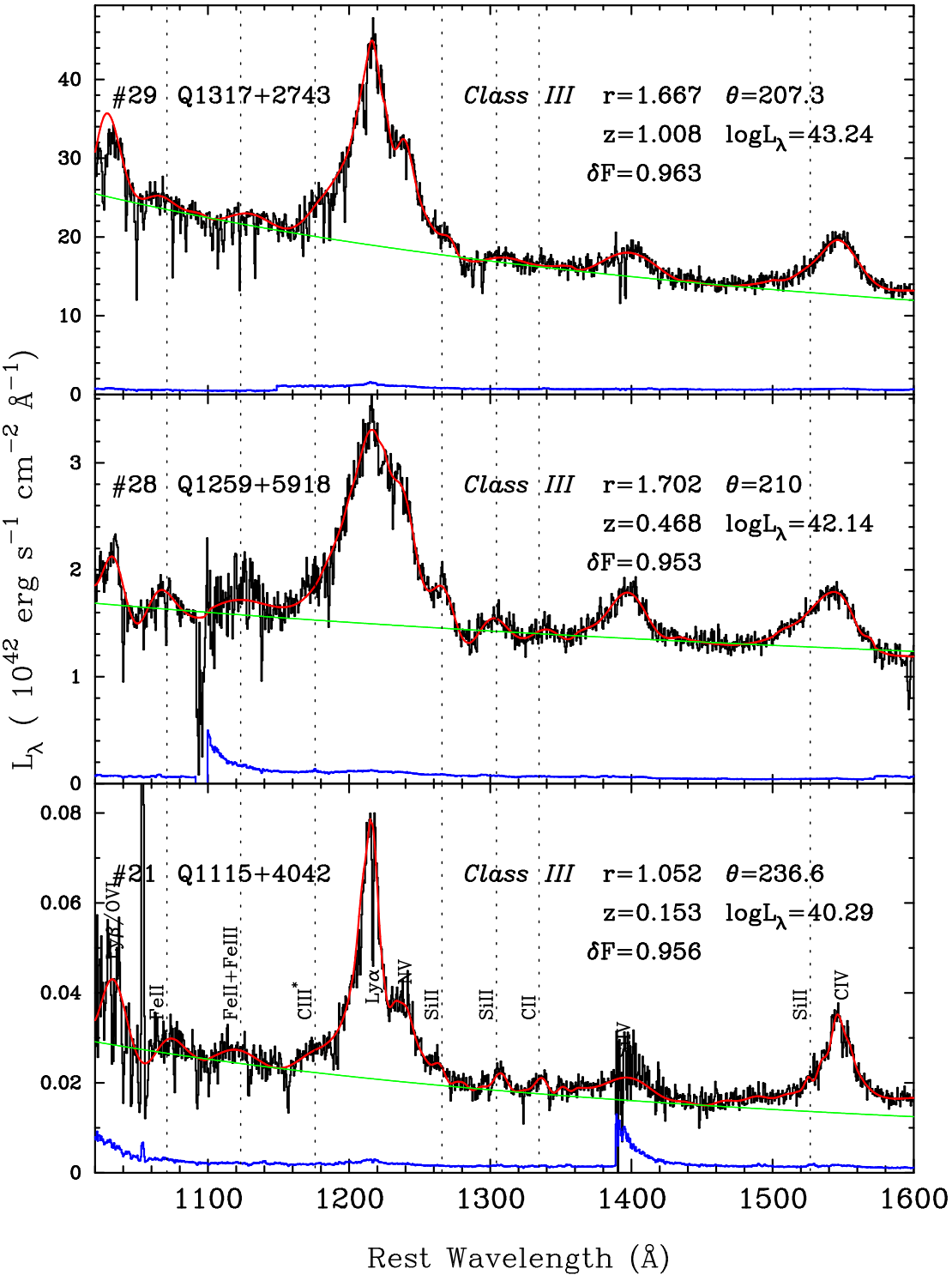

Figure 3.13: (continued)

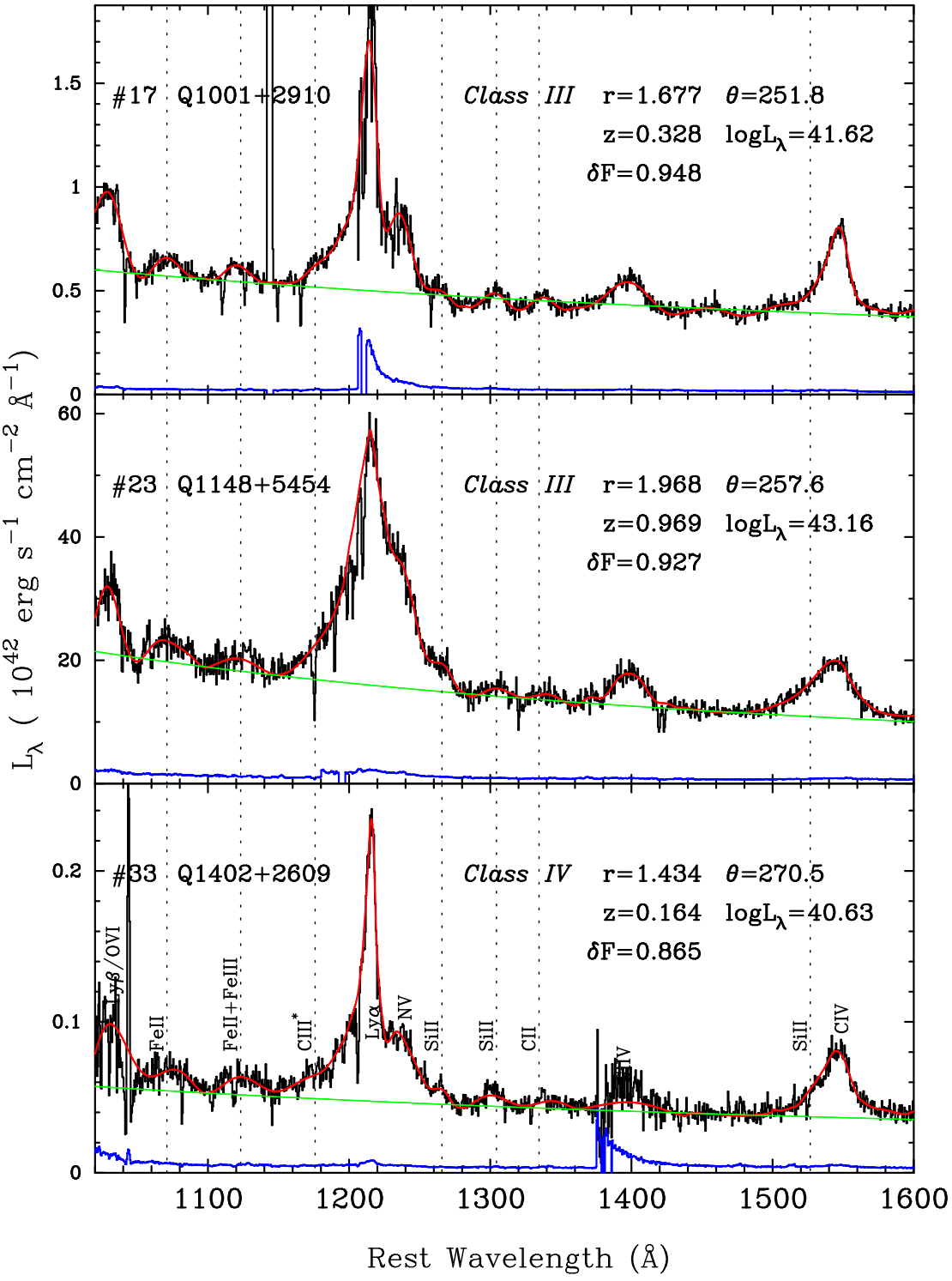

Figure 3.13: (continued)

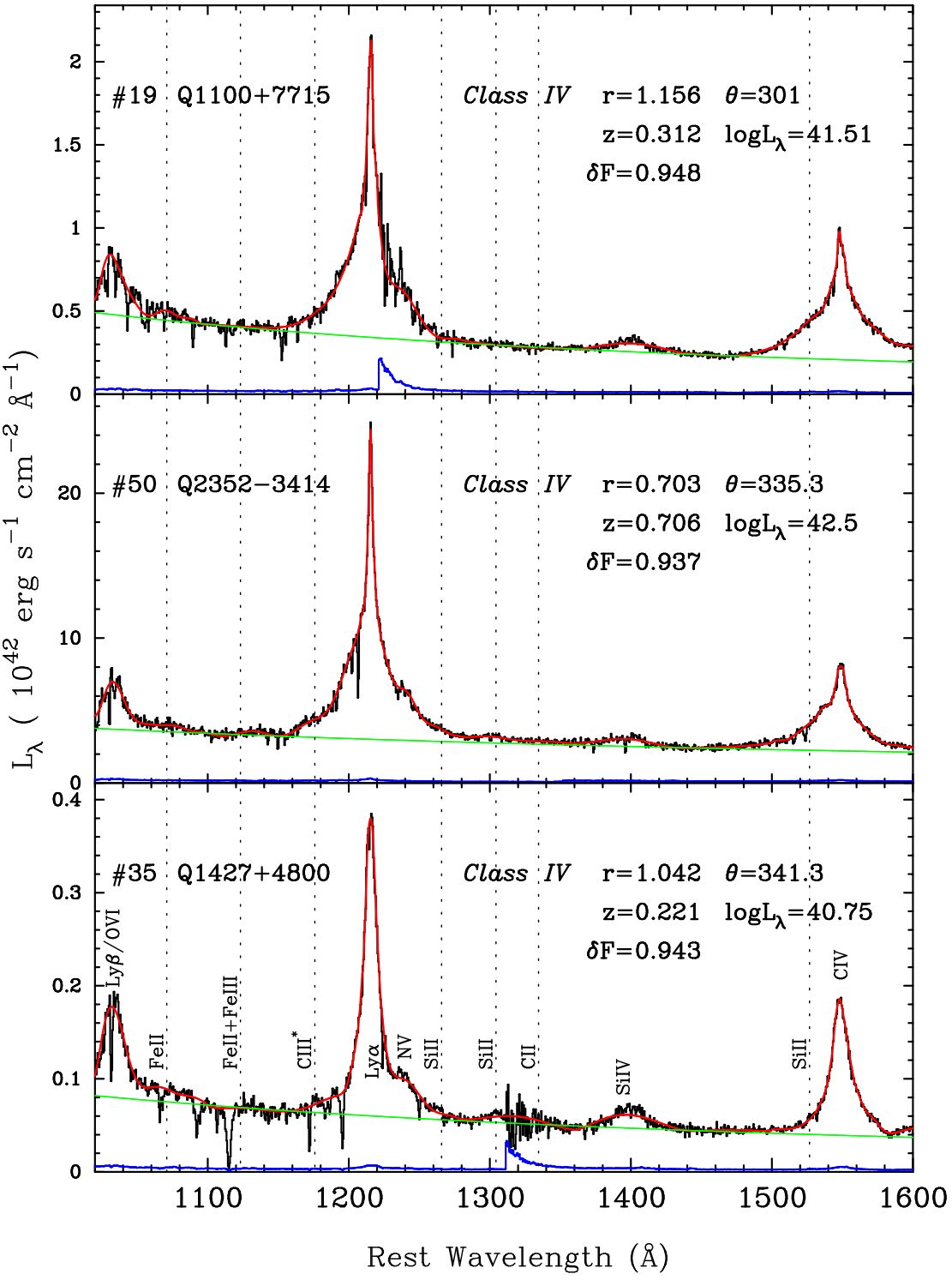

Figure 3.13: (continued)

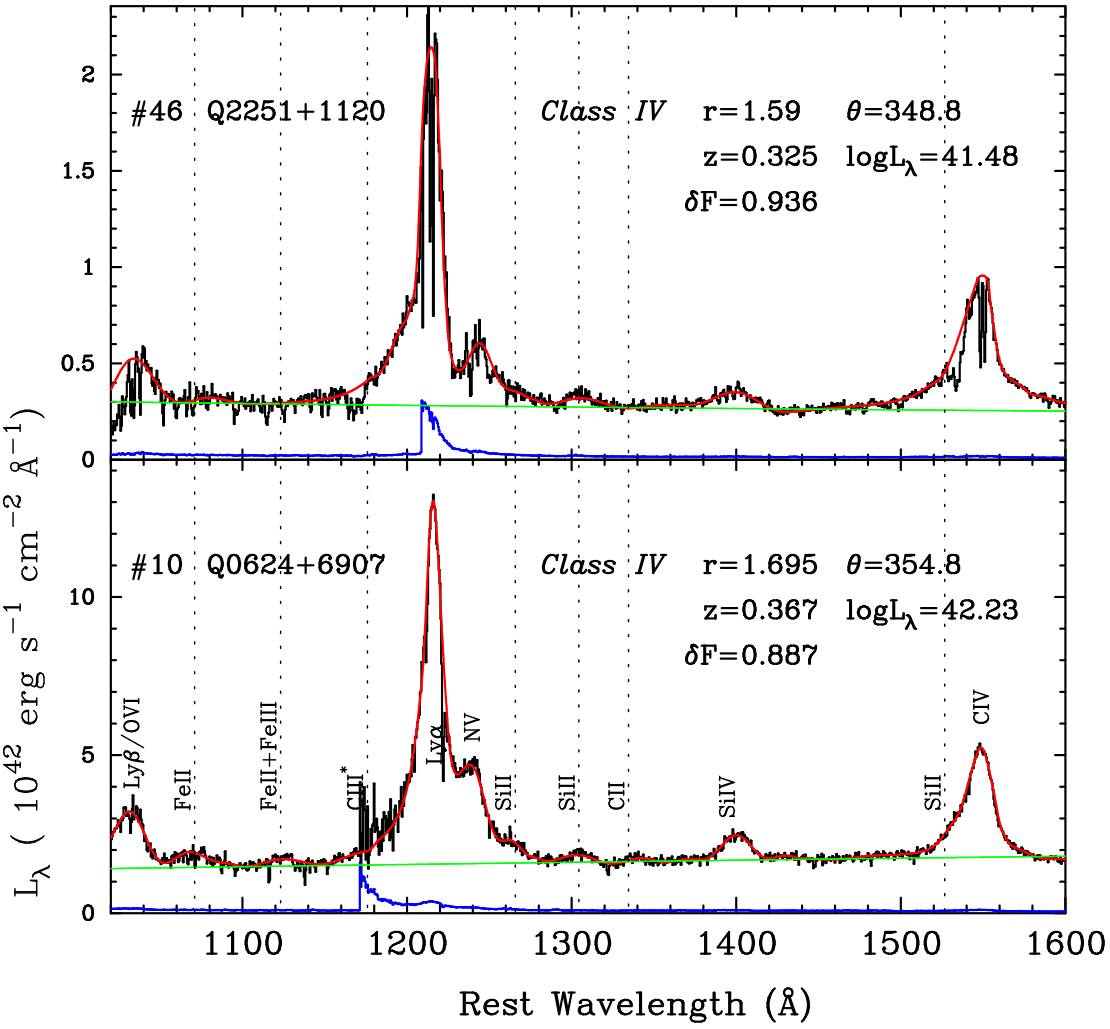

Figure 3.13: (continued)

Chapter 4

Relative Flux Calibration of Keck HIRES Echelle Spectra

4.1 Abstract

We describe a method to calibrate the relative flux levels in spectra from the HIRES echelle spectrograph on the Keck-I telescope. Standard data reduction techniques that transfer the instrument response between HIRES integrations leave errors in the flux of 5 – 10%, because the effective response varies during the night. The flux errors are most severe near the ends of each spectral order, where there can be discontinuous jumps. The source of these errors is uncertain, but may include changes in the vignetting connected to the optical alignment. Our flux calibration method uses a calibrated reference spectrum of each target to calibrate individual HIRES integrations. We determine the instrument response independently for each integration, and hence we avoid the need to transfer the instrument response between HIRES integrations. The procedure can be applied to any HIRES spectrum, or any other spectrum. While the accuracy of the method depends upon many factors, we have been able to flux calibrate a HIRES spectrum to 1% over scales of 200 Å that include order joins. We illustrate the method with spectra of Q1243+3047 towards which we have measured the deuterium to hydrogen abundance ratio.

4.2 Introduction

In recent decades, the combination of large aperture telescopes and high resolution spectrographs have allowed for precision analysis of a variety of astrophysical objects. Echelle spectrographs are the instrument of choice for high resolution, and most large telescopes now have one (Vogt, 1987; Diego et al., 1990; Dekker et al., 2000; Noguchi et al., 1998; Tull, 1998; McLean et al., 1998).

Echelle gratings can give spectra with high spectral resolution, with a large slit width, and a large wavelength range in a single setting (Schroeder, 1987). An echelle grating disperses the spectrum into many tens of spectral orders, which are then cross dispersed by a second dispersive element so that the orders can be placed, one above the other, on a rectangular CCD detector. It is difficult to combine the spectra from the many spectral orders of an echelle to produce a single continuous spectrum. This difficulty arises because the response varies rapidly across each order, and it is not the same at a given wavelength in adjacent orders.

High quality relative flux calibration of echelle spectra is highly desirable in many scientific applications. For example, accurate flux levels over a large range of wavelengths makes it much easier to place continuum levels on spectra with pervasive blended absorption, such as the Lyman alpha forest absorption seen in high redshift QSO spectra.

In this paper, we discuss the relative flux calibration of spectra from the HIRES echelle spectrograph on the Keck-I telescope (Vogt et al., 1994a). We do not discuss absolute flux calibration, as this requires additional calibration data and is not necessary for our absorption line work. We intend that a spectrum with relative flux calibration has the correct shape over some range of wavelengths, and differs from an absolute calibration in only the normalization.

We developed the methods described in this paper to improve our measurements of the primordial Deuterium to Hydrogen abundance ratio in QSO absorption systems, for which the bulk of our spectra come from HIRES. We have found that

we obtain more accurate and reliable estimates of the absorption column densities when we use spectra with accurate relative flux. High quality flux calibration was not a major design goal for HIRES, and we have found that special steps must be taken to obtain the quality of calibration that we need for our work on D/H. The usual (Willmarth & Barnes, 1994; Massey et al., 1992; Clayton, 1996) methods of echelle flux calibration appear inadequate for reasons that we report in Section 2 and Appendix A. This inadequacy motivated the development of the methods we describe.

We would like to both minimize the flux errors in our spectra, and to estimate the size of errors which remain after our calibrations. We shall find that the flux calibration errors depend on wavelength and they are correlated on various wavelength scales. We would like to estimate the size of the errors on these different scales. We would also like to make the error in the relative flux calibration less than the photon noise on some relevant scale. For example, when we fit a flat continuum level to a 50 pixel(105 km s^{-1}) segment of a HIRES spectrum with S/N of 100 per pixel, the photon noise on the continuum level is 0.14%.

We found that it is harder to approach a given accuracy in relative flux calibration in many places. These places include the regions where echelle orders join, regions where spectra have lower S/N, wavelengths in the near UV, and in general as the wavelength range increases. It is very hard to get flux calibration errors of $< 1\%$ over even a wavelength range of < 40 Å within one HIRES order. Fortunately for our absorption line work, errors that vary smoothly over wavelength scales > 40 Å are not as serious as errors on smaller scales.

In this paper, we describe a way of calibrating the relative flux in a HIRES spectrum using well calibrated reference spectra of the same target to transfer flux information from other spectrographs to the HIRES spectra. We force each HIRES spectrum to have the shape of these reference spectra. This method should correct a variety of flux calibration errors, both from variable vignetting and differences in spectrum extraction and reduction. The method could also be applied to spectra

from various spectrographs, and not just echelles. This method is based on that introduced by Burles (1997); Burles & Tytler (1998b) and applied with improvements to HS 0105+1619 in O'Meara et al. (2001).

The paper is organized as follows: we first describe the nature of inconsistencies between repeated HIRES observations of a target, and how this impacts flux calibration. Second, we describe the spectra we used to illustrate our flux calibration method. Third, we describe at first in overview, and then in detail, our methods for flux calibration and how we combine individual echelle orders. Then, we discuss the accuracy and errors of our method.

4.3 Description of the HIRES Flux Calibration Problem

The usual methods of flux calibration appear inadequate when applied to HIRES spectra. When we determine the instrument response by observing a spectrophotometric standard star, different exposures of the same star give different instrument response functions, even when we believe that the exposures were taken with the same instrument configuration. For example, in Figure 4.1, we show the signal extracted from two HIRES integrations of G191-B2B. The exposures were taken on consecutive nights, with similar instrument configurations. On the second night the star was 0.07 degrees higher in the sky and the image rotator (Appendix 4.13) physical angle differed by 0.071 degrees to compensate for the change in parallactic angle. The spectra were both extracted and sky subtracted with Tom Barlow's MAKEE software (April 2001 version). Counts are approximately "raw" ADU from the CCD.

The differences between the two exposures shown in Figure 4.1 are large and unexpected. In particular, even though the exposures were taken on different nights, we did not expect to see large ($\sim 10\%$) differences within a single order, even after the two exposures were normalized to have the same mean flux in that order. The differences are largest ($\sim 10\%$) at the ends of the order. Similar differences (both

in shape and magnitude) are present in each observed spectral order. However, the form of the difference is not precisely the same for each order, as demonstrated in Figure 4.2. Barlow & Sargent (1997) also noted the possibility of systematic flux errors of 10% near order overlaps.

Flux differences have also been reported for the Subaru telescope HDS echelle spectrograph that sometimes shows 10% changes during observations (Aoki, 2002).

We have examined approximately 20 other pairs of standard star integrations from HIRES that have similar instrumental setups. Most show differences of order 10%, though the shape of the differences is not always the same. In addition to the "U" shaped ratios (seen in Figure 4.1), we see three other shapes for ratios: near flat ratios, tilted and ogive (or "fallen S") shapes. In each case, the shapes of the ratios vary gradually order-to-order in a systematic way, such that adjacent orders have similar shapes. The shapes of the ratios vary much more between pairs of integrations than they do from order-to-order for a given pair of integrations.

Approximately 30% of integration pairs give flat ratios that indicate that the instrumental response was very similar for the two integrations, which should make flux calibration simple. A cursory examination did not show any predictors (e.g. telescope elevation, rotator angle, position of target on the slit, seeing) as to which pairs would be similar and which different.

In Figure 4.3, we show HIRES integrations on two stars that we flux calibrated in the usual manner, each using a response function determined from a HIRES exposure of a standard star. The spectra that we calibrated differ from the known flux levels by large amounts over a wide range of wavelengths. The main deviations are systematic across each HIRES order. We also see large differences at the order overlap wavelengths. Different ways of combining spectral orders leave different flux calibration errors. If we take the mean of the signals then the flux will jump in a single pixel, by up to 10%, where each order begins and ends. Therefore, in a complete HIRES spectrum, we expect to see approximately the same number

of jumps as the number of recorded echelle orders, which is typically 30 – 40.

In the past, we have attempted to reduce the flux errors by fitting continua to each order, and dividing by these continua, before we take the mean flux in a wavelength overlap. This method is unsatisfactory because it is very hard to ensure that the continua that we fit to adjacent orders have both the same flux levels and the same shapes, and we loose flux information.

For some unknown reason, long integrations on a QSO show smaller differences than short integrations on a bright star. A dependence on integration time might relate to some averaging, perhaps related to the target position on the slit. A dependence on brightness might relate to the 100 times lower signal in the QSO integrations, and perhaps subsequent differences in the spectrum extraction. We still have difficulty flux calibrating QSO exposures, even though they appear to be more stable than exposures on standard stars, because usual procedures still require that we determine the instrument response from a standard star exposure.

The variations we see in standard star exposures indicate that there is some instability in either Keck+HIRES, in our data reduction processes, or in both. We have investigated two possible origins for the instability: variable vignetting inside of HIRES, and inadequate the extraction of the spectra. We do not see a clear signature of either in our spectra, but we do know that the vignetting is expected to change.

We have explored the possibility of extraction errors by varying the type of profile used during extraction, and the profile width, but found no differences from the standard extraction results from MAKEE. We also measured flux ratios from the raw counts in the CCD images that were similar to those in the spectra extracted by MAKEE.

We expect that the vignetting inside HIRES changes with the position angle of the sky image on the HIRES slit and with the telescope elevation (Appendix 4.13). When the image rotator is used there are two main options. We can use the image rotator in "Vertical angle mode" to keep the local vertical direction along the

slit, so that the position angle varies with the position of the target in the sky. The rotator can also be used to keep a desired position angle along the slit. If the rotator is not used, the relevant angle depends on the telescope elevation. The variation in vignetting arises from a known mechanical and optical misalignment between the Keck-I telescope and HIRES, and the expected amount of change in the vignetting, from ray tracing kindly provided by Steve Vogt, is approximately 10%, consistent with our observations.

We can account for why the ratios of HIRES spectra have similar shapes across all orders if the variable vignetting happens after the echelle, and before leaving the cross-disperser. In this part of HIRES the light from the red end of each order is separated from that in the blue end, but all orders are coincident. We might explain the shape of the ratios, and the similarity from order-to-order, if a varying amount of light misses the top and bottom of the cross-disperser (the grooves are vertical), where the red and blue ends of the orders land. This variation could arise when the cone of light from the telescope tips up and down in the vertical plane that connects the center of the tertiary mirror and the HIRES slit.

However, we suspect that vignetting is not the sole cause of the variations in the flux, because we have seen variations in spectra taken under apparently identical instrumental conditions (same elevation, image rotator setting, and target location on the slit) on consecutive nights, as we saw in Figure 4.1.

The changes might also come from differences in the extraction of the spectra from the CCD image, e.g. if we do not extract a fixed proportion of the flux recorded at each wavelength. Differences in the extraction of spectra, including multiple integrations on a given target, are likely whenever there are changes in conditions, such as the location of the target along the slit, the seeing, the sky brightness and the amount of signal recorded. However, extraction problems seem an unlikely explanation for standard stars that have high S/N.

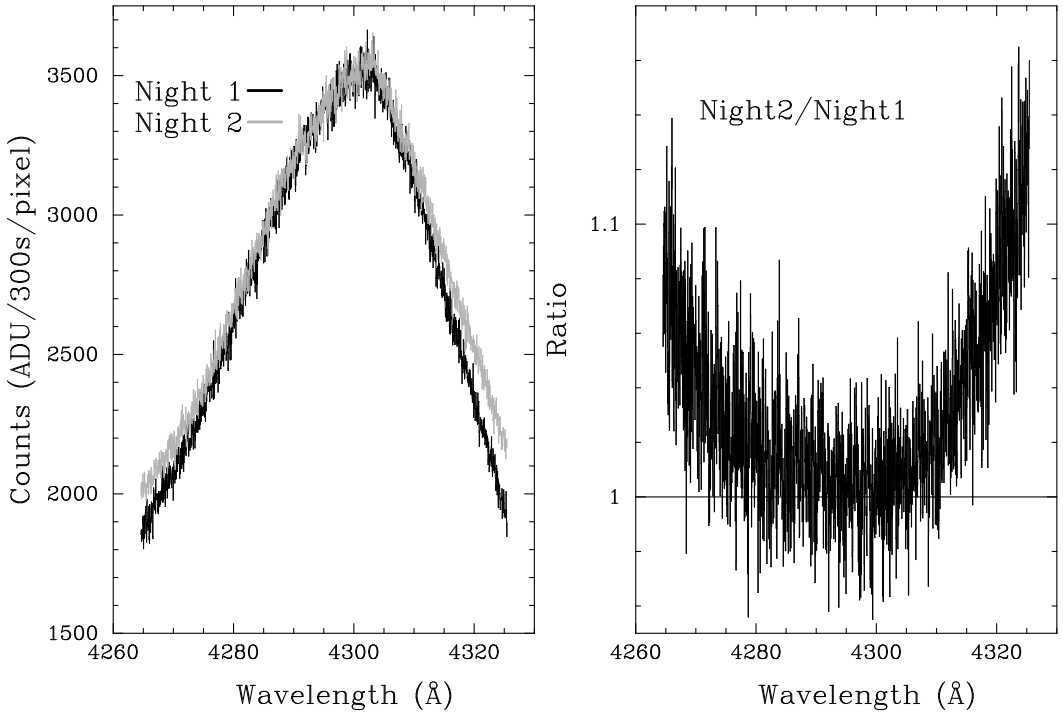

Figure 4.1: Two 300 second integrations of the star G191-B2B taken with near identical HIRES setups on consecutive nights: 19 (solid) and 20 (light) September, 2000. The right panel shows the ratio of the two. These spectra were taken with the C5 dekker (1.14 arcsec slit), and the image rotator was set to align the sky vertical along the slit. The September 19 integration had sidereal time ST = 05:16:48 hours, telescope elevation EL = 56.96 degrees, and image rotator physical angle, as measured looking at the prism, of IROT2ANG = 195.9357 degrees. For September 20th we had ST = 05:02:24, EL = 57.03 degrees and IROT2ANG = 195.8646. The September 20th spectrum was multiplied by 1.06 to give similar counts to the other near 4300 Å to correct for differences in the atmospheric transparency, seeing and the loss of light at the slit.

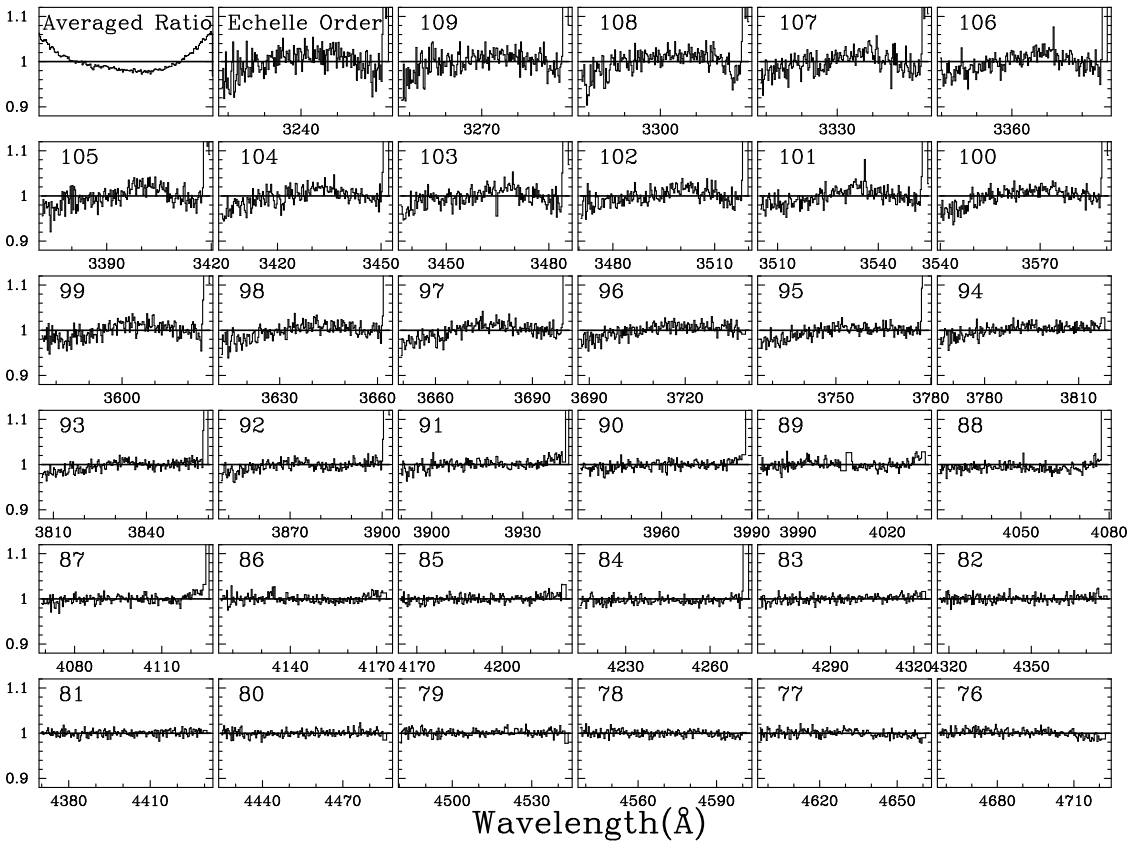

Figure 4.2: The ratio of the two spectra shown in Fig. 4.1, divided by average ratio from the ten orders with the largest wavelengths. We show this average in the top left panel, and other panels each show one HIRES order. We show the full amount of each order that fell on the CCD, which includes some wavelength overlap between adjacent orders. We have re-binned the original 2048 pixels into 205 pixels for presentation.

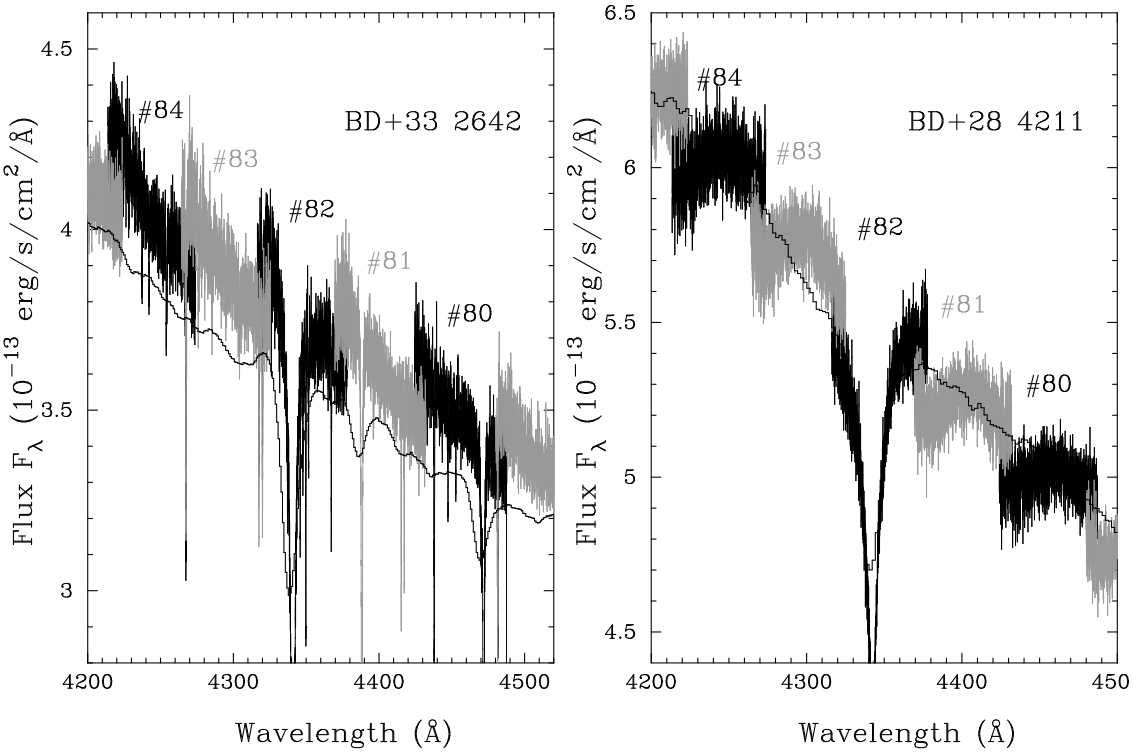

Figure 4.3: HIRES spectra of stars that we flux calibrated in the usual manner. In both cases we see large flux calibration errors. In other cases we can obtain smaller errors. Left, HIRES integration of star BD+33 2642. We determined the response function of HIRES by comparing a HIRES spectrum of G191-B2B, taken on the same night (September 19, 2000), to a model spectrum with known flux (Appendix 4.12). The continuous line shows a lower resolution HST FOS spectrum of BD+33 2642. We may adjust the HIRES spectrum vertically to account for slit losses. The right panel is the same, but for a HIRES integration of BD+28 4211 obtained October 10, 1999, calibrated with a HIRES spectrum of G191-B2B, taken on the same night. The continuous line is a STIS spectrum of BD+28 4211.

4.4 Spectra We will use to illustrate our Method

Here, we introduce the spectra that we will use to illustrate our method of relative flux calibration. This is the set of spectra that we used to measure D/H towards Q1243+3047 (z_{em} = 2.64, V=16.9; Kirkman *et al.* 2003). For our D/H work, we were mostly interested the flux calibration in a 40 Å region centered on the damped Lyα line near 4285 Å, and on the Lyman limit near 3210 Å. We began the development of the methods using a similar set of spectra of HS 0105+1619 that we had used to make an earlier D/H measurement (O'Meara et al., 2001).

We used 5 spectra from the Kast spectrograph on the Lick 3-m telescope, and one from the ESI echelle spectrograph on the Keck-II telescope. We used both the Kast and ESI spectra separately to make independent flux calibrations of 8 integrations from HIRES. Further details of the observations, including the dates, the resolution, the mean S/N, and plots of the spectra are in Kirkman et al. (2003). All of the spectra that we used were shifted into the heliocentric frame, and placed on a logarithmic wavelength scale with a constant velocity increment per pixel, although with different increments for different spectra.

4.4.1 Spectra from Kast

The Kast double spectrograph uses a beam splitter to record blue and red spectra simultaneously in two cameras. For Q1243+3047 we have five KAST integrations, one from 1997, and two each from 1999 and 2001. All integrations were obtained using the d46 dichroic that splits the spectrum near 4600 Å, the 830 line/mm grism blazed at 3460 Å for the blue side, and the 1200 line/mm grating blazed at 5000 Å for the red side. We reduced all exposures with the IRAF package `longslit`.

4.4.2 Spectra from ESI

ESI covers from 3900 – 11,000 Å in ten overlapping orders (Epps & Miller, 1998; Bigelow & Nelson, 1998; Sheinis et al., 2000). We have one exposure of Q1243+3047 using a 1" slit, taken in the echellette mode on January 11, 2000. From the same night, we also have an exposure of the flux standard star Feige 110.

4.4.3 Spectra from HIRES

Our HIRES spectra of Q1243+3047 all used similar instrumental setups. The angle of the HIRES echelle was the same for all exposures, and placed the center of each order near the center of the CCD. The cross-disperser angle was also similar for all exposures, except for one exposure that extended to much larger wavelengths. The image rotator (Appendix 4.13) was used in vertical mode, to minimize slit losses from atmospheric dispersion. We used the C5 decker, which provides an entrance aperture to the spectrograph with dimensions $1.15'' \times 7.5''$. In each case we placed the target near the middle of the slit. The spectra were all recorded on the engineering grade Tektronix CCD with 2048 × 2048 pixels that has been used in HIRES since 1994. The HIRES pixel size is 2.1 km s^{-1}.

The CCD is large enough to record beyond the free spectral range for all orders at wavelengths < 5200 Å, and we placed the spectra on the CCD such that we did record this flux for all such orders. All but one integration covered from near 3200Å out to 4700Å in approximately 36 orders. These integrations were 7200 – 9000 seconds long. The S/N in each integration is near 3 per 2.1 km s^{-1} pixel near the Lyman limit at ~ 3200 Å, and rises to near 35 at the peak of the Lyα emission line at ~ 4400 Å.

The HIRES spectra we use are the normal output from the MAKEE software, which are the raw counts spectrum divided by spectra extracted from flat field integrations. In addition, the CCD defects were marked with negative error values. These spectra differ from the raw counts that we discussed in the previous section in

that the flat field division has removed most of the variation across the orders due to the blaze and vignetting. Although this flat field division may introduce additional undesirable changes in the relative flux, we proceed with these spectra because it is imperative that the CCD defects have been removed.

HIRES Spectral Resolution

We measured the instrument resolution of HIRES by fitting Gaussian functions to narrow, apparently un-blended lines in a single Thorium-Argon arc integration taken before one of the QSO integrations. We fit hundreds of arc lines in all parts of the spectrum, and found a dispersion of $\sigma = 3.4 \pm 0.1$ km s^{-1}, which corresponds to a FWHM spectral resolution of 8.0 ± 0.2 km s^{-1}($b_{ins} = \sqrt{2}\sigma = 4.81 \pm 0.14$ km s^{-1}). We did not detect any variation in the resolution with wavelength. However, we did detect that the arc lines are not Gaussian in shape, with more extended wings, such that the best fitting σ increases when we extend the fitting range around an individual line. We also expect that the spectra will have slightly different FWHM from the arc spectra, because the illumination of the slit is different. The wavelength shifts that we describe in the next section suggest that the resolution will depend in part on the guiding and seeing.

HIRES Wavelength Shifts

We measured wavelength shifts between the HIRES integrations and we shifted the spectra onto the same scale to correct these shifts. We measured the cross-correlations between each of the 7 integrations with the eighth that we used as the reference. An example of the shifts is shown in Figure 4.4. Comparisons of other pairs of integrations often show a much larger dispersion in the measured shifts. In all cases, the shifts measured in each order are consistent with a single shift for each integration. The shifts had a standard deviation of 0.7 km s^{-1}, which is 30% of one HIRES CCD pixel. Each shift was measured to an accuracy of 0.13 km s^{-1}, which we determined from the scatter in the shifts that we measured separately for each

order.

These shifts may arise from differences in the placement of the QSO light in the HIRES slit, which projects to approximately 4 HIRES pixels. The 0.7 km s^{-1} rms shift is approximately 9% of the FWHM resolution, which itself is similar to the slit width. The shifts do not correlate with hour angle or the correction that was applied for the Earth's orbital motion (< 30 km s^{-1}) and spin (< 0.4 km s^{-1}). The shifts are also larger than we expect from wavelength scale errors. However, we did find much larger wavelength scale errors when we did not ensure that MAKEE used enough arc lines to determine the dispersion solution for each order.

4.5 Overview of the Method

There are three main steps in our procedure to apply relative flux calibration to HIRES spectra.

- Step 1: Flux calibrate a high quality reference spectrum of the target.
- Step 2: Flux calibrate the HIRES echelle orders with the reference spectrum. This imposes the long scale (> 10 Å) spectral shape of the reference spectrum upon each HIRES echelle order. The flux information on smaller scales (e.g. absorption line profiles) still comes from HIRES.
- Step 3: Combine the HIRES orders. We first sum the integrations and then join the orders to give one continuous spectrum.

These procedures do not replace standard CCD spectrum extraction procedures. Rather, they should be thought of as a "software patch", applied to correct errors that remain after the spectra have been extracted, and perhaps calibrated, in the usual way. Reasonably well calibrated HIRES spectra are required as inputs to our method, because the flux information on scales < 10 Å will still come directly from the HIRES spectra. The procedure is not unique, and we expect that

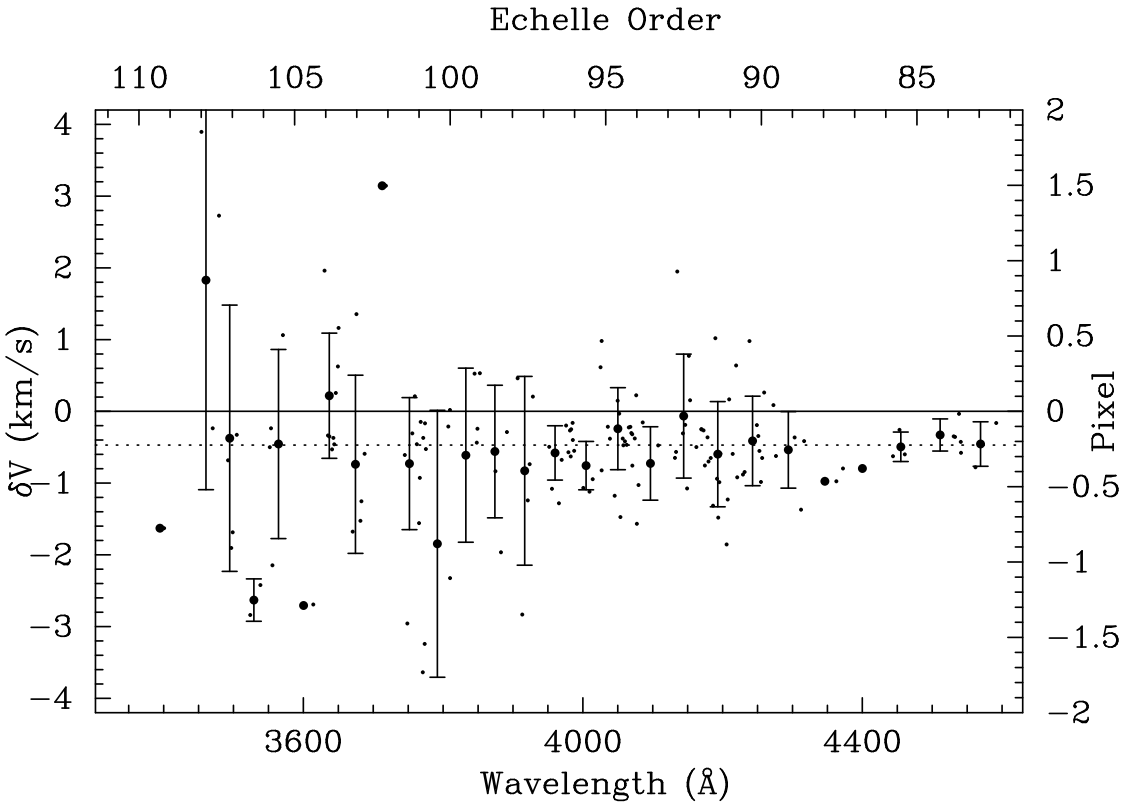

Figure 4.4: The wavelength shifts measured between two consecutive HIRES integrations for Q1243+3047, both taken on March 13, 2000. The small points show shifts measured by cross-correlating blocks of approximately 20 pixels that contain an absorption line. The larger points show the mean shift per order, and the vertical bars show $\pm 1\sigma$ from the distribution of the measurements in that order. The dotted line shows the mean shift between the two integrations.

other sequences might be appropriate for different spectra. We developed a semi-automated pipeline to match MAKEE-reduced HIRES spectra to the IRAF-reduced Kast spectra or the MAKEE-reduced ESI spectra.

We now discuss in further detail each of the steps outlined above.

4.6 Step 1: Flux Calibrating the Reference Spectra of the Target

Since we should not transfer information about the instrument response between exposures, we must "self-calibrate" each exposure we take with HIRES. The first step of our method is thus to obtain a well calibrated spectrum of the target. The reference spectrum must come from a well calibrated and stable spectrograph. In our work on Q1243+3047, we obtained reference spectra from both Lick+KAST and Keck+ESI, and compared them to gauge the accuracy of the final flux calibration.

4.6.1 Flux Calibration of Kast Spectra

To calibrate the flux in our Kast spectra of Q1243+3047, we took flux information from a model spectrum of G191 B2B for the 1997 spectrum, and a STIS spectrum of BD 28 4211 for the 1999 and 2001 exposures. We discuss the reasons behind our choice of these standard stars in Appendix A. We measured and matched the resolution of the observed and reference spectra of the standard stars before we used them to calculate the Kast response function. In Figure 4.5, we illustrate the flux calibration process. The dip in the response at the end of blue CCD and the beginning of red the CCD is due to the changing efficiency of the beam splitter.

The spectrum shows atmospheric ozone absorption lines (Schachter, 1991) as the wiggles of the raw CCD counts (panel b) below 3400 Å. Their strength depends on the temperature of the ozone layer and the effective airmass of the integration,

and we have not made appropriate adjustments. We left the wiggles un-smoothed in the response (Figure 4.5, panel d) to help partially remove their effect from the quasar spectrum.

In Figure 4.6, we show the accuracy of the flux calibration of a Kast spectrum of another star. The flux residuals between our calibrated KAST spectrum and a STIS spectrum of the same star are less than 3%.

Figure 4.5: Steps in the calibration of the flux in a Kast spectrum. Panel (a) shows the STIS spectrum of star BD+28 4211. Panel (b) shows the raw counts recorded in two simultaneous Kast integrations, one with the blue camera (left) and one with the red camera (right). We do not show the wavelength overlap on either side of the central wavelength of the dichroic beam splitter (called d46), which we show with the vertical line near 4450 Å. We had moved the "x-stage" that holds the CCD of the blue camera of Kast to sample wavelengths well beyond the peak of the Lyα emission line. Panel (c) shows the response function (b)/(a), and panel (d) shows the raw counts in one 5400 second integration on Q1243+3047. Panel (e) shows the flux calibrated spectrum, (d)/(c).

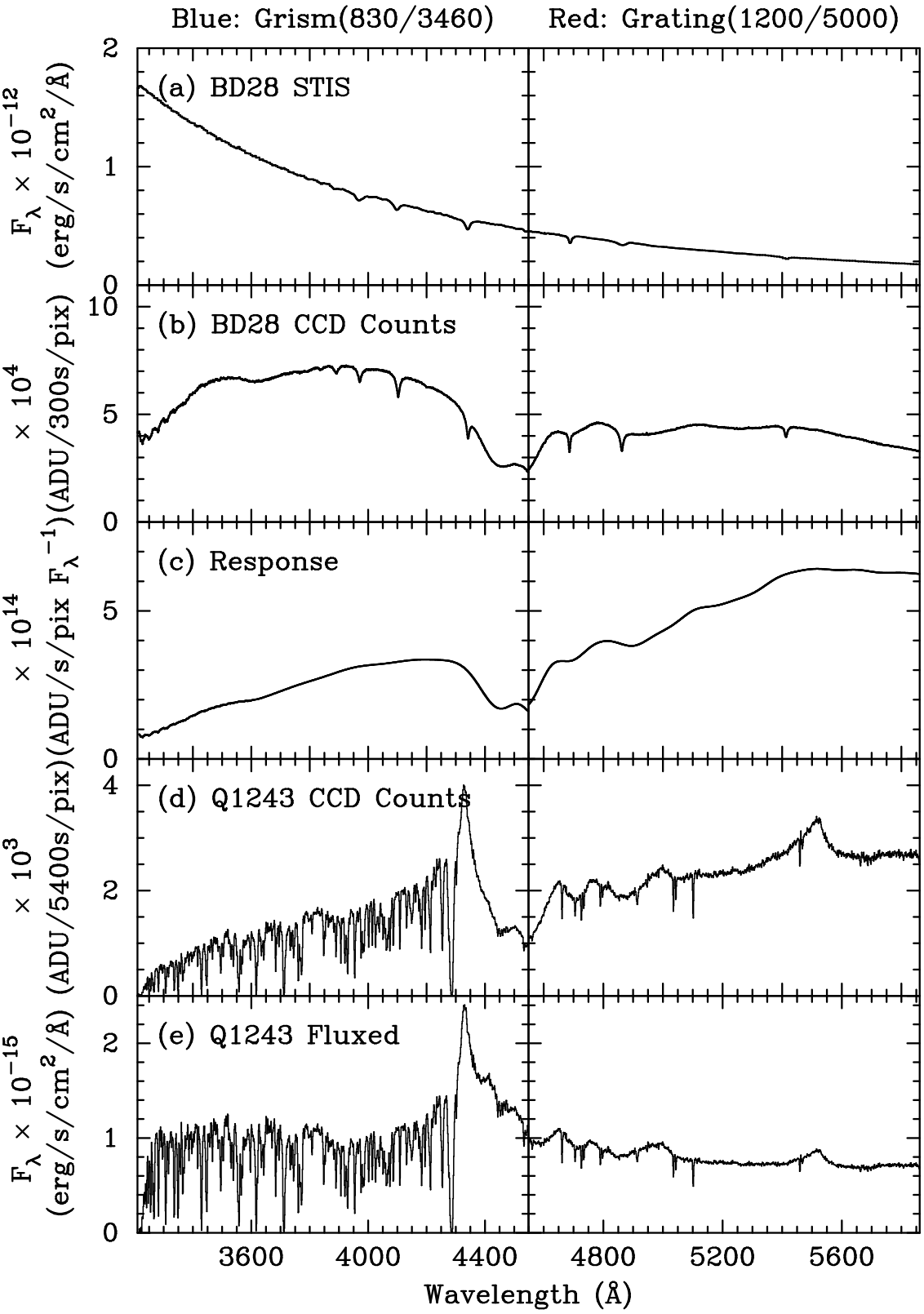
Blue: Grism(830/3460)
Red: Grating(1200/5000)
(a) BD28 STIS
(b) BD28 CCD Counts
(c) Response
(d) Q1243 CCD Counts
(e) Q1243 Fluxed
$F_\lambda \times 10^{-12}$ (erg/s/cm^2/Å)
$\times 10^4$ (ADU/300s/pix)
$\times 10^{14}$ (ADU/s/pix F_λ^{-1})
$\times 10^3$ (ADU/5400s/pix)
$F_\lambda \times 10^{-15}$ (erg/s/cm^2/Å)
Wavelength (Å)

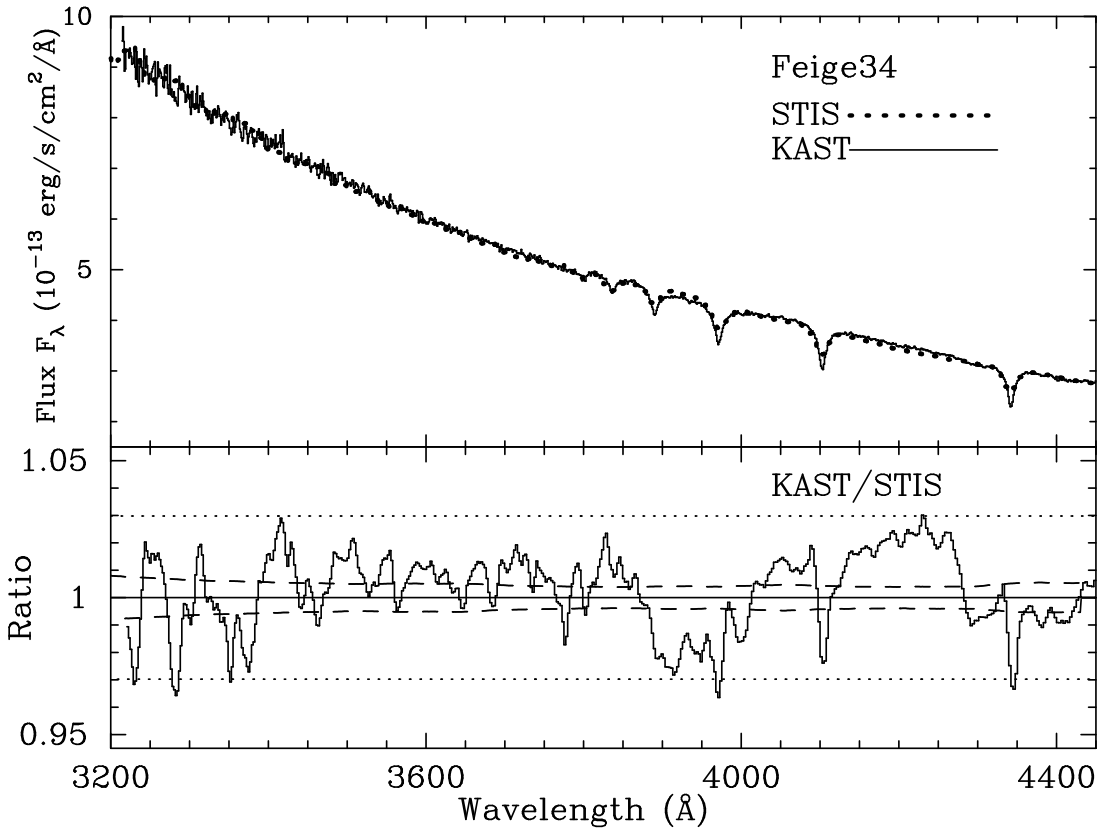

Figure 4.6: Top Panel: Two spectra of the star Feige 34, one from STIS (solid line, Bohlin et al. 2001), and the other a Kast spectrum that we have flux calibrated (dotted). We calibrated the Kast spectrum with Kast spectrum of the star BD+28 4211. We also normalized the Kast spectrum to have the same mean flux as the STIS spectrum to adjust for slit losses. Bottom Panel: Ratio of the two spectra in the top panel. The dotted line is the error for the STIS spectrum (approximately 1% random and 3% systematic), and the dashed line is the random error from the photon noise in the Kast spectrum. These errors are for 2 Å pixels.

4.6.2 Flux Calibration of ESI Spectrum

We flux calibrate ESI spectra in the same way as we do those from Kast. In Figure 4.7, we show the steps in the flux calibration of an ESI spectrum. The ESI orders overlap in wavelength, and in Figure 4.8, we see that the orders do not always have the same flux. These differences increase in size as we approach the end of an order. We have not investigated the origin of these flux differences. We cut off most of the regions where the differences exceeds 2% (which is the noise level in our spectrum) without leaving any gaps in the wavelength coverage. We do not know the size of the remaining error, especially in regions where there was no wavelength overlap, because we do not have redundant observations of bright stars. Nonetheless, the ESI spectra could have better relative flux calibration than HIRES spectra, for several reasons. ESI has fewer orders, each of which covers more wavelength range and a much larger portion of each order is sampled by adjacent orders. ESI has a fixed instrumental configuration and our ESI spectra have much higher S/N than our individual HIRES integrations, which may change the proportion of the flux that is extracted.

Figure 4.7: Steps in the flux calibration of an ESI integration of Q1243+3047 using an ESI spectrum of the star Feige 110 obtained on the same night. We show only 3 of the 10 ESI orders. Panel (a) at the top shows the STIS flux calibrated spectrum of star Feige 110. Panel (b) shows the raw CCD counts from an ESI spectrum of this star. Panel (c) shows the smoothed ratio (b)/(a) that is the response function of ESI. Panel (d) shows the raw counts from an integration of Q1243+3047, and panel (e) shows the same spectrum after relative flux calibration.

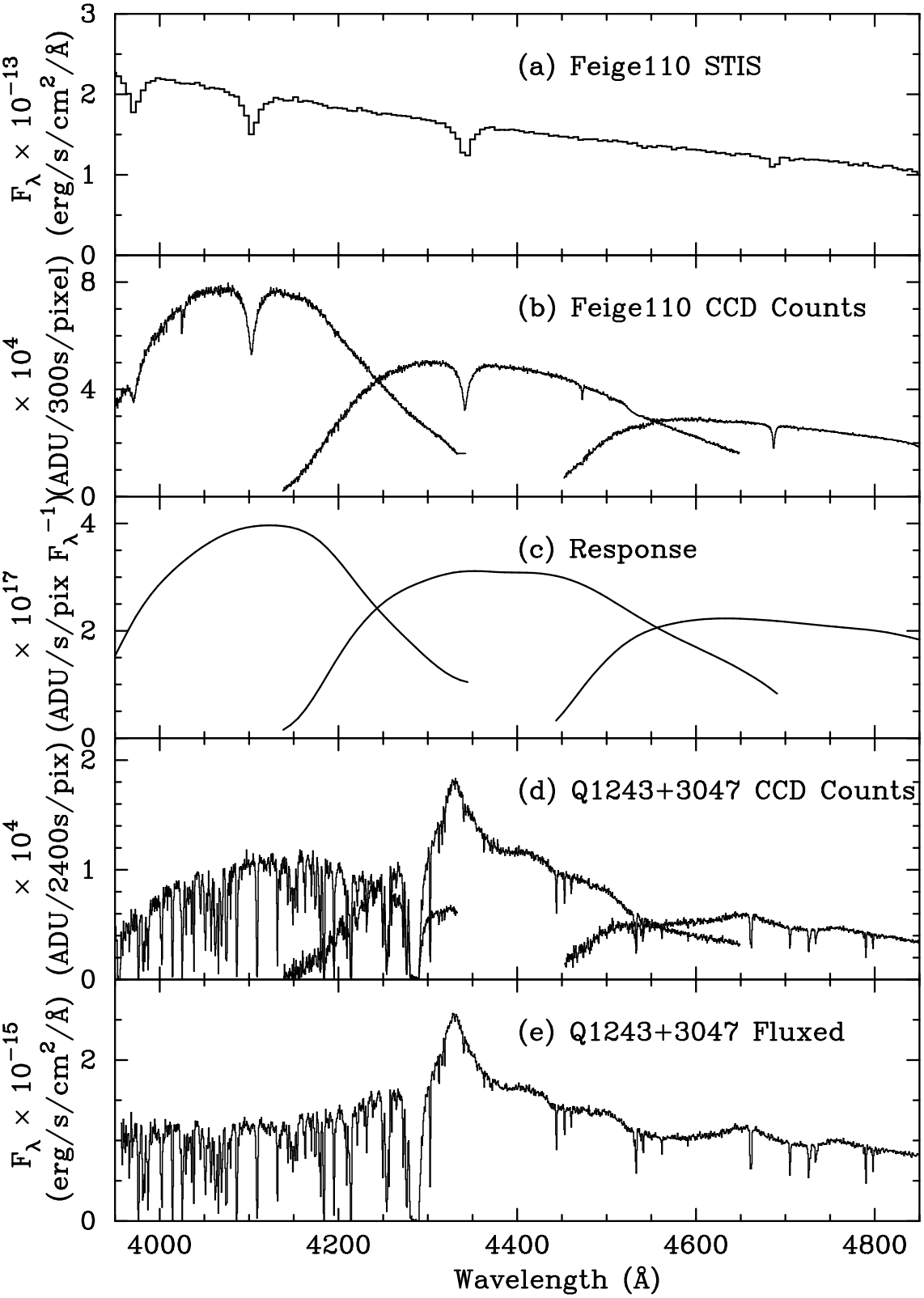
(a) Feige110 STIS
$F_\lambda \times 10^{-13}$ (erg/s/cm^2/Å)
(b) Feige110 CCD Counts
$\times 10^4$ (ADU/300s/pixel)
(c) Response
$\times 10^{17}$ (ADU/s/pix F_λ^{-1})
(d) Q1243+3047 CCD Counts
$\times 10^4$ (ADU/2400s/pix)
(e) Q1243+3047 Fluxed
$F_\lambda \times 10^{-15}$ (erg/s/cm^2/Å)
Wavelength (Å)

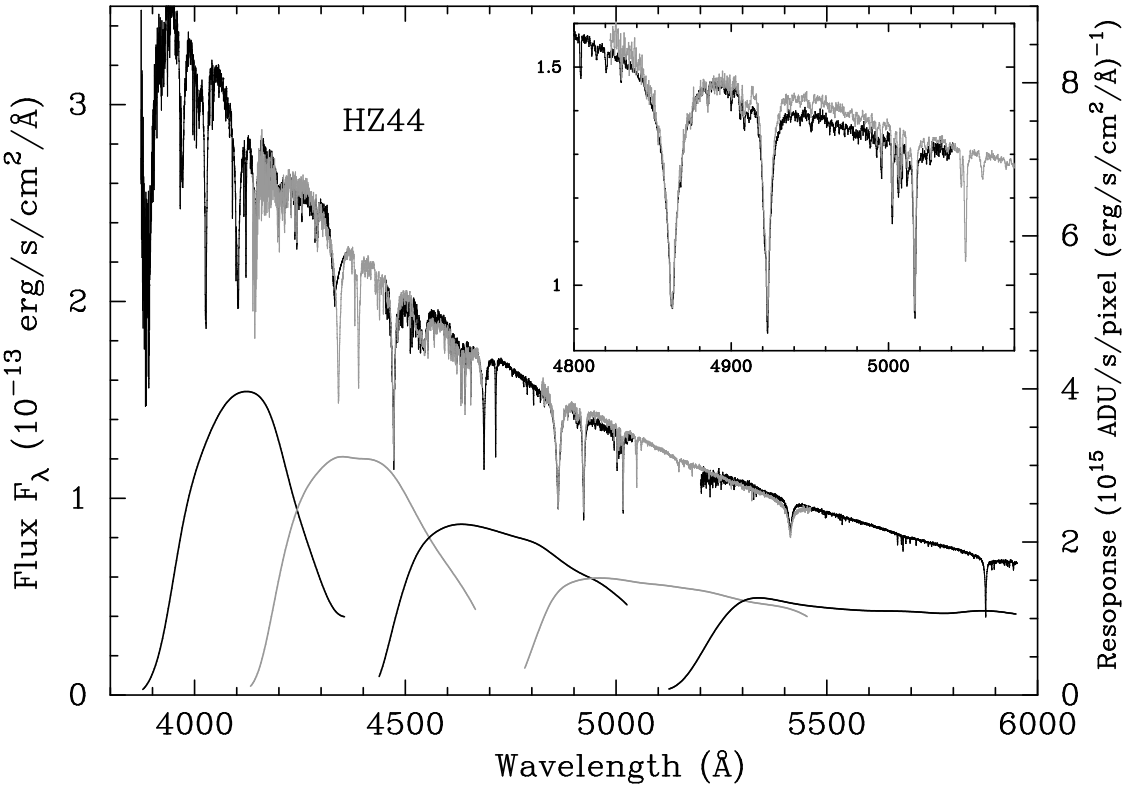

Figure 4.8: Demonstration of the errors in the flux calibration of an ESI spectrum of the star HZ44. The middle traces show the ESI orders after flux calibration using an ESI spectrum of star Feige 110. The lower smooth curves show the response function of these ESI orders. Here we use the usual flux calibration methods. The insert in the upper right is an enlargement of 4800 – 5100 Å that clearly shows that adjacent orders differ.

4.6.3 Errors in the Reference Spectra

The errors in the relative flux calibration of the reference spectrum are a fundamental limitation on how well we can apply relative flux calibration to the HIRES spectrum. One way to explore these errors is to compare different reference spectra. We will see that the differences increase with wavelength range and they are the main source of error in our calibration of our HIRES spectra of Q1243+3047.

We found that the 5 Kast spectra show two types of shape. The two from 1999 are similar, as are the two from 2001. We call the sum of the two flux calibrated spectra from 1999 K99, and the two from 2001 K01. KSUM is our name for the sum of all five spectra. The 1997 spectrum is similar to K01, but has much lower S/N.

These two groups, K99 and K01, differ in shape on the largest scales across the whole Lyα forest, but they do have very similar shapes across a few hundred Ångstroms after we normalize them to each other at those wavelengths. These differences are best seen when we smooth them slightly by differing amounts to reduce differences in the spectral resolution. The K01 spectra have up to 10% systematically higher flux at wavelengths < 3400 Å than do the K99 spectra. The K01 spectra had a few percent lower flux from 4000 – 4300 Å and higher flux across the Lyα emission line. We do not know the origin of these differences. Possible origins include variation in atmospheric extinction (Burki et al., 1995) or variation of the QSO.

We find that the ESI spectra differed from the various Kast spectra by typically 2% or less per Kast pixel, from 4100 – 4400 Å. The differences correlate over a few Kast pixels in the Lyα forest, with no large scale trends, except that to the red side of the Lyα emission line the ratio of the Kast to ESI flux increases by approximately 5% from 4300 – 4400 Å for all five Kast spectra.

4.7 Step 2: Flux Calibrating HIRES Echelle Orders with a Reference Spectrum

We calibrated the relative flux in a HIRES spectrum using a calibrated reference spectrum from either Kast or ESI. We divided a smoothed version of the HIRES spectrum by the reference spectrum to find the "Conversion Ratio" spectrum. We found that the smoothed HIRES spectrum and the reference had to have the same wavelength scale and resolution, because the Lyα forest absorption lines cause the flux to vary rapidly in wavelength. We calibrated the individual orders of each HIRES integration using a smooth function fitted to the conversion ratio spectra, one for each order of each integration.

In Figure 4.9, we illustrate the calibration of the relative flux in the HIRES orders that we describe in the following five sub-sections.

4.7.1 Wavelength Matching

Because the wavelengths from HIRES are more accurate, we shifted the Kast spectra onto the HIRES wavelength scale. We measured the shifts by cross-correlation of complete HIRES orders, and we confirmed the values by cross-correlating individual strong lines in the Lyα forest.

Figure 4.9: Illustration of the steps taken to apply relative flux to HIRES spectra of Q1243+3047 using Kast spectra of the same QSO. Panel (a) shows a flux calibrated Kast spectrum. It has been shifted in wavelength to match the HIRES wavelengths. Panel (b) shows the CCD counts recorded in the three HIRES orders that cover these wavelengths. This is a single HIRES integration, and the orders overlap in wavelength, although we do not show this here. Panel (c) shows the extracted HIRES orders that have been "flattened" by dividing by the flat field. This is the Flux-name.fits file that is the usual output from MAKEE. Panel (d) is shows the spectra from panel (c) after smoothing by a Gaussian filter to match the spectral resolution of the Kast spectrum in panel (a). The HIRES spectrum has been re-binned onto the Kast pixels. Panel (e) shows the ratio (d)/(a) that we call the conversion ratio. It has values at the Kast pixels, and two values at the wavelengths that appear in two HIRES orders. The smooth curves are low order fits to the pixels that sample the conversion ratio. Panel (f) is (c)/(e), the flux calibrated HIRES spectra. Notice that the jump in the HIRES flux at the order join near 4320 Å in panels (b), (c) and (d) is detected by the conversion ratio in (e) and corrected in (f). Panel (g) shows the sum of 8 HIRES integrations, each of which is corrected individually in the same manner. The order joins are not apparent. We do not plot most pixels in the high resolution spectra, to reduce the file size.

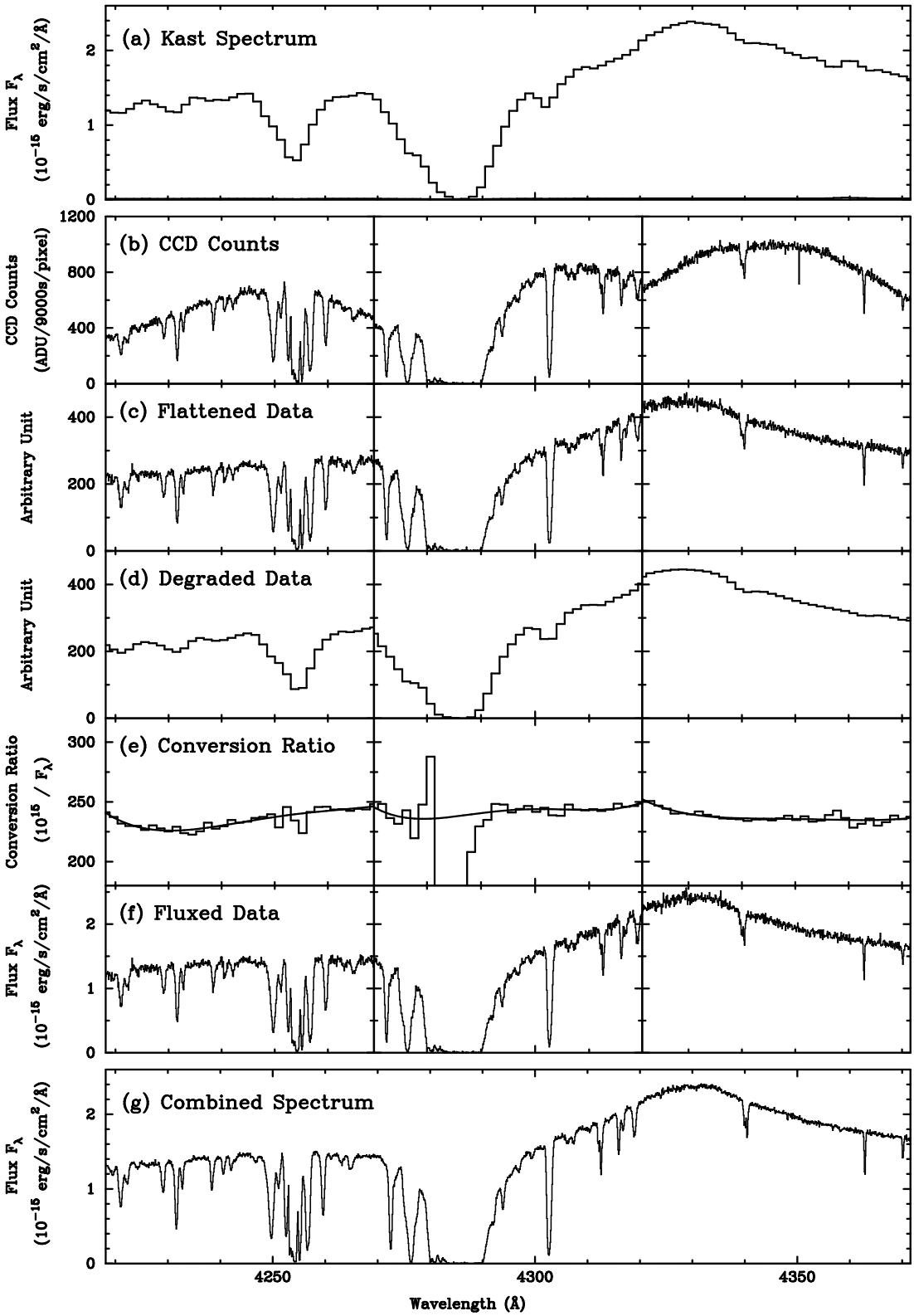
(a) Kast Spectrum
Flux F_λ (10^{-15} erg/s/cm^2/Å)
(b) CCD Counts
CCD Counts (ADU/9000s/pixel)
(c) Flattened Data
Arbitrary Unit
(d) Degraded Data
Arbitrary Unit
(e) Conversion Ratio
Conversion Ratio (10^{15} / F_λ)
(f) Fluxed Data
Flux F_λ (10^{-15} erg/s/cm^2/Å)
(g) Combined Spectrum
Flux F_λ (10^{-15} erg/s/cm^2/Å)
Wavelength (Å)

Some of the wavelength shifts may arise because the QSO was not exactly centered in the slit. This is a reasonable explanation for the typical shift which was 42 km s^{-1}, or 0.4 Kast pixels, only 17% of the projected width of a 2 arcsecond wide slit. These shifts should vary monotonically along a spectrum, and some Kast spectra show this. However, Figure 4.10 shows that other spectra have more complex wavelength shifts. In such cases we measured the mean shift for each HIRES order, and we fit a low order polynomial to these mean values, similar to that used to fit the arc line wavelengths, to give a smoothly changing wavelength scale without gaps or discontinuities.

We also placed the ESI spectra on the HIRES wavelength scale. This wavelength scale assignment was obtained by first smoothing the HIRES spectra to the approximate spectral resolution of ESI, and then finding the velocity shift by cross-correlation of the ESI with the HIRES integration. We shifted the complete ESI spectrum by +5.61 km s^{-1}, which is 7.5% of the projected 1 arcsec slit width. As with the Kast spectra, this shift is larger than we would expect from the wavelength fits to the arc calibration lines and may arise because the QSO was not exactly centered in the slit.

4.7.2 Resolution Matching

We smooth the HIRES spectrum to match the resolution of the Kast spectrum. This procedure is sensitive to wavelength shifts between the two spectra, and hence it was done after the wavelength scales were matched. In contrast, the wavelength scale matching is insensitive to the spectral resolution. We smoothed the HIRES spectrum, and sampled it in the wavelength bins of the Kast spectrum. We smoothed with a Gaussian function of known FWHM, truncated at 2σ, and normalized to unit area. We smoothed by different FWHM to find the amount of smoothing that left the smallest residuals between the smoothed HIRES and Kast spectra. These residuals appeared flat across strong absorption lines, which suggests that a Gaussian is an adequate approximation to the line spread function of the Kast

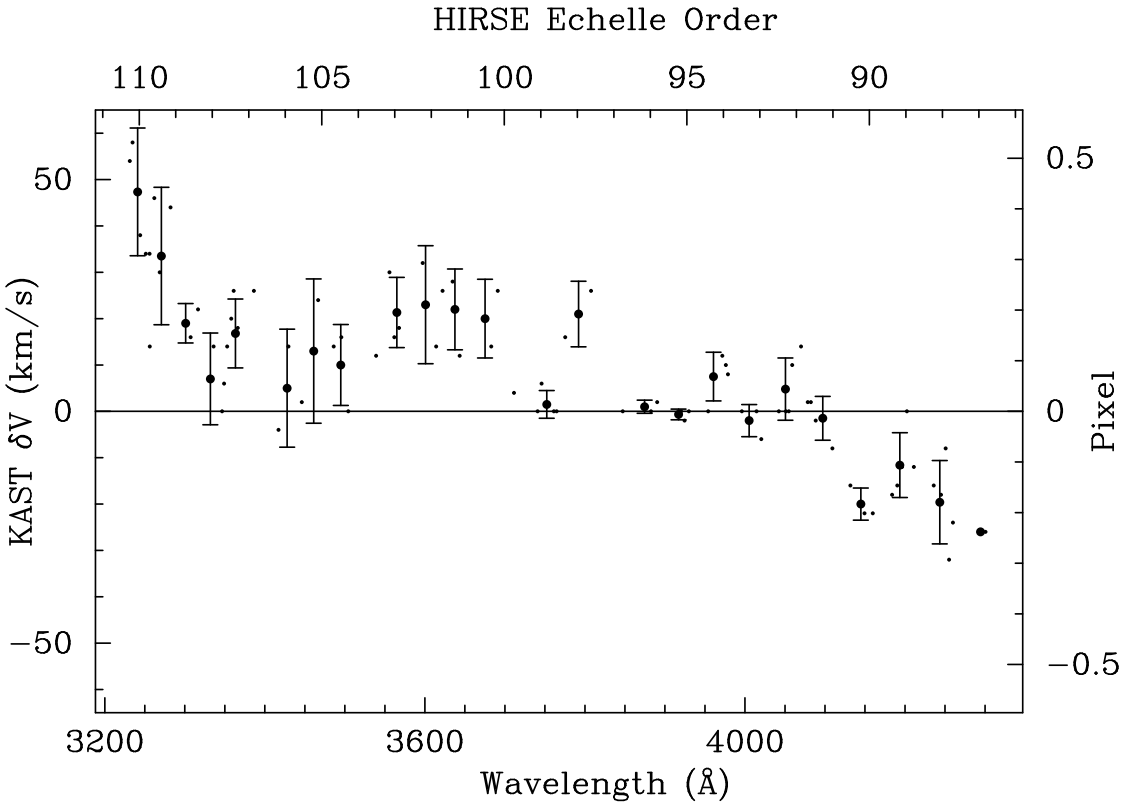

Figure 4.10: Shifts in the wavelength scale of a spectrum of Q1243+3047 from the Kast spectrograph measured relative to a HIRES spectrum of the same QSO. Each dot shows the shift measured by cross-correlating a region of spectrum that contains an absorption line. The bars show means of these dots, taken over the individual HIRES orders. We obtain similar shifts when we cross-correlate over complete HIRES orders. The sampling pixel size is 107.1 km s^{-1}.

spectrum. As with the wavelength matching, the Lyα forest provides the signal for resolution matching.

The Kast spectral resolution varies from spectrum to spectrum, and it can vary with wavelength in a spectrum, depending on where we chose to focus. We took the Kast resolution to be the FWHM of the smoothing applied to the HIRES, after subtracting the initial HIRES 8 km s^{-1} FWHM in quadrature. For example, in the 1999 spectra of Q1243+3047, the FWHM of the Kast spectrum is about 300 km s^{-1} near 3300 Å and from 3800 – 4300 Å but it improves to 220 km s^{-1} near 3500 Å, where the measurement error is approximately 10 – 30 km s^{-1}, depending on the region of the Lyα forest. We smoothed the HIRES spectrum by a single mean FWHM even when the resolution varied along the Kast spectrum. Using similar methods we found that the ESI spectrum had a FWHM of 63.2 $\pm$ 3.0 km s^{-1}.

4.7.3 Calculating the Conversion Ratio

We divide the smoothed HIRES spectrum by the Kast spectrum, to obtain the "conversion ratio" (CR) spectrum. The Lyα forest hinders our calculation of the CR, because we are very sensitive to slight remaining errors in the wavelengths and the resolution. When we calculate the CR, we weight the flux in the individual spectra by their errors, and we assign an error to each pixel in the CR. It is common to see increased error in the CR near strong absorption lines (e.g. near 4285 Å in panel (e) of Figure 4.9), but this error does not have a systematic shape when the wavelengths and resolution are well matched.

4.7.4 Smoothing the Conversion Ratio

We fit the CR spectra to obtain a smoothly changing function. The original CR spectra vary from pixel to pixel because of photon noise in the reference and HIRES spectra, especially in strong absorption lines. These variations can be much larger than the expected change in the flux calibration and hence we can improve the flux calibration by interpolating. We explored various ways of smoothing and fitting,

some in one dimension, along each order separately, and others in two dimensions, both along and between adjacent orders. The best choice will increase the S/N in the CR as much as possible without changing the structure.

We found that a 4th order Chebyshev polynomial fit to the CR spectrum for each HIRES order was a good choice for Kast spectra. We choose this order by trial and error. It leaves enough freedom to fit the shapes of the CR and give a reduced $\chi^2 \simeq 1$. To meet this criterion, we chose a 6th order Chebyshev polynomial for ESI spectra. Other fits would be appropriate in spectra with different amount of structure and S/N. In Figure 4.11, we show the CR spectra for many HIRES orders. We see that the CR spectra for adjacent orders are very similar in shape, but change systematically as we move across many orders. We also found that the changes in shape from order-to-order are larger than those between integrations for a given order, except for the effects of photon noise in the CR.

We calculate the CR twice, in an iterative fashion, to improve the accuracy near the ends of the HIRES orders. The first time, we stop the calculation before the order ends, where the filter, which we use to smooth the HIRES spectrum to the resolution of the reference spectrum, just touches the last pixel in the order. We cannot, at that time, calculate the CR for the remaining pixels because we do not know the flux from beyond the end of the order. This flux is needed when we smooth the HIRES spectrum to match the reference spectrum. We do, however, allow the fit to the CR to extrapolate to the end of the order, and we use that extrapolation to make the first estimate of the flux calibration. When we calculate the CR the second time, we know the HIRES flux from beyond the end of the order, because we have already calibrated the whole HIRES spectrum.

An example of the type of error that can occur in the CR at order ends is shown in Figure 4.12. In middle panel on the left, the CR is erroneously low in the first two pixels at the start of order 98. Here we calculated the CR once only, and we ignored the flux from beyond the end of the order, where there happens to be a Lyβ absorption line. This absorption line lowers the flux in the reference spectrum,

but not in the HIRES spectrum for that order.

The error in the relative flux calibration of a HIRES integration depends in part on the S/N in that HIRES integration. The conversion ratios in Figure 4.12 are for a second integration of Q1243+3047 that can be compared to the integration shown in Figure 4.11. The two integrations were calibrated using the same Kast spectrum, and hence the differences are caused by noise in the HIRES integration, especially at the shortest wavelengths.

We experimented with other ways of smoothing the CR to reduce the effects of photon noise. The moderate order polynomials smooth in wavelength along an order, but they do not use any information from adjacent orders. As is shown in Figure 4.2, adjacent orders should have similar CR. To take advantage of this similarity, we made a 2-dimensional map of the CR in the coordinate frame of the HIRES CCD detector, and we smoothed this map in both dimensions, both using a Gaussian filter and independently by fitting a 2D surface using Chebyshev polynomials. The Gaussian filter did not work well because the largest width that did not change the shape of the CR surface had a 4σ width of only 3 orders, not enough to reduce the noise significantly. If we widen FWHM of Gaussian filter, we can reduce the noise, but at the same time, it alters the shape of CR for more than a few percent which is unacceptable when we pursue 1% accuracy. In Figure 4.13, we show a 2D surface fit that was an improvement over the 1D polynomial fits, but we did not use this in Kirkman et al. (2003).

The error in the CR depends on the S/N in each CR pixel, and on the fitting or smoothing that we use. The error will correlate on the smoothing scale. When we apply a 4th order polynomial to each HIRES order of 40 Å, the correlation length is approximately 10 Å as can be seen from Figures 4.11 & 4.12. There are also strong correlations in the CR near the ends of orders, and near strong absorption where the errors are largest.

The contribution to the error in the CR from the S/N in the reference or HIRES spectra can be estimated from the number of pixels in the correlation length.

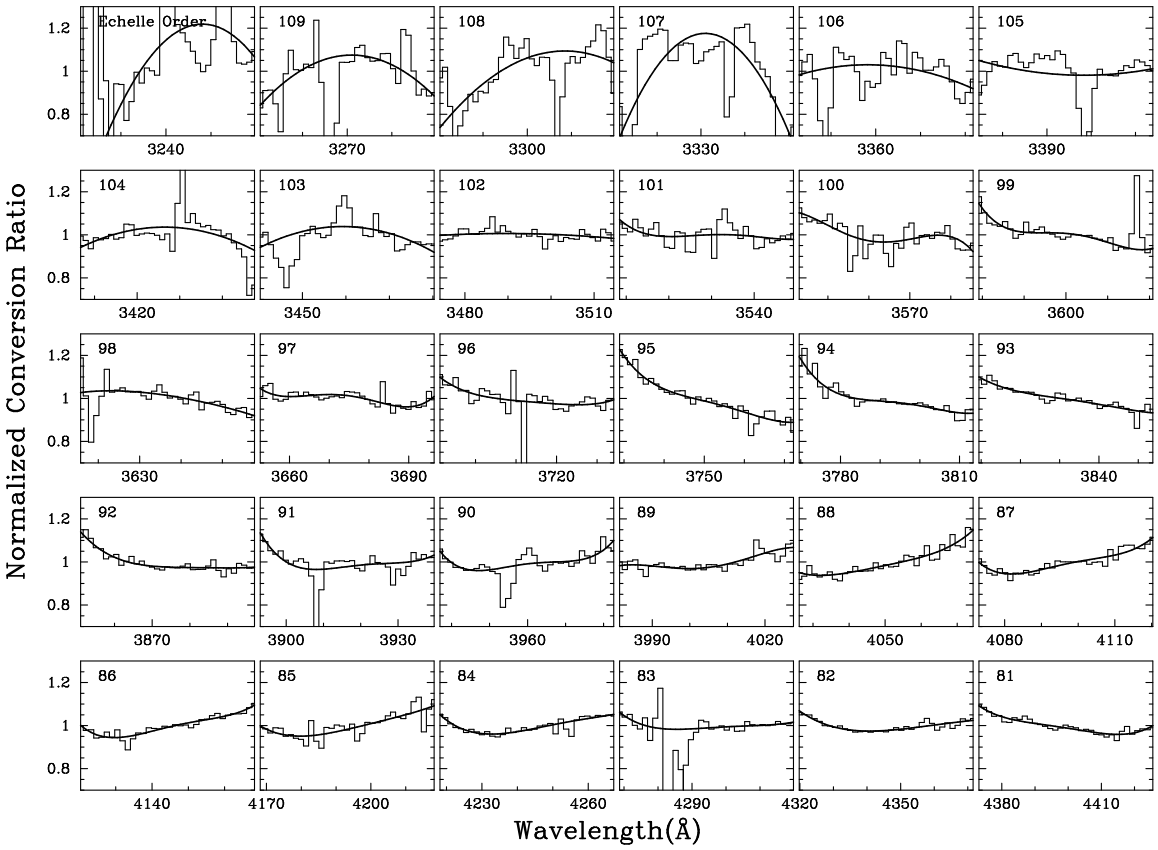

Figure 4.11: Conversion ratio for the 8100 second HIRES integration of Q1243+3047 taken April 4, 1999. The relative flux calibration uses a Kast spectrum from 2001. The mean level of the CR in each order has been normalized for the plot. The pixels sizes are from the Kast spectrum, and the curves show 4th order Chebyshev polynomial fits to each order.

There are approximately 34 pixels in a Kast spectrum per HIRES order, and hence 8.5 per correlation length. An individual Kast spectrum of Q1243+3047 has S/N 60 per pixel near 4250 Å and 20 near 3250 Å. The CR will then have errors of at least 0.6% near 4250 Å and 1.7% near 3250 Å.

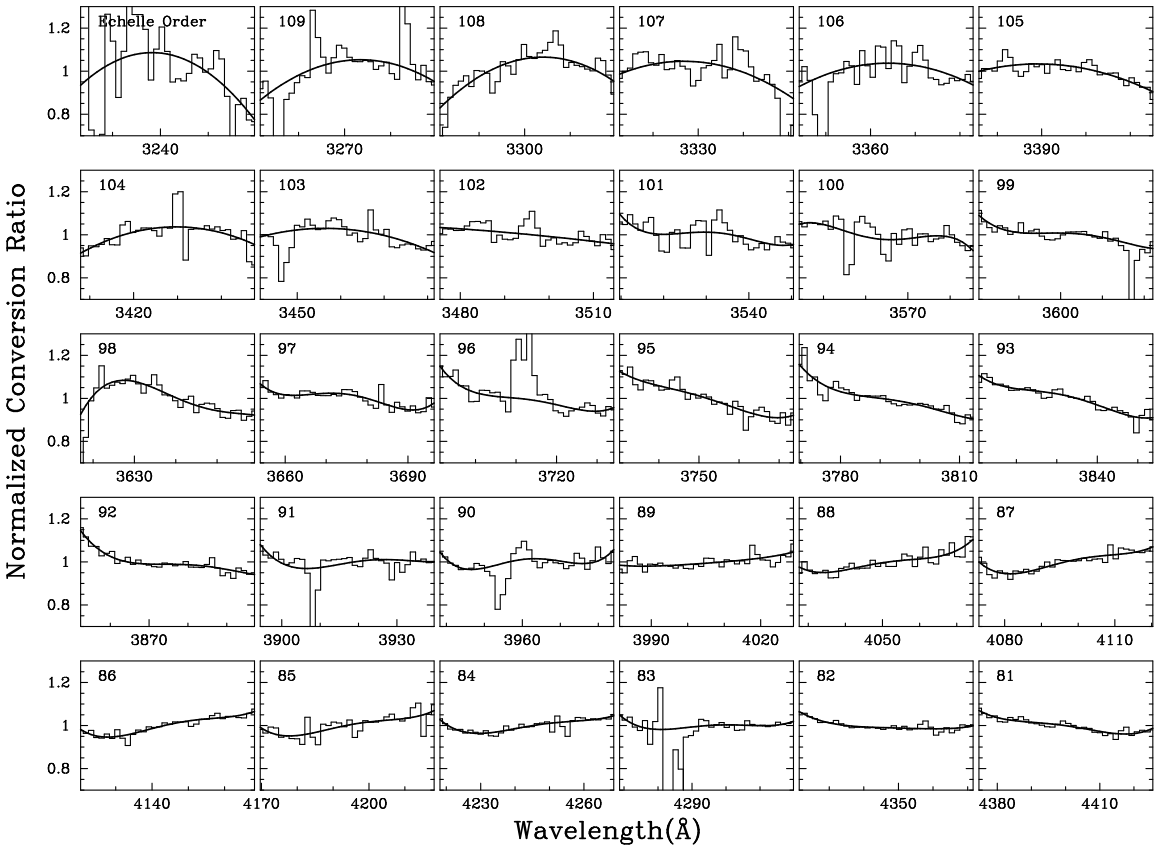

Figure 4.12: As Fig. 4.11, but for a 7200 second HIRES integration taken 11 months later on March 14, 2000.

Figure 4.13: The 2-D surface fitted conversion ratio for a HIRES integration of Q1243+3047. The fitted CR values are shown elevated above a plane that approximates the HIRES CCD. The "CCD pixel position" axis is the pixel along the direction of a HIRES order, with wavelength increasing to higher numbers. The "Echelle Order" axis is the HIRES order with wavelength increasing to low numbers. The orders are shown parallel to each other and with equal spacing. 5th order Chebyshev polynomials are used in both the CCD pixel and echelle order directions. The S/N in the reference ESI spectrum increases with wavelength, to the left. The CR have been normalized to have a mean CR = 1 in the middle 20% of each HIRES order. Prior to normalization, the CR varied systematically by approximately a factor of two.

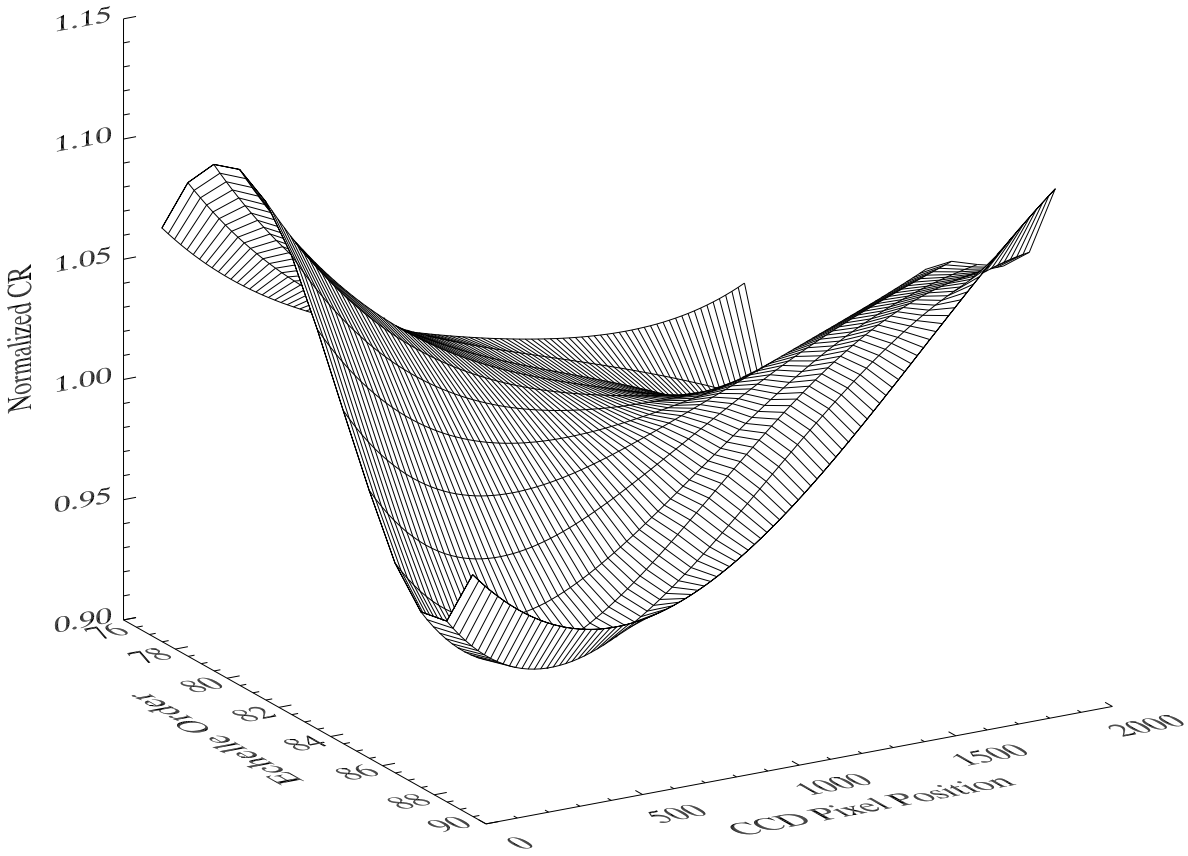
Normalized CR
1.15
1.10
1.05
1.00
0.95
0.90
Echelle Order
0
2
4
6
8
10
12
14
16
CCD Pixel Position
0
500
1000
1500
2000

4.7.5 Applying the Conversion Ratio

We divide the original HIRES integration, with full spectral resolution and pixels, by the 1D fits to the CR to obtain the desired flux calibrated HIRES spectrum. Since we have not merged the orders, the wavelength overlaps remain. The resulting HIRES integration now has relative flux calibration on each order.

4.8 Step 3: Combine the HIRES Orders

The final step is to combine the fluxed HIRES orders into a single spectrum. We add the HIRES integrations that have very similar wavelength coverage, order by order, and then we merge the orders. We choose this sequence because it facilitates checks of the relative flux calibration. We compare the flux in each order in multiple integrations before we sum the integrations. After they are summed, the enhanced S/N makes it easier to see errors in the flux calibration in the wavelength overlap between orders.

First, we place all orders from all HIRES integrations on a single wavelength scale, so that pixels from orders that overlap in wavelength sample exactly the same wavelengths. We choose a scale with a constant velocity increment of 2.1 km s^{-1} per pixel, equivalent to constant log wavelength increment. This choice has two advantages over constant wavelength: in velocity units, the spectral resolution of the echelle does not vary significantly with wavelength, and we use velocity units to describe the widths of absorption line systems.

We calculate the mean flux in each pixel, from all integrations, after rejecting large deviations that we identify by evaluating the χ^2 statistic for each pixel. We ignore the flux in a pixel from an individual integration if it is $> m\sigma_i$ away from the weighted mean for all integrations, where σ_i are the errors on the fluxes in the individual integrations. The value of m was determined iteratively to remove most pixels with conspicuously deviant flux values. For Q1243+3047, we use $m = 2$. The algorithm iterates, and re-derives the χ^2 after rejecting the flux value from one

integration. If all integrations are $> m\sigma$ away from the weighted mean, we examine the errors. If the errors in some of the integrations have data, shown by non-zero errors returned by MAKEE, we use the flux from the integration with the smallest error as the mean. If, however, there is no data in a particular pixel, for example because of a known CCD defect, then we use the weighted mean of the two pixels on either side, again using only those integrations that are within $m\sigma$ of the weighted mean for that wavelength. If none of the above criterion are met, we use the average of the fluxes in all integrations.

Finally, we verify that adjacent orders show similar flux levels where they overlap, and we used a weighted mean to combine the orders in these regions, producing a single flux calibrated spectrum. In Figure 4.14, we show order overlap for spectra of star Feige 34. This spectrum can be compared to the spectra in Figures 4.3 that show the flux calibration using usual methods. The ratio of the flux in adjacent orders shows most variation near 3250 Å : 0.92 – 1.08%, and decreases to 0.98 – 1.02 near 4300 Å, where the S/N is highest in the Kast spectrum that we used as a reference. The calibration of Feige 34 used the method and algorithm that we developed and applied to our spectra of Q1243+3047, with a few exceptions. The star does not have Lyα forest lines, and hence we matched the wavelength scale of the Kast and HIRES spectra using a single shift for the whole Kast spectrum. We fitted the CR with one 4th order polynomial per order. A 6th order fit would work better near 4300 Å where the S/N is high.

We consistently found, from many spectra, that the remaining difference between between the orders was largest at the end of an order, where the CR is less well known. Hence, we tapered the flux from each order using a weighting function that declined linearly from one, where the overlap begins, to zero, where the order ends.

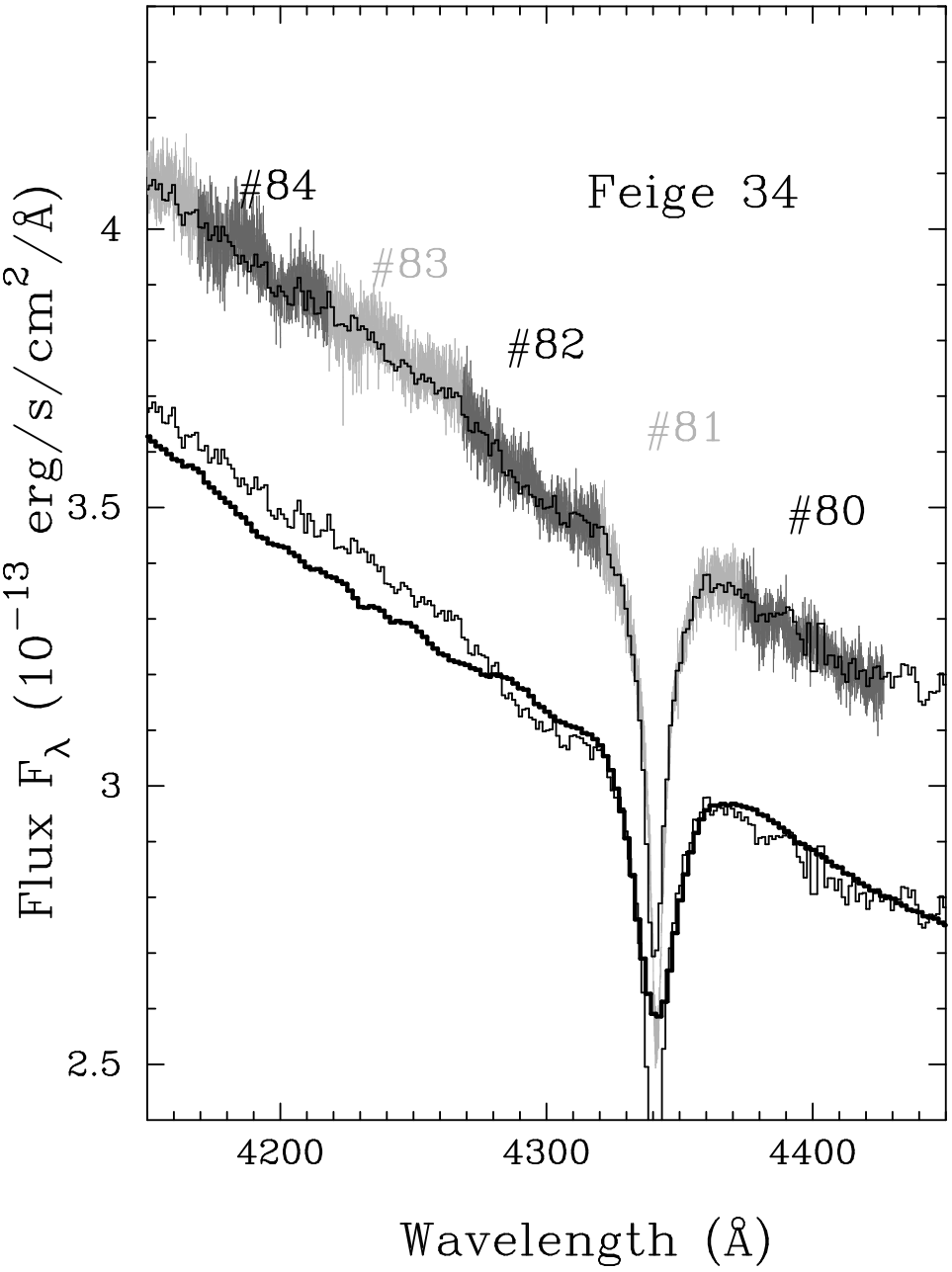

Figure 4.14: Spectra of star Feige 34 with relative flux calibration. The lower two spectra are from STIS (heavy line) and Kast (thin line), both from Fig. 4.6. The upper two spectra, displaced vertically by the same amount for clarity, are the same Kast reference spectrum and five and a half orders of a HIRES spectrum (faint trace with many pixels, darker in even numbered orders).

4.9 Comparison of Spectra of Q1243+3047 Calibrated with Different Reference Spectra

We made several different calibrations of the HIRES spectra of Q1243+3047 using different low resolution spectra to convey the flux information. We label these HIRES spectra by the spectra that we used for the flux calibration: hence, HK99 is the HIRES spectrum of Q1243+3047 calibrated using the Kast K99 spectrum of Q1243+3047, HKSUM was calibrated using the mean of all five Kast spectra and HESI was calibrated using the ESI spectrum of Q1243+3047.

We also made a spectrum, HH, which we calibrated using a HIRES spectrum of a standard star. This HH calibration is not typical of the accuracy that we usually obtain, but rather it is the best that we could obtain with our spectra. We made many calibrations using different HIRES integrations of standard stars, and we show the calibration that had the smoothest order joins. This HH calibration contrasts with the calibrations of the stars that we showed in Figure 4.3 that did not work as well.

In Figure 4.15, we show the ratios of HIRES spectra calibrated in these different ways. The top panel shows HK99 spectra divided by HESI. There is a 7% difference across the wavelength region shown. The HK01 differs from HESI by 5% at most, while the HKSUM calibration differs from HESI by 4%. The calibrations HH and HESI differ the least – only 3% – but show the largest jumps at order joins, e.g. near 4325 Å. The four gray bands of Figure 4.15 show the wavelength overlaps between the HIRES orders. We show three complete orders and two partial ones. The bottom panel shows QSO spectrum. We show the wavelength region centered on the strong Lyα lines that we have use to measure the H I column density that contributes to a D/H measurement. This Lyα line has damping wings that absorb approximately 1% of the flux near 4233 and 4340 Å and hence accurate flux calibration of this region helps us measure the column density, although most information comes from 20 Å on either side of the line center.

The differences between the calibrations have three origins. The largest differences, which are on the largest scales, come from the differences between the K99, K01 and ESI spectra. Other differences, especially near the order joins, are related to the fitting of the CR, and are sensitive to the S/N in the Kast and ESI spectra. A third type of difference occurs from pixel to pixel, and comes from the rejection of deviant pixels from among the 8 HIRES integrations. The CR fits are smooth curves, and the ratios would also be smooth were it not for differences in the pixels which are rejected when we took the sum of the 8 integrations. The numerous small $1-2\%$ deviations arise when a pixel is not used from one integration or another. The size of these deviations is given by the S/N of the individual integrations. The noise increases in the strong absorption lines where we are dividing two spectra, each of which has low S/N. Trends that are seen in more than one panel may come from differences of the ESI spectrum from the others.

We do not know which of the spectra is the more accurate. All of the spectra used in Figure 4.15 were calibrated with CR spectra that were fit order by order. We found that the 2-dimensional fits to the CR, like that shown in Figure 4.13, slightly reduced the deviations near the order joins.

For each fluxed spectrum, we measured the D/H value and found no significant differences in D/H between spectra. The lack of differences is likely related to our continuum fitting. The typical interval of continuum points we place on HIRES spectra is $40-50$ Å. The low frequency deviation shown in Figure 4.15, a few percent per an echelle order, could be absorbed by our smooth b-spline continuum fit on the spectra (Kirkman et al., 2003). For the same reason, absolute flux calibration is not necessary for our D/H measurement. Even if a QSO is variable, our flux calibration method and subsequent measurement will succeed, as long as the variation spectrum to spectrum is insignificant on scales similar to HIRES order length.

Figure 4.15: Ratios of the flux in different summations of the 8 HIRES integrations of Q1243+3047 that we have calibrated using different spectra. HK99, HK01 and HKSUM were all calibrated with Kast spectra, while HESI and HH are HIRES spectra calibrated using ESI spectra and a HIRES spectrum of a flux standard. Each of the top 4 panels shows the ratio of two HIRES spectra, each one of which looks similar to that shown in the bottom panel. The vertical bands show the wavelengths where the orders overlap. We do not plot most pixels, to reduce the file size. If we had plotted all pixels, the noise near the few strongest absorption lines would be much more conspicuous, and in each 10 Å interval we would see 1 – 20 fluctuations of 1 – 2%. We also do not plot pixels that have negative flux, because of the random noise in the sky subtraction.

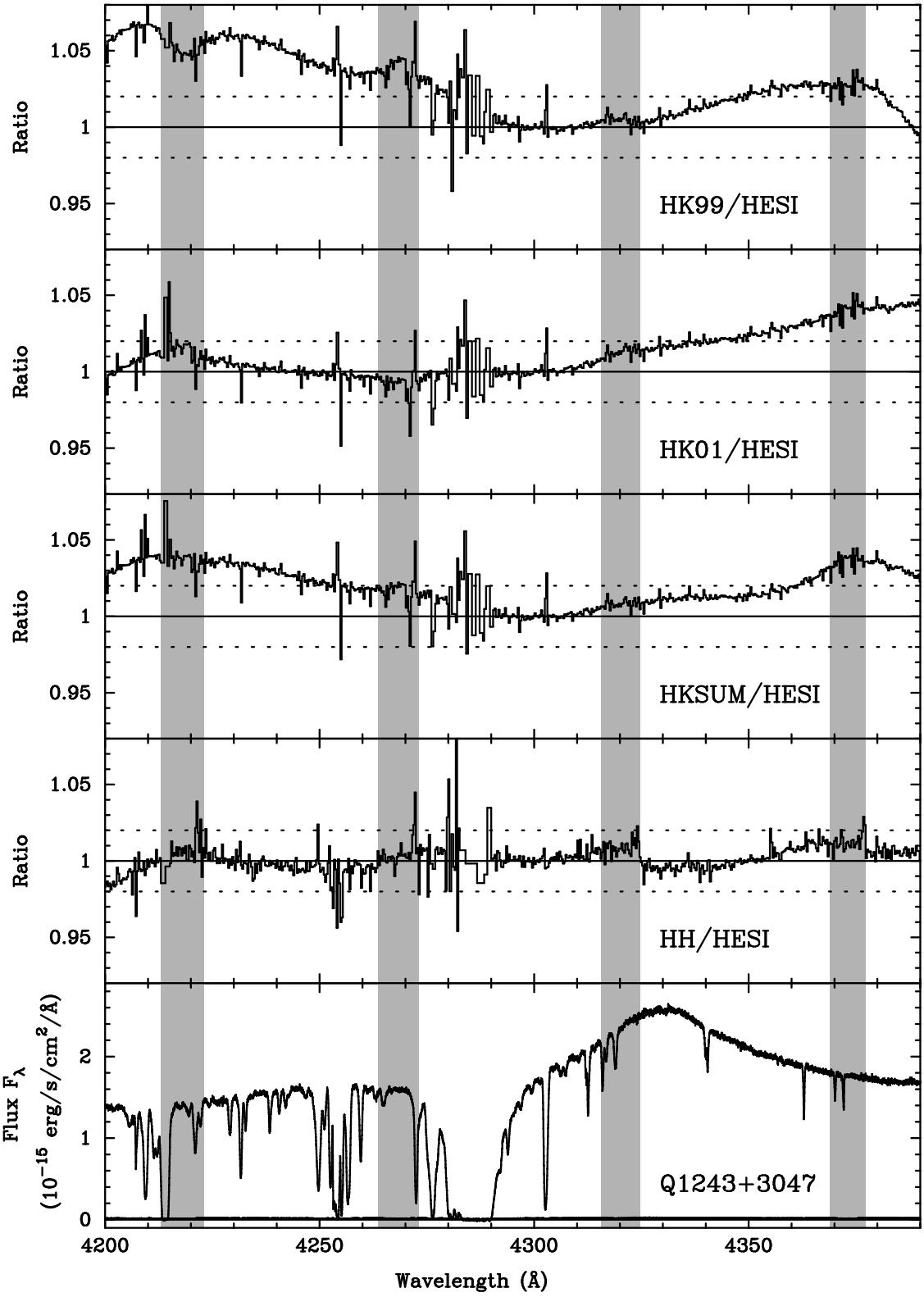
Ratio
1.05
1
0.95
HK99/HESI
HK01/HESI
HKSUM/HESI
HH/HESI
Flux F_λ
$(10^{-15}$ erg/s/cm^2/Å)
2
1
0
Q1243+3047
4200
4250
4300
4350
Wavelength (Å)

4.10 Discussion of the Accuracy of the Flux Calibration

Many factors contribute to the errors in the relative flux calibration, including:

- Errors in the flux reported for the standard star.
- Errors in our spectra of the standard star and reference. Common error sources include extinction and absorption in the Earth's atmosphere, slit losses that depend on wavelength, a dichroic in the spectrograph, variation of the target, variation with wavelength of the proportion of the flux extracted, and the S/N of the spectra.
- Errors calculating the response function that we use to calibrate the reference spectrum. Errors occur matching the resolution and wavelength scales of our spectrum of the standard to the published flux information. Such errors are especially conspicuous near absorption lines in the standard.
- Errors in the preparation of the HIRES spectrum, including the bias subtraction, flat field division and extraction.
- Errors applying the flux calibration to HIRES spectrum, including wavelength shifts, resolution differences, the S/N of the HIRES spectrum and fitting the CR.

We have found that many of these factors can produce 1 – 10% errors in flux calibration, but it is difficult to assign typical values for these errors.

The size of the error in the relative flux calibration depends on the wavelength and the wavelength range. We do not include errors from the CR in the usual error array because the CR errors are correlated over many pixels. In this paper we have concentrated on scales of a few orders, or approximately 120 Å that are most relevant to our work on D/H. We have paid much less attention to the relative flux calibration on larger scales that are dominated by a different set of factors, such

as the extinction at the time of observation. We expect errors due to extinction to monotonically increase with scale in our reference spectrum.

An indication of the accuracy we have attained in relative flux calibration is given in Figure 4.14. We compare three spectra of the flux standard star Feige 34: a HIRES spectrum that we flux calibrated using a Kast spectrum as the reference, the Kast reference spectrum, and STIS a spectrum. The Kast and STIS spectra are those shown in Figure 4.6. The STIS spectrum was not used in the calibration, except to provide the normalization of the Kast spectrum across the range 3200 – 4450 Å. We used a one-dimensional 4th order polynomial to fit the CR. In the wavelength region shown, the HIRES spectrum differs from its reference by at most 2.5%, except near the absorption line, and typically $< 1\%$. At wavelengths 3400 – 3800 Å, where the S/N is lower, the differences are twice as large. The differences correlate on scales > 5 Å. The flux in different HIRES orders joins smoothly, with no unusual structure. The remaining differences of the HIRES and STIS spectra come from the deviation of the Kast spectrum from the STIS, shown in Figure 4.14. This comparison demonstrates that the method can give errors of $< 1\%$ in the relative flux over approximately 200 Å. For Feige 34 the accuracy of the flux calibration was limited by the accuracy of the reference, and not by the method itself.

4.11 Summary

We found that the distribution of the signal recorded in HIRES integrations differs from integration to integration. We do not have a complete explanation for this behavior, although varying vignetting and inadequate extraction may be involved. We found that these differences persist even when the instrument is apparently unchanged. These changes mean that the usual methods of flux calibration are inadequate.

The methods we have described for applying relative flux calibration to a HIRES spectrum use three spectra: the HIRES spectrum of the target that we wish

to calibrate, and Kast or ESI spectra of both the target and a flux standard star. We use the latter to get the Kast or ESI response and calibrate the Kast or ESI spectrum of the target that we take as the reference spectrum. We use reference spectrum to impose flux calibration on the HIRES target spectrum.

This has method has three advantages. First, we can calibrate HIRES when normal calibrations using standard stars observed with HIRES alone are inadequate. Second, we can correct many types of error in the HIRES spectrum, including those from varying vignetting and inadequate extraction. Finally, we can obtain all the calibration spectra at a different time and on a different telescope.

The error in relative flux calibration, and the solution that we describe, could apply to any spectrum with inadequate relative flux calibration, whether from an unstable spectrograph or from inadequate extraction. Vignetting could vary in any spectrograph that was unstable. Instability could involve an optical misalignment, as with HIRES. Variable vignetting would be harder to recognize in a first order spectrum because we expect the largest changes near the largest field angles, but there is only one spectrum to show this change, and flux calibration is often harder near the ends of a single spectrum, for other reasons.

4.12 Appendix A: Choice of Standard Star

We used the calibrations of the flux in stars based on STIS spectra (Bohlin, Dickinson, & Calzetti, 2001). In Figure 4.16 we see that the STIS spectra do not show the wiggles at 3200-3850 Å that are present in the Oke (1990) spectrum of G191 B2B. This and other Oke spectra are widely used by default in the reduction packages IRAF and MIDAS. The differences between the Oke (1990) and STIS spectra can reach several percent, larger than our random photon noise. Based on the lack of features in the spectrum and the STIS data quality, we preferred the following stars for UV flux calibration near 3200 Å: G191 B2B, BD+28 4211, Feige 110, and Feige 34. For G191 B2B we have the additional choice of using

a model spectrum given by Bohlin et al. (2001). This model spectrum fits their STIS spectra to within 0.7 % in the continuum (Bohlin, 2000), and it simplifies flux calibration because it has full resolution.

We used the entire STIS spectrum for flux calibration, including the broad Balmer absorption lines. The Oke (1990) paper provides AB magnitudes at discrete continuum points in 5-50 Å intervals. These points skip the Balmer absorption lines, but we can not do this, because we then have insufficient information to calibrate several echelle orders, each of which is only 30-60 Å long.

Our use of the flux calibration information near the Balmer lines can help us avoid significant errors. In Figure 4.17 we show a spectrum from ESI echellette order 15 that has its sensitivity peak around 4350 Å that coincides with Balmer γ line, 4341.68 Å. Q1243+3047 (Kirkman et al., 2003) happens to have its Lyα emission at 4330 Å. In an early flux calibration of this order, poor interpolation across this Balmer line had led us to make an 8% calibration error that was three times the random error.

4.13 Appendix B: HIRES Image Rotator

The vignetting in HIRES depends on whether or not the image rotator is used, and on the mode in which the rotator is used.

HIRES is fixed to the Nasmyth platform of the Keck-I telescope with its slit approximately parallel to the horizon. When we look at the image of the sky on the HIRES slit, we see that the vertical direction in this image rotates at a rate given by the elevation (EL) of the telescope. This is because telescope is rotating in EL while HIRES is fixed. If the telescope is pointing at the horizon, and looking at an arrow in the sky that is pointing towards the zenith, the image of this arrow on the slit plane is also pointing towards the vertical, which is perpendicular to the length of the slit. As the telescope moves to higher EL, the arrow rotates until it is aligned along the slit when the telescope is pointing to the zenith.

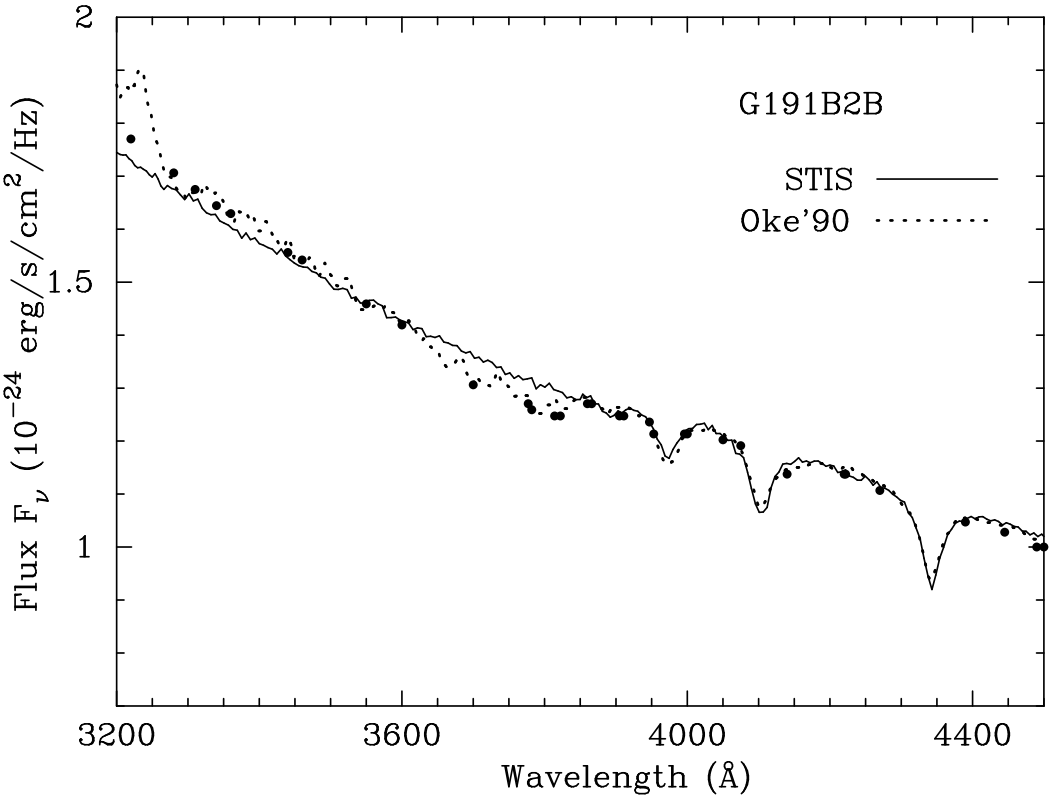

Figure 4.16: Flux calibrated spectra of the star G191-B2B. The continuous, wobbly line is a STIS spectrum from Bohlin (2000). The dotted line and points are from Oke (1990).

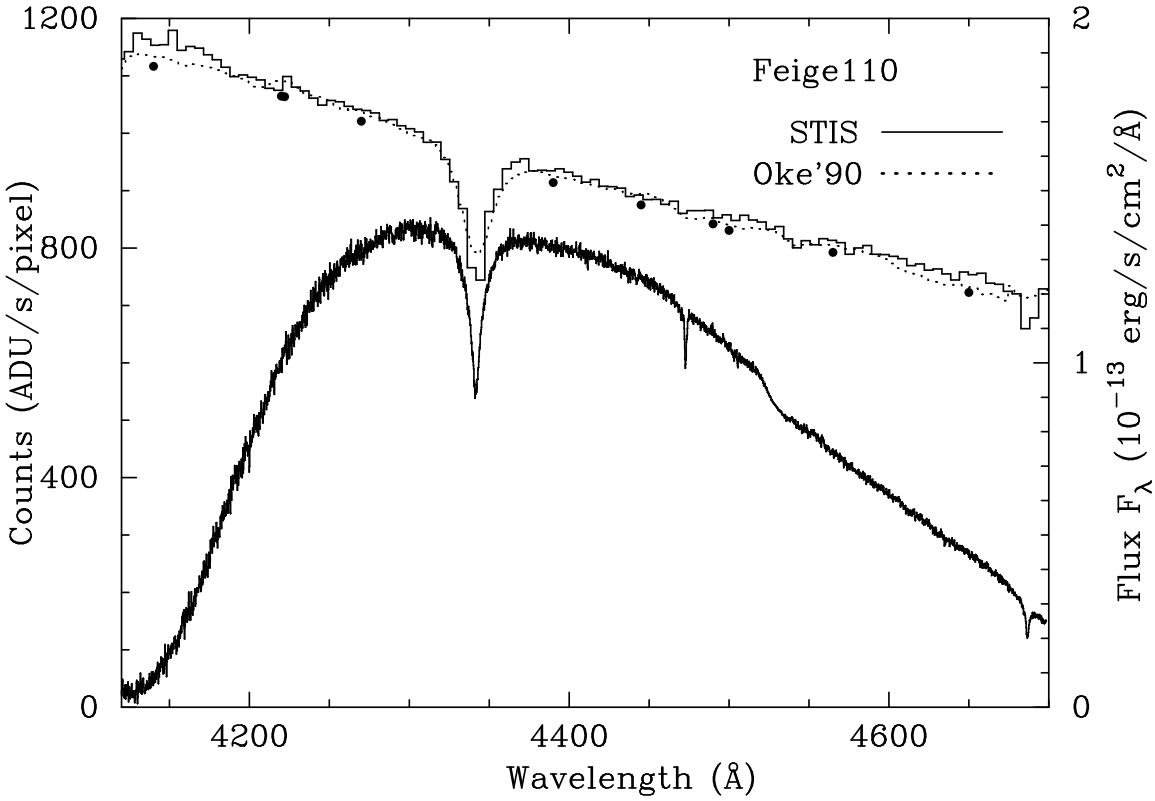

Figure 4.17: Spectra of the flux standard star Feige 110. The lowest trace shows the signal recorded in one ESI order. The dotted line shows the flux reported by Oke (1990) and the points show the flux values that he recommended to minimize sensitivity to spectral resolution. The STIS spectrum from (Bohlin, Dickinson, & Calzetti, 2001) is shown by the continuous trace comprising pixels that are easy to see on the plot.

The HIRES image rotator allows us to rotate the image of the sky on the slit plane in any way we like. We installed an image rotator in HIRES in late 1996. This is a large quartz prism that sits in front of the HIRES slit. The light from the Keck-I telescope tertiary mirror undergoes three total internal reflections in the prism before coming to a focus on the slit plane. The prism can rotate continuously in either direction about the axis of the beam that converges on the center of the slit. The prism is aligned so that the image of a star on the center of the slit moves by under 0.5 arc seconds when the prism is moved in or out of the beam, and when the prism is rotated. The prism can be spun rapidly to demonstrate this alignment. The prism does not vignette any of the beam that lands within 60 arc seconds of the center of the slit.

The image rotator has two main modes of operation: Position Angle and Vertical Angle. The position angle mode is used when we wish to keep two stars in the slit, where as the vertical angle mode is used to keep the vertical direction in the sky parallel with the slit, as a surrogate for an atmospheric dispersion compensator. When the image rotator was used in Vertical mode, the position angle along the slit is the parallactic angle, and this varies as we track a target. The parallactic angle is measured at the target, from the North Celestial Pole to the Zenith, in the direction from North via East. The parallactic angle is fixed for a given elevation and azimuth in the sky, but it changes when we track a target across the sky.

HIRES spectra are hard to flux calibrate in part because the vignetting can change by 10% from spectrum to spectrum. The vignetting changes because there is a known misalignment between the beam coming from tertiary mirror and the HIRES optical axis. When HIRES was installed, the center of the Keck telescope pupil was measured to be approximately 9 mm away from the collimator center, which corresponds to a beam misalignment of 7.4 arcminute. If a star is held at one position on the HIRES slit, the axis of the beam entering HIRES will rotate around the HIRES optical axis at a rate given by any change in the position angle of the sky image on the slit. If the position angle moves through 360 degrees, the

axis of the beam entering HIRES follows the surface of a cone with an apex angle of approximately 14.8 arcminutes. Steve Vogt used ray tracing to find that this rotation causes the vignetting to vary by approximately 10%, depending on the angle. The vignetting occurs due to a dewar which forms a central obstruction in the beam near the camera's prime focus.

4.14 Acknowledgments

This Chapter 4, in full, is a reprint of the material as it appears in *Publications of the Astronomical Society of the Pacific*, volume 115, page 1050, 2003. The dissertation author was the primary investigator and first author of this paper.

Chapter 5

The Measurement of the Deuterium to Hydrogen Ratio towards HS 0105+1619

5.1 Abstract

We report the measurement of the primordial D/H abundance ratio towards QSO HS 0105+1619. The column density of the neutral hydrogen in the $z \simeq 2.536$ Lyman limit system is high, log $N_{HI} = 19.422 \pm 0.009$ cm^{-2}, allowing for the deuterium to be seen in 5 Lyman series transitions. The measured value of the D/H ratio towards QSO HS 0105+1619 is found to be D/H= $2.54 \pm 0.23 \times 10^{-5}$. The metallicity of the system showing D/H is found to be $\simeq 0.01$ solar, indicating that the measured D/H is the primordial D/H within the measurement errors. The gas which shows D/H is neutral, unlike previous D/H systems which were more highly ionized. Thus, the determination of the D/H ratio becomes more secure since we are measuring it in different astrophysical environments, but the error is larger because we now see more dispersion between measurements.

5.2 Introduction

The D/H measurement of a system toward HS 0105+1619 is a joint effort of the Tytler group. In this chapter, I will present our result from O'Meara et al. (2001). I am in charge of data reduction and calibration. It was during this period when I developed a scheme to flux calibrate Keck HIRES spectrum. This was the first time when the HIRES data was successfully flux calibrated. The observed CCD image of the HIRES spectrum is segmented into approximately 40 pieces. The instrument is not designed to be able to flux calibrate. However, the flux calibration was the key to perform a precise measurement of D/H. Therefore, I developed a method described in Chapter 4, and the following work is the first application of the method.

5.2.1 A Brief History of Primordial Deuterium Measurement

The standard theory of big bang nucleosynthesis (SBBN) predicts the abundances of the light nuclei H, D, ^{3}He, ^{4}He, and ^{7}Li as a function of the cosmological baryon to photon ratio, $\eta = n_b/n_\gamma$ (Kolb & Turner 1990; Walker et al. 1991; Schramm & Turner 1998; Nollett & Burles 2000; Olive, Steigman & Walker 2000). A measurement of the ratio of any two primordial abundances gives η, and hence the baryon density, while a second ratio tests the theory. However, it is extremely difficult to measure primordial abundances, because in most places gas ejected from stars has changed the abundances.

Adams (1976) suggested that it might be possible to measure the primordial D/H ratio in absorption line systems towards QSOs. Although gas which has been inside a star will have lost all of its deuterium, in QSO absorption line systems having typical metal abundances of 0.001 to 0.01 of the solar value, about 0.1 – 1% of the deuterium will have been lost.

The advent of the HIRES spectrograph (Vogt 1994) on the W.M. Keck-I telescope gave the high signal-to-noise ratio (SNR) and spectral resolution needed

to reveal deuterium (Tytler et al. 2000) in high redshift absorption systems. We have previously measured D/H in two QSOs (Tytler, Fan & Burles 1996; Tytler & Burles 1997; Burles & Tytler 1998a; Burles & Tytler 1998b), and placed a strong upper limit on D/H in a third (Kirkman et al. 1999).

Other QSOs give less useful constraints on D/H, because their absorption systems are more complex, or existing spectra are inadequate. The Lyman limit system (LLS) at $z_{abs} = 0.701$ towards QSO PG 1718+4807 might allow ten times larger D/H, or it may give no useful constraints (Webb et al. 1997; Levshakov, Kegel, & Takahara 1998; Tytler et al. 1999). Molaro et al. (1999) claimed another QSO absorption system showed low D/H, but they and Levshakov et al. (2000) note that since only the Lyα line has been observed, the hydrogen velocity structure and the H I column density are poorly known, and the deuterium feature can be fit using hydrogen alone.

In this chapter, we present a fourth QSO, HS 0105+1619, which gives strong constraints on the primordial D/H ratio.

5.3 Observations and data reduction

We report the detection of deuterium in the QSO HS 0105+1619 (emission line redshift 2.64, V=16.9, B1950 RA 1h 5m 26.97s, DEC +16d 19m 50.1s; J2000 RA 1h 8m 6.4s, DEC +16d 35m 50.0s), which was discovered by Hagen et al. (1999), who very kindly gave us a finding chart and a low resolution spectrum prior to publication.

We present high quality, high SNR spectra of HS 0105+1619 in both low and high resolution. The low resolution spectra were obtained using the Kast double spectrograph on the Shane 3 meter telescope at Lick observatory. The high resolution spectra were obtained using the HIRES spectrograph on the Keck-I telescope. The observations are summarized in Table 5.1. All of the high resolution observations were taken using the HIRES image rotator to align the direction of

atmospheric dispersion along the slit, and were taken with the C5 decker, which provides an entrance aperture to the spectrograph with dimensions $1.15'' \times 7.5''$. The spectra were sampled in 2.1 km s^{-1} pixels with the Tektronix 2048x2048 CCD.

The HIRES spectra were flat-fielded, optimally extracted, and wavelength calibrated using Tom Barlow's set of echelle extraction MAKEE programs. The spectra were then co-added to produce a single spectrum. This spectrum was then flux calibrated using the low resolution Kast spectrum. Because the SNR decreases in both spectra at lower wavelengths, we use the flux calibrated data for wavelengths greater than 3800 Å and the co-added spectrum without flux calibration below 3800 Å. The details regarding the co-adding and fluxing are given in Suzuki et al. (2003). The wavelength scale has an external zero point error of approximately $\pm$10 km s^{-1}, which is the shift between spectra taken at different times, which we corrected. The internal error in the wavelength scale is a least 0.09 km s^{-1}, from the arc line fits, and may be approximately 1 – 2 km s^{-1}, which is the size of the error which we have noted in our analysis of other similar spectra (Levshakov et al., 1998). The final spectrum has 2.1 km s^{-1} wide pixels, and a SNR of approximately 80 and 10 at the Lyα and Lyman limit of the D/H system, respectively. In Figure 5.1, we show the flux calibrated Kast and HIRES spectra.

5.4 General Properties of the $z \simeq 2.536$ Lyman Limit System Towards HS 0105+1619

As can be seen in Figure 5.1, the low resolution Kast spectrum of HS 0105+1619 shows a steep Lyman break at a wavelength of approximately 3230 Å, which is caused by a Lyman limit system at a redshift of $z \simeq 2.54$. At this redshift we see a strong Lyα absorption line, near 4300 Å. Our analysis of the high resolution HIRES spectrum indicates that there is a Lyman limit system at a redshift of $z \simeq 2.536$, which shows deuterium and numerous metal absorption lines. We discuss the general features of the absorption below, and the best fits to the data in the following

Table 5.1. Observations of HS 0105+1619

Instrument	Date	Integration Time (seconds)	Wavelengths covered (Å)
Kast	August 16, 1998	2700	3200 – 5100
HIRES	October 10, 1999	7200	3200 – 4720
HIRES	October 11, 1999	2×8000	3200 – 4720
HIRES	November 9, 1999	1800	4220 – 6640 [a]
HIRES	September 19, 2000	2×7200	3200 – 4720
HIRES	September 20, 2000	8600, 10800	3200 – 4720
HIRES	September 20, 2000	4×7000	3200 – 4720
Total (HIRES):		86,800	

[a]The wavelength coverage for this observation was not continuous due to 1-10 Å spectral order gaps.

section.

5.4.1 Hydrogen Absorption

We observe hydrogen in all Lyman series transitions through Lyman-17, where the spectrum abruptly ends at 3233 Å due to line blending near the Lyman limit. The observed Lyman transitions are shown in Figure 5.2.

The column density of the hydrogen is high, as Figure 5.2 indicates. All of the Lyman series transitions are saturated through to the Lyman limit, indicating that the column density is at least $\log N_{HI} \geq 17.8$ cm^{-2}. The Lyα line has zero flux across about 200 km s^{-1} indicating that the column density of the system is approaching the levels found in damped Lyα systems.

Inspection of Figure 5.2 also indicates that the absorption system is very simple. The Ly-5, Ly-6, Ly-7, Ly-9, Ly-10, Ly-14, and Ly-15 transitions all appear symmetric and un-blended, allowing us to describe the absorber by a single component.

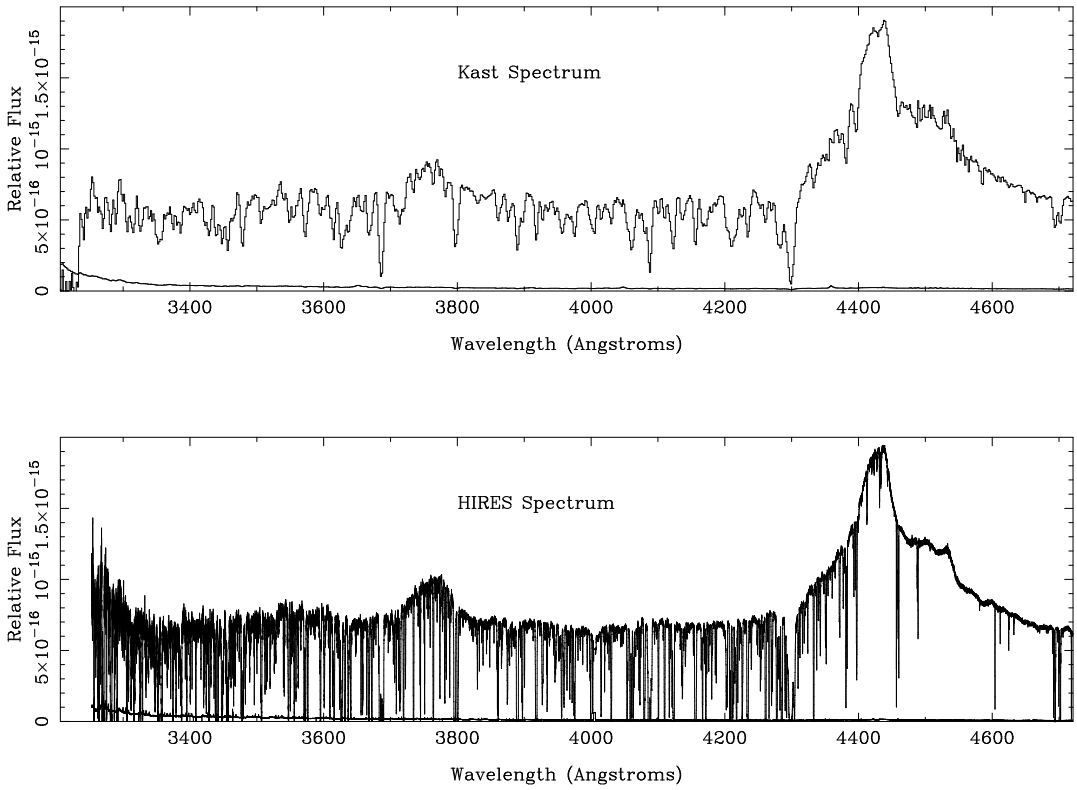

Figure 5.1: Spectrum of HS 0105+1619. The upper panel shows the low resolution flux calibrated spectrum obtained with the Kast spectrograph. The lower panel shows the flux calibrated HIRES spectrum. The flux calibration was noisy at wavelengths less than 3800 Å and was not applied to the Lyman limit, which is not shown above for the HIRES spectrum.

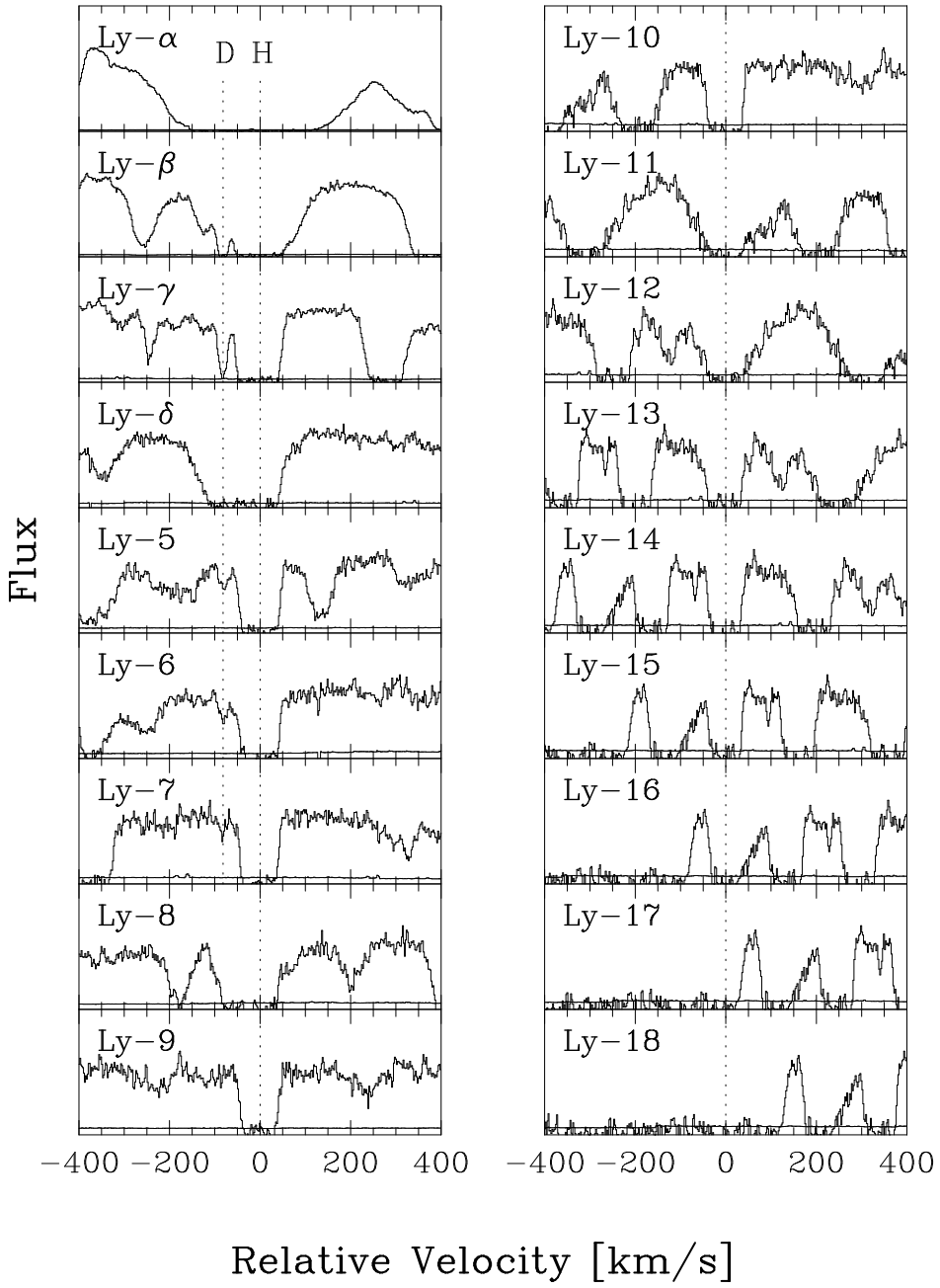

Figure 5.2: Lyman series absorption in the $z \simeq 2.536$ Lyman limit system towards HS 0105+1619. The velocities shown are relative to the H I redshift of $z = 2.535998$. The vertical scales are linear flux, from zero, and the lower traces are the 1σ error. The D I absorption is seen at -82 km s^{-1} in Lyβ, Lyγ, Ly-5, Ly-6 and Ly-7.

5.4.2 Deuterium Absorption

Since the column density of the hydrogen responsible for the Lyman limit appears high, we expect the associated deuterium absorption to be strong. For the first time, we observe absorption at the predicted position of deuterium, a velocity of $v = -81.64$ km s^{-1} in the frame of the H I, in 5 Lyman series transitions: Lyβ, Lyγ, Ly-5, Ly-6, and Ly-7. Deuterium Lyα was not observed since it is subsumed by the absorption of the hydrogen Lyα, and deuterium Ly-4 was not observed due to intervening Lyα forest absorption.

The observed absorption is narrow, and appears symmetric and free of strong contamination, suggesting that like the hydrogen, the absorption is simple and can be modeled with a single component.

In all transitions where absorption is observed, the velocity of the absorption appears centered about the same value, $v \simeq -82$ km s^{-1} , strongly indicating that the features are all Lyman transitions of the same absorber, and that the absorber is consistent with being deuterium. In a later section, we give a more rigorous discussion of why we believe the absorption is indeed deuterium, and not hydrogen or other ions.

5.4.3 Metal Line Absorption

The $z \simeq 2.536$ Lyman limit system shows a variety of metal ions, as seen in Figure 5.3. Unlike Lyman Limit systems with column densities in the range of log N_{HI}= 16.5–18 cm^{-2} which show absorption predominantly in the higher ionization states, this system shows metal line absorption in neutral, low, and high ionization states. Since the column density of the hydrogen appears high, we expect the neutral and low ionization metal lines to trace the H I, and with it the deuterium, in analogy with damped Lyα systems.

All of the low ionization metal lines are extremely narrow, and appear to be well described by a single component. Moreover, the low ions are all centered at

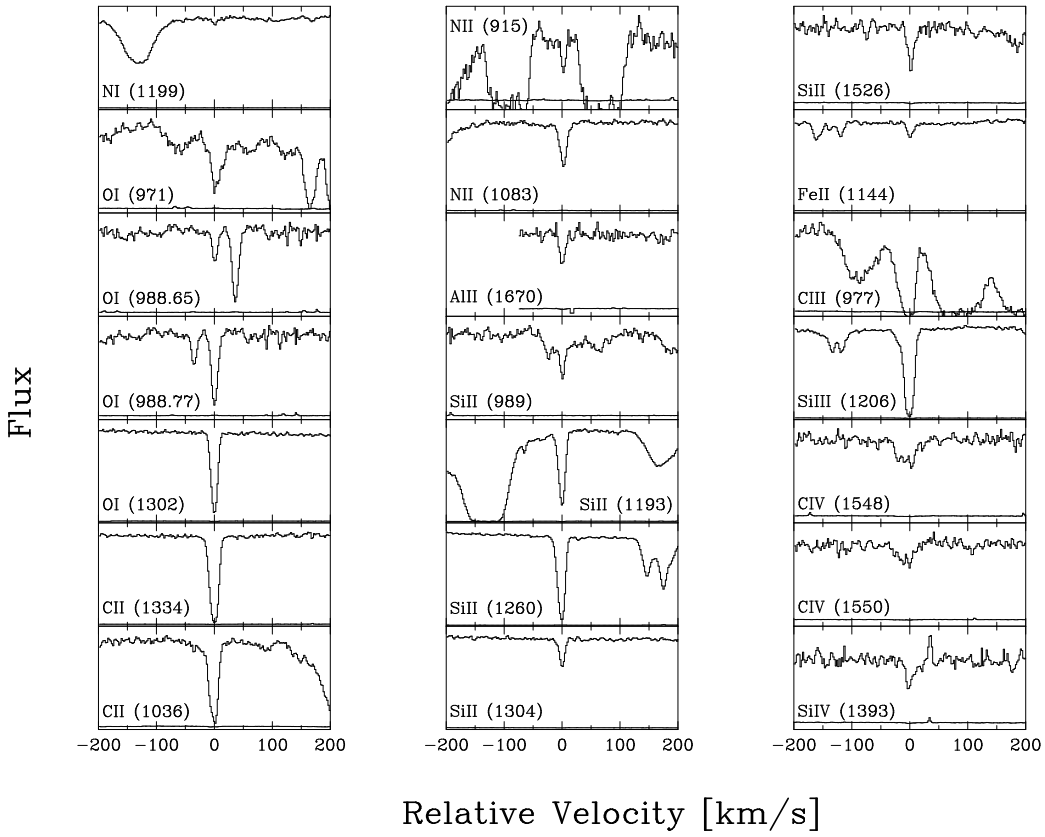

Figure 5.3: Observed metal line absorption associated with the $z \simeq 2.536$ Lyman limit system. The metals are grouped according to ionization state and are organized by atomic mass. The low ionization lines have simple, narrow profiles centered near 0 km s^{-1}.

$v \simeq 0$ km s^{-1}, implying that they arise in the same gas as the H I and D I.

5.5 Best Parameters for the $z \simeq 2.536$ Lyman Limit System

We now give the parameters which describe the absorption in the $z \simeq 2.536$ Lyman Limit system towards HS 0105+1619. For all measurements, a continuum was fit to the region under consideration to produce a unit normalized spectrum. The observed absorption features were then fit using the VPFIT Voigt profile line-fitting routine (Webb, 1987; kindly provided by Carswell) and re-verified using in-house routines. For each absorber, we obtain an estimate of the column density, N, the

redshift, z, and the velocity width, b, along with their respective 1σ errors. The results of this analysis are found in Table 5.2.

5.5.1 The Hydrogen

The parameters describing the hydrogen absorption responsible for the Lyman limit are obtained from various complementary parts of the spectrum, and are given by $\log N_{HI} = 19.422 \pm 0.009$ cm^{-2}, $b = 13.99 \pm 0.20$ km s^{-1}, and $z = 2.535998 \pm 0.000007$.

The deuterium and low ionization metal absorption lines give a strong indication that the H I can be modeled by a single component, whose redshift should be consistent with that of the other neutral ions observed, namely O I and N I. We find that a single component fit allows for an excellent description of the observed absorption, and we now consider the individual parameters.

Redshift

The redshift of the hydrogen was determined by simultaneously fitting the Lyman series absorption at Lyα, Lyβ, Lyγ, Ly-5, Ly-6, Ly-7, Ly-9, Ly-10, Ly-13, Ly-14, and Ly-15.

Velocity Width

The high column density of the absorber does not give us information on the velocity width at Lyα, so we must turn to the higher order Lyman series lines. To determine b, we fit the absorption in the Lyman series in transitions which appear to be least contaminated by interloping Lyα forest, specifically Ly-9, Ly-10, Ly-14, and Ly-15, simultaneously. The inclusion of all observed Lyman series transitions in the fitting procedure does not changed the measured b value.

Table 5.2. Ions Observed in the $z \simeq 2.536$ LLS towards HS 0105+1619[a]

Ion	log N (cm^{-2})	b[b] (km s^{-1})	z	v[c] (km s^{-1})
H I	19.422 ± 0.009[d]	13.99 ± 0.20	2.535998 ± 0.000007	0.0 ± 0.6[e]
D I	14.826 ± 0.039[f]	9.85 ± 0.42[f]	2.536002 ± 0.000008	0.4 ± 0.7
N I	12.306 ± 0.060	5.13 ± 1.57	2.535998 ± 0.000009	0.0 ± 0.8
O I	14.378 ± 0.024	4.30 ± 0.11	2.535991 ± 0.000001	-0.6 ± 0.1
C II	14.349 ± 0.069	5.44 ± 0.21	2.535985 ± 0.000001	-1.1 ± 0.1
Si II	13.156 ± 0.012	5.01 ± 0.09	2.535980 ± 0.000001	-1.5 ± 0.1
Al II	11.870 ± 0.040	9.69 ± 0.99	2.536019 ± 0.000009	$+1.8 \pm 0.8$
Fe II	12.913 ± 0.087	6.45 ± 2.33	2.535983 ± 0.000014	-1.3 ± 1.2
C III	13.716 ± 0.032	14.48 ± 0.56	2.535923 ± 0.000004	-6.4 ± 0.4
C IV[g]	13.277 ± 0.019	20.40 ± 1.07	2.535913 ± 0.000009	-7.2 ± 0.8
N II	13.501 ± 0.013	6.82 ± 0.30	2.536015 ± 0.000002	$+1.4 \pm 0.2$
Si III	13.097 ± 0.037	7.10 ± 0.24	2.535977 ± 0.000001	-1.8 ± 0.1
Si IV[g]	12.647 ± 0.053	9.16 ± 1.59	2.535995 ± 0.000014	-0.3 ± 1.2

[a] The three sections group ions by increasing ionization. For ions in the same gas, we expect the b values to decrease with increasing mass. Errors quoted in the table for the N and z values are from VPFIT alone, except for H I and D I.

[b] The intrinsic b value.

[c] Velocities are all relative to $z = 2.535998$. The errors in v values come from the errors listed on the z values: $\sigma(v)^2 = (c\sigma(z)/(1+z))^2 + 0.09^2$, where 0.09 km s^{-1} is the minimum internal uncertainty in the wavelength scale. The internal error may be 1 – 2 km s^{-1}, while the external error is approximately ± 10 km s^{-1}.

[d] The value for log N_{HI} is the weighted mean from the damping wings and core region of Lyα, and the error includes the continuum level error.

[e] The H I z defines $v = 0$. The 0.6 km s^{-1} error is the uncertainty in the v of the H lines in this frame.

[f] The N and b for the D I are the weighted means of the individual fits to the five D transitions, and the error on the N includes the contribution from the continuum uncertainty.

[g] The lines of this ion may be multiple component blends.

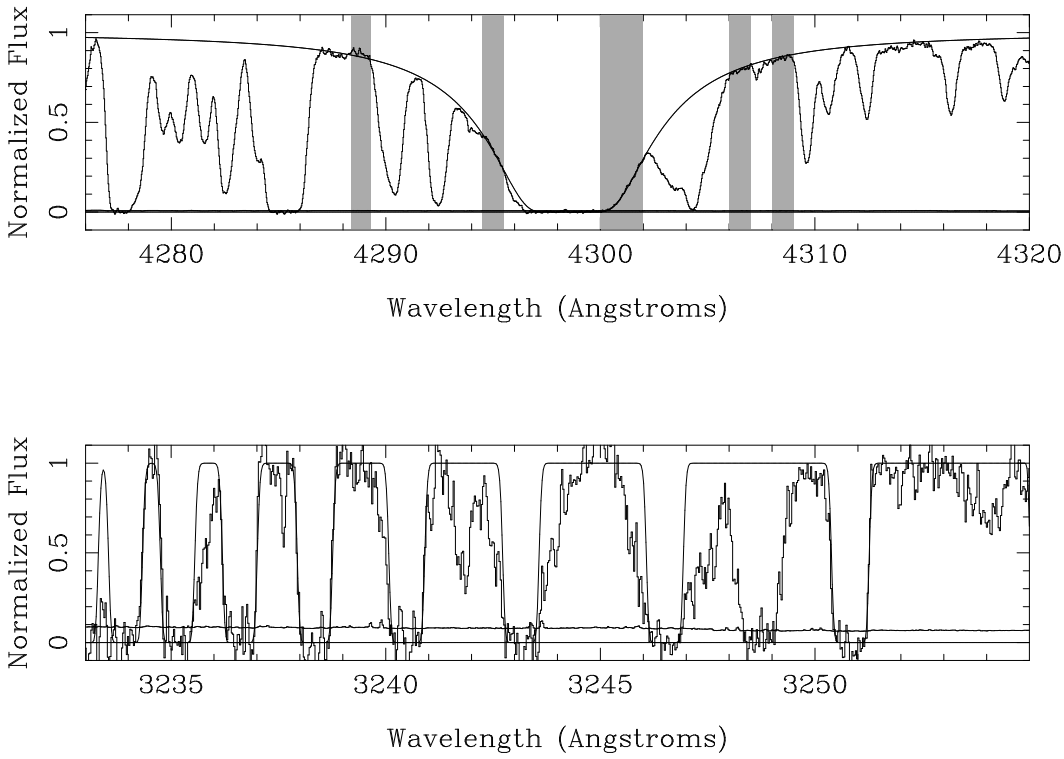

Figure 5.4: Spectral regions used to measure the H I column density. The upper panel shows the Lyα line, with the core and damping wing regions used in the fit shaded gray. The lower panel shows the absorption near the Lyman limit. Overlayed is the single component fit to the hydrogen with a column density of log N_{HI}= 19.422 cm^{-2} from Table 5.2 .

Column Density

Three regions of the spectrum allow us to determine the column density: the Lyman limit, the core of the Lyα, and the damping wings of the Lyα. These regions are shown in Figure 5.4 along with the single component best fit to the H I.

The Lyman limit allows for a lower limit to the column density of the hydrogen of log N_{HI}= 17.8 cm^{-2} since all observed Lyman series lines observed are saturated.

The Lyα line gives the most information regarding the hydrogen column density, because it is insensitive to the b value, even though it is sensitive to the continuum level. In Figure 5.5, we show the continuum used to fit the 250 Å region

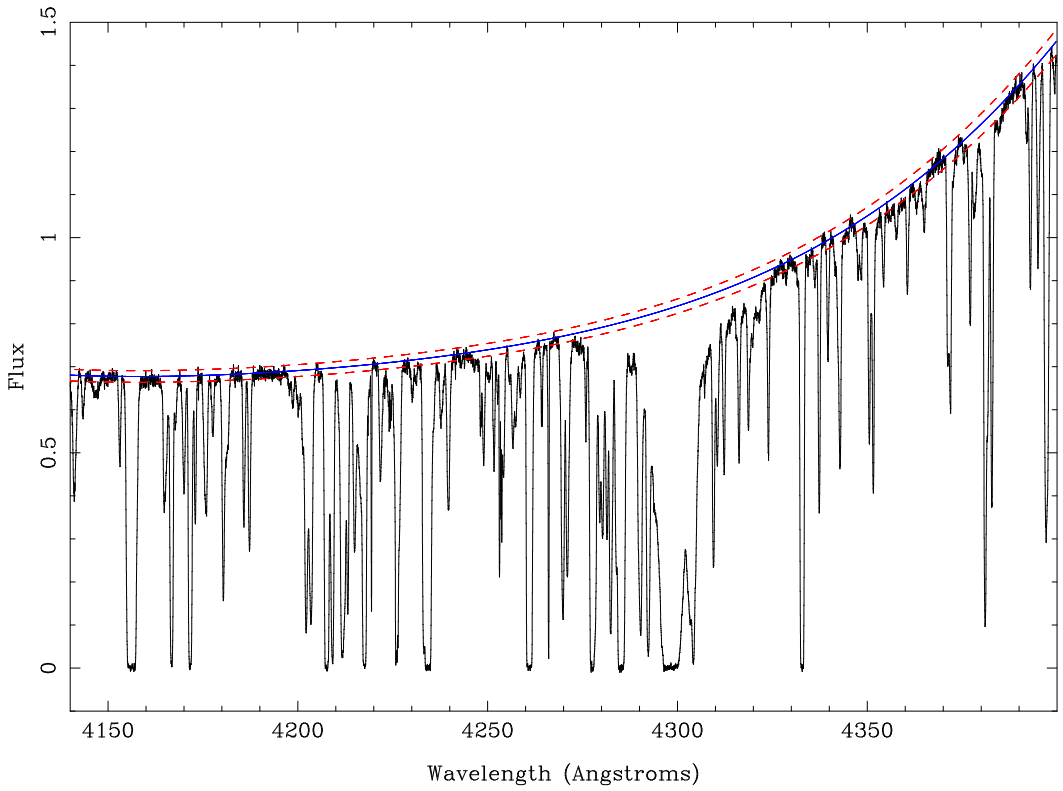

Figure 5.5: Lyα region of the $z \simeq 2.536$ Lyman limit system. Over-layed is the continuum fit (solid line) and the approximate 1σ error to the continuum fit (dashed line).

encompassing Lyα and the corresponding approximate 1σ levels, which amount to a $\pm 2\%$ continuum level change. To determine the effect of the continuum placement on the measured value on the column density, for all regions of the Lyα line, we obtain a fit using the best continuum estimate, and then move the continuum to the $\pm 1\sigma$ levels and re-fit. In all fits to the Lyα, we choose segments of the spectra which appear to be least contaminated by other absorption.

In Figure 5.6, we show the fit to the core of log $N_{HI} = 19.419 \pm 0.009$ cm^{-2}, where the error is the quadratic sum of the error from the continuum (0.007) and the error from the fit (0.006). This fit was made for two regions on either side of the line center: 4294.5–4295.5 and 4300–4302 Å. There is additional absorption in the core between 4295.5 and 4297 Å which is readily fit by two H I Lyα lines. Their

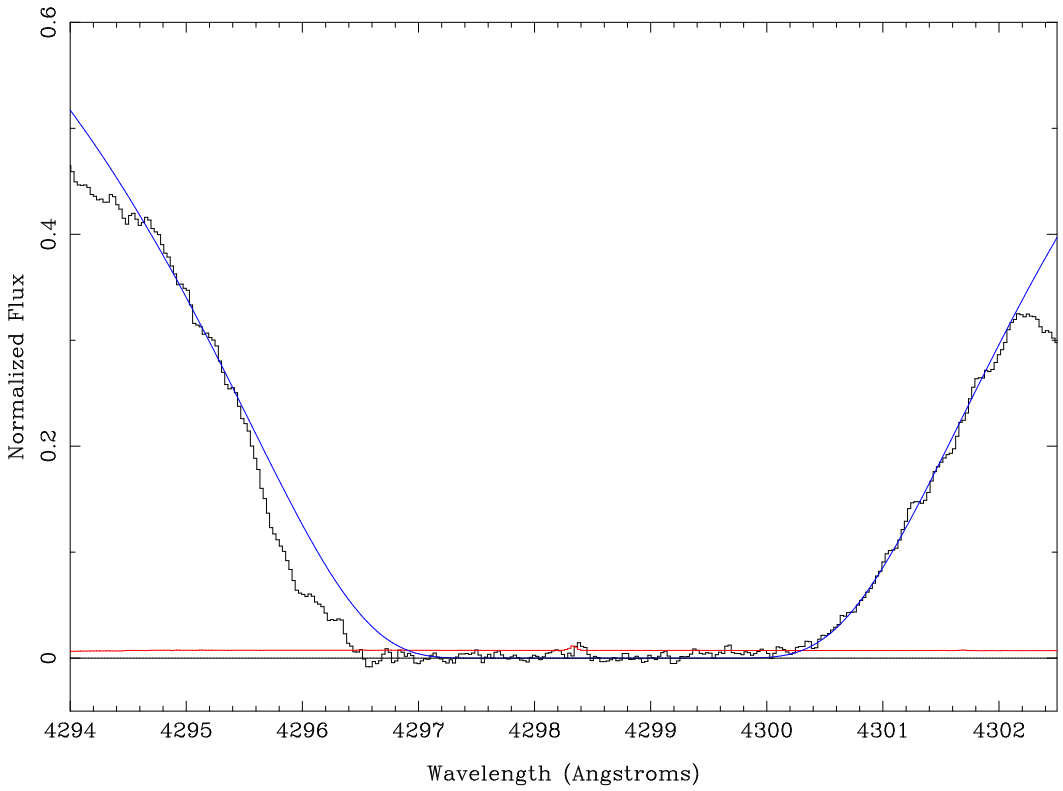

Figure 5.6: Fit to the core region of Lyα with log N_{HI}= 19.419 cm^{-2}.

absorption is seen and fit in Lyβ, but they contribute no significant optical depth to the lower wavelength (4294.5–4295.5 Å) region which gives the column density of the H I which shows deuterium.

We note that contamination of the core region is possible, and would lower the measured column density. However, we consider such contamination unlikely, since it would require at least two lines appearing in the right places, with a very restricted set of parameters, to produce enough absorption to fit both sides of the core region.

The damping wings of the Lyα absorber also give the column density, but the exact continuum placement is now the dominant source of error because the continuum uncertainty represents a larger fraction of the total absorption in these regions. Two damping wing regions were fit, one on either side of the line center. On the blue (lower wavelength) side, we fit the wavelengths 4288.4–4289.3

Å, which gave log N_{HI} = 19.406 ± 0.060 cm^{-2}, where the errors are the range in column density allowed by the ±2% range in the continuum placement. For the red (higher wavelength) side regions 4306–4307 and 4308–4309 Å were fit giving log N_{HI} = 19.4752 ± 0.040 cm^{-2}.

For our best value for the H I column density, we take the weighted mean of the three measurements from the core and wings: log N_{HI}= 19.422 ± 0.009 cm^{-2}. All three estimates of the column density are consistent with this mean.

5.5.2 The Deuterium

The determination of the parameters describing the deuterium absorption is relatively straightforward, given the presence of 5 un-blended transitions, most of which are unsaturated. We begin by fitting the D I transitions, and then assess possible sources of error.

The D I transitions are well fit by an absorber with log N_{DI}= 14.810 ± 0.029 cm^{-2} and a velocity width of b = 9.93 ± 0.29 km s^{-1}. This fit is shown in Figure 5.7. These values were determined by fitting the regions surrounding the deuterium in all 5 deuterium absorption regions simultaneously, with the redshift of the deuterium tied to the hydrogen, and the parameters for the hydrogen absorption fixed at log N_{HI}= 19.42 cm^{-2} and b = 13.99 km s^{-1}. In all fits, the regions used to fit deuterium were constrained to be those within approximately −150 and +20 km s^{-1} of the H I line center, and are listed in Table 5.3. Where needed, additional Lyα forest absorption was fit to model all absorption. The parameters for the additional lines are given in Table 5.4.

The uncertainty in the continuum level increases the error on the D I column density by a third. Independent estimates of the continuum levels at the D I transitions had a 1σ dispersion of approximately 10% , much larger than the 2% error near Lyα, where the data has been flux calibrated and has significantly higher SNR. To gauge the effect on the error in the D I column density, we determined the parameters of the deuterium absorption independently for each line, both for

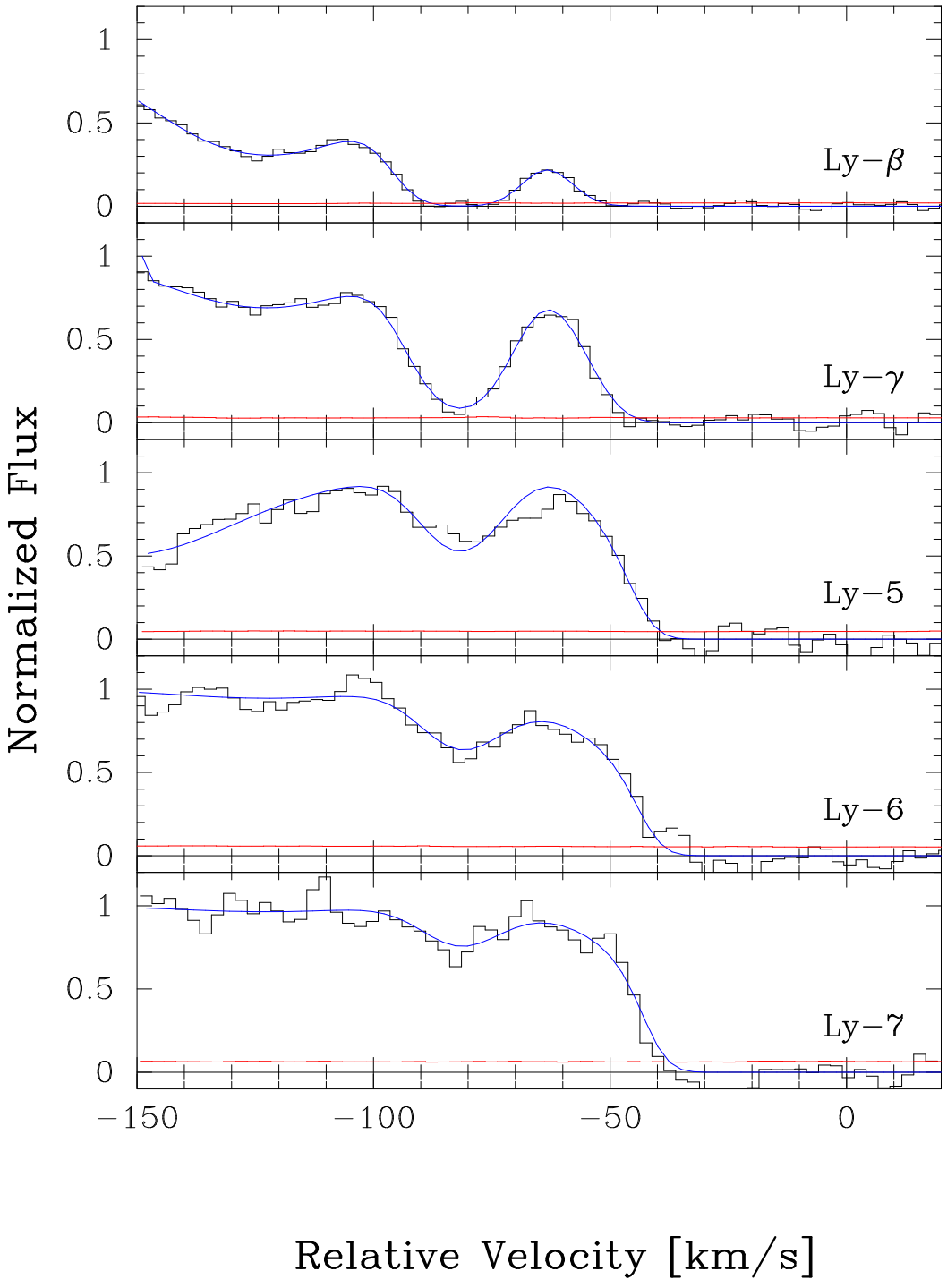

Figure 5.7: Simultaneous fit to the deuterium at -82 km s^{-1} in 5 Lyman series transitions with log N$_{\rm DI}$= 14.81 cm^{-2} and $b = 9.93$ km s^{-1}. Also included in the fit is the H at 0 km s^{-1} and additional Lyα forest absorption.

Table 5.3. Spectral Regions used to measure D I

Region	λ_{min} (Å)	λ_{max} (Å)
Lyβ	3625.1	3627.4
Lyγ	3437.2	3439.2
Ly-5	3314.2	3316.4
Ly-6	3289.4	3291.4
Ly-7	3273.5	3275.2

Table 5.4. Additional Lines used to fit D Regions

$\log N$ (cm^{-2})	b (km s^{-1})	z	Region[a]
14.324	25.2	2.53455	all[b]
14.901	18.2	2.53554	all[b]
13.365	26.2	1.72637	Ly-5
12.944	29.7	1.70682	Ly-6
12.770	39.7	1.69376	Ly-7

[a]The regions are defined in Table 5.3

[b]All D regions used: Lyα, Lyβ, Lyγ, Ly-5, Ly-6, and Ly-7

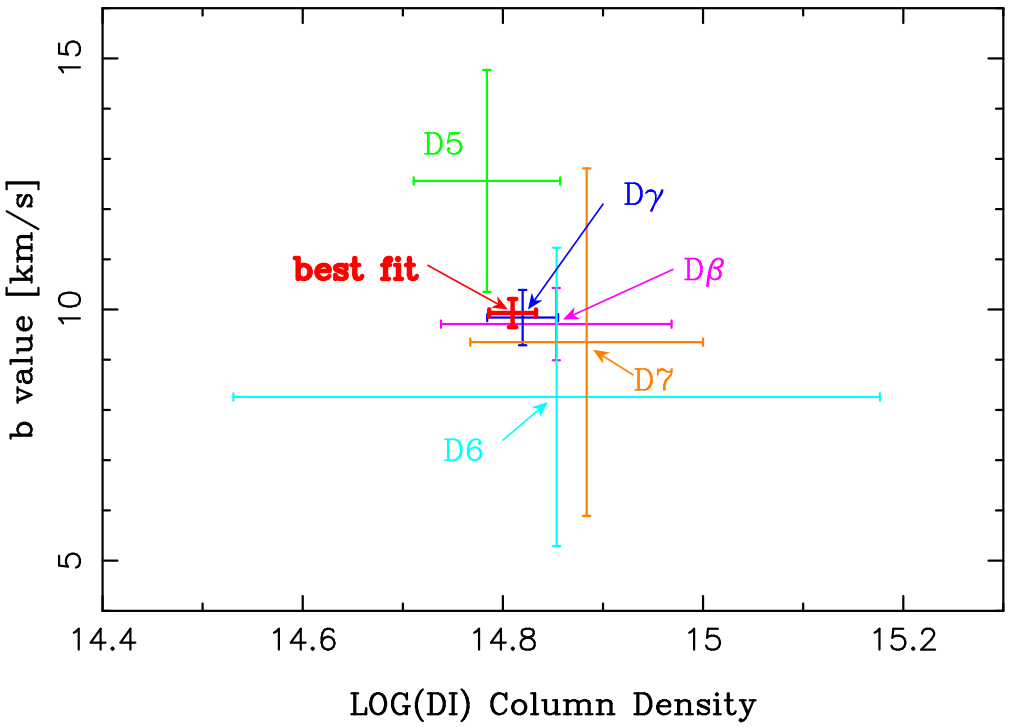

Figure 5.8: Values of the deuterium column density, log N_{DI} (cm^{-2}), and the absorption width parameter, b, for each of the 5 deuterium lines fit separately. The bold cross represents the values when all lines are fit simultaneously using the best estimate for the continuum level.

the best estimate of the continuum and for a 10% higher continuum level. The difference between these two is the contribution to the error from the choice of continuum level. For each each D I transition, this error was added in quadrature to the error obtained with the best continuum. The weighted mean for the five D I transitions gives log N_{DI}= 14.826 ± 0.039 cm^{-2} and $b = 9.85 \pm 0.42$km s^{-1}. The results of the independent fits to the different deuterium transitions with the best estimate of the continuum level can be seen in Figure 5.8.

The error on log N_{DI} is insensitive to a change in the redshift of 1 km s^{-1}, as found by both letting the deuterium fit freely to its own redshift, and by tying the redshift to the H at 1 km s^{-1} away from the best fit value. Both results gave a log N_{DI} which deviated by amounts significantly lower than the best fit 1σ errors.

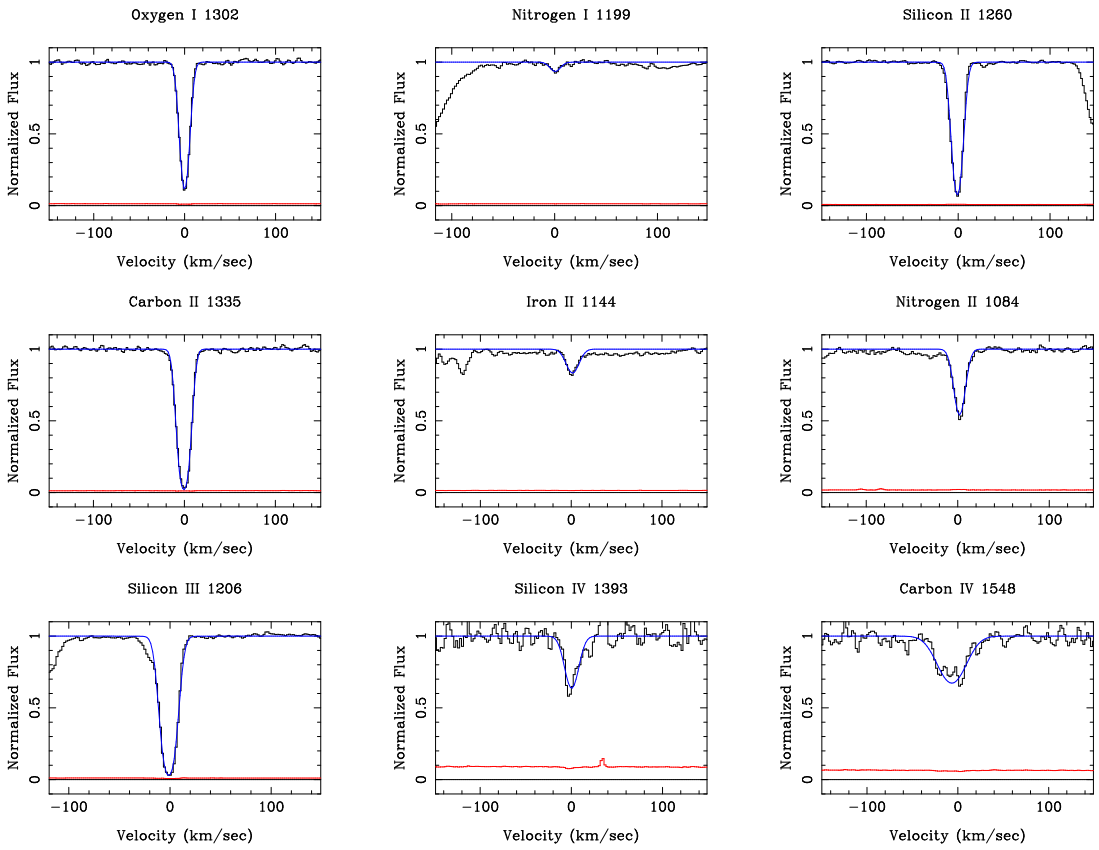

Figure 5.9: Best fit to metal lines associated with the $z \simeq 2.536$ LLS towards HS 0105+1619. The velocities shown are relative to $z = 2.535998$.

The effect of varying the main hydrogen by the 1σ errors in either column density or velocity width produced no effective change on the log N_{DI} since the main hydrogen component is well separated from the deuterium because the b of the hydrogen is very small.

5.5.3 The Metals

The results of fits to the many metal lines are given in Table 5.2, and a subset of the fits is shown in Figure 5.9. In all cases, the ions were best fit by a single component whose redshift, velocity width, and column density were all allowed to vary. Many of these ions show multiple transitions, and for any single ion, all transitions present in the spectra were fit simultaneously.

The metals were all found to lie within 8 km s^{-1} of the redshift of the hydrogen which shows deuterium. More importantly, since the column density of the hydrogen is so high, we expect the redshifts of the low and neutral ions to agree with the hydrogen since we expect the gas to be predominantly neutral. The neutral and singly ionized ions agree with the hydrogen redshift to within 2 km s^{-1}, while the neutral ions alone, in the top section of Table 5.2, agree to within approximately 1 km s^{-1}. The larger dispersion seen for the singly ionized ions, in the second section of the table, indicates that some of the gas making these lines is distinct from the neutral gas, but this dispersion could be insignificant, because the internal wavelength errors could be 1 –2 km s^{-1}.

The detection of O I is of particular importance in this system for two reasons. First, the ionization potential of O I is nearly identical to that of hydrogen, so it is ionized by the same photons that ionize the H I. Second, O I participates in electron transfer with H I, such that in cases where the gas is not highly ionized, O I/O is nearly identical to H I/H, and the distribution of O I should match that of the H I and the D I. The O I absorption gives information about the temperature, bulk motion, ionization and abundances in the neutral gas which shows the D I absorption. Since the O I is accurately modeled by a single, narrow component in four separate transitions, we gain confidence that a single component fit to the deuterium and to the hydrogen is sufficient. The implications of the measurement of O I on the metallicity and ionization are discussed in a later section.

Since O I and H I should arise in the same gas, we use these lines to obtain the temperature of the gas which shows D I and its turbulent velocity. We model the observed b as $b^2 = b_{inst}^2 + b_{int}^2$. The instrument line broadening, b_{inst}^2 was measured from arc lamp calibration spectra to be $b_{inst} = 4.81 \pm 0.14$ km s^{-1}. We model the intrinsic velocity width as $b_{int}^2 = b_{temp}^2 + b_{turb}^2$; a combination of thermal broadening and bulk motion. The thermal broadening, $b_{temp}^2 = 2kT/m = 166.41(T/10^4\mathrm{K})/\mathrm{mass(amu)}$, depends on the ion mass in atomic units, m, but the b_{turb} is the same for all ions. All of the b values quoted in this paper and listed

in Table 5.2 refer to intrinsic line widths, but the listed errors do not include the error in b_{inst}, because we do not know whether this error is correlated at different wavelengths.

Fitting O I, N I and H I alone gives $T = 1.15 \pm 0.02 \times 10^4$ K, and b_{turb}= 2.56 ± 0.12 km s^{-1}, which we show by the straight line in Figure 5.10. The errors quoted here are very much minimum values, because they do not include the error in the b_{inst} or the appropriateness of the model.

Ions C II, Si II and Fe II, are all wider than predicted by this fit, presumably because a part of each line arises in gas with different velocity structure. The lines from the higher ionization ions C III, C IV, N II, Si III and Si IV have velocities which differ by 0 to –7 km s^{-1} from the H I and low ionization ions. They are not relevant to the D/H because their ionization and velocities show that they arise in different gas, a common finding for absorption systems with high N_{HI} (Wolfe & Prochaska, 2000), but unlike absorption systems with much lower N_{HI}, including PKS 1937–1009 and PKS 1937–1009.

5.6 Is the Observed Absorption Deuterium?

Now that we have determined the parameters of the absorption at the position of deuterium, we turn to the issue of confirming that the absorption is indeed deuterium, and not inter-loping hydrogen or metal line contamination.

The primary concern with the absorption seen at the position of deuterium would be that it is caused not by deuterium, but instead by inter-loping hydrogen. Here we argue that this scenario is unlikely for the following reasons.

First, hydrogen lines in the Lyα forest with the appropriate column density, $\log N_{HI} \simeq 14.8$ cm^{-2} have $b > 20$ km s^{-1}, and not $b \simeq 10$ km s^{-1} (Kim et al., 1997; Kirkman & Tytler, 1997). However, such low values of b might be found in components of the LLS, which are the most likely contaminants. Second, we are able to predict the width of the deuterium using the measured widths of the other

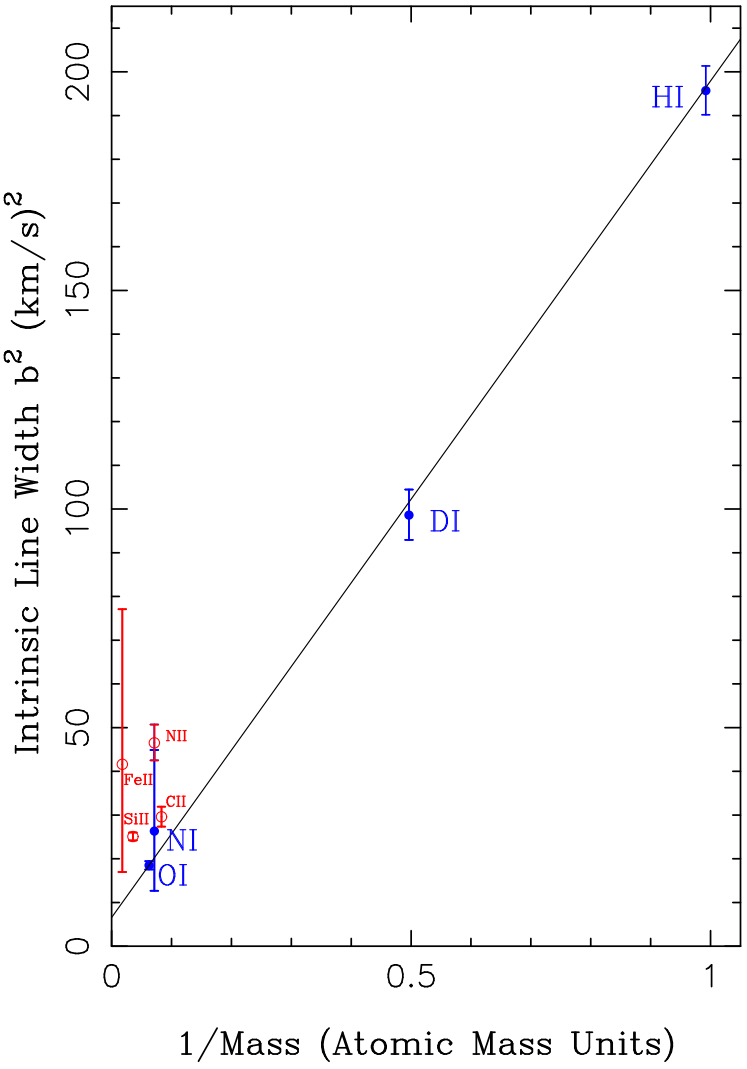

Figure 5.10: Intrinsic velocity widths measured for the neutral and low ionization ions. The straight line is the best fit to H I, N I, and O I alone. The slope of the line gives the temperature of the gas, $T = 1.15 \times 10^4$ K, and the intercept gives the turbulent velocity, $b_{turb} = 2.56$ km s^{-1}. The D I absorption comes from the same gas as the H I, N I and O I.

neutral ions observed which are present in the same gas. Figure 5.10 illustrates the concept. Since we have observed three other neutral ions (H I, O I, N I), we can use their widths to predict the width of deuterium. As Figure 5.10 shows, the measured value of $b(D)$ is consistent with its predicted value. Third, hydrogen lines with a log $N_{HI} \simeq 14.8$ cm^{-2} often show associated metal line absorption, but as is seen in Figure 5.9, there is no such absorption at -82 km s^{-1}. Finally, for the absorption to be hydrogen and not deuterium, its position would have to agree with that of deuterium to within 1 km s^{-1}. Taken together, these arguments indicate that the observed absorption is deuterium, and not hydrogen, but we can not quantify this because we do not know the properties of components of Lyman limit systems.

The scenario in which the absorption is metal line contamination is even less likely for a number of reasons. Any metal lines with a column density of log $N_{metal} \simeq 14.8$ cm^{-2} would show absorption in not only that ion, but many others along with strong associated hydrogen absorption, some of which would be easily observed in our spectrum, but were not. Also, for the observed absorption to be entirely derived from metal line contamination, such metal lines would have to appear in 5 different regions of the spectrum, all at positions within approximately 1 km s^{-1} of the predicted positions of deuterium, and with line strength scaling as the oscillator strengths expected for the deuterium Lyman series. A similar argument can be used to exclude the case whereby the absorption at the position of deuterium was hydrogen, but not in the corresponding Lyman series transition (e.g., the absorption at Ly-6 is an unrelated Lyα line).

5.7 Best Fit Values for HS 0105+1619

For the gas giving D/H in HS 0105+1619, the best values for various parameters, and the 1σ errors, are as follows:

- log $N_{HI} = 19.422 \pm 0.009$ cm^{-2} (2% error)
- log $N_{DI} = 14.826 \pm 0.039$ cm^{-2} (9% error)

- log D/H $= -4.596 \pm 0.040$ (10% error)
- D/H $= 2.54 \pm 0.23 \times 10^{-5}$
- temperature: $T = 1.15 \pm 0.02 \times 10^4$ K
- Gaussian turbulent velocity width: b_{turb}= 2.56 ± 0.12 km s^{-1}
- log oxygen abundance, on the solar scale: [O/H] $= -2.0$
- other limits: [C/H] ≤ -1.9, [Al/H] ≤ -2.1, [Fe/H] ≤ -1.9, [Si/H] ≤ -1.85, [N/H]$\simeq -3.1$
- neutral fraction: H I/H> 0.8
- gas density: $n > 0.01$ cm^{-3} (for $J_{912} \geq 10^{-21}$ erg cm^{-2} s^{-1} Hz^{-1} sr^{-1})
- extent of absorbing region along the line of sight: < 1 kpc
- mass of gas: $< 1.2 \times 10^5 M_\odot$.

For D/H, we added the errors on log N_{HI} and log N_{DI} in quadrature, because we expect little correlation.

5.8 Summary & Discussion

We have presented the fourth quasar, HS 0105+1619, which shows an absorption system having a low deuterium to hydrogen abundance ratio: D/H= $2.54 \pm 0.23 \times 10^{-5}$ in the $z \simeq 2.536$ Lyman limit absorption system. We first obtained low resolution spectra in our survey for D/H QSOs with the Lick 3 meter Shane telescope, and here we presented over 24 hours of spectra from the HIRES spectrograph on the Keck-I telescope.

The absorber has a high neutral hydrogen column density, log N_{HI}= 19.422$\pm$ 0.009 cm^{-2} which is 36 times larger than the next highest case studied for D/H, but 8–100 times less than standard damped Lyman alpha systems. Very little is known

about absorbers with log $N_{HI} \simeq 19$ cm^{-2}, and this absorber may not be representative of this class because it was selected to have a very simple velocity structure and low b values.

While the absorber towards HS 0105+1619 has by far the highest neutral H I column density of the absorbers which we have studied for D/H, it also has the lowest total Hydrogen column density, by a factor of 4 – 7, when we correct for the ionization.

We know little about the environment around the absorber. It might be in the outer parts of galaxy, as are LLS at low redshift, or in a disk, as are damped Lyman alpha absorbers at high redshift. Alternatively, it may be in a relatively isolated gas cloud, because see just one component, with an exceptionally small spread of velocities. In either case, numerical simulations of the growth of structure suggest that the absorbing gas has been incorporated into a galaxy by today.

For the first time, we detect deuterium absorption in 5 Lyman series transitions, and determine log $N_{DI} = 14.826 \pm 0.039$ cm^{-2}. We have strong arguments that the observed absorption is indeed deuterium, and not inter-loping hydrogen or metal line absorption.

We observe a number of associated metal line absorbers, from which we calculate that the gas is warm and neutral. The metallicity of the system is $\simeq 0.01$ times solar, indicating that the measured D/H is representative of primordial D/H.

We argue that HS 0105+1619 offers the most secure detection of D/H to date, and that the D/H ratio determined from all QSOs has been made more secure.

5.8.1 HS 0105+1619 gives the most secure measurement of primordial D/H

The measurement of primordial D/H towards HS 0105+1619 is more secure than our prior measurements towards PKS 1937–1009, PKS 1937–1009 and Q0130–4021 for several reasons. By secure we mean that we have the most information, and hence there is less chance of undetected errors which might greatly exceed those

quoted. We are not explicitly referring to the size of the quoted errors, which are similar for PKS 1937–1009 and HS 0105+1619, and larger for PKS 1937–1009 .

The absorption system in HS 0105+1619 is simple. Like Q0130–4021, the second most secure result, the absorber in HS 0105+1619 is modeled with a single component, which simplifies the measurement of the column densities. PKS 1937–1009 was modeled with two or three components, and PKS 1937–1009 with two to four.

HS 0105+1619 is the only case to show more than one strong deuterium line, which reduces the chance of contamination, and gives more reliable b values, and hence N_{DI}.

For HS 0105+1619 we listed above the many reasons why the absorption near the deuterium line position is deuterium. The chance of serious contamination from the Lyα forest will decrease with rising N_{DI}. Such contamination is least likely to be significant in HS 0105+1619, followed by PKS 1937–1009. There is some contamination in PKS 1937–1009 while for Q0130–4021 we see a lot of contamination, and obtain only an upper limit on N_{DI}. We do not know whether the chance of contamination by components of the Lyman limit system changes with N_{HI}.

We also expect that the chance of contamination decreases as the b value of the deuterium decreases, because H lines often have larger b values. Hence HS 0105+1619 is the most secure detection of deuterium.

For HS 0105+1619 we have the most information on the velocity field and b values because we see several D I, N I and O I lines.

For HS 0105+1619 the metal abundance is obtained with additional redundancy. The gas is nearly neutral, and hence we get the abundances of several elements: H, C, N, O, Al, Fe and Si. For the PKS 1937–1009 and PKS 1937–1009 we used a standard photoionization model to find the level of ionization which explained the relative abundances of ions such as C II, C III, C IV and Si II, Si III, Si IV. We obtained a solution for each element, and these agreed, which provided a check. For Q0130–4021 the ionization and metal abundances are both less well

known.

5.8.2 The primordial D/H becomes more secure

The new measurement makes the primordial D/H much more secure because in each case we are sampling gas with different physical conditions, and some systematic errors, including those associated with the measurement of column densities, may be different for each QSO. First, the new measurement is the most secure. Second, we have increased the number of QSOs in which we have measured deuterium from two to three. Third, we sample a new region of space. Each absorber is a different direction in the universe, and each samples a sight line of about 1 – 10 kpc, which requires about $10^5 - 10^6$ solar masses of gas. Fourth, the absorbing gas covers a factor of 240 range in N_{HI}. Fifth, the absorption systems have differing ionization, with a range of 2000 in the H I/H ratio.

There is less variation in other parameters. The metal abundances cover a factor of ten, which is the typical for QSO absorption line systems, while the redshifts cover most of the range observable from the ground.

Chapter 6

The Measurement of the Deuterium to Hydrogen Ratio towards Q1243+3047

6.1 Abstract

We report the detection of Deuterium absorption at redshift 2.525659 towards Q1243+3047. We describe improved methods to estimate the Deuterium to Hydrogen abundance ratio (D/H) in absorption systems, including improved modeling of the continuum level, the Lyα forest and the velocity structure of the absorption. Together with improved relative flux calibration, these methods give D/H $= 2.42^{+0.35}_{-0.25}\times10^{-5}$ from our Keck-I HIRES spectra of Q1243+3047, where the error is from the uncertainty in the shape of the continuum level and the amount of D absorption in a minor second component. The measured D/H is likely the primordial value because the [O/H] $= -2.79 \pm 0.05$. This absorption system has a neutral Hydrogen column density log $N_{HI} = 19.73 \pm 0.04$ cm^{-2}, it shows five D lines and is mostly ionized.

6.2 Introduction

The D/H measurement of a system toward Q1243+3047 is truly a joint effort of the Tytler group. In this chapter, I will present our result from Kirkman et al. (2003). I played a role in observation (HIRES, Kast) and I was in charge of all of the data reduction and calibration. The main uncertainty of the measurement comes from the continuum fitting to the Lyα absorber, therefore, careful calibration of the data was essential to help us find the accurate line profile. I developed a unique scheme, described in Chapter 4, to achieve 1% precision in the relative flux calibration. In particular, for this object, I identified the following items as the sources of the systematic errors on my way to achieve 1% precision in flux calibration:

1. Inaccuracy of the commonly used standard star spectra data
2. The standard star's Balmer γ line wavelength coincides the position of the Lyα absorber.
3. The weak emission lines in the Lyα forest wavelength
4. The ozone lines in UV spectrum

The details are discussed in the previous chapters. Here I summarize how they are related to the quasar spectrum. For the item 1, I found the commonly used standard star spectra, which translate the CCD counts to the physical value, are not accurate enough to achieve our goal. I switched to use *HST* STIS standard star from Oke (1990) and could remove unsmoothed features below 3800 Å. The Lyman series of the system– from the Ly4 to the Lyman Limint – are below 3800 Å and they are all affected. For the item 2, the Balmer γ line of a standard star is at the wavelength of the Lyα absorber by coincidence. The careful calibration changed the relative flux by 8% in the neighborhood of Lyα emission line and in blueward of our main Lyα absorber. This correction was essential to the measurement of the column density of Lyα absorber. For the item 3, the flux calibrated spectra showed that there exist

emission lines in the Lyα forest which were not well known before. Attempts to were made in the past by Press et al. (1993); Zheng et al. (1997); **?**); Bernardi et al. (2003); Scott et al. (2004). It is important for the studies of Lyα forest to include these emission lines when we fit the continuum to the spectra. We saw bumpy continua in UV spectrum. We originally thought that they are calibration error, but they turned out to be real quasar emission lines. For the item 4, I realized there are a series of ozone line features at the UV end of the spectra: wavelength below 3400 Å. These wavelengths are very important to study the Lyman limit of the absorber which also gives us a clue to measure the accurate column density. For now, this ozone features are corrected when we find the response of the CCD from the standard star. Since we use the *HST* standard star which does not have ozone features, broad ozone features are printed as a part of response.

Without above findings 1% precision in flux calibration would not be possible, and these are my main contribution to this measurement.

6.3 Observations and Data Reduction

We report the detection of D absorption in the QSO Case Stellar Object CSO 0167, which we call by its B1950 coordinate name: Q1243+3047. This QSO was reported as a V = 17 blue object at B1950 RA 12h 43m 44.9s DEC +30d 47.9', with a 15" error, (equivalent to J2000 12h 46m 10.9s +30d 31m 31.2s) in an objective prism photograph by Sanduleak & Pesch (1984), and identified as a QSO at emission line redshift z_{em} = 2.56 by Everett & Wagner (1995). This QSO is not well known. The NASA extra-galactic database (NED) gives no other primary references except for a 2MASS QSO search.

We have spectra with three different spectral resolutions, from three spectrographs, summarized in Tables 6.1 and 6.2, and shown in Figures 6.1 and 6.2. To improve the relative flux levels along each spectrum, all observations were taken with the spectrograph slits aligned with the local vertical.

We obtained five spectra of Q1243+3047 from the Kast double spectrograph on the Lick Observatory 3.1m Shane telescope. These low resolution spectra are used to flux calibrate the HIRES spectra. We compare these spectra to check the flux calibration, and we can sum them to improve the S/N. All integrations were obtained using the d46 dichroic that splits the spectrum near 4600 Å, the 830 line/mm grism blazed at 3460 Å for the blue side, and the 1200 line/mm grating blazed at 5000 Å for the red side.

We have one intermediate resolution spectrum from the ESI spectrograph (Sheinis et al., 2000), mounted at the Cassegrain focus of Keck-II. This echellette covers from 3900 – 11,000 Å in a single setting in ten overlapping orders. We also use this spectrum to flux calibrate the HIRES spectra, and to look for metal line absorption at wavelengths larger than those covered in our HIRES spectra.

We have eight high resolution spectra from the HIRES spectrograph (Vogt et al., 1994a) on the Keck-I 10m telescope. These were obtained using the C5 dekker that has a 1.14" slit width and gives a FWHM of 8.0 km s^{-1} sampled with 2.1 km s^{-1} per pixel on the original HIRES Tektronix 2048x2048 CCD. All but one of these spectra cover down to wavelengths below the Lyman limit break in the absorption system that shows D, while the exception extends to larger wavelengths to cover some metal lines. The S/N per pixel in the summed HIRES spectra (Table 6.2) increases linearly with wavelength up to 4200 Å, and then rises faster in the Lyα emission line, reaching 105 on either side of the Lyα absorber of the D/H system. The S/N in the center of an echelle order is approximately 1.4 times greater than that at the ends.

We describe the data reduction and flux calibration in detail in Suzuki et al. (2003). The error in the wavelength solution for the HIRES spectra is at least 0.05 – 0.1 pixels, or 0.1 – 0.2 km s^{-1}, and may be as large as 1 – 2 km s^{-1}. Our analysis of other similar spectra (Levshakov et al., 1999) revealed errors of order 1 km s^{-1}. We placed all the HIRES integrations on the same logarithmic wavelength scale, which has a constant velocity of 2.1 km s^{-1} per pixel, similar to the original pixel size,

Table 6.1. Observations of Q1243+3047

Instrument	Date[a]	Integration Time (seconds)	Slit (arcsec)	Wavelengths Observed (Å)
Kast	February 13, 1997	3300	3	3120 – 5800
Kast	May 10, 1999	6982	2	3137 – 7188
Kast	May 11, 1999	7200	2	3137 – 7188
Kast	May 17, 2001	5400	2	3191 – 5881
Kast	May 17, 2001	5400	2	3191 – 5881
ESI	January 11, 2000	1364	1	4000 - 10,000
HIRES	April 15, 1999	3600	1.14	3494 – 5842
HIRES	April 16, 1999	7200	1.14	3168 – 4705
HIRES	April 17, 1999	8100	1.14	3168 – 4705
HIRES	April 17, 1999	8100	1.14	3168 – 4705
HIRES	March 12, 2000	9000	1.14	3214 – 4705
HIRES	March 12, 2000	9000	1.14	3214 – 4705
HIRES	March 13, 2000	7200	1.14	3214 – 4705
HIRES	March 13, 2000	7200	1.14	3214 – 4705

[a]We list the local calendar date at sunset at the start of the night.

and we shifted the Kast and ESI spectra to put them on a similar wavelength scale. All spectra were also converted to vacuum wavelengths and shifted to the solar rest frame. We applied a relative flux calibration to the HIRES spectra using the Kast and ESI spectra to transfer the flux information from standard stars to the QSO spectra.

6.4 Velocity Structure of the 2.526 absorption system

Ideally we would measure velocity structure directly from the H and D absorption, because we expect that the H I and the D I should have identical velocity distributions, except for the effects of thermal broadening. However, the H lines give little information because the are all saturated, broad and blended. Instead, we use

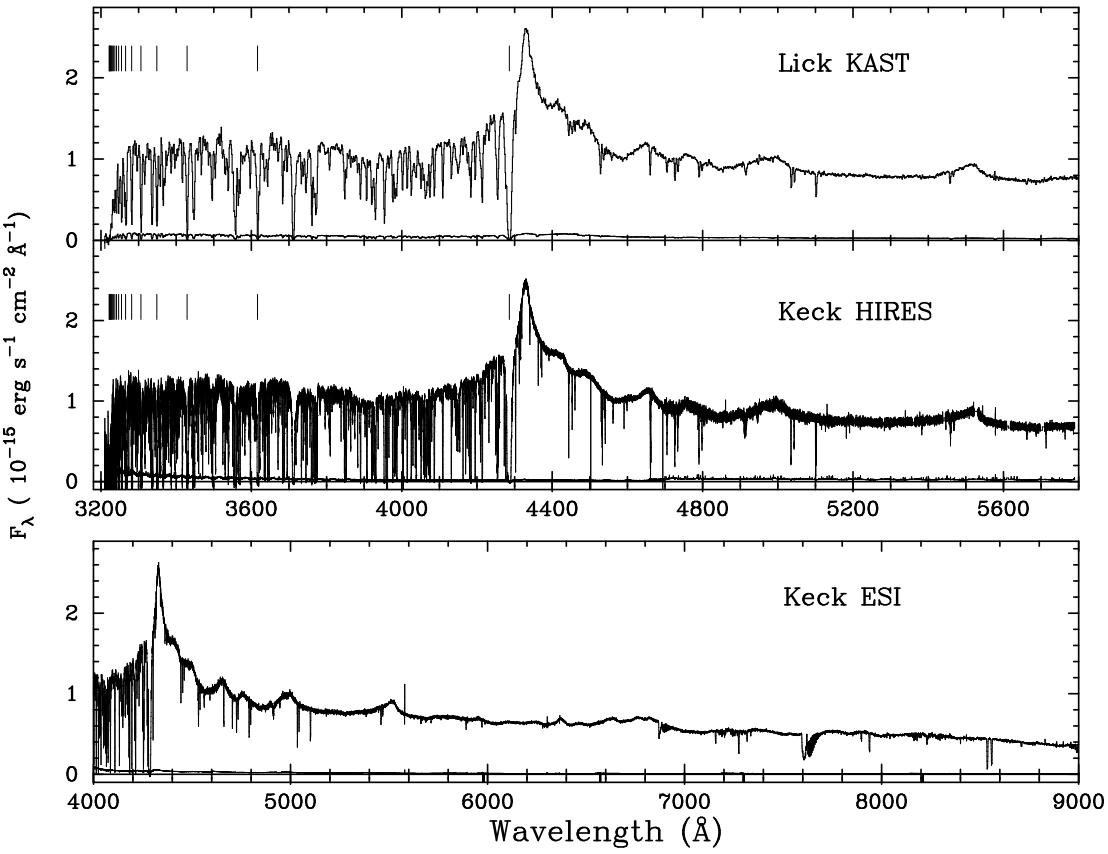

Figure 6.1: The spectra of Q1243+3047 from the KAST spectrograph (top), HIRES (middle) and ESI (bottom). We show the complete wavelength coverage for the Kast and HIRES spectra, but not for the ESI, which extends to 10,000 Å. We have applied relative flux calibration to all three spectra. The emission lines blend to give a continuously undulating continuum level from 4400 – 5000 Å. The vertical marks above the Kast and HIRES spectra show the positions of the Lyman series lines in the absorption system at 2.526 that gives the D/H value. The Lyα absorption line of this system, from which we get the H I column density, is near 4285 Å, just to the left of the peak of the Lyα emission line.

Table 6.2. Resolution and S/N OF Spectra

Spectrograph	Slit (arcsec)	Pixel Width (kms^{-1})	S/N[a] (3250Å)	S/N[a] (4250Å)	FWHM (kms^{-1})
Kast	2	105[b]	20	60	283 ± 25
ESI	1	11.5	–	40	63.2 ± 3.0
HIRES	1.14	2.1	10	90	8.0 ± 0.2

[a]S/N per pixel.

[b]Mean value. We measure variation with wavelength and from spectrum to spectrum.

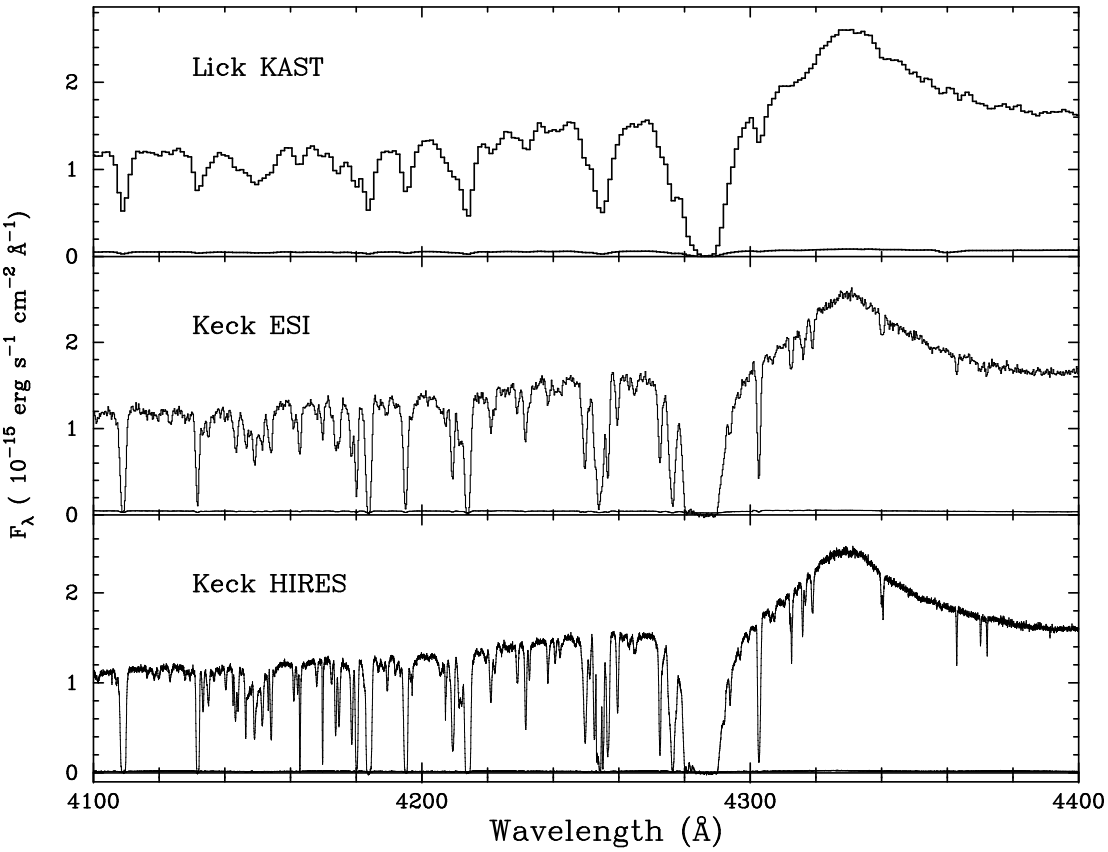

Figure 6.2: Expansion of the Kast, ESI and HIRES spectra from Figure 1. The Lyα absorption near 4285 Å is from the system in which we measure D/H.

the unsaturated metal lines, especially the O I lines, as guides.

We do not know how closely the metal lines will trace the velocity structure of the H I and D I. We expect to find some H I wherever we find metals, but the metal lines can have different velocity distributions in detail because the ionization and metal abundance can vary from component to component, and perhaps with velocity inside a component.

In Figure 6.3, we present the regions of the spectrum where we expect metal line absorption. We observe strong absorption in only a few metal ions: O I, C II, and Si II. C III and Si III also show absorption, but are poorly constrained since their lines appear saturated and may be highly contaminated by Lyα forest absorption. We see weak C IV and Si IV absorption that has very different velocity structure from the low ionization metals.

The O I absorption suggests that two components will be needed to model the velocity distribution of the gas that shows the D. O I provides the best indication of the velocity distribution of the H I and D I absorption, because O I/H I is similar to O/H in gas of low ionization (O'Meara et al., 2001). The O I 1302 transition is in a high S/N region of the spectrum well separated from other lines. In Figure 6.4 we see that this line is asymmetric, with extra absorption at larger wavelengths. We fit the O I with the two components that we list in Table 6.3.

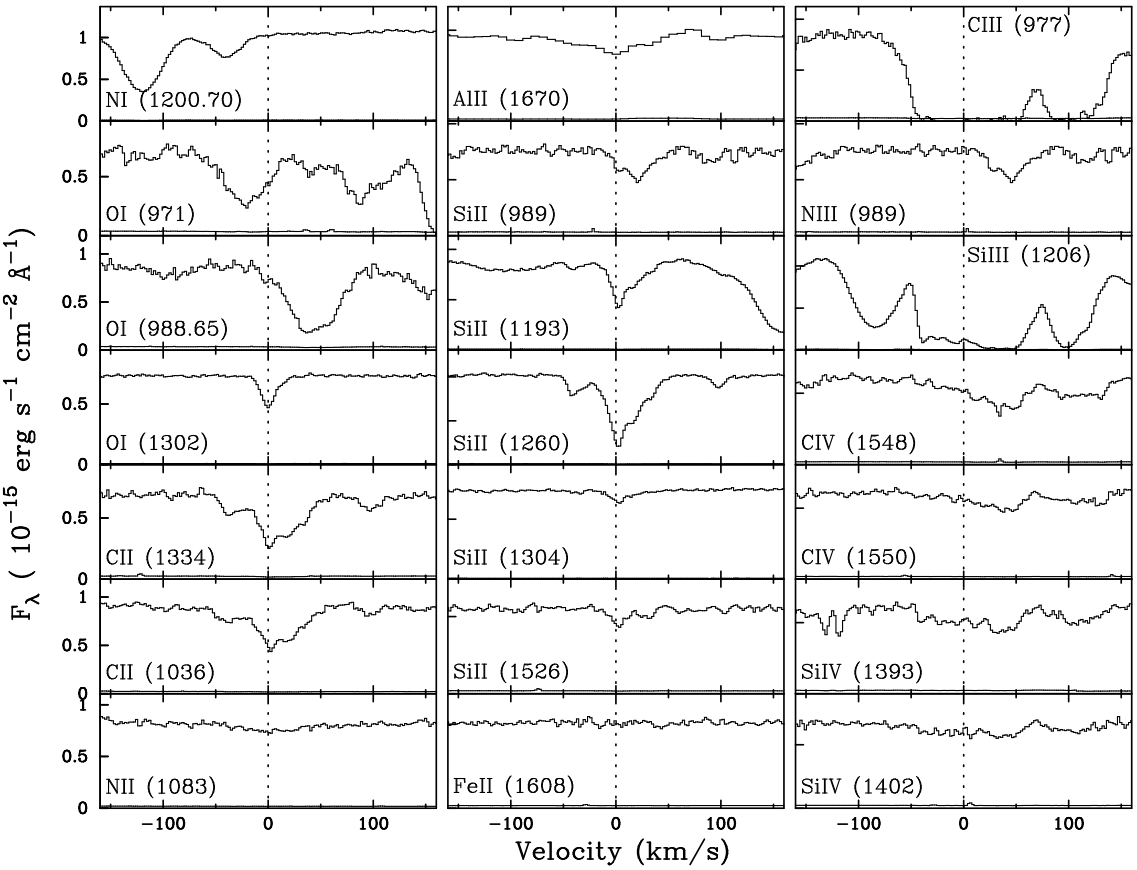

Figure 6.3: Most of the metal absorption lines near $z = 2.526$. We shifted the Al II 1670 spectrum, which is the only one from ESI, by -16.5 km s^{-1} to correct for a likely error in the ESI wavelength solution. We see three types of components, grouped by ionization; the low ionization lines represented by O I alone, intermediate ions C II, Si II and high ionization C IV and Si IV.

Table 6.3. Ions in the $z \simeq 2.526$ Absorption System towards Q1243+3047

Ion	log N (cm^{-2})	b^g (km s^{-1})	z	v (km s^{-1})
H I total[a]	19.73 ± 0.04	...	...	...
H I (H-3)	15.90 ± 0.03	17.0 ± 1.0	2.525171	-44.3 ± 7.0
H I (H-1)	19.63	14.8 ± 2.9	2.525659	-2.8
H I (H-2)	19.05	10.9 ± 3.3	2.525804	9.5
H I (H-4)	16.25 ± 0.02	25.8 ± 0.9	2.526939	106.0 ± 0.7
H I (H-5)	16.35 ± 0.02	26.6 ± 0.5	2.528108	205.4 ± 0.3
D I total	$15.113^{+0.042}_{-0.026}$	...	...	...
D I (D-1)	15.058 ± 0.03	9.2 ± 0.2	2.525659	-2.8 ± 0.6
D I (D-2)	14.191 ± 0.10	< 12	2.525804	$9.2^{+2}_{-3.5}$
O I (O-1)[b]	13.570	6.766	2.525692	0.0[c]
O I (O-2)[b]	12.755	6.766	2.525848	13.3[c]
Si II	11.884	3.44	2.525209	-41.0
Si II	11.783	5.89	2.525342	-29.8
Si II	12.020	7.85	2.525568	-10.5
Si II	11.830	3.76	2.525635	-4.8[c]
Si II	12.766	4.46	2.525728	3.1[c]
Si II	12.473	5.99	2.525885	16.4[c]
Si II	11.508	3.27	2.525984	24.8
Si II	12.120	7.41	2.526083	33.3
Si II	11.751	5.97	2.526856	99.0
C II	12.521	3.03	2.525215	-40.5
C II	12.987	11.06	2.525324	-31.2
C II	12.693	9.97	2.525552	-11.9
C II	12.956	7.58	2.525626	-5.6
C II	13.344	5.21	2.525708	1.4[c]
C II	13.260	7.17	2.525872	15.4[c]
C II	12.921	12.73	2.525959	22.8
C II	13.150	10.40	2.526076	32.7
C II	12.916	10.59	2.526834	97.1

Table 6.3—Continued

Ion	log N (cm^{-2})	b[g] (km s^{-1})	z	v (km s^{-1})
Al II[d]	< 12.2	7	...	0[c]
Si III[e]	< 13.0	7	...	0[c]
C IV[f]	< 12.75	7	...	0[c]
C II*	< 12.3	...	...	0
C IV	13.190	38.81	2.525750	4.9
C IV	13.256	20.98	2.526171	40.8
C IV	13.248	29.53	2.526985	110.0
C IV	12.514	14.11	2.528017	197.7
Si IV[f]	< 12.4	7	...	0[c]
Si IV	12.905	37.64	2.525560	−11.2
Si IV	12.730	17.21	2.526145	38.6
Si IV	12.709	24.33	2.526944	106.5
Si IV	11.920	10.71	2.527978	194.4

[a]Includes components H-1 and H-2 only.

[b]Values correspond to model where the b of O-1 and O-2 have been set to equal each other.

[c] The column density for this component was used to constrain the ionization in components 1 & 2.

[d]This ion was observed in the ESI spectrum only. The quoted upper limit on the column density is obtained when we fix $b = 7.0$ km s^{-1}, $v = 0$ km s^{-1} and fit the entire region from –60 km s^{-1} to +60 km s^{-1}.

[e] Not fit because strongly blended. We quote the maximum column near $v = 0$ for $b = 7$ km s^{-1} that is consistent with the residual flux.

[f] The upper limit comes from a fit with fixed $b = 7$ km s^{-1} and $v = 0$ km s^{-1}.

[g] The b values in this paper are all intrinsic values, since we have convolved the intrinsic line profiles by the instrumental broadening before we fit to the spectrum.

The O I might have a different velocity structure from the H I and the D I if O/H varies and is correlated with velocity. For example, we can imagine that all of the H I, D I and O I come from a single component. This component might have a Gaussian distribution of velocities. The O-1 component would be centered at +2.8 km s^{-1} in the frame of the D-1 because O/H is larger at larger velocities, and the O-2 component might arise from the O/H gradient alone. In this case we should model the H and D with a single component. We do not favor this model, because C II and Si II (shown in Figure 6.4) show components 1 & 2. However, we can fit to the H I lines with a single component, and this can have a b-value that is consistent with the D and O lines (§6.6). If we have a single component the log N_{HI} is unchanged (§6.7), while the D/H is lower because log N_{DI} tends to be lower when we loose D-2.

The C II and Si II fits are listed in Table 6.3 and shown in Figures 6.4 & 6.5. Irrespective of the exact model used, the C II and Si II require gas at $v \simeq -40$, $\simeq 0$, and $\simeq 95$ km s^{-1}, blended with additional absorption between 16 and 35 km s^{-1}.

The system shows components at $v = -40$, 0, 13, 20, 40, 95, & 200 km s^{-1}. But the D/H measurement will depend on just three.

- Component 1, near $v = 0$ km s^{-1}, is the strongest component in O I, C II, Si II and D I. We will refer to the D I absorption in this component as D-1, with column density N_{DI}(D-1) and velocity dispersion b(D-1) and similarly for the other ions. The parameters of the O-1 and D-1 components are well determined and they contain approximately 90% of the column density. We use the redshift of the O-1 component, z (O-1)= 2.5256916, to define a reference frame with radial velocity $v = 0$ km s^{-1}. In this frame, we measure the velocity of the O-1 as $v = 0.00 \pm 0.14$ km s^{-1}, where the error is from the fit alone and ignores the poorly known wavelength scale error.

- Component 2, near $v = 13$ km s^{-1}, is seen as an asymmetric extension of the O I that we call component O-2. There is also some C II and Si II near this

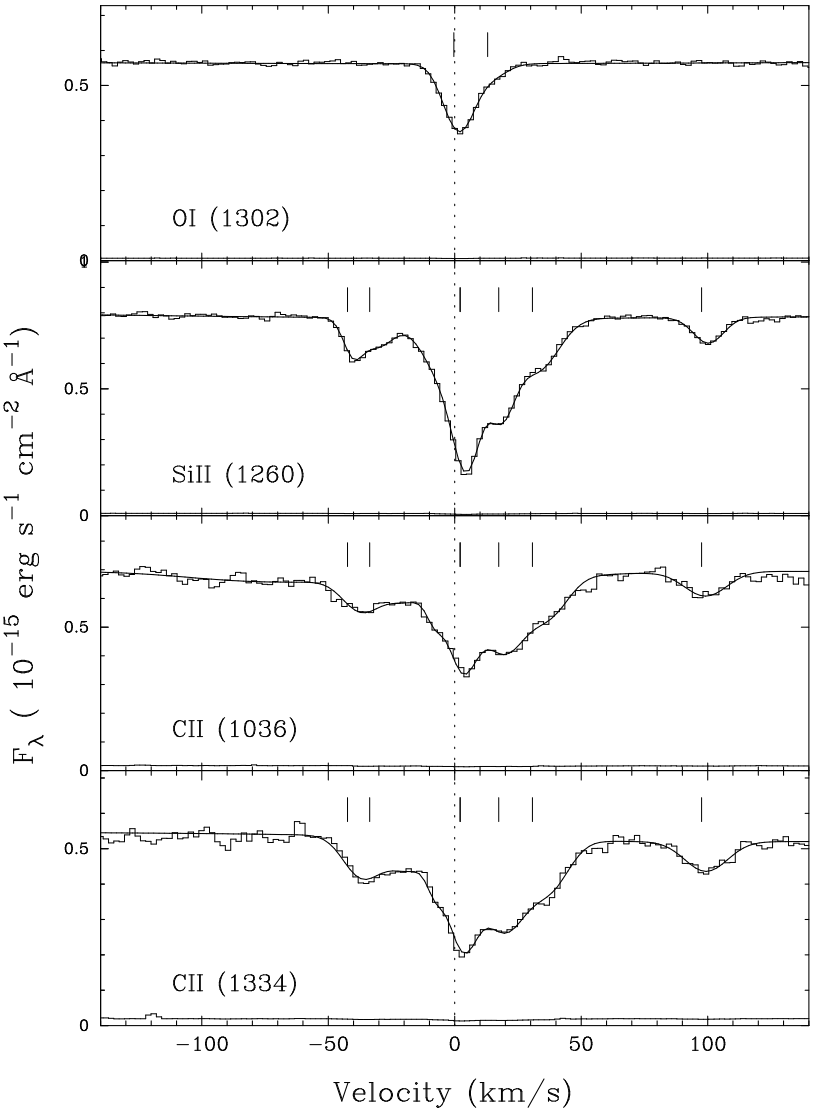

Figure 6.4: Voigt profile fits to the lines of the low ionization ions. The line parameters used to generate these profiles are given in Table 6.3. The data is our combined HIRES spectrum, with 1σ errors shown just above the zero flux level. Flux is in units of 10^{-16} erg s^{-1} cm^{-2} Å $^{-1}$. The O I absorption shows a well defined component 1 at $v = 0.0$ km s^{-1}, and additional absorption in component 2 near +13 km s^{-1}. C II and Si II show several components, including a main component near $v = 0$ km s^{-1} for C II (1334) or 3 km s^{-1} for C II (1036) and Si II, and a second component near 16 km s^{-1}. We see no absorption near –82 km s^{-1}.

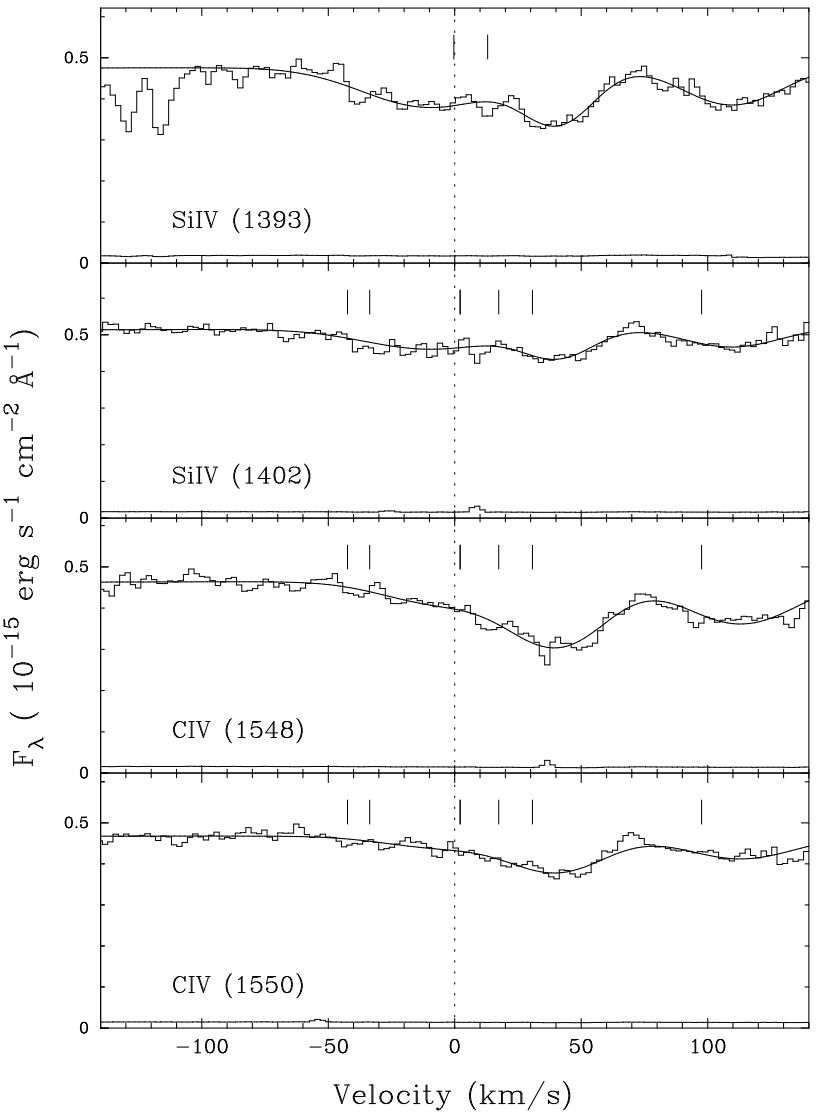

Figure 6.5: As Figure 6.4, but here we show the lines of the high ionization ions. Again, there is no evidence of metal line absorption near –82 km s^{-1}.

velocity. We call other associated lines D-2 and H-2. Neither the velocity nor the b-value of the O-2 component are well known, and they are correlated. Smaller b-values are needed as the line center moves to larger wavelengths. If we have some additional velocity or b-value information, then the second component is well determined. For example, if both O I components have the same b-value, this value is 6.77 km s^{-1}, component 2 is at 13.3 km s^{-1}, and its column density at 11% of the total.

- Component 3, near $v = -40$ km s^{-1}, is an even weaker component in C II and Si II. We will refer to the H I absorption from this component as H-3, which is at $v(H-3) = -44.3 \pm 7.0$ km s^{-1}, with log N$_{\rm HI}(3) = 15.90 \pm 0.03$ cm^{-2} from the higher order Lyman lines. This log N$_{\rm HI}$ value is low enough that we would not expect to see O I or D I and neither is seen. H-3 effects D/H because the short wavelength side of the Lyman lines from H-3 accidentally blend with the long wavelength side of the D-2 lines, and hence some of the absorption near –70 km s^{-1} can be explained by either H-3 or D-2.

There is a large amount of H I absorption, log N$_{\rm HI} \simeq$ 19.7 cm^{-2}, near components 1 and 2, but we have little information on the velocity distribution of this H I. In Figure 6.7 we show the Lyman series lines. The spectra require H I Lyman lines corresponding to the metal line components near $v = -40$, 0, 95 and 200 km s^{-1}. The spectra are also consistent with, but do not need, components at 13, 20 and 40km s^{-1}. The parameters that we find for these components are in Table 6.3. If there is H I absorption at 40 km s^{-1} with $b > 10$ km s^{-1}, the blue edge of the higher order Lyman lines show that it has log N$_{\rm HI} < 16.4$ cm^{-2}. Figure 6.7 shows there is no flux in the range -40 to 40 km s^{-1} in lines up to Ly-14, and in higher order lines the S/N is rather low, and the Lyman lines start to overlap. We can measure the shape and width of the higher order lines, but unfortunately this tells us little about the gas at $v = 0 - 13.3$ km s^{-1}. The absorption on the negative velocity side of these lines is determined by the H I at –40 km s^{-1} with

log $N_{HI} \sim 16$ cm^{-2}, and the positive velocity side of these lines may be influenced by log $N_{HI} \sim 16$ cm^{-2} absorption at 40 km s^{-1}.

A single component at $v = 0$ km s^{-1} with a $b \simeq 17.7$ km s^{-1} gives a fair fit to all of the H lines without separate lines at ± 40 km s^{-1} . This b-value is an upper limit on the b-value for the H I in component 1, since we must use a lower b-value when we include separate lines at ± 40 km s^{-1} . We will see below that we can also obtain an excellent fit to the H lines using components H-1 and H-2.

6.5 Measurement of the D column density

Most of the information on the D is in transitions Ly-3 to 8, which we show in Figure 6.6. In each transition we see absorption that has all the expected characteristics of component D-1 associated with H-1 and O-1. In Ly-4 to 8 we see an apparently resolved D line that is well separated from the H absorption, while in Ly-2 and 3 the D absorption is fully blended with the H lines, as we expected because the H line is wider.

Two of the D-1 lines are contaminated by other lines. The Ly-5 D line contains a second narrow Ly-3 line at $z = 2.3987515$ that has log N_{HI} 14.459 cm^{-2} and $b = 28.81$ km s^{-1}. This contaminant is well determined by its other Ly lines and we fit it when we fit the Ly-5 D line. The D Ly-3 line includes a slight contribution from a Lyβ line with $z = 2.342177$, $b = 35.6$ km s^{-1} and log $N_{HI} = 13.81$ cm^{-2}.

6.6 The Absorption near the D-1 Position is mostly D

Several lines of argument imply that the absorption that we identify as D-1 is mostly D. The evidence is convincing, but not as strong as for some other QSOs. Ideally, we would compare the velocity structures of the D I and H I lines, which would be identical if we have correctly identified the transitions and there is minimal contamination. This comparison is not possible for Q1243+3047 because the velocity structure of the H I is not observed, and hence we are less certain that

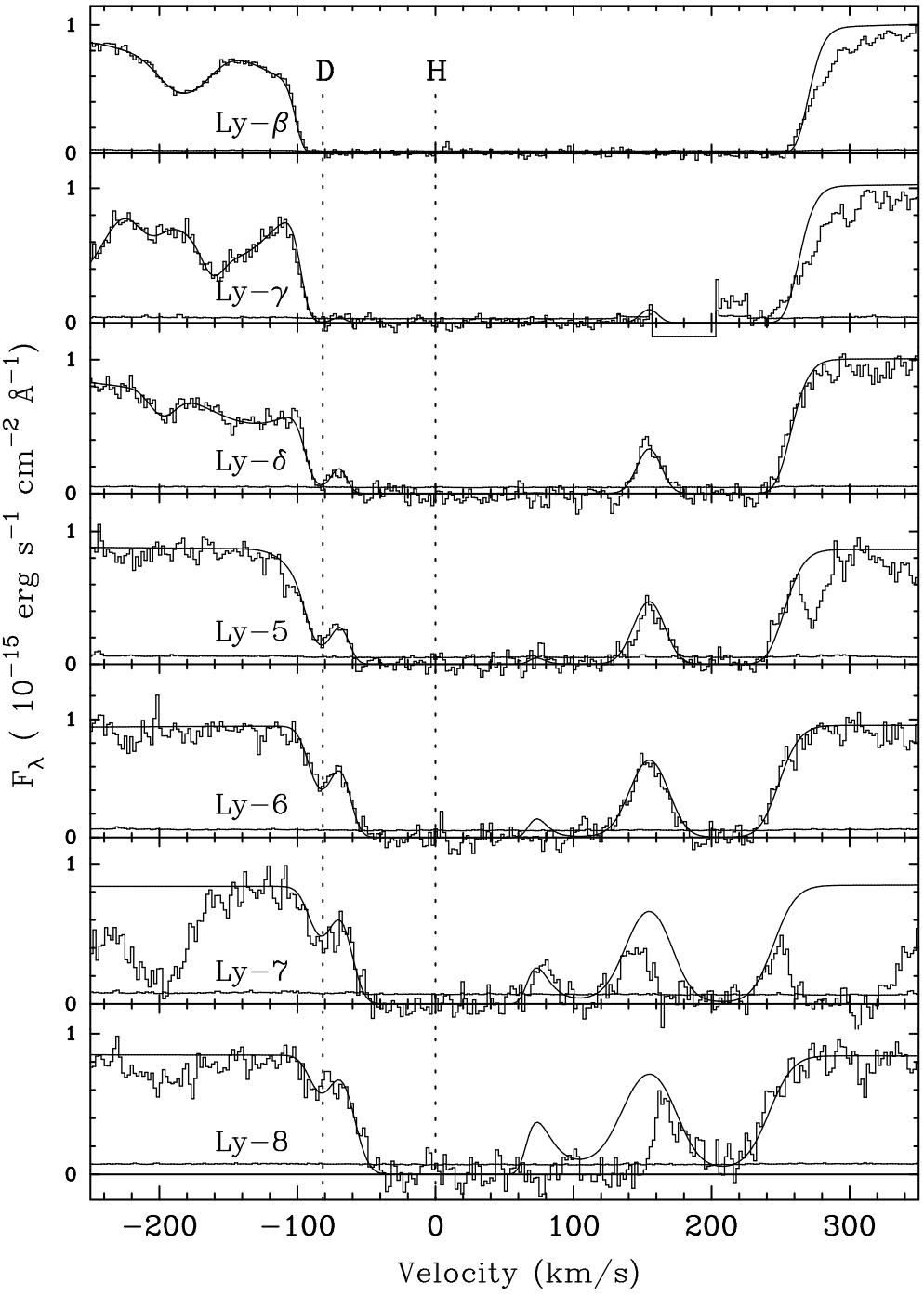

Figure 6.6: The HIRES spectrum of Lyβ to Ly8, together with our model of the system, as given in Table 6.3.

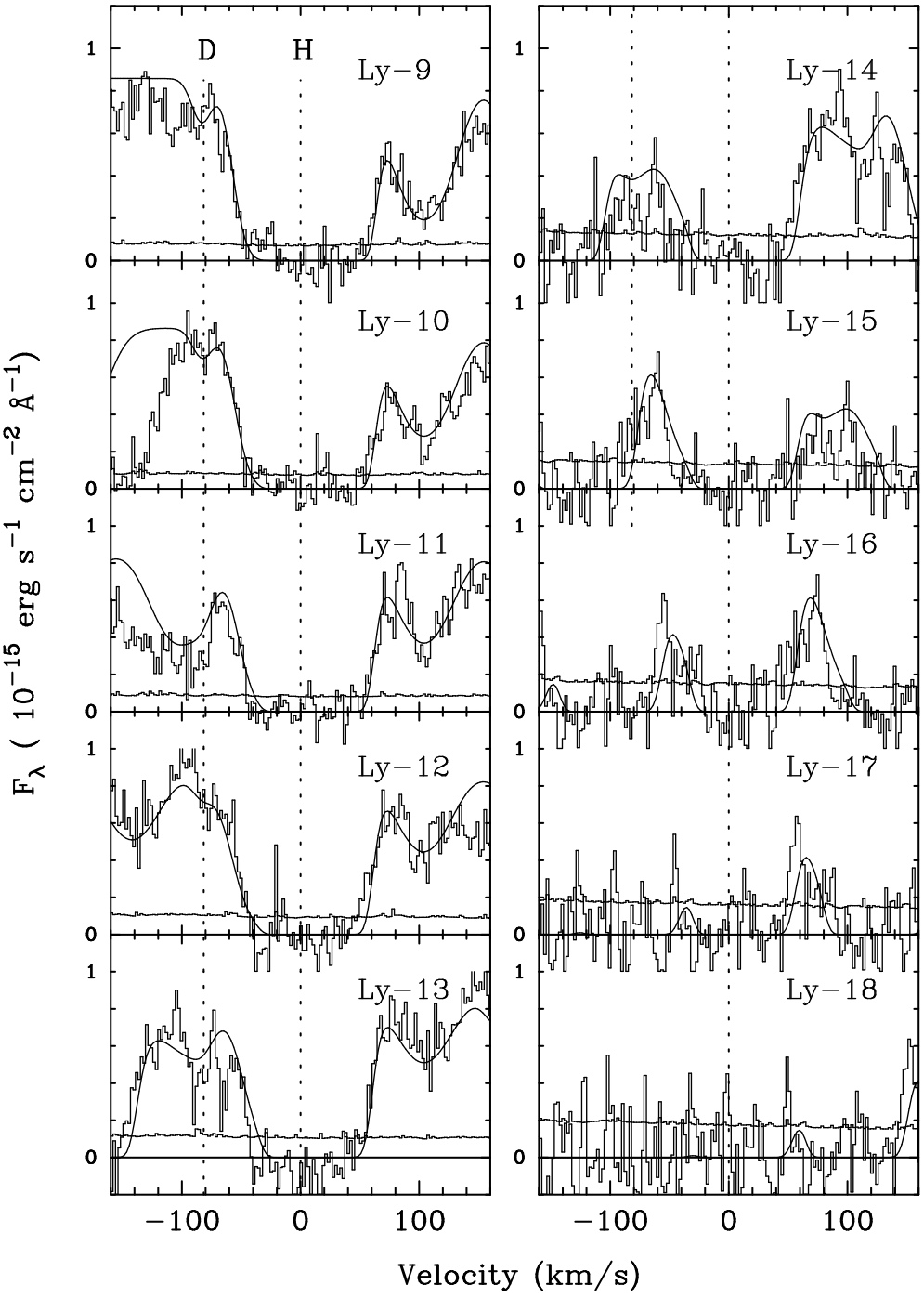

Figure 6.7: Same as Figure 6.6 but the HIRES spectrum of Ly-9 to 18.

we have seen D than we were in other QSOs. The only reasonable identifications for D-1 are D and H, because D-1 shows a Lyman series. If the D-1 absorption is H, b(D-1) implies a low temperature of < 5130 K. There are no metals at the redshift of H at the position of D-1, but this is not significant, since metals would not be seen if their abundances were low.

There are three main reasons why D-1 is D: its velocity, line width, and column density are all close to the values that we expect. In the frame of the main component of the O-1, D-1 is at -2.8 ± 0.6 km s^{-1}, where the error is from the line fit alone. This is close enough to show that D-1 is mostly D, since the D-1 and O-1 lines overlap in velocity.

The observed width of the D-1 component agrees with the prediction from the widths of the O-1 and H-1 components, given in Table 6.3, and shown in Fig. 6.8. Following O'Meara *et al.* (2001), the intrinsic b value of the lines, b_{int} is given by $b_{int}^2 = b_{temp}^2 + b_{turb}^2$, where the temperature term is $b_{temp}^2 = 2kT/m = 166.41(\mathrm{km\ s^{-1}})^2(T/10^4\ K)/\mathrm{mass\ (amu)}$, where T is the gas temperature and b_{turb} represents the bulk turbulent motions, and m is the mass in atomic mass units. This agreement suggests that D-1 is D and not H. We note, however, that both the b(H-1) value and its error are poorly constrained

When we accept that the D-1 component is D, we can use D-1 together with the H-1 and O-1 to improve our estimates of the gas properties. We find $T = 0.55 \pm 0.04 \times 10^4$ K, which is low but reasonable for the large log $\mathrm{N_{HI}}$, and $b_{turb} = 6.3 \pm 0.2$ km s^{-1}. The data are also fully consistent with this fit, which we show as the dashed line in Fig. 6.8. Compared to this line, the measurements give $\chi^2 = 1.38$ for one degree of freedom, where $\mathrm{Prob}(\chi_1^2 > 1.38) = 0.24$.

We suspect that D-2 is D for three reasons. First, the absorption that we fit with D-2 is very narrow, narrower than typical H I lines. Second, the separation of D-2 from D-1, 12 km s^{-1}, with a 1σ range of 8.5 – 14 km s^{-1}, matches the separation of the O I components, that is $\simeq 13.3$ km s^{-1}. In the grid search we examined D separations from 4 – 20 km s^{-1}, and the D separation could have been different

from that of the O I. This argument is weak, because while the velocity separation between components is the same, the D-1 and O-1 have slightly different zero point velocities. Third, the fraction of the D in D-2 ($0.12^{+0.16}_{-0.05}$) matches the fraction of O in O-2, 0.13, when we force b(O-1) = b(O-2).

6.7 Measurement of the H column density

Most information on the N_{HI} comes from the shape of the damped Lyα line at 4285 Å that shows damping wings. Compared to the methods we used to get log N_{DI}, for the log N_{HI} we use different ways to fit the continuum and Lyα forest, to explore the parameter values and to assign an error to log N_{HI} since the main error comes from the continuum fitting, not from the velocity structure of the system.

We can quickly establish that the DLA has log $N_{HI} \simeq 19.7$ cm^{-2}. First we note that the clear presence of O I absorption at $v = 0$ (Figure 6.4) indicates log $N_{HI} > 19$ cm^{-2}. If we fit the HIRES spectrum by a Lyα line with a lower column density, there remains unexplained absorption which looks like damping wings. This is very clear when log $N_{HI} \leq 19.5$ cm^{-2}, and can still be seen at larger log N_{HI}. On the other hand, when we fit with log N_{HI}= 19.8 cm^{-2} we absorb flux which is seen, which is un-physical. To allow this extra absorption, the QSO continuum, including any emission line flux, would have to bend upward on either side of the damped line, near 4288 Å and 4293 Å, which is best seen when we divide the spectrum by the line profile. We then know that $19.5 <$ log N_{HI} cm^{-2} < 19.8, where the larger limit is twice the smaller, a range that is 20 times the 1σ range on the log N_{DI} (total).

6.7.1 The Best Estimate for log N_{HI} and its Error

The observed profile of the Lyα line is a function of the continuum fitting, b-value, and the column density that we wish to know. Kirkman et al. (2003) performed a grid parameter search to find the model that best explains the observed spectrum. We fit the continuum, Lyα and D I lines, and the associated Lyα forest

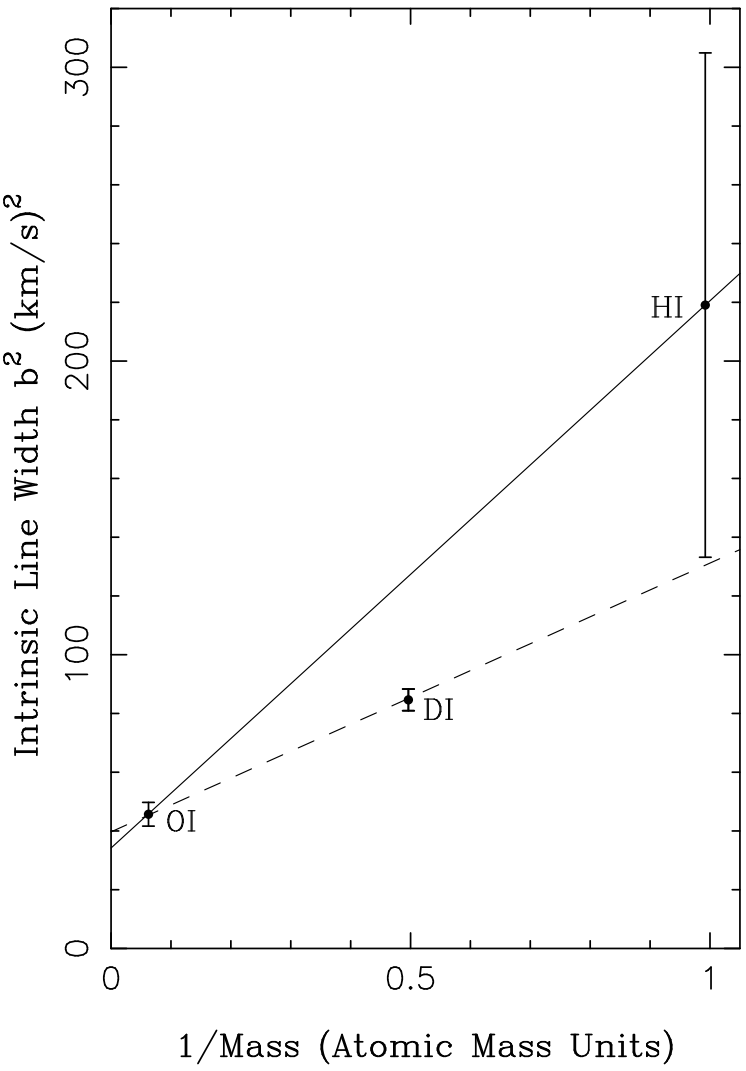

Figure 6.8: Square of the intrinsic width of the lines of ions as a function of 1/mass of the ion in atomic mass units. We plot the b_{int}^2 for the main components of the O I, D I and H I (components O-1, D-1 and H-1). The solid line connects the O I and H I points and ignores the D I. The slope of this line gives a temperature $T = 1.1 \pm 0.6 \times 10^4$ K and the intercept gives the turbulent velocity of $b_{turb} = 5.8 \pm 0.6$ km s^{-1}. The line predicts $b(D-1) = 11.3 \pm 1.8$ km s^{-1}. The observed $b(D-1) = 9.2 \pm 0.2$ km s^{-1} is 1.2σ below, and consistent with this prediction. The dashed line is the best fit to O, H and D. The data are also consistent with this fit, which we prefer. Although the b-value of the H-1 component is not well known, the data shown on this plot provide evidence that D-1 is D rather than H.

lines simultaneously and optimized model parameters to minimize χ^2. To avoid finding local minima, we varied the initial conditions as well. The errors are estimated by knowing the range of the minimum ${\chi^2}_{min}$ and ${\chi^2}_{min} + 1$.

Our best estimate for the column of the H I in components 1 and 2, that is associated with log N_{DI} in the same components, is then

$$\log N_{HI}(total) = 19.73 \pm 0.04 \text{ cm}^{-2}, \tag{6.1}$$

which is a 1σ error of 9%, similar to the error on the log N_{DI}.

6.8 Best Fit Values For Q1243+3047

We have made the following estimates for the parameters that describe the gas in which we measure D/H:

- The velocity structure of the gas has two main components that we see in the asymmetry of the O I line.
- Our grid search of models that fit the D lines showed that the components are separated by 12 km s^{-1}, with a 1σ range of 8.5 – 14 km s^{-1}, consistent with the asymmetry of the O I line.
- The main D component, D-1, is at $z = 2.525659$ and has $b = 9.2 \pm 0.2$ km s^{-1}.
- The wavelength, b-value and column density show that D-1 is D absorption. We believe that the D-2 component is D because it is very narrow, the separation of the D-1 and D-2 components is the same as that of the O-1 and O-2 components, and the fraction of the D in D-1 is similar to the fraction of the O in O-1 (§6.6). However, these arguments are weak because D-2 is not well defined.
- The grid search also indicated that component D-2, at the larger redshift, contains 12% of the total D column density, with a range of 7% to 28% depending

on how much of the absorption near component 2 is H in another component, H-3.

- Total log N_{DI}= $15.113^{+0.042}_{-0.026}$ cm^{-2}, (i.e. +10%, −6%) where the error range includes fits with $\chi^2 < \chi^2_{min} + 1$. The errors are larger for higher values of log N_{DI} because of the second component can make a significant contribution.

- Total log N_{HI}= 19.73 ± 0.04 cm^{-2} (9%), where the error is a Gaussian distribution centered on the log N_{HI} value that consistently gave the best fits. We set the width of the Gaussian to give an 80% chance that the true log N_{HI} lies in the range 19.68 – 19.78 cm^{-2} where we found acceptable fits to the Lyα line, the continuum and Lyα forest.

- log (D/H) = $-4.617^{+0.058}_{-0.048}$ (+14%, –10%).

- D/H = $2.42^{+0.35}_{-0.25} \times 10^{-5}$ cm^{-2}.

- [O/H] = -2.79 ± 0.05.

- The absorber is probably mostly ionized, with of order 21% of H atoms neutral

.

6.9 Acknowledgment

This Chapter 6, in part, is a reprint of the material as it appears in *Astrophysical Journal Supplement*, volume 149, page 1, 2003. The dissertation author did some of the observations, the bulk of data reduction and calibration and the third author of this paper.

Chapter 7

The Primordial Deuterium Abundance and the Baryon Density

7.1 Introduction

In this chapter I compare D/H measurements from other QSOs, and discuss the best estimates of the primordial D/H ratio. Once again, this work is a team effort but I was in charge of the study of chemical evolution and investigated the D/H evolution with metals. I was advised by Dr. Marti on this subject.

I compiled the measurements of other light elements – ^{4}He, ^{3}He and ^{7}Li – from the literature and discuss if we have a concordance model in the framework of the Standard Big Bang Nucleosynthesis.

I also compiled the measurements of baryon density from the observations of Cosmic Microwave Background (CMB). They use completely different method, physics and probe different epoch of the cosmic time. We compare our measurements with CMB observations.

7.2 The Primordial D/H Ratio

In this section we compare D/H measurements from different QSOs, we discuss the dispersion in these values, and whether D/H might correlate with metal abundance or N_{HI}, and we give our estimate for the primordial D/H value.

7.2.1 The Weighted Mean D/H from Five QSOs and the Dispersion of the Values

We find the weighted mean of the D/H values from five QSOs and we show that the individual values show more dispersion than we expect. In Tables 7.1 & 7.2 we list all reported D/H measurements that remain viable. We have previously measured D/H in three QSOs (Tytler et al., 1996; Tytler & Burles, 1997; Burles & Tytler, 1998a,b; O'Meara et al., 2001), and placed a strong upper limit on D/H in a fourth (Kirkman et al., 2000). We will also use the D/H measurement by Pettini & Bowen (2001) towards Q2206–199, although this measurement is less secure because the HST spectra are of much lower S/N and resolution than those from the ground.

The weighted mean of the first five log D/H values from Table 7.2 is

$$log\ D/H = -4.556 \tag{7.1}$$

where the weights we use are the 1σ errors on the quantity $Y_i = log(D/H)_i$. We use log values because they were used to find all but one of the individual D/H values and errors. We obtain a slightly smaller mean D/H if we instead work with the linear D/H values.

The D/H measurements towards the five QSOs are more dispersed than we expect. In O'Meara *et al.* (2001) we noted that the dispersion in the first three measurements was larger than expected, with a 3% chance of a larger χ^2 value. We interpreted this to mean that we had underestimated one or more of those errors. With the addition Q1243+3047 the dispersion of log D/H remains approximately 0.10, but adding the low D/H from Q2206–199 increased the dispersion to 0.14, the

χ^2 value for all five measurements increases to 12.35 for 4 degrees of freedom, and the probability that we would have obtained a larger χ^2 value by chance drops to 1.5%.

Table 7.1. D/H Measurements towards QSOs

QSO	z_{DH}	D/H $\pm1\sigma$ ($\times10^{-5}$)	logD/H	X_i[a]	b(D) (km s^{-1}) predicted	observed
PKS 1937–1009[b]	3.572	3.25 ± 0.3	-4.49 ± 0.04	+1.65	12.5 ± 2.1[c]	14.0 ± 1.0
Q1009+299[d]	2.504	$3.98^{+0.59}_{-0.67}$	$-4.40^{+0.06}_{-0.08}$	+1.95	13.5 ± 0.5[c]	15.7 ± 2.1
HS 0105+1619	2.536	2.54 ± 0.23	-4.596 ± 0.040	−1.00	10.1 ± 0.3[c]	9.85 ± 0.42
Q1243+3047	2.525675	$2.42^{+0.35}_{-0.25}$	$-4.617^{+0.058}_{-0.048}$	−1.05	11.3 ± 1.8	9.2 ± 0.2
Q2206–199[e]	2.0762	1.65 ± 0.35[f]	$-4.78^{+0.08}_{-0.10}$	−2.80	10.6	–
Q0347–3819[g]	3.024855	3.75 ± 0.25[f]	-4.43 ± 0.03	+4.20	3,14.1,16.2	–
Q0130–403[j]	2.799	< 6.8	< -4.17	–	16.2 ± 0.3[c]	–

[a] $X_i = (Y_i - mean)/\sigma(Y_i)$, where $Y_i = log(D/H)_i$ and we use the weighted mean of the first five QSOs, log D/H = -4.556 ± 0.064.

[b] We list combined results for the two components, from Tytler, Fan & Burles (1996); Burles & Tytler (1998a).

[c] Calculated from the published data and first presented here.

[d] We list combined results for the two components, from Tytler & Burles (1997) and Burles & Tytler (1998b).

[e]Pettini & Bowen 2001.

[f]Discussed in the appendix of Kirkman *et al.* 2003.

[g]First analyzed by D'Odorico *et al.* 2001. We quote results from Levshakov *et al.* 2002.

[j]From Kirkman *et al.* 2000.

Table 7.2. Column Densities and Metal Abundances where D/H is measured

QSO	log N_{HI} (cm^{-2})	Element α	Abundance $[\alpha/H]$
PKS 1937–1009[a]	17.86 ± 0.02	Si	$-2.7, -1.9$
Q1009+299[b]	17.39 ± 0.06	Si	$-2.4, -2.7$
HS 0105+1619	19.422 ± 0.009	O[c]	-1.73
Q1243+3047	19.73 ± 0.04	O[c]	-2.79 ± 0.05
Q2206–199[d]	20.436 ± 0.008	Si	-2.23[e]
Q0347–3819[f]	20.626 ± 0.005	Si	-1
Q0130–403[g]	16.66 ± 0.02	Si	-2.6

[a] We list the parameters for each of the two components, where available, from Tytler, Fan & Burles (1996); Burles & Tytler (1998a).

[b] We list the parameters for each of the two components, where available, from Tytler & Burles (1997) and Burles & Tytler (1998b).

[c]Using log O/H = −3.31 from Allende Prieto, Lambert & Asplund (2001).

[d]Pettini & Bowen 2001.

[e]Prochaska & Wolfe 1997.

[f]Levshakov *et al.* 2002.

[g]Kirkman *et al.* 1999.

Figure 7.1: Measurements of D/H as a function of the Silicon or Oxygen abundance in the gas. The solid circles are from our group, Q2206–199 is from Pettini & Bowen (2001) and the diamond is the local interstellar medium (LISM) measurement (Oliveira *et al.* 2003). The error bars are intended to be 1σ but we suspect that in some cases they have been underestimated. The curves show a closed box model for the expected D/H evolution. The solid curve is normalized to the primordial D/H from five QSOs while the dotted curve uses the D/H value in the LISM. The orange colored horizontal band is our best D/H measurement from five QSOs, and the purple horizontal band is from the measurement from the first year WMAP CMB observation.

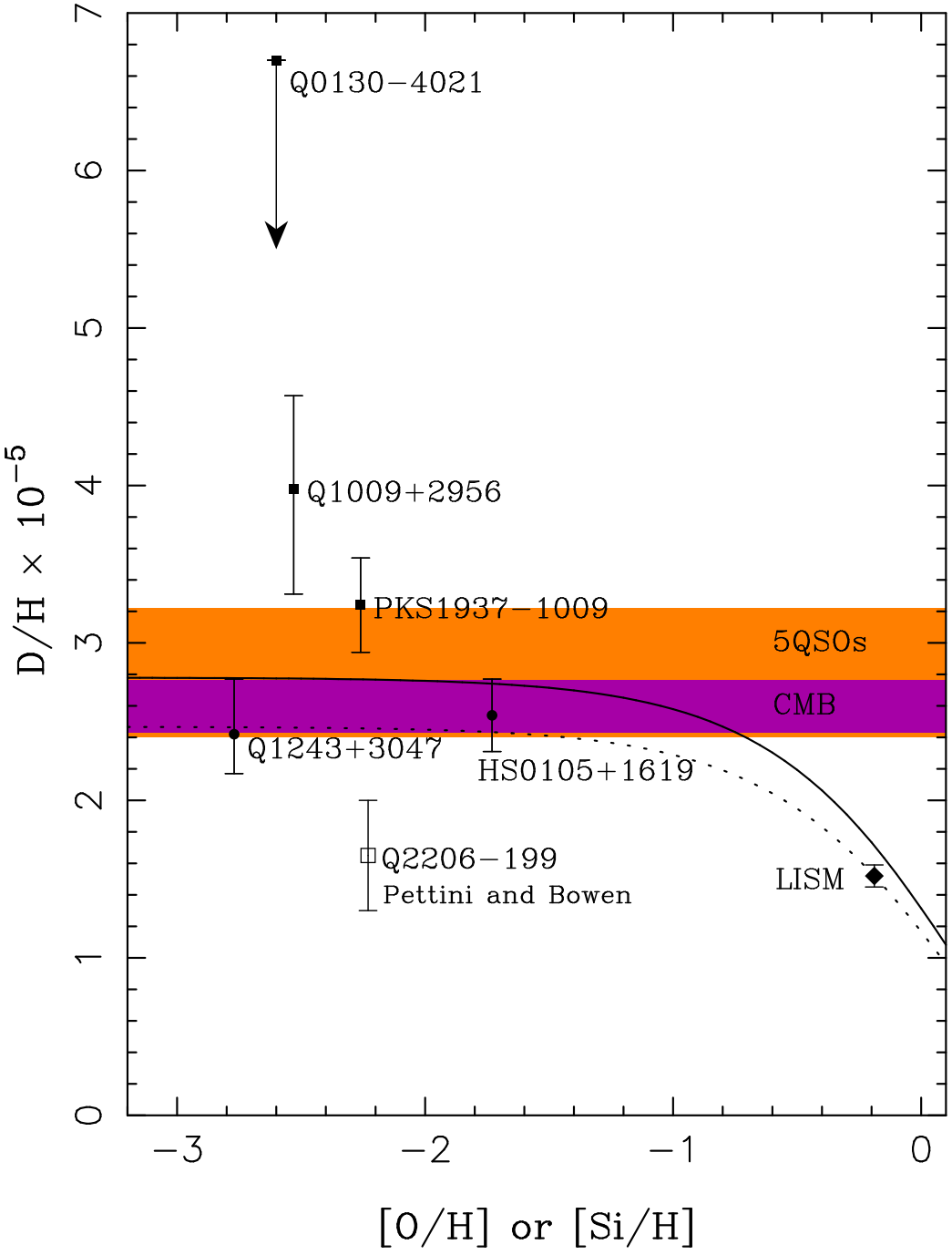
Q0130−4021
Q1009+2956
PKS1937−1009
5QSOs
CMB
Q1243+3047
HS0105+1619
Q2206−199
Pettini and Bowen
LISM
D/H × 10^−5
[O/H] or [Si/H]
0
1
2
3
4
5
6
7
−3
−2
−1
0

7.2.2 The Dispersion in the D/H Values May Come from Measurement Errors

We suspect that the dispersion in the D/H values arises from measurement errors and is not real. If the measurement errors have been underestimated for at least one QSO, then we can explain the excess χ^2 value.

The dispersion of the D/H values is not much larger than we expect. In Table 7.1 we list $X_i = (Y_i - \mathrm{mean})/\sigma(\mathrm{Y_i})$, the deviation of each measurement from the weighted mean, in units of the individual measurement errors. The D/H from Q1009+2956 is 1.95σ above the weighted mean, while the D/H from Q2206–199 is 2.8σ below. A $\chi^2 < 9.5$ would have been expected if all five log D/H values were consistent with the weighted mean, since $\mathrm{Prob}(\chi^2_4 > 9.5) = 0.05$. We would obtain $\chi^2 < 9.5$ if either Q1009+2956 or Q2206–199 were within 1σ of the mean, or if the measurement errors on all five QSOs were increased by 1.14, both small changes. However, to obtain a typical $\chi^2 = 3.36$, where $\mathrm{Prob}(\chi^2_4 > 3.36) = 0.5$, 3 or more D/H values, or their errors, would need to change, or the measurement errors on all five QSOs would need to increase by a factor of 1.92. These are a large, but still credible changes.

7.2.3 How D/H Depend on Metal Abundance: D/H Chemical Evolution

The mean D/H from QSOs is similar to the primordial D/H value that we would predict from the D/H and metal abundance in the local interstellar medium (LISM) using standard Galactic chemical evolution. However, chemical evolution can not account for the dispersion in the D/H values from QSOs.

With the two latest D/H measurements, there is no longer a hint of a correlation between D/H and metal abundance in the QSO absorbers that we noted in O'Meara *et al.* (2001). Prantzos & Ishimaru (2001) showed that standard chemical evolution could not reproduce the correlation, while Fields et al. (2001) discussed an unconventional scenario that could. In Fig. 7.1 we show D/H values against metal

abundance.

With the elimination of the correlation, Galactic chemical evolution more clearly supports the idea that our D/H measurement towards Q1243+3047, and the mean D/H from five QSOs are very close to the primordial D/H value. We include two curves in Fig. 7.1 that show the expected decrease of D/H against metal abundance in a simple closed box model, without in-fall, and with the instantaneous recycling approximation (Tinsley, 1974, 1980; Ostriker & Tinsley, 1975). We normalized the two curves in different ways. The solid curve uses the mean D/H from Eqn. 7.1 as the primordial D/H and predicts D/H as a function of metal abundances, including that in the LISM. The dotted curve is normalized to give the D/H abundance in the LISM (Moos et al., 2002; Oliveira et al., 2003) and it then predicts the primordial D/H abundance, $(\mathrm{D/H})_p$. To draw these curves, we use the equation

$$\mathrm{D/H} = (\mathrm{D/H})_\mathrm{p} \times \exp\left(-\frac{Z}{y}\frac{R}{1-R}\right), \tag{7.2}$$

and the values for two parameters from Prantzos & Ishimaru(2001); the returned mass fraction $R = 0.31$, and the yield $y = 0.6$, where Z is the metallicity, or metal abundance in solar units, on a linear scale. The choice of parameters and D/H chemical evolution are discussed in Steigman & Tosi (1992), Vangioni-Flam et al. (1994), Galli et al. (1995), Prantzos (1996) and Prantzos & Silk (1998).

Both curves connect the D/H values towards Q1243+3047 and HS 0105+1619 to the D/H in the LISM, over three orders of magnitudes in metallicity. The curves show that the decline in D/H, as stars eject gas that lacks D, is insignificant when metal abundances are low; e.g. $[\mathrm{O/H}] < -1$. The simple closed box model (Eqn. 7.2) predicts that by the metal abundance of Q1243+3047, $(\mathrm{D/H}) = 0.9987(\mathrm{D/H})_\mathrm{p}$, and for HS 0105+1619, 0.986. We have not applied these corrections because they are much smaller than our measurement errors.

We predict the primordial D/H when we normalize the simple model to give the D/H in the LISM. Ostriker & Tinsley (1975) predicted the primordial D/H would be 1.5 – 2 times that in the LISM. With the modern parameters given above,

the same model predicts 1.62 times, again without using any D/H measurements. Using the D/H and Z measurements in the LISM from FUSE and HST spectra, $\mathrm{D/H_{LISM}} = 1.52 \pm 0.07 \times 10^{-5}$, and [O/H] = −0.189 or $Z = 0.647$ (Oliveira *et al.* 2002, and using the solar $\log \mathrm{O/H} = -3.310$ from Allende Prieto, Lambert & Asplund 2001), the predicted primordial abundance is $(\mathrm{D/H})_p = 2.47 \pm 0.13 \times 10^{-5}$, very similar to the value from Q1243+3047 and from Eqn. 7.1: 2.78×10^{-5}. The errors on the prediction are substantial. When we allow the two parameters to simultaneously take values that maximize the change in D/H, from $0.26 < \mathrm{R} < 0.36$ and $0.5 Z_\odot <$ yield $< 0.9 Z_\odot$ (Prantzos, private communication), we find $(\mathrm{D/H})_p$ = 1.94 – 3.16×10^{-5}. The range is further increased when we consider in-fall of gas to the Galactic disk (Lubowich et al., 2000) and dispersion of D/H in the LISM (Vidal-Madjar et al., 1998; Sonneborn et al., 2000). Hence, although the D/H values from both Q1243+3047 and HS 0105+1619 are closest to the predicted D/H, we can not use the chemical evolution model to rule out primordial D/H values that are suggested by the measurement to the other QSOs.

7.2.4 Does D/H Depend on $\mathrm{N_{HI}}$?

The D/H values appear to decline with increasing $\log \mathrm{N_{HI}}$, as shown in Figure 7.2. This trend was apparent with just the three D/H values discussed by O'Meara *et al.* (2001) and it was accentuated by Q2206-199 from Pettini & Bowen (2001). The trend rests upon the relatively high D/H for the two LLS (PKS 1937–1009 and Q1009+2956), and the relatively low D/H for Q2206–199 and Q1243+3047 that we will call DLAs. We do not believe that this correlation is real, because we suspect that the dispersion in the D/H values is not real (§7.2.2).

We are not aware of any systematic error in the measurements of PKS 1937–1009, Q1009+2956, HS 0105+1619 and Q1243+3047 that could readily account for all of the trend with $\mathrm{N_{HI}}$. Rather, we expect that potential errors are complex, and specific to each spectrum.

We note that D/H measurements in LLS may have different systematic

errors than measurements of D/H in DLAs. However, we have no evidence that LLS and DLAs actually do suffer from different kinds of systematic errors.

If D/H were correlated with log N_{HI}, the correlation in Fig. 7.2 suggests that the D/H ratio has a range of approximately a factor of 2.4. The explanation might involve inhomogeneous BBN, or the creation, removal or destruction of D. No plausible mechanisms are known.

Inhomogeneous BBN scenarios (e.g. Kainulainen, Kurki-Suonio, & Sihvola 1999) run into trouble because the inhomogeneity needs to be > 100 kpc in order to avoid mixing before the time of observation (Mike Norman, private communication). The scale is also limited to < 1 Mpc by the near isotropy of the CMB (Jedamzik & Fuller, 1997; Copi et al., 1998; Jedamzik, 2002). There are alternative schemes which produce inhomogeneities on scales of 100 – 1000 Mpc (Dolgov & Pagel, 1999; Kurki-Suonio, 2000; Whitmire & Scherrer, 2000; Dolgov, 2002) that rely on inhomogeneities of the different neutrino flavors that add up to leave the CMB unchanged.

Fields et al. (2001) discuss a highly unconventional chemical evolution models and find three constraints on the conditions required to destroy significant D while keeping metal abundances very low. Most observed baryons must have been inside an early generation of stars, the early stars must all have had intermediate initial masses in the range $2 - 8 M_{\odot}$, and they must not have ejected much C or N.

Other astrophysical explanations seem equally unlikely (Epstein et al., 1976; Jedamzik & Fuller, 1997; Fuller & Shi, 1997; Famiano et al., 2002; Pruet et al., 2002; Jedamzik, 2002). We can not hide significant D in dust or molecules because neither are abundant enough in typical absorption systems. We would require $> 10\%$ of all the gas to be molecular if $HD/H_2 \simeq 10^{-4}$, or a large proportion of all heavy elements to be in dust, neither of which are likely, except in molecular clouds.

Table 7.3. Inferred Physical Conditions where D/H is measured

.

QSO	$\log H\ I/H$	$\log H$ (cm^{-2})	Size (kpc)	Hydrogen Gas Mass ($M_\odot$)
PKS 1937–1009[a,b]	$-2.35, -2.29$	20.05,19.74	0.9, 0.4	3.9×10^5,2.9×10^4
Q1009+299[b,c]	$-2.97, -2.84$	19.90, 19.93	1.8, 1.5	1.1×10^6,7.5×10^6
HS 0105+1619[b]	> -0.1	< 19.52	< 1.1	$< 1.6 \times 10^5$
Q1243+3047	-0.69	20.42	2.7	8.0×10^6
Q2206–199[d]	unknown[e]	unknown	unknown	unknown
Q0347–3819[f]	> -0.3	< 20.93	0.014	211
Q0130–403[g]	-3.4	20.06	30[h]	4.5×10^8

[a] We list the parameters for each of the two components, where available, from Tytler, Fan & Burles (1996); Burles & Tytler (1998a).

[b]Scaled from previous references to $J_{912} = 10^{-21}$ ergs cm^{-2} s^{-1} Hz^{-1} sr^{-1}

[c] We list the parameters for each of the two components, where available, from Tytler & Burles (1997) and Burles & Tytler (1998b).

[d]Pettini & Bowen 2001.

[e]Currently, there is not enough diagnostic information to measure the ionization state in this absorber, yet it is presumably neutral, given the log $\mathrm{N_{HI}}$.

[f]Levshakov *et al.* 2002.

[g]Kirkman *et al.* 1999.

[h]Calculated from $log\ n_H = -2.9$ cm^{-3} from Kirkman *et al.* 2000 and $log\ n_{HI}/n_H = -3.4$ from O'Meara *et al.* 2001.

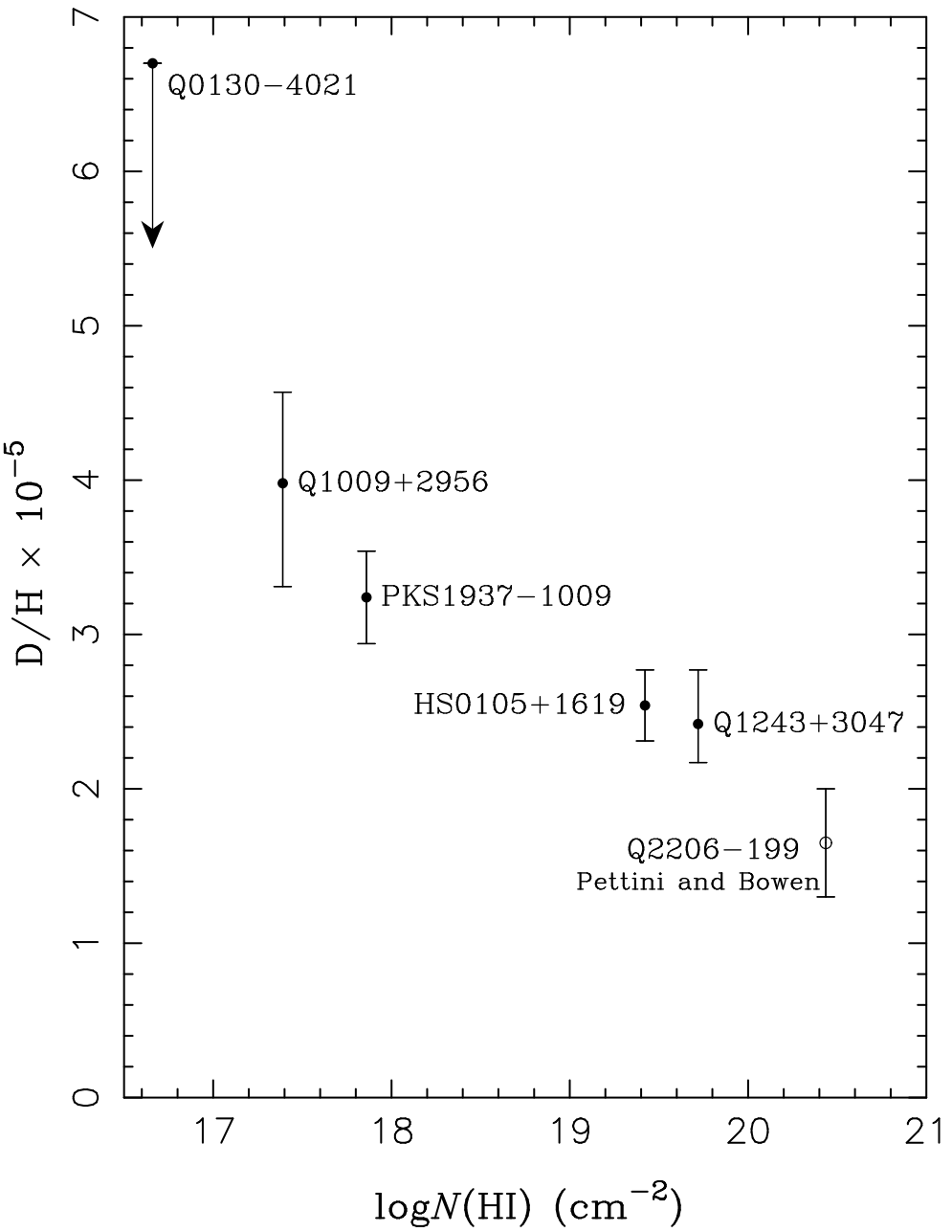

Figure 7.2: As Fig. 7.1 but showing D/H as a function of the H I column density. This correlation is unexpected and we believe it is an accident.

7.2.5 Our Estimate for the Primordial D/H from all QSOs

We believe that the best value for primordial D/H is the weighted mean (§7.2.1) of the log D/H values for the first five QSOs listed in Table 7.1:

$$logD/H = -4.556 \pm 0.064, \tag{7.3}$$

(1σ error of 15%), which is equivalent to D/H= $2.78^{+0.44}_{-0.38}\times\ 10^{-5}$, where the errors are the 1σ errors on the mean, given by the standard deviation of the five log D/H values divided by $\sqrt{5}$. We use this error on the mean instead of the usual error on the weighted mean because the individual D/H values show more dispersion than we expect. The error on the mean depends on just the dispersion of the D/H values, and the number of measurements, but not on the errors on the values. Had the D/H values been consistent with a single value (§7.2.1) we would have used the error on the weighted mean, and if the errors on the individual values were also unchanged, this error would have been 0.023, or 1/3 of the error we quote.

The new D/H is 0.6σ lower than the value we gave in O'Meara *et al.* (2001), log D/H = -4.52 ± 0.06, because the two new values since that paper are both lower. However, the error, which is the error on the mean in both cases, has not changed significantly. Although the dispersion in the D/H values is now larger, the error on the mean is not larger because we have two more measurements, Q2206–199 and Q1243+3047.

When we take the primordial D/H from the weighted mean, we assumed that the quoted errors on each D/H value are too small by the same factor. However, if this assumption is not true, other ways of combining the measurements of D/H will give a better estimate of the primordial D/H. As an example, we could speculate that Q1243+3047 and HS 0105+1619 give the two most reliable D/H values because Q1243+3047 has the most thorough treatment of the errors, and HS 0105+1619 is the simplest measurement with the most supporting evidence. A similar line of argument was explored by Pettini & Bowen (2001) when they derived a D/H value using three DLA systems alone, although the value they gave is no longer acceptable

because the D/H to Q0347–3819 has since increased and now seems the least secure.

7.3 BBN Related Cosmological Parameters

We use SBBN calculations to obtain the η and $\Omega_b h^2$ values that correspond to the primordial D/H. We use this η value to predict the abundance of the other light nuclei, and we compare with measurements. There are differences that may be caused by systematic errors. We also compare with other estimates of the $\Omega_b h^2$ and find good agreement.

7.3.1 Baryon Density from Light Elements

Using the SBBN calculations of Burles et al. (2001), our best estimate for primordial D/H leads to the following predictions: $\eta = 5.9 \pm 0.5 \times 10^{-10}$, $\Omega_b h^2 = 0.0214 \pm 0.0020$ (9.3%), $Y_p = 0.2476 \pm 0.0010$ (predicted mass fraction of ^{4}He), ^{3}He/H $= 1.04 \pm 0.06 \times 10^{-5}$ and ^{7}Li/H $= 4.5^{+0.9}_{-0.8} \times 10^{-10}$. In the above, the error on Y_p is the quadratic sum of 0.0009 from the error on the D/H measurement and 0.0004 from the uncertainty in the Y_p for a given η (Lopez & Turner, 1999). We obtain slightly different central values if we use values from Esposito et al. (2000b,a). The differences are 10% or less of the error from D/H alone, except for ^{7}Li/H (Esposito *et al.* equations give 4.05×10^{-10}) and ^{3}He/H (1.06×10^{-5}). In Fig. 7.3 we compare the predicted abundances with some recent measurements. The vertical band shows the range of η and $\Omega_b h^2$ values that SBBN specifies for our primordial D/H value. Measurements of primordial ^{3}He are consistent, but all ^{7}Li and most ^{4}He measurements prefer lower η.

Bania et al. (2002) report a limit on the primordial ^{3}He/H ratio from their detailed long term study of 60 Galactic H II regions and 6 planetary nebulae. In 17 Galactic H II regions for which the ionization corrections were relatively simple, they find a mean ^{3}He/H $= 1.9 \pm 0.6 \times 10^{-5}$, which will be an upper limit on the primordial ratio if stars have not on average destroyed ^{3}He. They propose that the

best value for the upper limit on the primordial ^{3}He/H is the value they measured for one H II region that has the lowest metal abundance in their sample, the third lowest ^{3}He/H ratio, excellent data and a small ionization correction of 22%. They then quote $^3\mathrm{He/H} < 1.1 \pm 0.2 \times 10^{-5}$ that is consistent with the value predicted by D/H and SBBN. Given the potential complexity of the chemical evolution of ^{3}He, the relatively small range and high mean metal abundance in the gas where they have made measurements ($0.1 < [\mathrm{O/H}] < -0.5$), and the other possible ways of extracting the primordial abundance from the data, we suspect that the errors are larger than quoted, as with D and ^{4}He.

The main isotope of He, ^{4}He, is measured in many tens of extragalactic H II regions to much higher accuracy than either D or ^{3}He. But ^{4}He is fairly insensitive to η and the differences between the measurements allow a large range of η. Izotov & Thuan (1998) report relatively high values for ^{4}He/H that are closest to the D/H prediction, but at $\mathrm{Y}_p = 0.2443 \pm 0.0013$ they are still approximately 2σ below our prediction from D/H (in units of their error). Thuan & Izotov (2002) estimate that their 1998 Y_p value may be too small by 0.0005 – 0.0010, which still leaves Y_p 1.5σ below the prediction from D/H. Although Izotov & Thuan found absorption lines that might explain why Olive et al. (1997) found less ^{4}He in some objects, it is uncertain whether the Y_p is as high as indicated by D/H. Both Pagel (2000) and Fields et al. (2001) conclude that Y_p could be as high as 0.25 due to systematic errors, and Olive & Skillman (2001) state that systematic errors were underestimated for many measurements. But Peimbert et al. (2002) argue that the systematic errors can be ten times smaller.

^{7}Li also prefers a lower η than the value given by SBBN and D/H. There are many tens of high accuracy measurements of ^{7}Li in the atmospheres of metal poor halo stars. There is very little scatter, and hence the abundance ratio in these stars is well determined at $1 - 2 \times 10^{-10}$ (Ryan *et al.* 2000 and references therein). Authors differ on whether the amount of depletion that would be required for concordance between ^{7}Li and D is reasonable. Pinsonneault et al. (2002) quote

a primordial ^{7}Li/H $= 2.51^{+1.74}_{-0.93} \times 10^{-10}$ from models of stellar rotational mixing and the measurements of Ryan et al. (1999). This value is 1σ below the D/H prediction. However, Ryan et al. (2000) claim that the depletion correction is only $0.02^{+0.08}_{-0.02}$ in the log, and that D/H is not consistent with ^{7}Li/H. In Fig. 7.3 we show their primordial ^{7}Li/H value that includes all their corrections, including their depletion correction. Vangioni-Flam et al. (2000) also believe that the ^{7}Li depletion is small.

Figure 7.3: Comparison of predicted and measured abundances of four light nuclei as a function of the baryon density. Orange colored vertical band is the constraint from our best D/H measurement, while purple colored vertical band is the constraint from the first year WMAP CMB observation (Spergel et al., 2003). The figure has three vertical panels each with a different linear scale. The curves show the abundance ratios predicted for SBBN, from the calculations by Burles, Nollett and Turner(2001). The top curve is the ^{4}He mass as a fraction of the mass of all baryons, while the three lower curves are the number fractions D/H, ^{3}He/H and ^{7}Li/H. The vertical widths of the curves show the uncertainties in the predictions. The four boxes show measurements, where the vertical extension is the 1σ random error, and the horizontal range is adjusted to overlap the prediction curves. The ^{4}He box is from Izotov & Thuan (2004). The D/H box is the mean from five QSOs from this work. The ^{3}He from Bania et al. (2002) is an upper limit. The ^{7}Li is from Ryan et al. (2000). We expect that all the data boxes should overlap the vertical band that covers the D/H data. They do not, probably because of systematic errors.

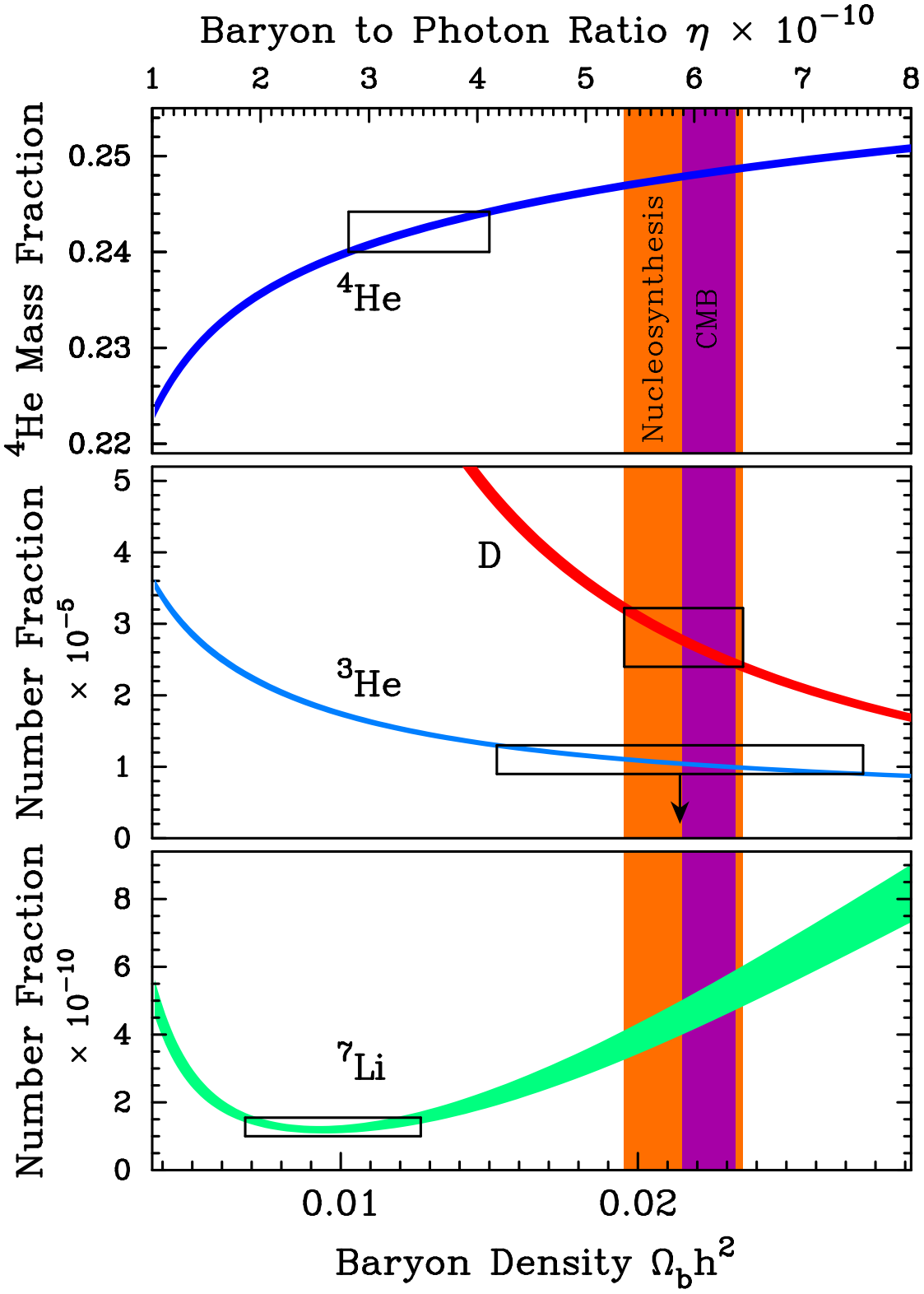
Baryon to Photon Ratio $\eta \times 10^{-10}$
1
2
3
4
5
6
7
8
^{4}He Mass Fraction
0.25
0.24
0.23
0.22
^{4}He
Nucleosynthesis
CMB
Number Fraction $\times 10^{-5}$
5
4
3
2
1
0
D
^{3}He
Number Fraction $\times 10^{-10}$
8
6
4
2
0
^{7}Li
0.01
0.02
Baryon Density $\Omega_b h^2$

7.3.2 Baryon Density from Other Observations

The estimates of $\Omega_b h^2$ from different CMB experiments, listed in Table 7.4, are consistent with each other and with the $\Omega_b h^2$ from D/H and SBBN. Other methods of measuring the Ω_b have lower accuracy. The Lyα forest at redshifts $z \simeq 3$ typically indicates higher $\Omega_b h^2$ values (e.g. Hui *et al.* 2002), while the baryon fraction in clusters of galaxies gives consistent values. For example, Steigman (2002) multiplied the Ω_m derived from SnIa, assuming the universe is flat, by the baryon fraction in clusters of galaxies to obtain $\Omega_b h^2 = 0.019^{+0.007}_{-0.005}$.

The relevance of D/H measurements is changing. SBBN and D/H gave the best estimate of $\Omega_b h^2$ until 2003. However, the CMB measurements now give $\Omega_b h^2$ more accurately than the estimate from SBBN. When we use $\Omega_b h^2$ from the CMB in SBBN, the D/H is predicted with no free parameters, and hence the main value of D/H will be as a test of physics during SBBN (di Bari & Foot, 2001; Kaplinghat & Turner, 2001; Cyburt et al., 2003; Kneller & Steigman, 2003; Abazajian, 2003). Such tests can be made now, comparing the abundances of the light nuclei, but the measurement errors are not well established, and hence the precision will improve when $\Omega_b h^2$ comes from the CMB and we can use D/H alone to test the physics in SBBN.

7.4 Acknowledgment

This Chapter 7, in part, is a reprint of the material as it appears in *Astrophysical Journal Supplement*, volume 149, page 1, 2003. The dissertation author did some of the observations, the bulk of data reduction and calibration, chemical evolution analysis, compilation of cosmological parameter data and the third author of this paper.

Table 7.4. Recent Estimates of the Baryon Density

Method	$\Omega_b h^2$	Ref.
BBN + D/H	0.0214 ± 0.002	Kirkman *et al.* 2003
CMB: WMAP	0.0224 ± 0.001	Spergel *et al.* 2003
Lyα Forest[a]	0.0210 ± 0.0011	Tytler *et al.* 2004
Clusters + SNIa	$0.019^{+0.007}_{-0.005}$	Steigman 2002

[a]using h=0.71

Chapter 8

The Concordance Model

In the following chapters, we attempt to test the ΛCDM model using the Lyα forest. We use quasars as a background light source and investigate the foreground neutral hydrogen gas which we call the Lyα forest. The amount of neutral hydrogen is sensitive to the density, the ionizing UV background radiation and other cosmological parameters. In this section, I introduce the basic ideas, notations and terminologies we use in the following chapters.

8.1 The Evolution of the Lyα Forest

I will review the basic idea of how the neutral fraction of hydrogen gas changes with redshift using the equation of photoionization equilibrium. The thickness of the Lyα forest changes with redshift as is shown in Figure 8.1. This is because the density and the neutral fraction of the hydrogen gas changes with redshift. What we can measure is the flux decrement of the quasar spectrum which reflects the total amount of the neutral hydrogen in the intergalactic medium. Thus, we are investigating the neutral fraction of hydrogen and inferring the underlying density and ionizing UV background.

The equation of photoionization equilibrium is:

$$n_{HI} \int_{\nu_0}^{\infty} \frac{4\pi J_\nu}{h\nu} \alpha_\nu(HI) d\nu = n_p n_e \alpha_{rr}(HI, T), \tag{8.1}$$

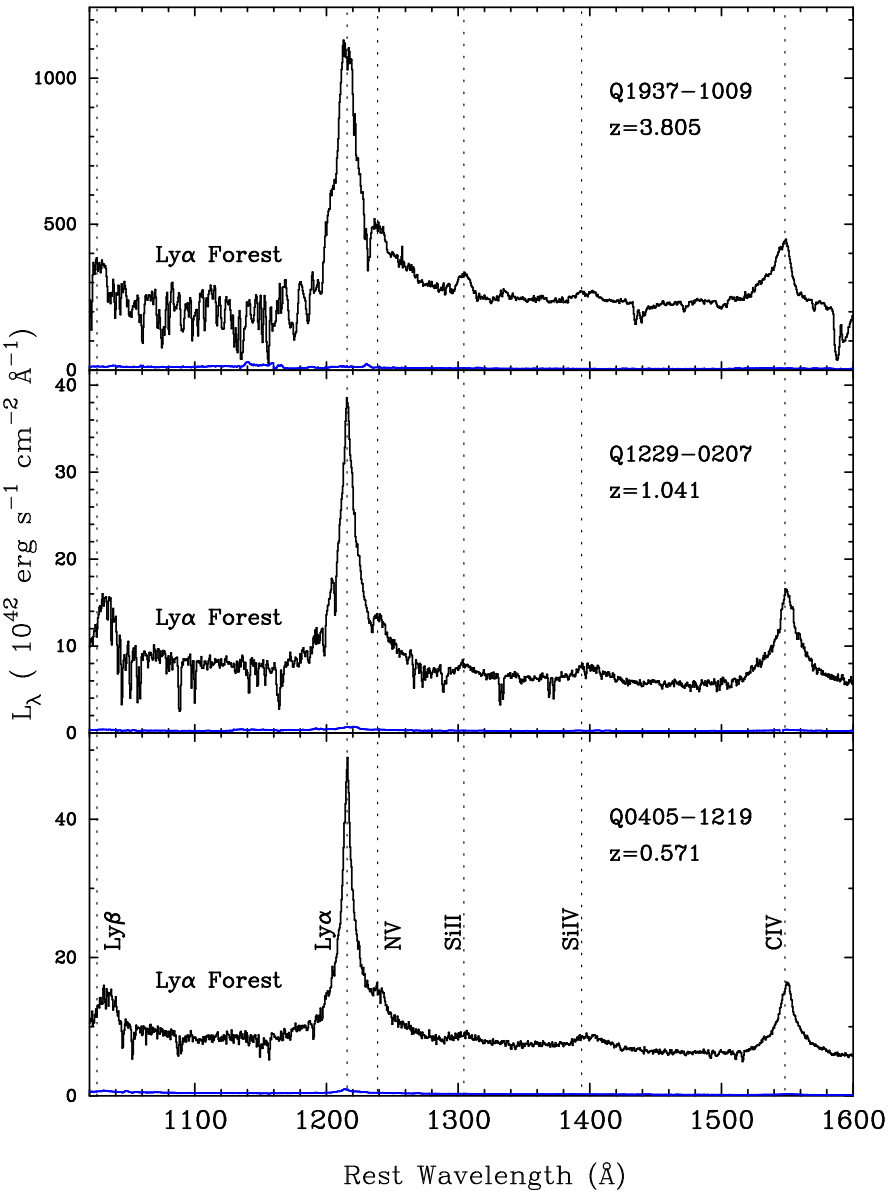

Figure 8.1: The redshift evolution of the Lyα forest is shown with three quasar spectra at different redshifts: 3.805, 1.041, and 0.571 from the top to the bottom panel. The Lyα forest is a series of neutral hydrogen gas in the intergalactic medium which lies in the line of sight. Note that the forest is getting thin towards the low redshifts. The evolution is caused by the competition between the density evolution and the UV background evolution.

where n_{HI}, n_p, n_e are neutral hydrogen, proton and electron number densities per unit volume. $\alpha_{rr}(HI,T)$ is the recombination rate of hydrogen, and it is a function of temperature T. J_ν is the mean intensity of radiation, thus $4\pi J_\nu/h\nu$ is the number of photons per unit area per unit time per unit frequency interval, and $\alpha_\nu(HI)$ is the ionization cross section for hydrogen. The left hand side of the above equation gives the number of photoionizations per unit time per unit volume while the right hand side gives the number of recombinations per unit time per unit volume.

To simplify our notation, we introduce the photoionization rate as follows:

$$\Gamma_{912} = \int_{\nu_{912}}^{\infty} \frac{4\pi J_\nu}{h\nu} \alpha_\nu(HI) d\nu, \tag{8.2}$$

where ν_{912} is the frequency of a photon which is equivalent to the wavelength of 912 Å. This is the energy that can ionize neutral hydrogen. Likewise, we define Γ_{228}:

$$\Gamma_{228} = \int_{\nu_{228}}^{\infty} \frac{4\pi J_\nu}{h\nu} \alpha_\nu(HI) d\nu, \tag{8.3}$$

where ν_{228} is a frequency of a photon with a wavelength 228 Å that can ionize He II which plays an important role in the IGM at redshift 1 to 3. Utilizing Γ, we can rewrite the equation of photoionization equilibrium:

$$n_{HI}\Gamma = n_p n_e \alpha_{rr}(HI,T). \tag{8.4}$$

We are interested in the fraction of the neutral hydrogen, X_{HI}:

$$X_{HI} = \frac{n_{HI}}{n}, \tag{8.5}$$

where n is the total number density of the hydrogen, namely:$n = n_{HI} + n_{HII}$. In general, the IGM is highly ionized and we know the order of the neutral fraction at redshift 2 is $X_{HI} \sim 10^{-5}$ (Rauch, 1998). Therefore, we have $n \sim n_p \sim n_e$, and we can rewrite the above equation as:

$$n_{HI}\Gamma = n^2 \alpha_{rr}, \tag{8.6}$$

and with the neutral fraction X_{HI}:

$$X_{HI} = \frac{n\alpha_{rr}}{\Gamma}. \tag{8.7}$$

Now, we wish to describe how the neutral fraction X_{HI} changes with redshift. We know the averaged density of the universe, $\bar{\rho}$, changes with the volume of the expanding universe as

$$\bar{\rho} \propto (1+z)^3. \tag{8.8}$$

We also know the density fluctuation $\delta\rho/\bar{\rho}$ grows in time (for CDM Model):

$$\frac{\delta\rho}{\bar{\rho}} \propto \frac{1}{1+z}. \tag{8.9}$$

Although this growth factor depends on the cosmological models we discuss later, the above equation is true for the Einstein - de Sitter model. What we are observing as the Lyα forest are the over dense regions: $\delta\rho/\bar{\rho} > 1$. Thus the density n that we are interested in corresponds to $\delta\rho$, and we have:

$$\delta\rho \propto (1+z)^2. \tag{8.10}$$

Therefore, the neutral fraction and the redshift can be related as:

$$X_{HI} \propto \frac{\alpha_{rr}}{\Gamma}(1+z)^2. \tag{8.11}$$

As a first approximation, if we suppose the recombination rate, α_{rr}, and the photoionization rate, Γ, do not change with redshift, we can see that the neutral fraction decreases toward low redshift, meaning the universe is getting ionized in time.

In fact, the photoionization rate changes with redshift since the source of the UV radiation changes its spectrum and population along with the redshift. In the next section, I introduce the theoretical estimate of Γ, and I present our measurement of the Γ in the following chapters.

8.2 The Evolution of the Photoionization Rate

The intensity of the UV background changes with redshift because of the evolution of the source of UV photons. Quasars are the major source of UV photons at redshift 2. Unlike galaxies or stars, the nature of the quasar spectrum is non-thermal, meaning that there is no exponential cut off in ultraviolet. Instead they

have a power-law spectrum and emit far ultraviolet photons (Malkan & Sargent, 1982; Sanders et al., 1989; Elvis et al., 1994). The number of quasars are at maximum around redshift 2. We believe this is because the quasar phenomena are related to galaxy mergers and the rate is peaked around redshift 2 (Sanders et al., 1988; Bahcall et al., 1997). Star forming galaxies are another source of UV photons, and now we know the star formation rate is high at redshifts greater than 2 (Madau et al., 1996; Steidel et al., 2001). Although the intensity of an individual galaxy is not as strong as a quasar, the number of galaxies far exceeds the number of quasars.

Madau et al. (1999) use the luminosity functions of quasars (Pei, 1995) and high redshift galaxies (Steidel et al., 2001) to estimate the total number of UV photons per volume knowing their spectral index of quasars (Zheng et al., 1997) and galaxies (Bruzual A. & Charlot, 1993). The analytically estimated UV background by Madau et al. (1999), namely the photoionization rate, Γ, for hydrogen and helium is shown in Figure 8.2. Γ peaks around redshift 2 which coincides with the peak of the number of quasars, meaning that the UV background is dominated by the quasars in this redshift range. This estimation was done by counting the number of emitted photons. In the following chapters, we attempt to count the number of absorbed photons, quantify the amount of neutral hydrogen seen in absorption lines, and to measure Γ at redshift 1.95.

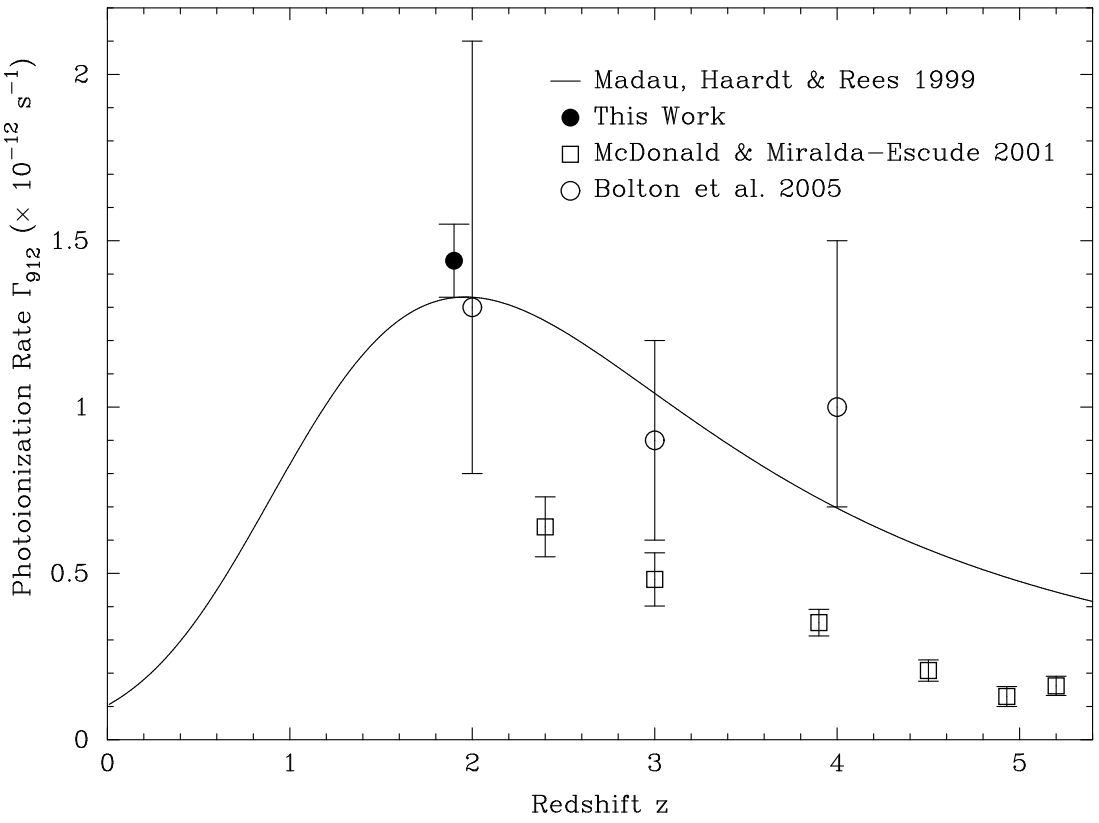

Figure 8.2: The redshift evolution of the photoionization rate Γ . The curve peaks around redshift 2 because the UV background is dominated by the quasars, and the quasar population peaks around 2. The solid line is the theoretical estimation by Madau et al. (1999). They are counting the photons emitted by quasars and the galaxies. The data points are the measurements using the Lyα forest. We are counting the number of photons absorbed by the neutral hydrogen in the intergalactic medium.

Chapter 9

The Kast Quasar Survey

9.1 Abstract

We present spectra of 79 bright quasars obtained with the Kast spectrograph on the Shane 3m telescope at Lick observatory. The quasars have emission redshifts 1.89 – 2.45 and most are near the mean value of $z_{\rm em}$= 2.17. Two of them, one a new discovery, are broad absorption lines (BAL) quasars. The spectra have $\sim$ 250 km s^{-1} resolution and they cover 3175–5880 Å with signal-to-noise ratios of 6–20 per 1.13 Å pixel in the Lyα forest between Lyα and Lyβ. We show the continuum levels that we used in Tytler *et al.* (2004) to make a calibrated measurement of the amount of absorption in the Lyα forest a $z = 1.9$. We measure redshifts for 140 absorption line systems and we list the metal ions that we see in each system. We identify 526 emission lines, and we list their observed wavelengths which we use to obtain new emission redshifts. We find that three emission lines, or line blends, in the forest have mean rest wavelengths of 1070.95 ± 1.00, 1123.13 ± 0.51, and 1175.88 ± 0.30 Å.

9.2 Introduction

This survey is a joint effort of the Tytler group. I participated in observation from the beginning, led the target selection and devised up the database and

its maintenance. We investigate the Lyα forest in the redshift range from 1.6 to 2.5 where the ongoing Sloan Digital Sky Survey cannot cover because of the shortage of their wavelength coverage, although this redshift range is the best to test the geometry of the universe from the Lyα forest. Here I present 79 spectra we observed and will discuss analysis in the coming chapters.

9.3 Observations and Data Reduction

We obtained the spectra of the QSOs using the Kast double spectrograph on the Shane 3m telescope at Lick observatory from 2001 to 2003. In most cases, we used the 2 arcsecond slit width, although we changed to the 3 arcsecond slit to accommodate poor seeing conditions. In good seeing we used a 1.5 arcsecond slit. For all observations, we rotated the spectrograph to place the long axis of the slit in the vertical direction at the effective middle of the exposure to minimize losses due to atmospheric dispersion. For each QSO in the sample, we took exposures using both the blue and red cameras on Kast. The blue camera used the 830/4360 grism, and the red camera used the 1200/5000 grating, with a dispersion of 1.13 and 1.17 Å per pixel respectively ($\sim$ 3 pixels per resolution element). We employed the d46 dichroic to split the light between the cameras. The blue camera exposures covered the approximate wavelength range of 3175–4540 Å, and the red camera exposures covered the approximate wavelength range 4475–5880 Å. Because of differences in the exact location of the blue camera CCD on a given observing run, the starting and ending wavelengths vary by approximately $\pm$ 5 Å from run to run.

We chose the quasars from the NED extragalactic database [1] using three constraints. They should have emission redshift between $z_{\rm em}$= 1.9 and $z_{\rm em}$= 2.4, be of sufficient brightness to keep exposure times less than a few hours, and not show BAL absorption. The $z_{\rm em}$ constraint was made to maximize coverage of the Lyα forest at $z \simeq 1.9$. We chose to avoid BAL QSOs to minimize absorption in

[1] http://nedwww.ipac.caltech.edu

the spectra that do not come from the IGM. We obtained and present spectra for two QSOs, Q1542+5408 and Q2310+0018, which we found to show BAL absorption. Q1542+5408 is discussed in Green et al. (2001), and the BAL nature of Q2310+0018 is first reported here. These two QSOs, noted as BAL in several of the Tables in this paper, were not used by Tytler et al. (2004a). Other than these constraints, the survey is unbiased with respect to the quasars observed.

Table 9.1 lists the QSOs observed, along with their B1950 and J2000 coordinates, the V magnitude given by NED, the approximate redshift, and the exposure time. For simplicity, and to aid comparison with published spectra, we choose to name the QSOs by their abbreviated B1950 coordinates. Table 9.2 lists the observation date, slit width and signal to noise ratio for each QSO.

In Table 9.2 we list the signal to noise ratio at two rest wavelengths in the Lyα forest, 1070Å and 1170Å. These are the starting and ending wavelengths that we used in Tytler et al. (2004a) for the measurement of the mean amount of absorption. The values are the mean signal to noise ratios over 20 Å (rest frame) centered about these wavelengths. The signal to noise ratio of the unabsorbed continuum level would general be higher, because absorption from the Lyα forest has lowered the mean signal. Figure 9.1 shows the distribution of the signal to noise ratios from Table 9.2.

We chose the exposure times to obtain S/N > 10.0 at wavelengths greater than the Lyβ emission line of each QSO. Most of the spectra reach this goal, except those observed in poor conditions. We do not present QSOs for which we obtained S/N < 2.

We obtained, but do not present spectra for 6 objects which upon reduction, are not QSOs. Two of these spectra are likely due to telescope pointing error. It is possible that the 4 other objects, Q1456+5404 (14h56m47.71 +54d04m25.6 $z_{\rm em}$= 2.300 V=16.50), Q1742+3749 (17h42m 5.55 +37d49m08.3 $z_{\rm em}$= 1.958 V=16.40), Q1755+5749 (17h55m15.97 +57d49m06.9 $z_{\rm em}$= 2.110 V=18.00), and Q2113+3004 (21h13m59.42 +30d04m02.4 $z_{\rm em}$= 2.080 V=17.30) are not QSOs.

We reduced the spectra and calibrated their wavelength scale using the standard long-slit reduction tools in IRAF. We took an exposure of arc lamps after each QSO exposure and while the telescope was tracking the QSO to minimize wavelength errors caused by flexure. The wavelength solutions have typical errors less than 1 Å. All the observed wavelengths in this paper are vacuum values in the Earth frame of reference at the time of observation, without correction to the heliocentric frame. For each night, a number of spectrophotometric flux standard stars were observed for the purposes of flux calibration. We list these stars in Table 9.3. As discussed in Suzuki et al. (2003), our errors in relative flux calibration could be as low as a few percent. Finally, the spectra were cleaned of any deviant pixels resulting from poor sky or cosmic ray subtraction by replacing these pixels with their neighboring flux values.

Table 9.1. Kast $z \simeq 2$ Spectra of 79 QSOs : Coordinates and Redshifts

Name (1950)	Coordinates (B1950)	Coordinates (J2000)	V	$z_{\rm em}$ [a]
Q0001–2340	00 01 11.50 –23 40 37.0	00 03 44.95 –23 23 54.7	16.70	2.26
Q0014–0420	00 14 09.36 –04 20 57.0	00 16 42.80 –04 04 17.0	16.65	1.96
Q0049+0124	00 49 59.56 +01 24 23.3	00 52 33.71 +01 40 40.5	17.00	2.29
Q0109+0213	01 09 42.31 +02 13 53.1	01 12 16.91 +02 29 47.6	17.64	2.34
Q0150–2015	01 50 04.98 –20 15 52.6	01 52 27.30 –20 01 06.0	17.10	2.14
Q0153+7428	01 53 04.33 +74 28 05.6	01 57 34.96 +74 42 43.2	16.00	2.34
Q0218+3707	02 18 02.70 +37 07 04.1	02 21 05.50 +37 20 46.0	17.50	2.41
Q0226–0350	02 26 22.08 –03 50 58.6	02 28 53.21 –03 37 37.1	16.96	2.07
Q0248+3402	02 48 23.35 +34 02 22.0	02 51 27.70 +34 14 41.0	17.70	2.22
Q0348+0610	03 48 36.62 +06 10 15.5	03 51 16.53 +06 19 14.2	17.60	2.05
Q0421+0157	04 21 32.67 +01 57 32.7	04 24 08.56 +02 04 24.9	17.04	2.04
Q0424–1309	04 24 47.81 –13 09 32.9	04 27 07.30 –13 02 53.0	17.50	2.16
Q0450–1310	04 50 54.00 –13 10 39.0	04 53 12.83 –13 05 46.1	16.50	2.25
Q0726+2531	07 26 25.23 +25 31 07.2	07 29 28.47 +25 24 51.9	17.81	2.30
Q0743+6601	07 43 58.60 +66 01 00.0	07 48 46.22 +65 53 31.4	17.00	2.20
Q0748+6105	07 48 01.84 +61 05 35.9	07 52 22.50 +60 57 52.0	17.50	2.49
Q0752+3429	07 52 10.00 +34 29 31.3	07 55 24.00 +34 21 34.0	17.80	2.12
Q0800+3031	08 00 34.43 +30 31 24.1	08 03 42.00 +30 22 55.0	16.70	2.02
Q0836+7104	08 36 21.53 +71 04 22.5	08 41 24.36 +70 53 42.2	16.50	2.18
Q0854+3324	08 54 21.61 +33 24 53.0	08 57 26.95 +33 13 17.2	17.43	2.33
Q0907+3811	09 07 44.95 +38 11 31.9	09 10 54.20 +37 59 15.0	17.30	2.15
Q0936+3653	09 36 32.36 +36 53 35.9	09 39 35.10 +36 40 00.0	17.00	2.02
Q0937–1818	09 37 30.22 –18 18 37.3	09 39 51.10 –18 32 15.0	16.20	2.36
Q1023+3009	10 23 58.86 +30 09 29.9	10 26 48.10 +29 54 12.0	17.10	2.33
Q1103+6416	11 03 03.98 +64 16 21.9	11 06 10.70 +64 00 09.0	15.80	2.20
Q1116+2106	11 16 44.49 +21 06 11.4	11 19 22.90 +20 49 46.0	17.30	2.46
Q1122–1648	11 22 12.28 –16 48 47.4	11 24 42.80 –17 05 17.0	16.50	2.40
Q1130+3135	11 30 06.36 +31 35 24.3	11 32 45.20 +31 18 50.0	17.00	2.29
Q1147+6556	11 47 53.77 +65 56 08.8	11 50 34.50 +65 39 28.0	16.20	2.21
Q1222+2251	12 22 56.58 +22 51 49.3	12 25 27.40 +22 35 13.0	15.49	2.05
Q1224–0812	12 24 02.65 –08 12 52.8	12 26 37.50 –08 29 29.0	16.83	2.16
Q1224+2905	12 24 57.90 +29 05 23.0	12 27 27.40 +28 48 47.0	17.00	2.25
Q1225+3145	12 25 56.07 +31 45 12.6	12 28 24.96 +31 28 37.6	15.87	2.18
Q1231+2924	12 31 27.08 +29 24 20.8	12 33 55.51 +29 07 48.9	16.84	2.01
Q1247+2657	12 47 39.09 +26 47 27.1	12 50 05.75 +26 31 07.7	15.80	2.03
Q1251+2636	12 51 56.97 +26 36 21.8	12 54 23.08 +26 20 06.5	16.45	2.03
Q1307+4617	13 07 58.49 +46 17 20.8	13 10 11.60 +46 01 24.0	16.74	2.13

Table 9.1—Continued

Name (1950)	Coordinates (B1950)	Coordinates (J2000)	V	z_{em} [a]
Q1312+7837	13 12 30.24 +78 37 44.6	13 13 21.30 +78 21 53.0	16.40	2.00
Q1326+3923	13 26 10.24 +39 23 47.2	13 28 23.70 +39 08 17.0	16.60	2.32
Q1329+4117	13 29 29.82 +41 17 22.7	13 31 41.10 +41 01 58.0	16.30	1.93
Q1331+1704	13 31 10.00 +17 04 25.8	13 33 35.78 +16 49 04.0	16.71	2.08
Q1416+0906	14 16 23.30 +09 06 14.0	14 18 51.09 +08 52 27.1	17.00	2.01
Q1418+2254	14 18 51.06 +22 54 58.3	14 21 08.72 +22 41 17.4	16.60	2.19
Q1422+4224	14 22 37.86 +42 24 01.6	14 24 36.00 +42 10 30.0	17.10	2.21
Q1425–1338	14 25 02.87 –13 38 19.4	14 27 46.40 –13 51 44.0	17.19	2.03
Q1435+6349	14 35 37.25 +63 49 36.0	14 36 45.80 +63 36 37.8	15.00	2.06
Q1517+2556	15 17 08.11 +23 56 52.0	15 19 19.40 +23 46 02.0	16.40	1.90
Q1542+3104	15 42 48.48 +31 04 42.0	15 44 49.00 +30 55 21.0	17.00	2.28
Q1542+5408[b]	15 42 41.88 +54 08 25.6	15 43 59.40 +53 59 03.0	16.00	2.36
Q1559+0853	15 59 57.80 +08 53 53.0	16 02 22.56 +08 45 36.3	16.70	2.26
Q1611+4719	16 11 10.53 +47 19 32.2	16 12 39.90 +47 11 57.0	17.60	2.38
Q1618+5303	16 18 28.71 +53 03 20.0	16 19 42.30 +52 56 13.0	17.50	2.34
Q1626+6433	16 26 20.41 +64 33 32.3	16 26 45.60 +64 26 55.0	15.80	2.31
Q1632+3209	16 32 17.96 +32 09 45.7	16 34 12.78 +32 03 35.4	16.93	2.34
Q1649+4007	16 49 57.45 +40 07 16.7	16 51 37.56 +40 02 18.7	17.18	2.33
Q1703+5350	17 03 01.49 +53 50 57.2	17 04 06.70 +53 46 53.0	17.40	2.37
Q1705+7101	17 05 00.60 +71 01 34.0	17 04 26.08 +70 57 34.7	17.50	2.01
Q1716+4619	17 16 01.69 +46 19 39.0	17 17 26.80 +46 16 31.0	17.10	2.11
Q1720+2501	17 20 49.93 +25 01 20.6	17 22 52.99 +24 58 34.7	17.10	2.25
Q1754+3818	17 54 58.67 +38 18 10.2	17 56 39.70 +38 17 52.0	17.50	2.16
Q1833+5811	18 33 09.83 +58 11 07.8	18 33 57.00 +58 13 34.0	17.00	2.03
Q1834+6117	18 34 46.51 +61 17 07.3	18 35 19.68 +61 19 40.0	17.60	2.27
Q1848+6705	18 48 26.30 +67 05 07.0	18 48 25.35 +67 08 37.2	17.50	2.03
Q2044–1650	20 44 30.78 –16 50 09.4	20 47 19.67 –16 39 05.8	17.36	1.94
Q2103+1843	21 03 50.50 +18 43 46.0	21 06 08.52 +18 55 49.9	16.80	2.21
Q2134+0028	21 34 05.21 +00 28 25.0	21 36 38.59 +00 41 54.2	16.79	1.94
Q2134+1531	21 34 01.07 +15 31 38.2	21 36 23.80 +15 45 07.0	17.30	2.13
Q2135+1326	21 35 40.84 +13 26 19.9	21 38 05.20 +13 39 53.0	17.10	2.30
Q2140+2403	21 40 31.75 +24 03 33.0	21 42 48.50 +24 17 18.0	16.80	2.16
Q2147–0825	21 47 09.10 –08 25 17.9	21 49 48.17 –08 11 16.2	16.18	2.12
Q2150+0522	21 50 54.30 +05 22 08.6	21 53 24.67 +05 36 18.9	17.77	1.98
Q2157–0036	21 57 20.39 –00 36 15.3	21 59 54.45 –00 21 50.3	16.98	1.96
Q2241–2418	22 41 56.68 –24 18 48.8	22 44 40.30 –24 03 02.0	16.95	1.96

Table 9.1—Continued

Name (1950)	Coordinates (B1950)	Coordinates (J2000)	V	z_{em}[a]
Q2245+2531	22 45 03.78 +25 31 39.3	22 47 27.40 +25 47 30.0	17.60	2.16
Q2310+0018[b]	23 10 50.80 +00 18 24.1	23 13 24.45 +00 34 44.5	17.00	2.08
Q2310+3831	23 10 36.18 +38 31 22.7	23 12 58.79 +38 47 42.6	17.50	2.18
Q2320+0755	23 20 03.91 +07 55 33.6	23 22 36.08 +08 12 01.6	17.50	2.08
Q2329-0204	23 29 02.27 –02 04 40.4	23 31 36.33 –01 48 06.5	17.00	1.89
Q2332+2917	23 32 32.03 +29 17 39.5	23 35 01.50 +29 34 15.0	17.60	2.07

[a]This redshift is approximate

[b]BAL QSO

Table 9.2. Kast $z \simeq 2$ Spectra of 79 QSOs : Observation Log

Name (1950)	Observation Date	Slit Width (arcseconds)	Exposure Time (seconds)	SNR (1070 Å)	SNR (1170 Å)
Q0001–2340	2001-07-20	3.0	1380	9.04	14.33
Q0014–0420	2001-07-19	3.0	720	3.19	8.88
Q0049+0124	2001-09-13	3.0	2700	15.24	24.00
Q0109+0213	2001-12-16	2.0	4800	22.73	34.25
Q0150–2015	2001-09-13	3.0	2700	9.26	19.29
Q0153+7428	2001-09-13	3.0	1800	7.53	13.14
Q0218+3707	2002-01-11	2.0	3600	22.08	29.59
Q0226–0350	2003-01-30	2.0	2400	5.45	14.12
Q0248+3402	2002-01-11	2.0	4200	23.27	36.34
Q0348+0610	2003-01-30	2.0	3600	6.02	16.54
Q0421+0157	2001-12-16	2.0	3000	6.19	16.09
Q0424–1309	2002-01-11	2.0	4200	1.71	2.95
Q0450–1310	2003-01-29	2.0	3600	11.99	19.20
Q0726+2531	2003-01-31	2.0	4800	8.94	14.36
Q0743+6601	2001-12-16	2.0	3600	17.36	25.15
Q0748+6105	2001-12-16	2.0	4200	16.62	20.73
Q0752+3429	2003-01-30	2.0	4500	9.18	15.98
Q0800+3031	2002-04-09	1.5	3600	8.09	21.69
Q0836+7104	2002-03-09	2.0	2400	15.92	23.20
Q0854+3324	2003-01-30	2.0	4200	7.29	11.77
Q0907+3811	2003-01-31	2.0	3000	5.42	9.70
Q0936+3653	2003-01-31	2.0	2400	1.24	5.50
Q0937–1818	2003-01-29	2.0	3000	9.59	15.87
Q1023+3009	2002-04-09	1.5	3600	6.28	9.02
Q1103+6416	2003-01-31	2.0	1800	15.16	24.08
Q1116+2106	2002-04-11	1.5	3600	4.44	5.64
Q1122–1648	2003-01-29	2.0	2700	15.23	25.84
Q1130+3135	2003-01-30	2.0	2400	9.69	15.89
Q1147+6556	2002-04-09	1.5	2360	3.54	6.55
Q1222+2251	2003-01-29	2.0	3000	9.24	22.63
Q1224–0812	2003-01-31	2.0	2400	6.48	12.82
Q1224+2905	2002-04-11	1.5	3600	4.85	6.54
Q1225+3145	2001-05-19	3.0	2100	27.77	45.87
Q1231+2924	2003-01-30	2.0	2400	10.16	22.86
Q1247+2657	2001-05-19	2.0	1200	21.49	45.37
Q1251+2636	2001-05-19	2.0	2100	5.28	15.57
Q1307+4617	2002-03-09	2.0	3000	13.89	24.74

Table 9.2—Continued

Name (1950)	Observation Date	Slit Width (arcseconds)	Exposure Time (seconds)	SNR (1070 Å)	SNR (1170 Å)
Q1312+7837	2003-01-29	2.0	2400	8.36	20.90
Q1326+3923	2003-01-31	2.0	2100	11.63	16.66
Q1329+4117	2003-07-28	2.0	4500	– [A]	9.49
Q1331+1704	2002-04-11	1.5	2700	7.53	14.35
Q1416+0906	2003-01-29	2.0	2400	3.37	10.42
Q1418+2254	2001-05-19	2.0	1800	11.98	20.80
Q1422+4224	2002-03-09	2.0	4200	5.22	9.53
Q1425–1338	2003-01-30	2.0	2400	1.50	6.34
Q1435+6349	2001-05-19	2.0	1500	8.14	18.13
Q1517+2556	2003-07-29	2.0	4500	– [A]	8.31
Q1542+3104	2001-05-18	2.0	2400	7.83	9.60
Q1542+5408[B]	2001-05-19	2.0	1800	17.20	21.52
Q1559+0853	2001-07-19	3.0	2400	12.65	21.96
Q1611+4719	2002-04-11	1.5	3600	8.94	16.60
Q1618+5303	2001-07-20	3.0	4500	39.17	54.79
Q1626+6433	2001-07-18	3.0	1800	30.55	45.82
Q1632+3209	2001-05-19	2.0	2100	9.99	16.28
Q1649+4007	2001-07-18	3.0	2400	18.98	27.32
Q1703+5350	2001-07-18	3.0	3600	32.88	43.43
Q1705+7101	2001-07-19	2.0	4200	2.74	8.52
Q1716+4619	2001-05-18	3.0	2400	13.29	19.53
Q1720+2501	2001-07-17	3.0	4000	12.49	18.50
Q1754+3818	2001-05-19	2.0	2700	7.90	26.11
Q1833+5811	2001-05-18	3.0	1800	3.41	8.42
Q1834+6117	2001-05-19	2.0	2700	9.29	14.67
Q1848+6705	2001-05-18	3.0	1500	3.71	8.38
Q2044–1650	2001-07-18	3.0	3600	– [A]	15.63
Q2103+1843	2001-07-17	3.0	2400	32.90	46.93
Q2134+0028	2001-07-19	3.0	2400	– [A]	22.77
Q2134+1531	2001-07-18	3.0	3600	15.16	25.12
Q2135+1326	2001-07-17	3.0	2700	15.78	24.27
Q2140+2403	2001-07-17	3.0	2400	17.08	31.21
Q2147–0825	2003-07-28	2.0	2400	4.36	9.49
Q2150+0522	2003-07-29	2.0	6000	3.97	7.96
Q2157–0036	2003-07-28	2.0	4200	– [A]	20.79
Q2241–2418	2001-07-17	3.0	1800	2.69	10.95

Table 9.2—Continued

Name (1950)	Observation Date	Slit Width (arcseconds)	Exposure Time (seconds)	SNR (1070 Å)	SNR (1170 Å)
Q2245+2531	2003-07-28	2.0	6000	13.23	26.09
Q2310+0018[B]	2001-07-11	3.0	1800	11.71	20.45
Q2310+3831	2001-07-18	3.0	3000	10.80	17.77
Q2320+0755	2001-07-20	3.0	4500	6.38	12.66
Q2329-0204	2001-07-19	3.0	2400	6.38	12.66
Q2332+2917	2003-07-29	2.0	6000	8.43	21.88

[A]This rest wavelength was not covered by this spectrum

[B]BAL QSO

9.4 The Kast $z \simeq 2$ Survey

We now present the spectra of the survey, comment on absorbers in individual QSOs, and tabulate the emission lines.

9.4.1 Spectra

In Figures 9.2, we show the blue and red camera exposures of the 79 quasars which comprise the survey. For each blue exposure, the flux (solid line), error (dotted line), and continuum (dashed line) level is shown. For the red camera exposures, we display the flux and error levels. The spectra have well calibrated relative flux, but we do not assign a numerical value to the flux, since absolute flux calibration was not a goal for the survey, and few exposures were made under photometric conditions.

We placed a continuum level on each blue side spectrum. The level was determined by eye, and recorded using the b-spline fits discussed in Kirkman et al. (2003) and Tytler et al. (2004a). We also fit continua to artificial spectra that we made to mimic the real ones. Our continuum fits to those spectra had a typical

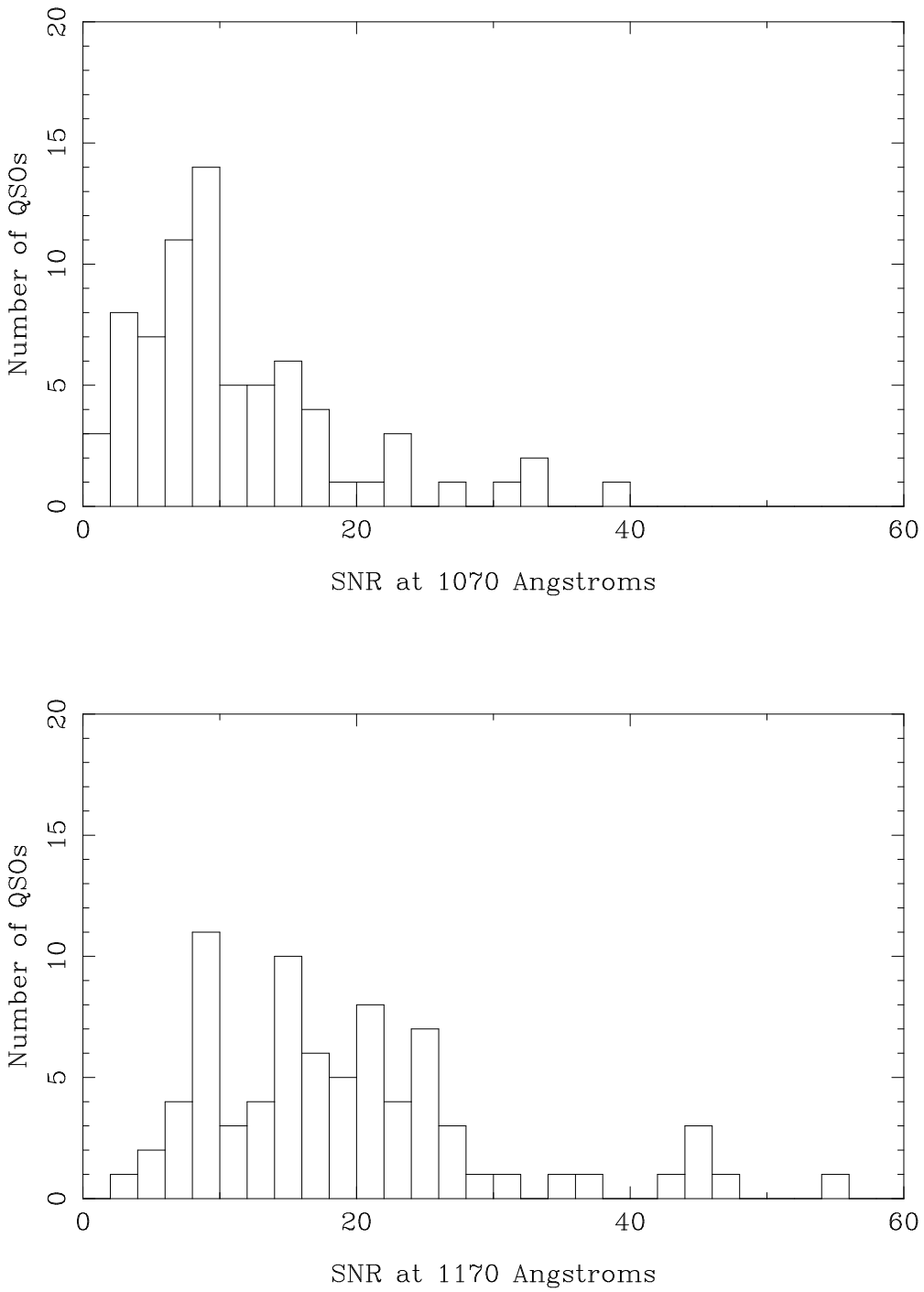

Figure 9.1: Signal to noise distribution for the 79 quasars in the survey. The upper panel shows the distribution of the mean signal to noise ratios per pixel sampled over 20 Å (rest) centered at 1070 Å, while the lower panel shows the distribution sampled over 20 Å centered at 1170 Å.

Table 9.3. Standard Stars used for Flux Calibration

Name	Coordinates (J2000)	V	Spectral Type
G191B2B	05 05 30.6 + 52 49 54	11.78	DAO
Feige 34	10 39 36.7 + 43 06 10	11.18	DO
Feige 67	12 41 51.8 + 17 31 20	11.81	sdO
BD+33d2642	15 51 59.9 + 32 56 55	10.81	B2IV
BD+28d4211	21 51 11.1 + 28 51 52	10.51	0p
Feige 110	23 19 58.4 – 05 09 56	11.82	DOp

error of 3.5%. Averaged over 77 QSOs, excluding the two QSOs that we label BAL in Tables 1 and 2, the mean continuum level error is 1-2% except at S/N < 6 per pixel, where we systematically placed the continuum too high. The continua that we show on the Kast spectra in Figures 9.2–**??** are the equivalents of the the original "F1" fits to the artificial spectra that we discuss in detail in Tytler et al. (2004a). We believe that they have errors similar to those on the artificial spectra. We have not placed continua on the exposures with the red camera.

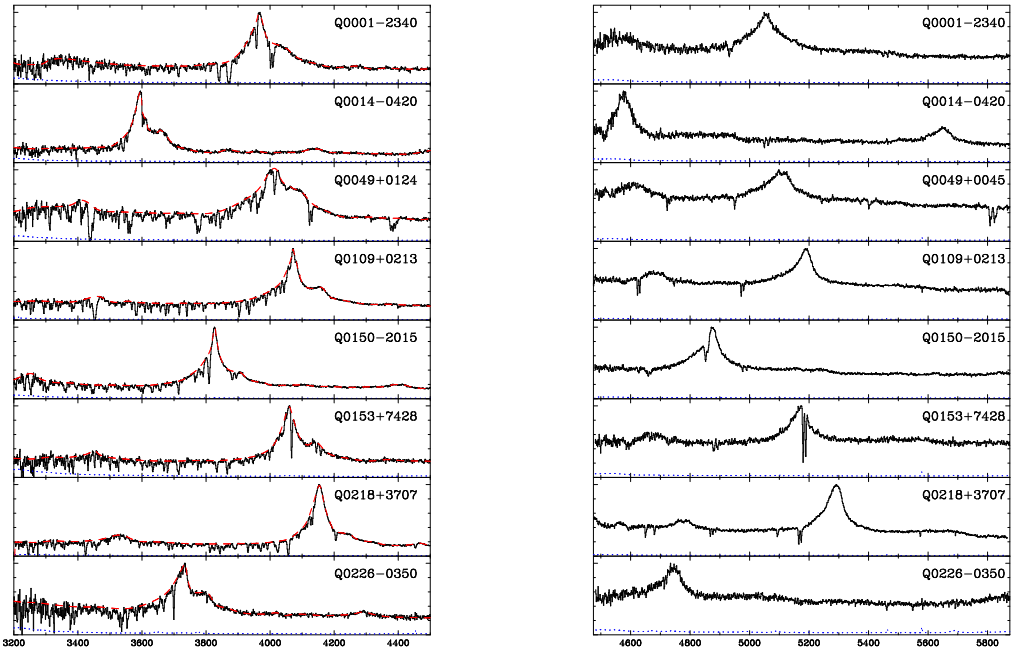

Figure 9.2: For each QSO, the flux is shown as the thick line, the 1σ error in the flux as the dotted line, and the dashed line represents the fit to the continuum level. The **y** axis is the flux level, in erg sec^{-1} cm^{-2} Å^{-1}, on a linear scale with zero flux at the bottom, and the **x** axis is in Å.

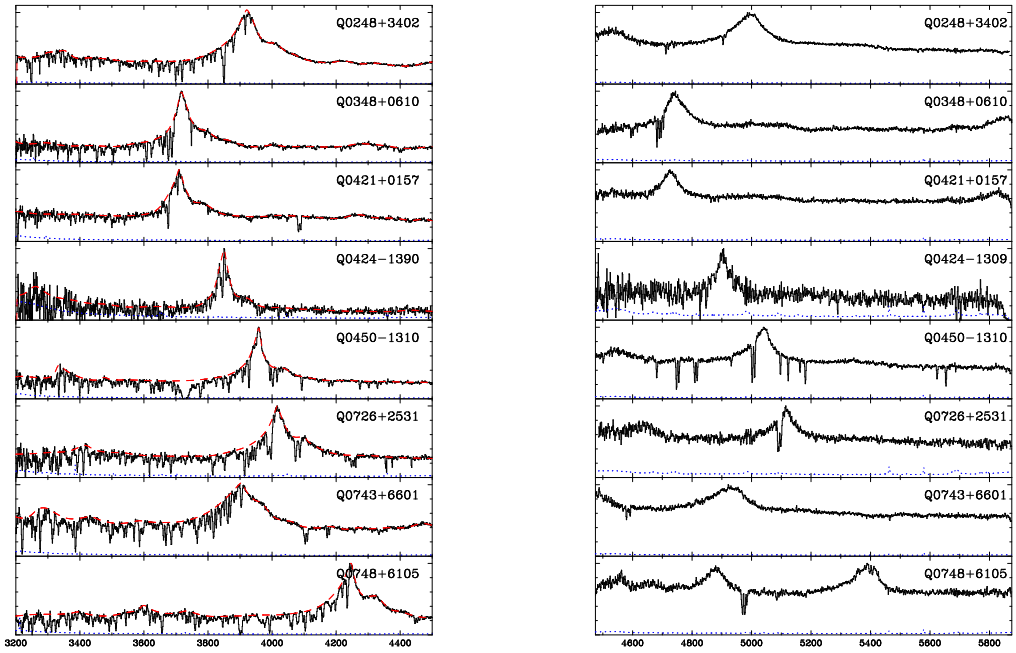

Figure 9.2: (continued)

9.5 Acknowledgment

This Chapter 9, in part, is a reprint of the material as it appears in *Astronomical Journal*, volume 128, page 1058, 2004. The dissertation author led the target selection, the database maintenance for the survey, did bulk of observations and the third author of this paper.

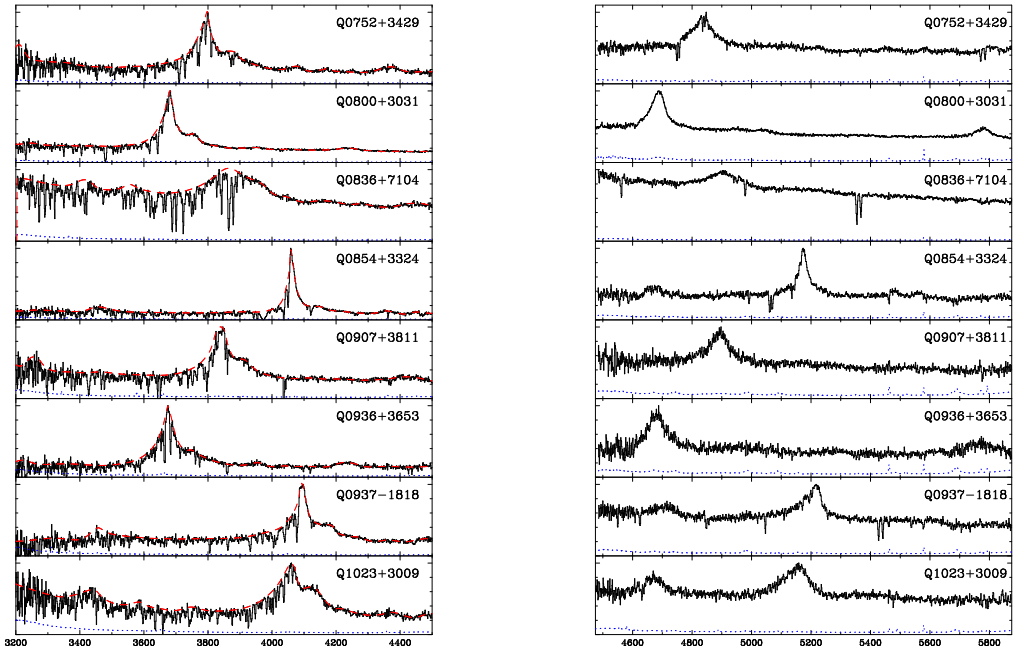

Figure 9.2: (continued)

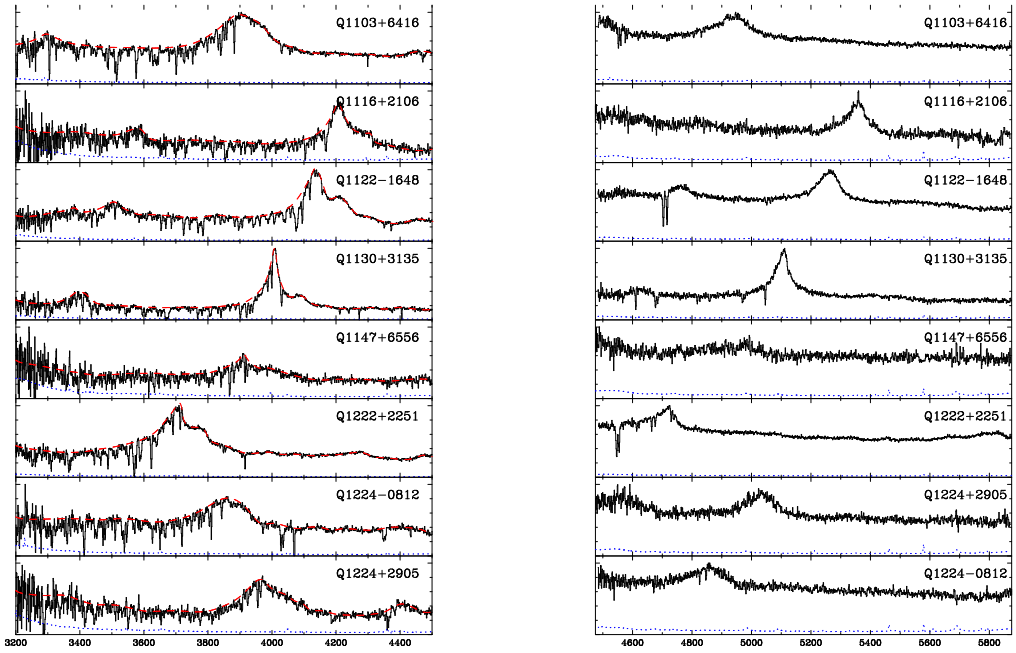

Figure 9.2: (continued)

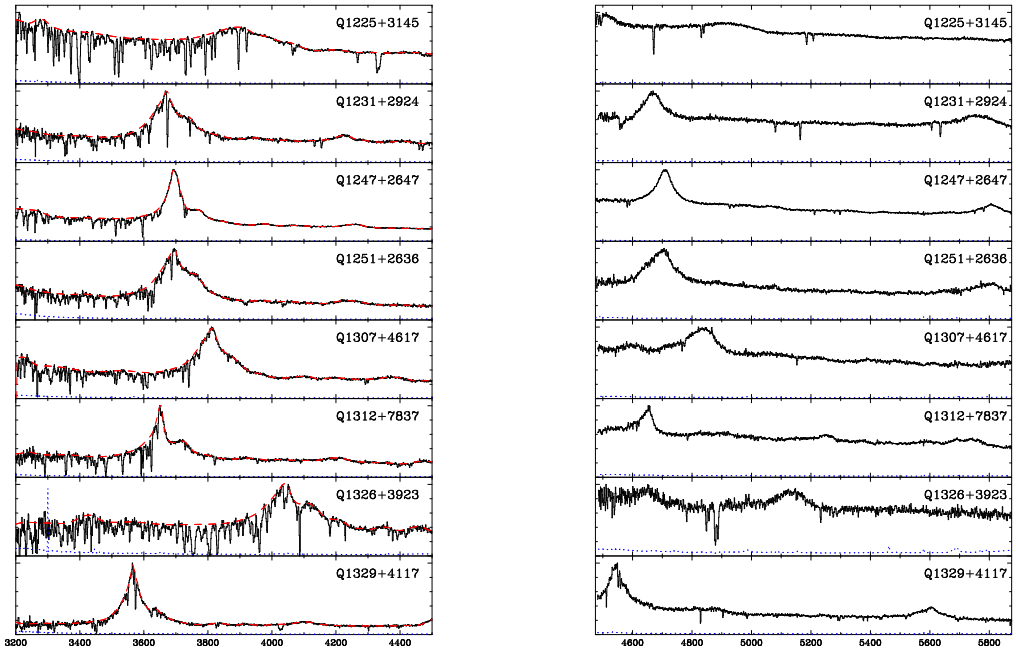

Figure 9.2: (continued)

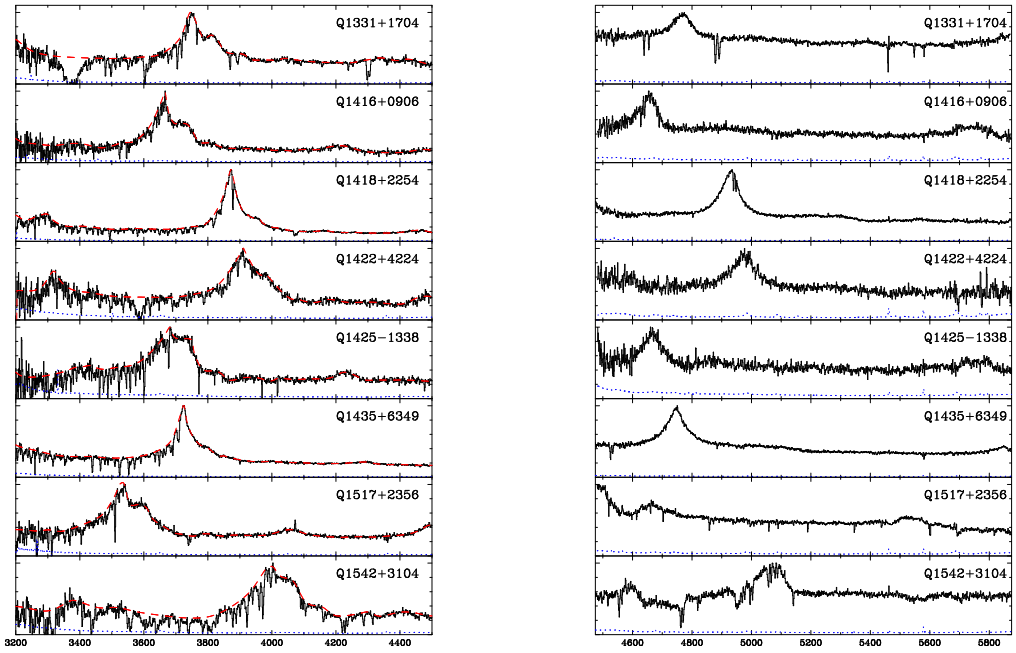

Figure 9.2: (continued)

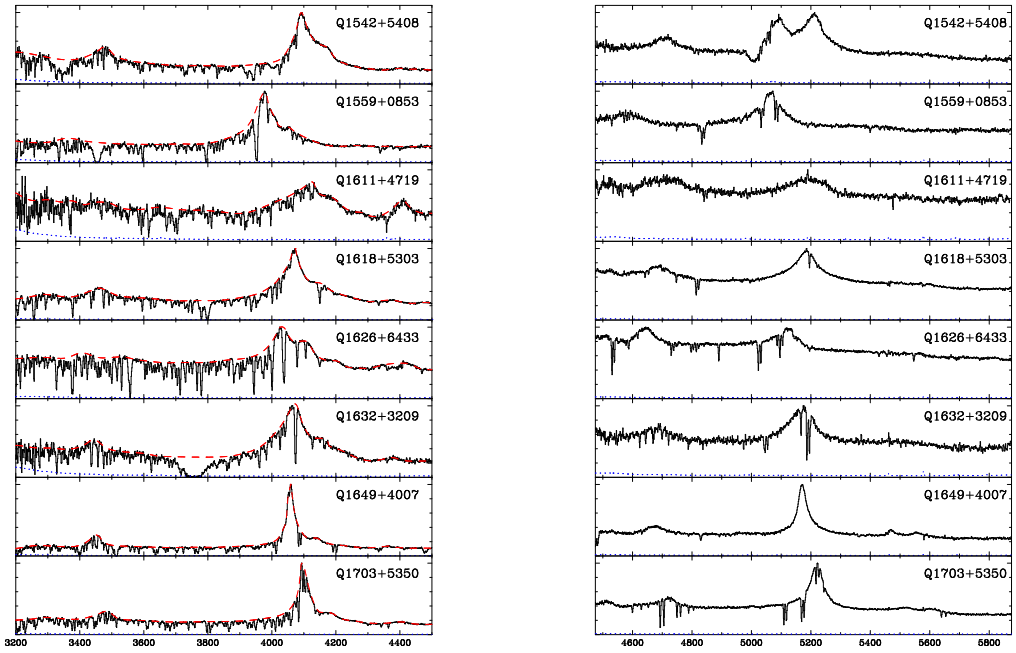

Figure 9.2: (continued)

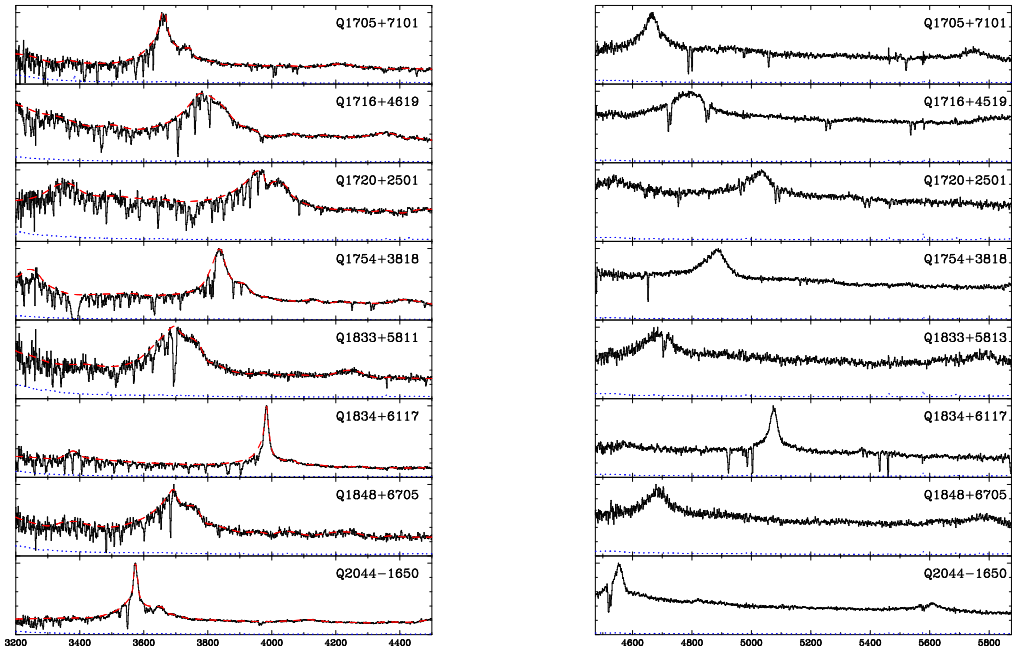

Figure 9.2: (continued)

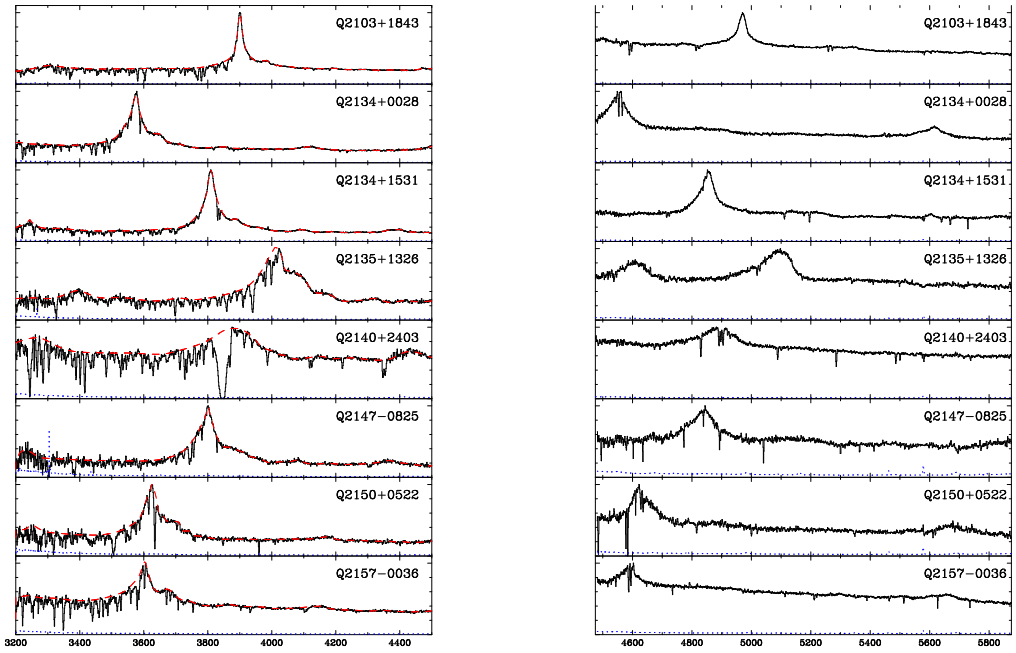

Figure 9.2: (continued)

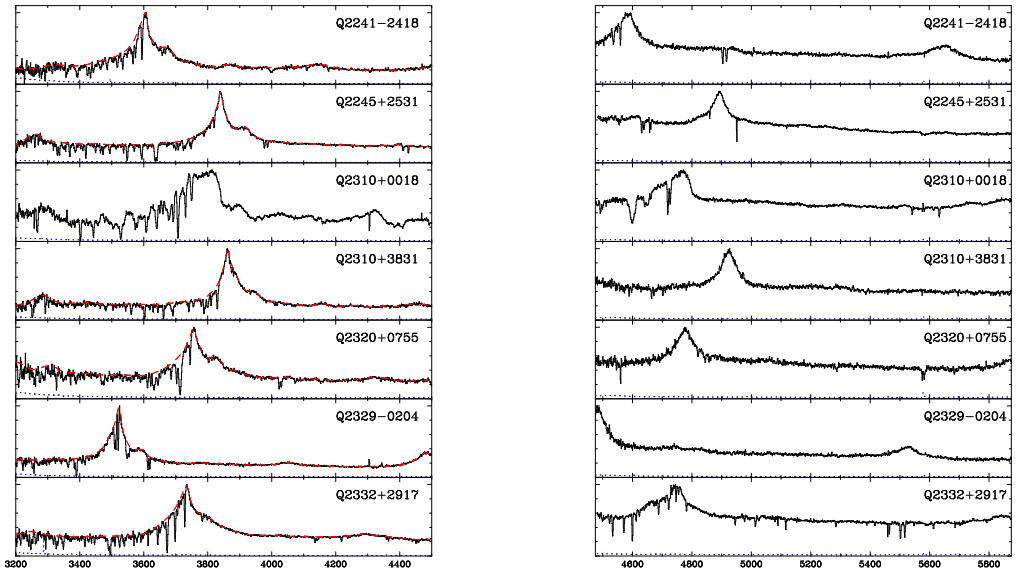

Figure 9.2: (continued)

Chapter 10

Cosmological Parameters from the Mean Flux Decrement at z $\sim$ 1.9

10.1 Abstract

We identify a concordant model for the intergalactic medium (IGM) at redshift $z = 1.9$ that uses popular values for cosmological and astrophysical parameters and accounts for all baryons with an uncertainty of 5%. The amount of absorption by H I in the IGM provides the best evidence on the physical conditions in the IGM, especially the combination of the mean gas density, the density fluctuations, the intensity of the ionizing flux, and the level of ionization. We have measured the amount of absorption, known as the flux decrement, DA, in the Lyα forest at redshift 1.9. We used spectra of 77 QSO that we obtained with 250 km s^{-1} resolution from the Kast spectrograph on the Lick observatory 3m telescope. We find that a hydrodynamic simulation on a 1024^3 grid in a 75.7 Mpc box reproduces the observed DA from the low density IGM alone when we use popular parameters values $H_o = 71$ km s^{-1}Mpc^{-1}, $\Omega_b = 0.044$, $\Omega_m = 0.27$, $\Omega_\Lambda = 0.73$, $\sigma_8 = 0.9$ and an ultraviolet background (UVB) that has an ionization rate per H I atom of $\Gamma_{912} = (1.44 \pm 0.11) \times 10^{-12}$ s^{-1}. This is 1.08 ± 0.08 times the prediction by Madau, Haardt & Rees (1999) with 61% from QSOs and 39% from stars. Our measurement

of DA gives a new joint constraint on these parameters, and DA is very sensitive to each parameter. Given fixed values for all other parameters, and assuming the simulation has insignificant errors, the error of our DA measurement gives an error on H_o of 10%, Ω_Λ of 6%, Ω_b of 5% and σ_8 of 4%, comparable to the best measurements by other methods.

10.2 Introduction

Using our Kast Quasar Survey data, we measure the total amount of neutral hydrogen in quasar spectra which we call the flux decrement, D_A. The shape of the quasar continuum in the Lyα forest was not well understood before, so we tested and calibrated our continuum fitting using artificial quasar spectra I generated. This calibration was done for the first time, and it was the key to perform precise measurement. I devised up the quasar database, led the target selection and the bulk of the observations and generating the artificial quasar emission spectra.

In the analysis part, I performed a calculation to estimate the flux variance expected from the linear theory and simulations. The formulated and calculated the amplitude of the one dimensional flux power fluctuation. I started from the primordial 3D mass power spectrum, based on the linear perturbation theory, and evolved it using a proper growth factor with the first year WMAP cosmological parameters. I used the bias from McDonald (2003) which translates the matter power spectrum to the flux power spectrum, and projected 3D power to one dimensional power spectrum. I formulated the one dimensional window function to extract the flux fluctuation from the flux power spectrum. We can directly compare this flux fluctuation from the theory to the observed flux fluctuation, we report they are in a good agreement.

10.2.1 Background

Our physical understanding of the IGM comes from the detailed comparison of numerical simulations of the growth of structure in the universe with observations of the Lyα absorption from the H I in the IGM. Analytic models show that the amount of Lyα absorption depends on a combination of at least four factors: the mean density of H in the IGM, the power spectrum of the matter distribution that determines the amount of clumping of the H on various scales, the temperature of the gas, and especially the mean intensity of the UVB radiation that photoionizes the gas. Together these parameters, and their variation, give the density of H I down the line of sight to a QSO, something we observe with Lyα absorption.

The mean amount of absorption is a sensitive measure of the physical properties of the IGM. If we make some assumptions about the growth of structure and the temperature of the IGM, then the optical depth of the Lyα forest scales like (Rauch et al., 1997, Eqn. 17)

$$\tau_{\mathrm{Ly}\alpha} \propto (1+z)^6 H(z)^{-1} (\Omega_b h^2)^2 T^{-0.7} (\rho/\overline{\rho})^2 \Gamma_{912}^{-1}, \tag{10.1}$$

where ρ is the baryon density, $\overline{\rho}$ is the mean baryon density, Γ_{912} is the photoionization rate per H I atom, and T is the gas temperature.

10.2.2 Definition of D_A

Following Oke & Korycansky (1982) we define $\mathrm{D}_A = 1 - \langle F \rangle$ where $\langle F \rangle =$ (observed flux)/C, $C =$ (estimated unabsorbed continuum flux) which includes both the underlying power law and the flux from emission lines. It is common to see D_A expressed as $\langle F \rangle$, or as the mean effective optical depth, $\tau_{\mathrm{eff}} = -ln \langle F \rangle$.

We will measure D_A in individual pixels, and we will add suffixes to D_A to label averages over various wavelengths between the Lyα and Lyβ emission lines, sometimes averaged over many QSOs. We restrict our measurement of D_A to rest frame wavelengths

$$\mathrm{D_A wavelength\ range} = 1070 \text{ to } 1170 \text{ Å}. \tag{10.2}$$

The D_A is dominated by Lyα lines from the IGM, but it includes all absorption, including metal lines and the Lyα lines from Lyman limit systems (LLS) that are defined to have H I column densities log N_{HI}> 17.2 cm^{-2}. The LLS by definition include all damped Lyα lines (DLAs) that have $N_{HI} > 2 \times 10^{20}$ cm^{-2}.

10.3 Kast QSO Spectra

We obtained spectra of the Lyα forest of over 80 bright QSOs at $1.85 < z_{em} < 2.5$. We maintained a list of all such QSOs listed in NED, and updated it before each observing run. We found about 6000 QSOs of all magnitudes. We rejected those noted as BAL in NED, and we then observed the brightest remaining at declination North of -30 degrees. Most were 17th magnitude. We observed nearly all that were brighter than 17.5 and some that were 18th magnitude. We rejected BAL QSOs because they tend to show much more absorption than other QSOs. In the Lyα forest region this absorption is from N V, and other ions. BAL QSOs would also bias our estimates of the mean amount of metal line absorption because they can have huge amounts of C IV and Si IV absorption.

10.3.1 Observations

We obtained spectra from 2001 January 26 to 2003 July 28 with the Kast double spectrograph on the Shane 3m telescope at Lick observatory. We present the observing log and spectra in Tytler et al. (2004b). Here we use spectra obtained with the blue camera, using the grism with 830 groves per mm, blazed at 3460 Å, and covering approximately 3150 – 4300 Å.

We know from prior work with this instrument (Suzuki et al., 2003) that the typical dispersion is 1.13 Å per /pixel (107 km s^{-1}), and the FWHM resolution is 250 km s^{-1} (2.5 pixels), with a range of 200 – 300 km s^{-1}, depending on the temperature and the focus that we chose for that observing run. The spectral resolution varies with wavelength, and from run to run, even when the slit is unchanged. We

describe the data reduction and flux calibration in Tytler et al. (2004b).

We changed the flux in the occasional pixel, under 1% of all pixels, that was clearly erroneous because of poor cosmic ray or sky subtraction. We set such pixels to the expected level, to reduce the effect on the continuum fitting and the D_A estimate. Hence the spectra are cosmetically unusually clean.

10.4 D_A Measurement and its Error

We wish to compare the observed flux decrement D_A with the numerical simulation to extract cosmological parameters. However, as of today, it is difficult to simulate metal lines and DLA/LLS (Damped Lyman Alpha system / Lyman Limit System) which has a column density greater than log N_{HI} = 17.2 cm^{-2}since they have non-linear properties and complexed evolution mechanism. Therefore, it is essential to remove these contributions from the observed data.

We first measured D_A using 77 Kast spectra which includes Lyα, DLA/LLS, and the metal lines. We calibrated the measurements with artificial spectra which we know the continuum levels. We estimated the contribution from the DLA/LLS and metals from the statistics in the literature. We adopted 0.023 ± 0.005 for the metal line contribution and 0.01 ± 0.004 for the DLA/LLS contribution. Here I summarize the result. The detailed discussions can be found in Tytler et al. (2004a).

- Observed and flux calibrated D_A :

$$D_A(z = 1.9; Ly\alpha Forest + DLA/LLS + metals) = 0.151 \pm 0.007, \quad (10.3)$$

- D_A with metal lines subtraction :

$$D_A(z = 1.9; Ly\alpha Forest + DLA/LLS) = 0.128 \pm 0.009, \quad (10.4)$$

- D_A with metal lines and DLA/LLS subtraction :

$$D_A(z = 1.9; Ly\alpha Forest) = 0.118 \pm 0.01. \quad (10.5)$$

10.4.1 D_A Measurement Error

The absolute 1σ error terms associated with our D_A estimate are:

- 0.0064: Estimated from the dispersion in quarters of our sample. This includes sample variance and that part of the calibration error that varies between the quarters.
- 0.0032: Calibration error.
- 0.0048: Sample variance. from the size of our sample, (sometimes called cosmic variance).
- 0.005: Uncertainty in the amount of metal absorption.
- 0.004: uncertainty in the amount of absorption from Lyα lines with log N_{HI} > 17.2 cm^{-2}.

We obtained the 1 σ error = 0.01 by adding the above error terms in quadrature.

10.5 Variance of D_A and its Error

The variance of the flux decrement is as important as the mean flux decrement D_A. The variance of the Lyα forest directly reflects the density fluctuations of the universe that we are trying to measure.

- Observed and flux calibrated the standard deviation of D_A :

$$STD(D_A(z = 1.9); Ly\alpha Forest + DLA/LLS + metals) = 0.0612 \pm 0.0035, \tag{10.6}$$

- The standard deviation of the DLA/LLS :

$$STD(D_A(z = 1.9); DLA/LLS) = 0.0351 \pm 0.0047, \tag{10.7}$$

- The standard deviation of the metal lines :

$$STD(D_A(z = 1.9); metals) = 0.031, \tag{10.8}$$

- The estimated standard deviation of the Lyα forest :

$$STD(D_A(z = 1.9); Ly\alpha Forest) = 0.039^{+0.005}_{-0.007}. \quad (10.9)$$

As we have seen in the previous section, the amount of the flux decrement, D_A, is dominated by the Lyα forest (78%). The metal lines (15%) and DLA/LLS (7%) do not contribute a large fraction. However, to our surprise, the variance is equally divided by the Lyα forest (40%), DLA/LLS (33%) and metals (26%). In terms of standard deviation, the contributions are: Lyα forest (37%), DLA/LLS (33%), metals (30%). In Figure 10.1, we visualize these fraction. This observational fact means that if we have DLA/LLS in the spectrum, we have lots of metal lines associated with that system. On the other hand, if we don't have DLA/LLS, we do not see metal lines. This all or nothing effect makes. That is why the variance of metals and DLA/LLS are so large.

10.6 Dispersion of the D_A Value from a Simulation

We can calculate the expected variation in the amount of absorption in a spectrum. We restrict the calculation to the absorption from the Lyα lines in the lower density portions of the IGM, excluding absorption by the Lyα lines of LLS and metal lines. We introduce the notation $\sigma(\Delta z)$ for the standard deviation of the mean D_A in spectral segments of length $\Delta z = 0.1$. The $\sigma(\Delta z = 0.1)$ values are the 1D flux analogues of the 3D mass σ_8 values, (Kolb & Turner, 1990, Eqn 9.18, Fig 9.2). The $\sigma(\Delta z = 0.1)$ value is of great interest because it is a measure of the power in flux in the Lyα forest on scales of 153 Mpc, and it is related to the mass power spectrum.

McDonald (2003, Fig. 10a) shows that the relationship between the 3D matter and flux power depends on scale. On large scales the flux power is proportional to the matter power, and hence to σ_8^2. On small scales an increase in the matter power leads to larger velocities that smooth the fluctuations in the flux, and

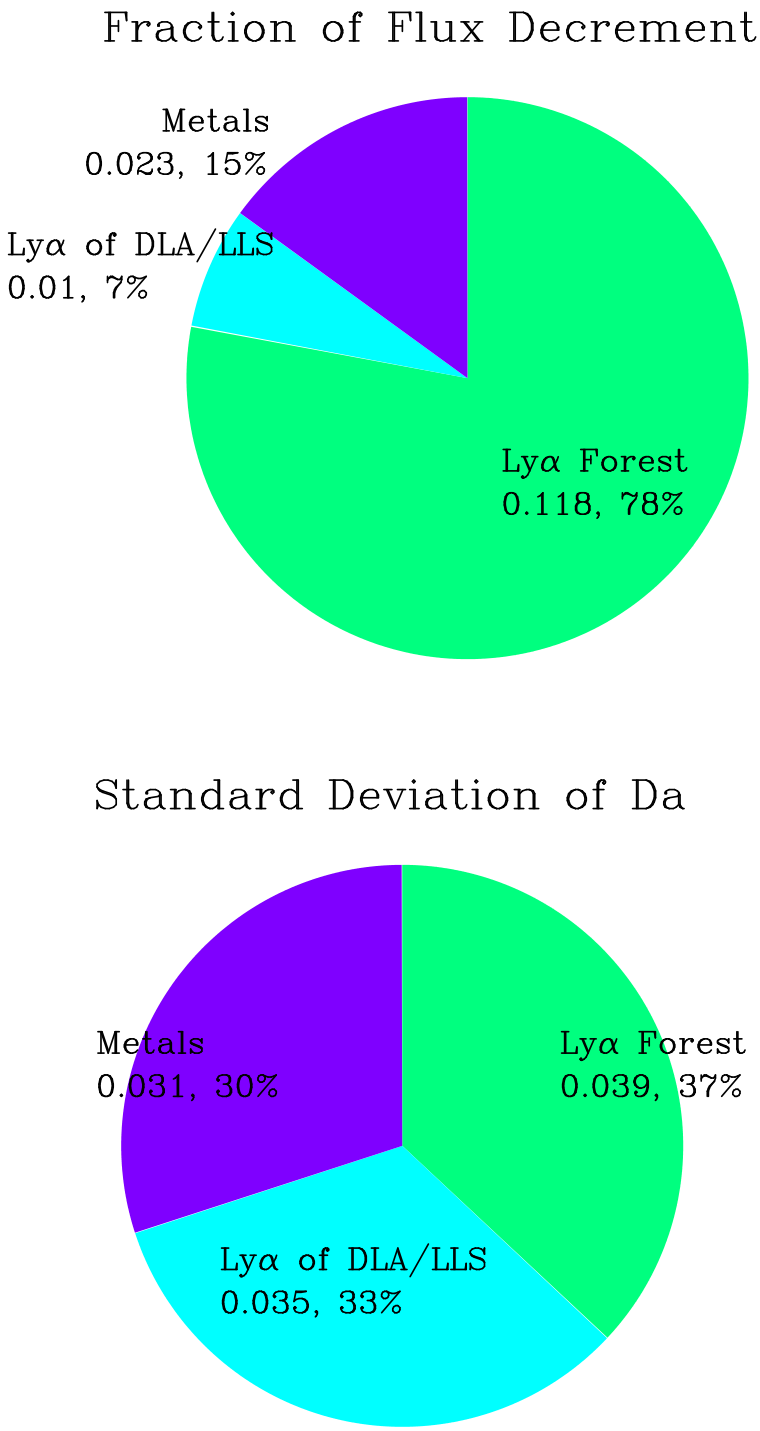

Figure 10.1: Fraction of the mean flux decrement D_A (top panel) and its standard deviating (bottom panel).

decrease the flux power. At a scale of $k \simeq 0.013$ (s/km) (1.5 Mpc) the flux power is insensitive to the mass power.

We can derive the variance of the D_A(Lyα forest) values by integrating the power spectrum of the flux over a top hat window function of width $\Delta z = 0.1$. First we generate the one dimensional flux power spectrum, $P_{F1D}(k)$, following McDonald (2003, Table 1). We use $\Omega_m = 0.23$, $\Omega_\Lambda = 0.73$, h=0.71, $\sigma_8 = 0.9$ and $n = 0.95$. For these values, and $z = 1.9$, we calculate $\delta A_1 = 0.6375$, where A_1 is the amplitude of the mass power spectrum at wavenumber $k_1 = 2\pi(h^{-1}\mathrm{Mpc})^{-1}$. We also use $\delta\overline{F} = 0.082$ to match the mean flux to our measured value, where $\overline{F} = 1 - D_A$ is the mean flux, and the δ values are the deviations from the values chosen by McDonald (2003). Then we calculate,

$$\sigma(\Delta z = 0.1)^2 = \frac{\langle F \rangle^2}{2\pi} \int_{-\infty}^{\infty} P_{F1D}(k) W^2(kR) dk \tag{10.10}$$

where $W(kR)$ is the top hat window function. We correct the result to our definitions of flux, since in our units McDonald (2003) uses $(F - < F >)/ < F >$, a flux deviation divided by the global mean flux at that z. For the one dimensional case, we have

$$W^2(kR) = \frac{2(1 - cos(kR))}{(kR)^2} \tag{10.11}$$

where $R = 152.57$ Mpc for $\Delta z = 0.1$.

We obtain $\sigma(\Delta z = 0.1) = 0.0386$ at $z = 1.9$ using $\sigma_8 = 0.9$, $n = 0.95$ and D_A=0.118 for the low density IGM alone.

The $\sigma(\Delta z = 0.1)$ value that we measured, $0.039^{+0.005}_{-0.007}$ is identical within the errors to the value that we calculated: 0.0386 for $\sigma_8 = 0.9$ and $n = 0.95$. Systematic effects from the photon noise, continuum fit and LLS – metal correlations should all have made our measured value too large, and hence the errors in the measurement may be larger than the values we quote. For fixed n and a fixed and known (McDonald, 2003) relationship between the flux and matter power spectra, $\sigma(\Delta z = 0.1) \propto \sigma_8$ and the errors that we quote on $\sigma(\Delta z = 0.1)$ imply $\sigma_8 = 0.90^{+0.13}_{-0.16}$. With improved measurements, quantities like $\sigma(\Delta z = 0.1)$ will provide useful new measurements of

the matter power spectrum, on larger scales than have been explored using the flux power spectrum (Croft et al., 2002b).

10.7 Comparison with Hydrodynamic Simulations

Parameters Derived from D_A

The values in Table 10.1 show that our measurement of D_A is accurate enough to give significant new cosmological information. This information is difficult to extract because D_A depends on at least six parameters. We would need to know all the other parameters to derive an unknown using D_A alone. We need to explore a six dimensions space to find the best concordance model, and to find the full errors on derived parameters. Hydrodynamic simulations on modern supercomputers are now up to this task that has become practical because we now have accurate prior measurement for the parameters.

The values collected in Table 10.1 show that the changes required in five of the six parameters of simulations A to match the observed D_A are modest. The exception is γ_{228} because D_A is insensitive to this parameter.

The uncertainties on the prior measurement of the six parameters lead to errors on D_A that have a factor of five range. The logarithmic mean of this range is similar in size to the error on our measurement of D_A. D_A responds to cosmological parameters much as do other observable quantities. It is not surprising that D_A depends on all six parameters, since these are the set required to model the universe in general, with the addition of the two γ parameters for the IGM. These six parameters provide a realization of Eqn. 10.1.

Our D_A value gives γ_{912} to higher accuracy than has been possible before, since the error of 0.1 on γ_{912} from Madau et al. (1999) seems optimistic and the proximity effect gives larger errors (Liske & Williger, 2001; Scott et al., 2002). We find $\gamma_{912} = 1.08 \pm 0.27$ or $\Gamma = (1.44 \pm 0.36) \times 10^{-12}$ s^{-1}, where the error now includes the contributions from the errors on Ω_b, σ_8 and D_A. Using Eqn. 3 of

Table 10.1. D_A for Various combinations of Cosmological Parameters

Parameter measured	Ω_b	σ_8	γ_{912}	γ_{228}	Da
all	0.0444 ± 0.0018	0.9 ± 0.1	1.0 ± 0.1	1.8	0.118 ± 0.010
DA in sim.	0.0440	0.9	1.0	1.8	0.1287 ± 0.0027
γ_{912}	0.0440	0.9	1.08 ± 0.08	1.8	0.118
σ_8	0.0440	0.94 ± 0.04	1.0	1.8	0.118
Ω_b	0.0417 ± 0.0022	0.9	1.0	1.8	0.118
γ_{912}	0.0444 ± 0.0018	0.9 ± 0.1	1.08 ± 0.27	1.8	0.118 ± 0.010

Note. — γ_{912} and γ_{228} are in unit of Haardt & Madau (1996).

Hui et al. (2002), this Γ_{912} value corresponds to an intensity of the UVB $J_{HI} = 0.33 \pm 0.08 \times 10^{-21}$ erg s^{-1} cm^{-2} Hz^{-1} sr^{-1}. The main contribution to this error is from the uncertainty in σ_8. We illustrated this in Figure **??**. We do not include the contributions to the error from Ω_Λ, H_o and γ_{228} because we do not know how these parameters are correlated with the others. However, from Table 10.1, they appear to add little to the total error on γ_{912}.

10.8 Acknowledgment

This Chapter 10, in part, is a reprint of the material as it appears in *Astrophysical Journal*, volume 617, page 1, 2004. The dissertation author led the target selection, devised up the database, did the bulk of the observations and generated artificial emission spectra and the fourth author of this paper.

Chapter 11

The HI Opacity of the IGM at redshifts $1.6 < z < 3.2$

11.1 Abstract

We use high quality echelle spectra of 24 QSOs to provide a calibrated measurement of the total amount of Lyα forest absorption (D_A) over the redshift range $2.2 < z < 3.2$. Our measurement of D_A excludes absorption from metal lines or the Lyα lines of Lyman limit systems and damped Lyα systems. We use artificial spectra with realistic flux calibration errors to show that we are able to place continuum levels that are accurate to better than 1%. When we combine our results with our previous results between $1.6 < z < 2.2$, we find that the redshift evolution of D_A is well described over $1.6 < z < 3.2$ as $A(1+z)^\gamma$, where $A = 0.0062$ and $\gamma = 2.75$. We detect no significant deviations from a smooth power law evolution over the redshift range studied. We find that the UV background at $z = 3$ is higher than expected, with an H I ionization rate of $\Gamma = 1.3 \times 10^{-12}$ s^{-1}, 1.3 times greater than the value given by Haardt & Madau III.

11.2 Introduction

This is another attempt to measure the flux decrement using Keck HIRES spectra. The advantage of high resolution spectrum is that the pixels are more likely to hit the continuum and makes our continuum fitting easier and more accurate. Also we can resolve sharp metal lines, and in the future, we plan to remove them by fitting all of the metal lines. In this chapter, we removed them statistically.

I led the data reduction, generated artificial quasar emission spectrum, and trained undergraduate students. I re-reduced and flux calibrated more than 600 Keck HIRES exposures with approximately 70 quasars. I established a library of response functions and high resolution standard star spectra, and developed a scheme to calibrate flux. Using the PCA technique, I generated 5,000 artificial quasar spectra to test our continuum fitting. I worked with undergraduate students. I gave a series of one hour lectures for the undergraduates over the last summer so that they can understand the basics of quasar spectrum. They are now well trained and can fit the continua very well. Here I present the results.

11.3 Background

The mean optical depth of the H I Lyα forest observed in the spectra of high redshift QSOs is one of the main pieces of information on the physical state of the intergalactic medium (IGM). This is because the optical depth of the Lyα forest ($\tau_{\rm eff}$) is sensitive to the combination of a wide variety of effects that we can collect under two main headings (Rauch et al., 1997). First, $\tau_{\rm eff}$ is sensitive to all the familiar parameters of the cosmological model, including Ω_Λ, Ω_m, Ω_b, the Hubble parameter and the parameters that describe the primordial power spectrum of density fluctuations. These parameters determine the density of Hydrogen per unit length, the conversion from Mpc to wavelength in a spectrum, and the spatial variations of the density. The second set of parameters are astrophysical, rather than primordial, and they determine the ionization of the Hydrogen. The IGM is highly photoionized

by ultraviolet photons from early stars and AGN. The $\tau_{\rm eff}$ is then sensitive to the time history of the intensity and spectrum of the UV background, or UVB. The energy input per photoionization, and the competition between photoheating and the cooling from the expansion together give the temperature of the IGM, an output rather than an input parameter.

Over the last decade numerical hydrodynamic simulations of the IGM have steadily improved in accuracy. We make artificial QSO spectra from the simulations and measure the statistical properties of the Lyα forest absorption in those spectra. As expected, we find that the absorption in the artificial spectra depends on the complete set of cosmological and astrophysical parameters. In Tytler et al. (2004, T04b) and Jena et al. (2005, J05) we showed how we can choose sets of input parameters for simulations that give artificial spectra that are statistically equivalent to the largest and best samples of real spectra. We can now use the simulations to decode the IGM.

When we match simulations to real QSO spectra we obtain joint constraints on the full set of cosmological and astrophysical parameters that we input to the simulations. We do not obtain constraints on individual input parameters, except when we fix all the many other parameters at values obtained from other observations.

We find that the statistical properties of the Lyα forest are highly sensitive to many of the input parameters (Tytler et al., 2004; Bolton et al., 2004; Jena et al., 2005). When we compare to calibrated real spectra, we can expect to obtain joint constraints on sets of parameters that are competitive with the best measurements from other types of observations. This motivates us to improve the accuracy of the measurement of the IGM.

We also find that the comparison between numerical simulations and real spectra of the Lyα forest provides the most accurate measurements of the intensity of the UVB (Rauch et al., 1997; Tytler et al., 2004; Jena et al., 2005; Bolton et al., 2004).

We have found that two statistics in particular provide a good summary

of the Lyα forest. One is the mean absorption $\tau_{\rm eff}$, and the other some measure of the clumping and temperature of the gas, such as the line width distribution, or the power spectrum of the QSO flux. In T04 we measured $\tau_{\rm eff}$ to high precision over the redshift range $1.6 < z < 2.2$. The aim of this paper is to extend the redshift range over which we can make detailed comparisons between simulations and data by providing a calibrated and precise measurement of the H I Lyα forest opacity over the redshift range $2.2 < z < 3.2$.

11.3.1 Previous Work

There has been extensive previous work dedicated to measuring the total amount of absorption in the Lyα forest, summarized in part by T04b and Meiksin & White (2004) and the references therein. Many of these measurements appear to differ, but Meiksin & White (2004) showed that much, but not all, of the disagreement between some measurements was caused by differences in treating errors. T04b discuss other differences that remain.

Although we have had spectra of the Lyα forest since 1972, it is only recently that we have had simulations of the quality to match highly accurate measurements of the mean amount of absorption.

The mean absorption is hard to measure for three reasons discussed at length in T04b: the continuum level, metal lines and sample size.

To measure the amount of absorption we must first guess the continuum prior to the absorption. This is relatively easy at $z \simeq 2$, hard at $z \simeq 3$ and very hard at $z > 4$ where there is little if any unabsorbed continuum remaining in the Lyα forest. T04b dealt with the continuum level by making and fitting artificial spectra that looked similar to the real spectra. They saw and fitted the emission lines in the Lyα forest of each individual spectrum (Tytler et al., 2004b). These lines vary a lot from QSO to QSO (Tytler et al., 2004b; Suzuki et al., 2005). Using the artificial spectra we were able to show that their continuum level was accurate to approximately 0.3%, after correction, and averaging over the Lyα forest of 77

QSOs.

The simulations that we compare to the Lyα forest spectra typically lack the resolution and physics required to give realistic metal absorption lines and Lyα lines from regions with column densities log N_{HI}> 17.2 cm^{-2} We then need a prescription for dealing with metal lines and strong Lyα lines in the Lyα forest. Some measurements ignore these lines, while others subtract some or most of them. At $z = 1.9$ T04b showed that the metal lines contributed 15% and strong Lyα lines 7% of the absorption in the Lyα forest. However, they each contributed about the same amount to the total variance of the absorption as did the Lyα absorption in the low density IGM.

The last requirement for an accurate measurement of the mean amount of absorption in the Lyα forest is a large sample, ideally at least tens of QSOs. It had long been noted that there is conspicuous variation in the amount of Lyα forest absorption from QSO to QSO (Carswell et al., 1982; Kim et al., 2001), and T04b showed that the amount of variation on scales of $\Delta z = 0.1$ (121 Å in the observed frame) is consistent with large scale structure for a primordial spectrum of perturbations with slope $n = 0.95$, and present amplitude $\sigma_8 = 0.9$

Following Oke & Korycansky (1982) we define D_A(z) = 1 - $\overline{F}(z)$, where $F(z)$ is the observed flux divided by the continuum level, and $\overline{F}(z)$ is the mean over many spectra at a given redshift. T04b found that D_A(z=1.9) = 0.151 ± 0.006 including all absorption at rest frame wavelengths 1070 – 1170 Å towards 77 QSOs. The error here is partly from the continuum level, and partly from the sample size. T04b estimated the metal line absorption from wavelengths between the Lyα and C IV emission lines, from both their own spectra and from spectra of Sargent et al. (1988). They estimated the strong Lyα lines from the statistics of such lines in other spectra. When they subtracted both the metal lines and strong Lyα lines the D_A drops to 0.118 ± 0.010. T04b estimated that approximately 5 ideal spectra, all at the same z_{em} with no continuum errors, and no metal lines or strong Lyα lines would give D_A with an error of 0.01 at a single redshift, $z = 1.9$. High resolution

spectra might approach this limit.

In Jena et al. (2005) we presented a set of 40 fully hydrodynamic simulations of the IGM at $z = 2$. We derived scaling laws that related the parameters of simulated spectra to the parameters that we input to the simulations. When we apply the scaling laws to a simulation, we can predict the output parameters to higher accuracy than the typical measurement error in real spectra. We were able to predict the most common line width (b-value) to 0.3 km s^{-1} and the $\tau_{\rm eff}$ to 0.0027, both approximately a factor of four smaller than the measurement errors in the real spectra. In this paper we address the need for improved measurements.

11.3.2 Our Approach

We apply the methods of T04b to make a calibrated measurement of D_A at $2.2 < z < 3.2$. The basic idea is that we will ensure that our continuum fitting is unbiased by simultaneously fitting our real data and artificial spectra that have been carefully prepared to exhibit the types of errors shown in real spectra. The hope is that any systematic errors in our continuum fitting will manifest themselves in our continuum fits to both the real data and the artificial data. We can then measure them in the artificial data and apply the appropriate corrections to our real data.

We will generally follow the details of T04b, with some specific exceptions. Here we made artificial continuum and emission line spectra using principal component spectra, rather than real HST spectra (Suzuki et al., 2005). We made the Lyα forest absorption from randomly placed Voigt profiles with parameter distribution functions taken from the literature, instead of using a simplified model of the IGM to produce the Lyα forest absorption. In addition, we added metal and strong Lyα lines to the artificial spectra. However the main difference is that we now use HIRES spectra with 8 km s^{-1} resolution in place of the 250 km s^{-1} resolution spectra that we used in T04b. The higher resolution comes with many times more photons per Å and allows us to place accurate continua at higher redshifts.

11.4 Data Sample

We use a collection of QSO spectra obtained with the HIRES spectrograph on the Keck telescope (Vogt et al., 1994b). These spectra were collected between 1994 and 2004, for a variety of programs. The 24 QSOs that we use in this paper were selected from among our HIRES spectra for the following reasons: (1) they have significant coverage for Lyα lines with $2.2 < z < 3.2$, (2) they have SNR 8 – 70 per 2.1 km s^{-1}, with a mean of 20 and (3) we were able to perform high quality flux calibration of the QSO spectra. The list of spectra we use in this paper is given in Table 1.

The spectra were all obtained with the original Tektronix 2048 x 2048 24 micron pixel CCD in HIRES up until August 2004. We used Tom Barlow's makee package to extract the CCD images and apply the wavelength calibration. The individual exposures were flux calibrated and combined via the procedure described in Suzuki et al. (2003). We measured the redshift of each QSO from the estimated peak of the Lyα emission line, which is given in Table 11.1 as $z_{\rm em}$ (e.g. $z_{\rm em}$ is not the systemic redshift of the QSO).

A histogram of the number of different QSOs that contribute to each $\Delta z = 0.1$ redshift bin is shown in Figure 11.1.

11.5 Artificial Spectra

We attempted to make artificial spectra that mimic real spectra in every important way, including emission lines, cosmic ray hits, echelle blaze, and flux calibration errors. For each real spectrum, we made four artificial spectra with the same redshift and noise properties and various absorption lines.

We made the unabsorbed continuum shape, including emission lines with the principal component spectra described by Suzuki et al. (2005). The artificial spectra have a wide variety of shapes, and include realistic emission lines between Lyα and Lyβ. The exact shape and strength of the emission lines was different for

Table 11.1. HIRES Lyα forest spectra used to measure D_A

Name	RA (B1950)	DEC (B1950)	$z_{\rm em}$	V
Q0014+8118	00 14 04.45	+81 18 28.6	3.366	16.50
Q0042-2627	00 42 06.42	-26 27 45.3	3.289	18.47
Q0100+1300	01 00 33.38	+13 00 12.1	2.681	16.57
Q0105+1619	01 05 26.97	+16 19 50.1	2.640	16.90
Q0119+1432	01 19 16.21	+14 32 43.2	2.870	16.70
Q0130-4021	01 30 50.28	−40 21 51.0	3.023	17.02
Q0139+0008	01 39 40.85	+00 08 17.8	3.405	18.32
Q0301−0035	03 01 07.70	−00 35 03.0	3.231	17.62
Q0322−3213	03 22 11.18	−32 13 34.6	3.302	17.95
Q0450−1310	04 50 54.00	−13 10 39.0	2.300	16.50
Q0449−1645	04 49 59.00	−16 45 09.0	2.677	17.00
Q0741+4741	07 41 42.05	+47 41 53.4	3.210	17.50
Q0930+2858	09 30 41.40	+28 58 53.0	3.428	17.50
Q1005+3638	10 05 44.13	+36 38 02.4	3.125	17.85
Q1155+2640	11 55 07.62	+26 40 37.0	2.850	17.60
Q1200+1539	12 00 57.62	+15 39 36.1	2.981	17.10
Q1208+1011	12 08 23.81	+10 11 08.5	3.822	17.90
Q1243+3047	12 43 44.90	+30 47 54.0	2.560	17.00
Q1244+3143	12 44 48.83	+31 43 02.9	2.961	17.90
Q1320+3927	13 20 41.02	+39 27 46.8	2.985	17.06
Q1337+2123	13 37 47.92	+21 23 54.1	2.700	17.90
Q2223+2024	22 23 13.32	+20 24 58.5	3.560	18.38
Q2337+1845	23 37 13.08	+18 45 12.2	2.620	17.00
Q2344+1229	23 44 13.2	+12 28 50	2.784	17.5

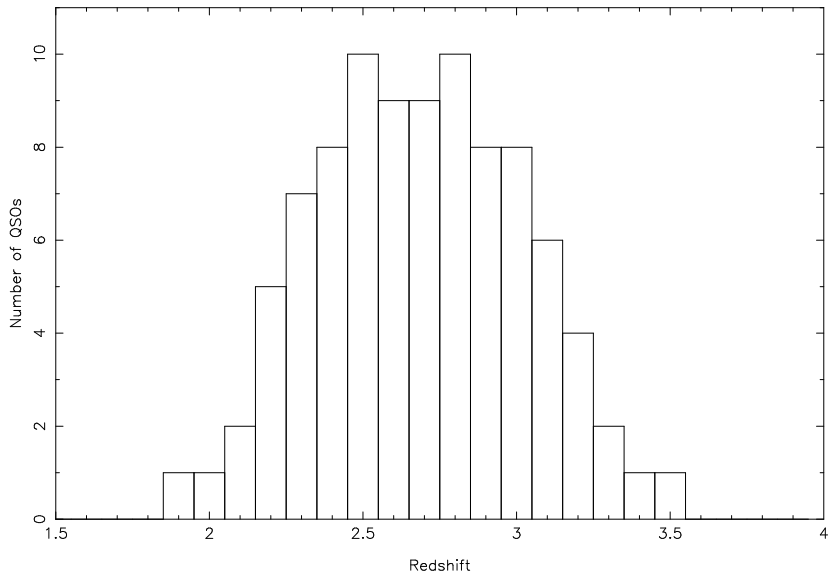

Figure 11.1: The number of HIRES QSOs which have complete Lyα forest coverage in different redshift bins

each artificial spectrum.

We made the H I absorption from discrete lines, with the line distribution functions given in Kirkman & Tytler (1997). The artificial spectra used in this paper have lines of all column densities, $10^{10} < \mathrm{N_{HI}} < 10^{18}$ cm^{-2}, and we placed lines at random redshifts, from the z_{em} listed in Table 1, down to zero redshift.

If a real spectrum had a DLA with log $\mathrm{N_{HI}} > 10^{19.5}$ cm^{-2}, we added a line with the same log $\mathrm{N_{HI}}$ at the same wavelength to all the accompanying artificial spectra.

With each H I absorber, we also added the strong doublet absorption lines of C IV, Si IV, and Mg II to the artificial spectrum. We held the H I/X column density ratio constant for each metal ion, and the width of each metal absorber was calculated by assuming that the H I b values were entirely thermal. This resulted in a artificial metal forest that was superimposed on the H I forest, which made the artificial spectra look more realistic when inspected closely.

The artificial spectra used in this paper were generated differently than the spectra we used for the same purpose in T04b. The spectra in T04b were generated

via a toy model of the IGM that mimicked the large scale structure, but we did not add metal lines of the Lyα lines of Lyman limit systems.

We added noise to the artificial spectrum, and attempted to match the approximate SNR level of each real spectrum. We based the noise levels in our simulated spectra upon the estimated error estimates in the real echelle spectra. The resulting artificial spectra have SNR similar to their real spectra except for three of the five with SNR > 45, where the artificial have lower SNR too low by approximately 1.5.

We also added a blaze effect to the artificial noise levels to simulate the increased SNR obtained at the center of each echelle order. Furthermore, we added small fluxing errors, by offsetting different echelle orders by the blaze function multiplied by a Gaussian random deviate with $\sigma = 2\%$, which is larger than the expected fluxing errors in the data (Suzuki et al., 2003). In Figure 11.2 we show an example of artificial spectra, below the real spectra they approximate.

Although we see differences between our artificial and real spectra, they do not concern us. Since we placed the Lyα lines at random redshifts, the artificial spectra lack large scale structure. The artificial spectra also show more total absorption than real spectra, generally about 5% more total absorption over the redshift range $2.4 < z < 3.0$. As we show in the next section, we are able to fit continua very well for a wide range of total absorption, so we do not believe that the minor differences between our real spectra and the artificial ones have significantly changed our results.

11.6 Continuum Fitting

Four undergraduate authors, SH, KJ, CM, and GS, took a training program to fit to fit QSO continua. They fit artificial QSO spectra that were not matched to any specific QSO. These spectra had a variety of emission redshifts, SNR, emission line profiles, and flux calibration errors. The four all fit the same spectra, and after

they completed a few spectra, we revealed the true continuum level and we discussed their fit. Within a few weeks two of them were able to fit continua as well as any of us.

After this training completed, we asked them to fit the real and matched artificial spectra. We provided spectra in sets comprising one real spectrum and two artificial ones matched to that real one. Each fitter was given the same copy of the real spectrum, but different versions of the artificial spectra. We did not reveal which was the real spectrum in a set.

The results indicate that the two best fitters were excellent. The other two fitters were less accurate, and more importantly, occasionally had made large fitting errors. Thus for the measurement of D_A, we used the average continuum of the two best fitters, and do not discuss the results of the other two fitters any further.

The standard deviation of the continuum fit errors per spectral segments of length $\Delta z = 0.1$ is 1.2%. We fit a total of 96 artificial spectra, four per QSO (two per fitter per QSO), and there were a total of 275 segments of length $\Delta z = 0.1$ in these artificial spectra. Averaged over all 275 segments, the continua of the two best fitters were above the true continua by 0.29 %. If the fits were unbiased, and the errors per segment were uncorrelated we would expect the bias to be $1.2\sqrt{275} = 0.07$ %. As in T04b we have measured a small bias.

In Figure 11.3 we show a weak correlation between the error in the continuum fit to the artificial spectra and the mean amount of absorption in a spectral segment of length $\Delta z = 0.1$. We fit this correlation as bias $B = 0.0098 - 0.0249 D_A$ and we corrected all our real continua using this fit to remove the trend. After this correction the when we average over all artificial spectra there is no remaining bias. All the data on the real HIRES spectra that we give in the paper have had this correction applied. We followed a similar procedure in T04b. After removing the bias associated with mean flux of each spectral segment, we see no correlation between the error in the continuum fit to the artificial spectra and their SNR. We have not measured whether the bias varies from object to object, or as a function

of z.

Based upon our ability to continuum fit artificial spectra, we conclude that errors in continuum placement are not a significant source of error when measuring D_A in high resolution, moderate SNR spectra at $z < 3.0$.

11.7 Measurement of the Mean Flux

To avoid confusion between multiple Lyman series lines, we restrict our analysis to the region between the Lyα and Lyβ emission lines of each QSO. To avoid continuum fitting problems associated with rapidly changing emission line profiles, and possible contamination from the proximity effect, we further restrict our measurement of D_A to the rest frame wavelengths 1070 – 1170 Å.

We removed DLA/LLS systems which have the column density log N_{HI} greater than 17.2 cm^{-2}, and masked their associated metal lines. They are collapsed highly non-linear systems, but what we want to extract from the Lyα forest is the signature of the primordial density fluctuations. Thus, we need to remove these systems as well as metal lines which we cannot simulate. For the metal lines, we removed them statistically Tytler et al. (2004a).

11.7.1 Measurement of mean D_A in $\Delta z = 0.1$ spectral segments

After masking targeted Deuterium systems and LLS with obvious Lyα lines, we measured the mean flux in spectral segments of $\Delta z = 0.1$. We started at a rest wavelength of 1070 Å (or the lowest wavelength with data in cases of incomplete spectral coverage) in each QSO, and computed the mean flux of all segments that are fully contained between the rest wavelengths of 1070 and 1170 Å. There are typically three $\Delta z = 0.1$ segments in an individual QSO spectrum. We discard incomplete segments and any segment with more than 10% of it's flux masked for any reason, e.g. a DLA in a spectrum will cause at least one, and frequently two segments in a given QSO spectrum to be discarded. Finally, we subtracted the anticipated metal

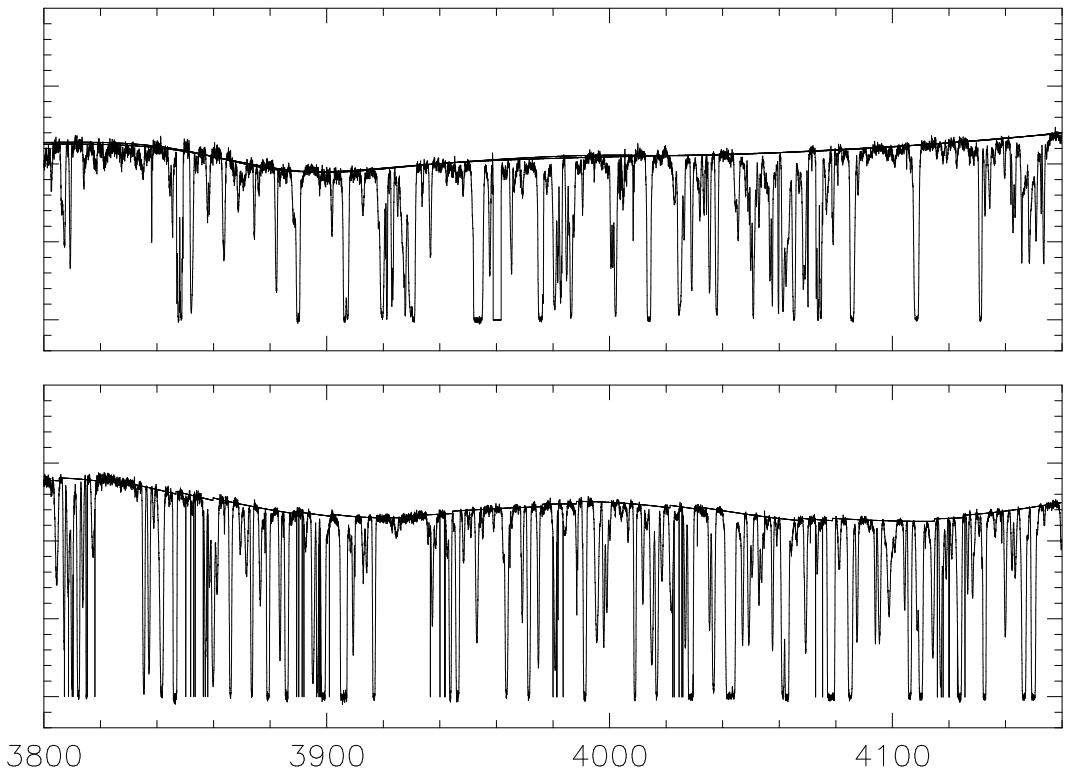

Figure 11.2: Example of our data, our continuum fits, and the artificial spectra we used to verify our continuum fitting ability. The top panel shows the spectrum of Q1243+3047 along with the individual continuum fits of our two best fitters. The bottom panel shows one of the four artificial spectra that we made similar to the Q1243+3047 spectrum. Q1243+3047 is representative of the spectra at the top end of the SNR distribution for spectra used in this paper. The lowest major tick mark is the zero flux level. We show rest wavelengths 1070 – 1170 Å.

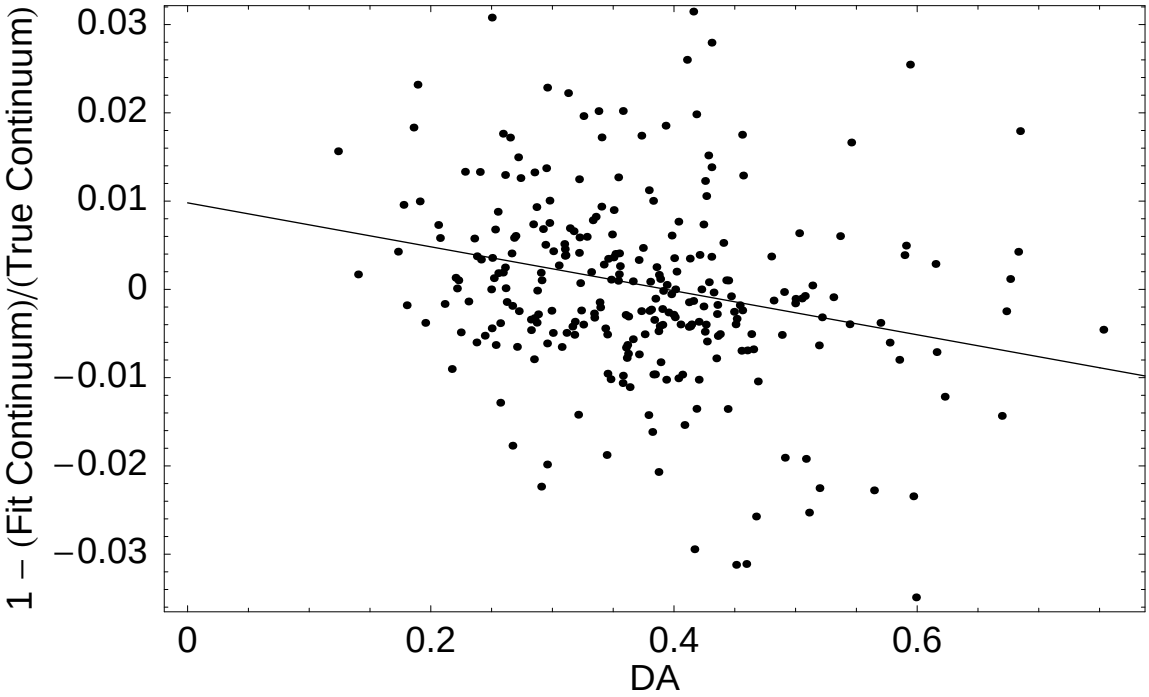

Figure 11.3: The difference between the fit continuum level and the true continuum level for each $\Delta z = 0.1$ segment in the artificial spectra. We plot this difference against the mean D_A in each spectral segment. There is a weak trend with the amount of absorption, which we fit with the solid line. There are more points on this plot than we have in our real data, because we fit four artificial spectra for each real spectrum in our analysis. Note that the magnitude of the effect is quite small.

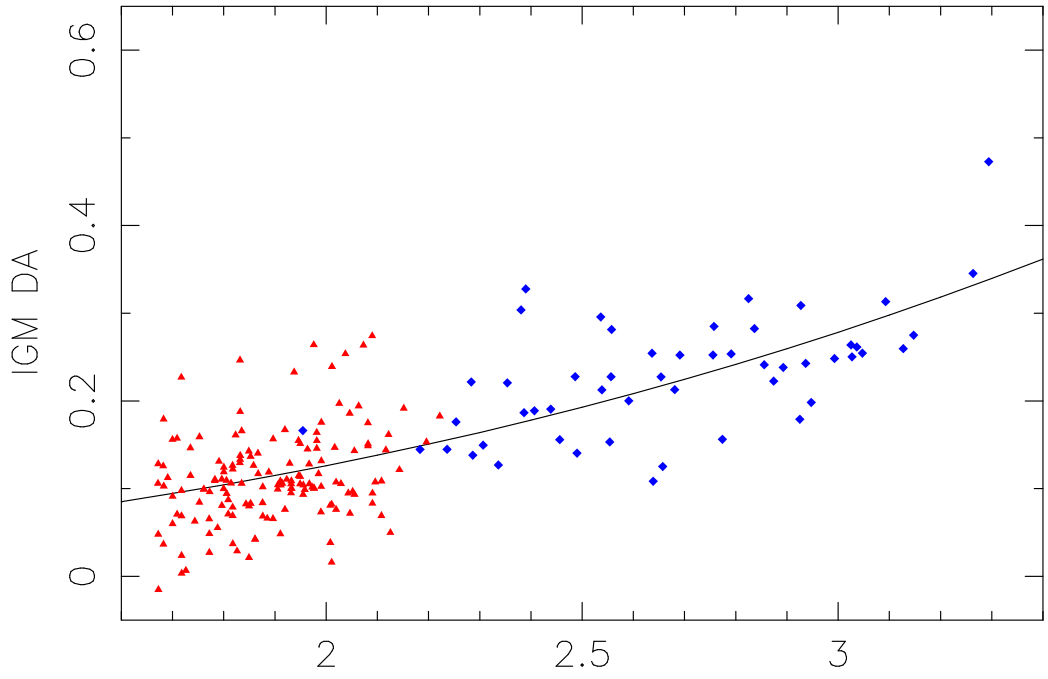

Figure 11.4: D_A as a function of redshift. Each point shows the D_A measured along a particular line of sight over a path of length $\Delta z = 0.1$. The light triangles are the data from 77 QSOs used by T04b (observed total absorption, minus mean absorption by Lyα of LLS and metals), while the dark diamonds show the new data from 24 QSOs from this paper (excluding individual Lyα of LLS, and minus the mean metal absorption). This plot does not show part of the data at the higher redshift end of each spectrum because we do not show bins that are partly sampled by a spectrum.

absorption from each segment.

Our results are shown in Figure 11.4, where we also show the results for the Kast spectra from T04b. Figure 11.4 shows only the absorption of the low column density Lyα forest – we have attempted to remove the Lyα of all LLS and all metal line absorption for all the Kast and HIRES spectra. For both the HIRES and Kast spectra we subtracted the same mean amount of metal absorption from each Kast point. For the Lyα of the LLS we subtracted the mean for all the Kast points, but we masked individual Lyα lines for the HIRES points.

Table 11.2. Measured IGM D_A values in $\Delta z = 0.2$ redshift bins

z center	D_A	STD D_A	Fit D_A	Fit STD D_A
1.6	0.098	0.015	0.0851	0.0057
1.8	0.099	0.006	0.1044	0.0055
2.0	0.128	0.006	0.1262	0.0055
2.2	0.143	0.013	0.1507	0.0054
2.4	0.202	0.014	0.1780	0.0059
2.6	0.213	0.014	0.2083	0.0074
2.8	0.250	0.016	0.2417	0.0101
3.0	0.252	0.015	0.2783	0.0139
3.2	0.338	0.024	0.3183	0.0187

11.7.2 D_A as a function of redshift

To tabulate the mean D_A as a function of redshift, we binned the data shown in Figure 11.4 into redshift bins of width $\Delta z = 0.2$. We estimated the mean D_A of each bin to be simply the mean value of the points in the bin. We estimated the error to be the standard deviation of *all* the points (see §11.7.3, we compute the standard deviation from the best power law fit to the data) divided by the square root of the number of points in each bin. Using the standard deviation of all points instead of the standard deviation of just the points in each bin gives nearly identical results for bins with large numbers of points, but seems to be much better behaved for bins with small numbers of points. Our results are in Table 11.2 and shown in Figure 11.5.

D_A as a function of z is well fit by a power law of the form $A(1+z)^\gamma$. Minimizing χ^2 to the points in Table 11.2 gives $A = 0.0062$ and $\gamma = 2.75$. The χ^2 of the best fit is 8.69 and the reduced χ^2 for 7 degrees of freedom (9 data points - 2 parameters) is 1.24.

The dashed lines in Figure 11.4 enclose the $\pm 1\sigma$ confidence interval fits.

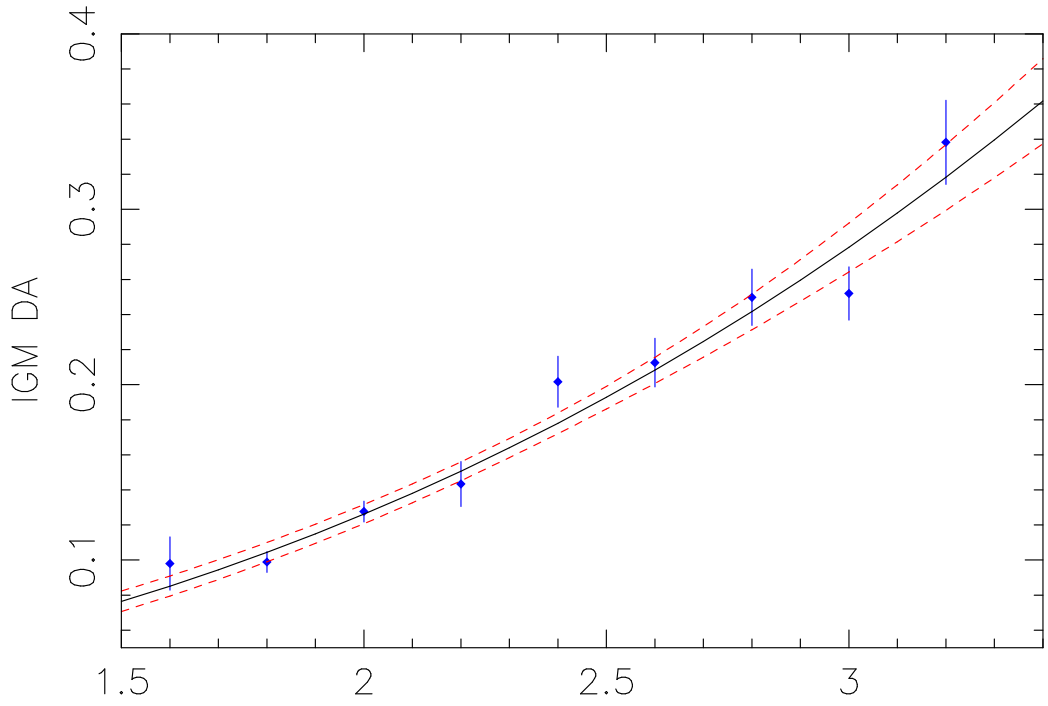

Figure 11.5: D_A as a function of redshift. Here we have binned the data points shown in Figure 11.4 into bins of $\Delta z = 0.2$. The solid line shows the minimum χ^2 fit of the function $A(1+z)^\gamma$. We find $A = 0.0062$ and $\gamma = 2.75$ give $\chi^2 = 8.69$ for seven degrees of freedom. The dashed lines show the $\pm 1\sigma$ confidence interval on the fit.

They are produced by taking the envelope that contains all power law fits with $\chi^2 < \chi^2_{\rm min} + 2.3$. Thus the plotted error bounds are not power laws, but each point on the error curves corresponds to a point on a power law that fits our data. The last column in Table 11.2 gives the difference between the bounds divided by two.

We do not give errors for A or for γ. The $A - \gamma$ χ^2 manifold is complex, and it is not well approximated by only two number (σ for A and γ). Attempts to do so in the past (Steidel & Sargent, 1987; Press et al., 1993; Kim et al., 2001), have led to all sorts of confusion in the literature – consider the efforts of Seljak et al. (2003) and Meiksin & White (2004) to determine the allowed values of $\tau_{\rm eff}$ at various redshifts. We recommend use of the results given in Table 11.2.

Note that the small dip in $\rm D_A$ that we observed at $z > 2.2$ in Fig. 22 of T04b is not present in the new HIRES data. The combined HIRES + KAST data seems to be well fit by a single power law, and no significant deviations from a power law are present in our data.

11.7.3 Dispersion of $\rm D_A$ in $\Delta z = 0.1$ spectral segments

The new points from this work show less dispersion than the points in T04b. This is consistent with the fact that we have removed LLS absorption before calculating the mean flux in each point, while T04b calculated the mean flux in each point with the LLS present, and then subtracted the LLS absorption statistically. While both results will give the same mean value for the H I Lyα forest opacity, the T04b method will include the substantial dispersion of the LLS absorption.

The standard deviation of the HIRES $\rm D_A$ points (each covering $\Delta z = 0.1$) about the mean given by the power law fit is $\sigma_{D_A} 5.2^{+0.6}_{-0.4}$ % over redshifts $2.2 < z < 3.2$. This σ_{D_A} value includes the intrinsic variance of the Lyα forest, the variance of metal line absorption (we removed the mean, not the individual metal absorption), and the variance of our continuum fitting errors. It should not include a significant contribution from LLS absorption, since we masked the Lyα absorption associated with LLS before measuring any $\rm D_A$ values.

We can subtract variances (squares of standard deviations) to estimate the standard deviation of the absorption by Lyα from the low density IGM alone. As in T04 §9, we work with mean values in segments of length $\Delta z = 0.1$. We now repeat the calculations given in T04, considering only the HIRES spectra. We take the standard deviation of the metal absorption as 3.7 %, where we have scaled the value 3.1 % in Table 4 of T04b by the mean metal absorption which is now DM = 2.76 %, up from 2.3 %. We also use the standard deviation of the continuum fitting errors 1.2 % (§11.6). We find that the intrinsic variation of the mean amount of absorption in the Lyα forest over $\Delta z = 0.1$ segments is $\sigma(\Delta z = 0.1) = 3.4^{+1.0}_{-1.2}$ %). This value is a mean from the whole z range, centered near $z = 2.7$. At $z = 2.7$ the mean total D_A per segment, including metals but not Lyα lines of LLS, is 0.246, and after subtracting the metals it drops to 0.2246.

The $\sigma(\Delta z = 0.1)$ value from HIRES spectra agrees with the value that we calculated in T04b (section 9.4) for Kast spectra: $\sigma(\Delta z = 0.1) = 3.9^{+0.5}_{-0.7}$ % at $z = 1.9$. The error is larger now, because we have fewer D_A measurements giving a larger error on the measurement of the standard deviation of the D_A values. We expect that $\sigma(\Delta z = 0.1)$ will increase with increasing z because the power spectrum of the flux in the Lyα forest increases with increasing redshift (Croft et al., 2002b; McDonald et al., 2004). We do not see this, but this may be because our measurement errors are large and not well determined. In T04b we did not subtract the continuum fitting error because it appeared to be small, and was not well determined. We found contradictory evidence that the continuum fit error might be large, in which case the $\sigma(\Delta z = 0.1)$ value should be less than the $3.9^{+0.5}_{-0.7}$ %.

We conclude that 24 QSOs is adequate to get the mean D_A, but we would prefer far more QSOs to obtain an accurate measurement of the variance in the D_A.

11.8 Discussion

Our D_A results are in general agreement with the values of the literature summary given in Meiksin & White (2004, Table B1). However, we find approximately 0.03 less absorption at all redshifts. This is consistent with the fact that we have attempted to measure only the absorption due to the Lyα forest, while Meiksin & White (2004) gave values for all absorption in the Lyα forest region of a spectrum.

At $z = 2.2$, our results are also consistent with Schaye et al. (2003), who also attempted to measure only the absorption associated with the Lyα forest. They only removed metals absorption they could identify directly in the absorption spectra, so their removal completeness is unknown, and is probably a function of redshift. However, we find a shallower redshift evolution and less absorption at $z = 3.0$.

The best fit value of $D_A = 0.278$ at $z = 3.0$ is lower than we expected to find when we started this work. In T04b and J05 we developed a concordance model of the Lyα forest at $z = 1.9$ – this model is referred to as model "A" in T04b and J05. Model A uses a uniform UVB with the shape and redshift evolution due to Haardt & Madau (2001), and displayed graphically in Paschos & Norman (2005). Model A, while giving the measured value of D_A at $z = 1.9$, predicts $D_A = 0.34$ at $z = 3$. The clear implication is that there are more ionizing photons at $z = 3$ than predicted by Haardt & Madau (2001). J05 showed that the naive expectation that $\tau_{\rm eff}$ scales like the H I ionization rate is valid at $z = 2$. Assuming that this result holds at $z = 3$, and translating D_A into $\tau_{\rm eff}$, we find an H I ionization rate of $\Gamma_{-12} = 1.3 \pm 0.1$ s^{-1}, or 1.3 ± 0.1 times the value predicted by Haardt & Madau (2001). It will be interesting to try to find the source of these extra photons.

11.9 Acknowledgment

This Chapter 11, in part, is a reprint of the material as it appears in *Monthly Notices of Royal Astronomical Society*, volume 360, page 1373, 2005. The

dissertation author did the bulk of the data reduction and calibration and the third author of this paper.

Appendix A

Flux Calibration Tools

A.1 Introduction

This appendix describes the algorithm used in chapters 4, 5, 6 and 11. As is discussed in these chapters, the flux calibration plays an important role in precise measurements. The Keck HIRES spectrograph is not designed to produce flux calibrated data, and we should expect the change of the effective response due to vignetting.

I developed two methods to flux calibrate HIRES data. The first method is to make use of a simple well flux calibrated one dimensional spectrum taken by Lick Kast spectrograph or Keck ESI. The second method is a simple flux calibration using high resolution standard star spectrum. The following two sections will describe how the algorithm works with examples.

A.2 Flux Calibration with KAST/ESI

A.2.1 How to use the code:

The program is installed on our machine called **genesis**. To run the program, all we need to prepare is an input file which contains the basic information on the quasar and the list of relevant FITS data. An example for a D/H quasar

q1243+3047 is located in our cvs directory: **cvs/fluxtools/q1243**. Then, type:

```
>cd cvs/fluxtools/q1243
>../nsbin/fluxhires_with_kast inputfile_kast
```

It would create a new directory, called "fluxed_data_kast", and all of the relevant postscript files and calibrated FITS and ascii files are stored in that directory. An example of an input file called "inputfile_kast" contains the following information.

```
CC HIRES Fluxing using KAST data

            reference='kast'    ! Name of the Reference Spectrograph

CC Quasar's Properties:
              lylimit=3215.0    ! Ly Limit(abs) Wavelength (A)
           lyemission=4330.0    ! Ly alpha Emission Wavelength (A)

CC Kast Data Properties:
          db_lickvpix=107.1d0   ! Kast Data Pixel Size (km/s)
         defaultvfwhm=285.0     ! Starting Default Kast FWHM (km/s)

CC Input Kast Spectrum
      orglickfluxname='./rawfits/q1243lickstis01f.fits'
       orglickerrname='./rawfits/q1243lickstis01e.fits'

CC Input  : A List of HIRES Spectra
        hiresfluxlist='./rawfits/q1243hiresflux.list'
         hireserrlist='./rawfits/q1243hireserr.list'

CC Output : Velocity Corrected/Shifted Kast Spectrum
```

```
          lickfluxname='./rawfits/q1243lickstis01rf.fits'
           lickerrname='./rawfits/q1243lickstis01re.fits'

cc Output : Flux Calibrated 1D Spectrum
       fluxed_1d_ascii='./q1243_kast01fluxed_v68.dat'
       fluxed_1d_fitsf='./q1243_kast01_v68f.fits'
       fluxed_1d_fitse='./q1243_kast01_v68e.fits'
```

Flux calibration with KAST or ESI uses the same code with different inputfile. The flux calibrated output data should have a unit of Angstrom (Å) in wavelength and cgs ($F_\lambda : 10^{-15} erg/s/cm^2/\mathring{A}$) in flux. The wavelengths are binned in log linear scale.

A.2.2 Limitations of the code and cases when the code breaks

Case 1: FWHM and Pixel Sizes of the Reference Spectrum

Now, the code is optimized for KAST/ESI spectrum. If we wish to use data from other spectrograph, we need to adjust the resolution (FWHM) and the pixel size. The relevant subroutines are `subroutine lick_crosscorr` and `subroutine lick_vfwhm`. Both of them searches a certain number of pixels to find the best cross-correlation and the best FWHM. We need to optimize the number of pixels to search.

Case 2: Log linear binning

The input reference spectrum has to be in a log linear binning. If it is in linear binning, the code fails.

Case 3: MAKEE Output

We assume the HIRES data is reduced by MAKEE. If we use something else, we may need to adjust the data array which is defined on the top of the code. The code writes out and uses an include file called 'prototype.inc' in which we define

the size of the data array. For now, we assume the maximum number of pixels per row is 2048 and the number of echelle orders is 50. Thus we have a number of data array which has a dimension of (2048,50). We may need to change the size of the dimension if we wish to apply larger CCD chip or outputs other than MAKEE.

A.2.3 Overview

In this section, we describe the algorithms used in the flux calibration code. The main body of the code consists of seven subroutines which correspond to the following seven steps. The basic ideas are described in chapter 4, and the relevant section and subroutines are shown in the parenthesis below.

Step 1: Matching Wavelength (§4.7.1, `subroutine lick_crosscorr`)

Step 2: Matching Resolution (§4.7.2, `subroutine lick_vfwhm`)

Step 3: Calculating the Conversion Ratio (§4.7.3, `subroutine get_cr`)

Step 4: Smoothing the Conversion Ratio (§4.7.4, `subroutine smooth_cr`)

Step 5: Applying the Conversion Ratio (§4.7.5, `subroutine xtest_fluxhires`)

Step 6: Calculating the Mean Spectrum (§4.8, `subroutine xgetmeanflux`)

Step 7: Combine Echelle Orders (§4.8, `subroutine xtestmergeorders`)

In the following sections, we stick with practical procedures. We introduce an example and show their results.

A.2.4 Algorithms and Subroutines

Step 1: Matching Wavelength (§4.7.1, `subroutine lick_crosscorr`)

The accuracy of wavelength calibration of the KAST or ESI data is not as high as the HIRES data. They typically has an offset by a half pixel even after we apply vacuum and heliocentric correction to the spectrum. Kast and ESI has a pixel size of 107.1 km/s and 11.5 km/s respectively while HIRES has 2.1 km/s. Thus a half pixel offset of the KAST/ESI data corresponds to a large number of HIRES pixels, and the wavelength mismatch causes errors in flux calibration. We have not yet identified

the source of these wavelength errors. But it is necessary to correct wavelength error using HIRES data. First we measure the wavelength shift using cross-correlation. Using default FWHM, we generate degraded HIRES spectrum and obtain rebinned spectrum, $h(\lambda_i)$. We follow HIRES reduction software MAKEE's binning scheme whenever we need to introduce rebinning.

$$\lambda_j = \lambda_0 \cdot exp\left(\frac{\Delta v}{c} \cdot (j-1)\right), \tag{A.1}$$

where Δv is the binning size in velocity (km/s), c is the speed of light, λ_0 is the zero wavelength which we take 3000 Å and j is the pixel ID. This equation relates the wavelength in velocity to the wavelength in Å. We take cross-correlation $c(n)$ from degraded and rebinned HIRES spectrum $h(\lambda_i)$ and KAST/ESI spectrum $f(\lambda_i)$:

$$c(n) = \frac{1}{N s_f s_h} \sum_{i=1}^{N} f(\lambda_i) h(\lambda_i + n), \tag{A.2}$$

where n is the number of shifted HIRES pixel, N is the total number of pixels in an echelle order, λ_i is the pixel counting of the spectrum in an echelle order, and s_h and s_g are defined as:

$$s_h^2 = \frac{1}{N} \sum_{i=1}^{N} h^2(\lambda_i). \tag{A.3}$$

In practice, we calculate above procedures, degradation and cross-correlation, in Fourier space to make the code faster. The cross-correlation n vs. $c(n)$ is shown in Figure A.1. c(n) peaks at n_{max} where both HIRES and KAST/ESI data match in wavelength. In Figure A.2, we plot n_{max} vs. wavelength and each data point corresponds to an echelle order. We fit a smooth chebyshev polynomial curve to the data points (Figure A.2), apply the fitted curve (wavelength shift) to KAST/ESI data and generate a wavelength corrected KAST/ESI spectrum.

We run the code again to check if the wavelength is properly corrected. In Figure A.3 and A.4, we plot the same properties as in Figure A.1 and A.2, and we detect no obvious wavelength shift. Thus, we claim that the wavelength of KAST/ESI data is well corrected.

Step 2: Matching Resolution (§4.7.2, `subroutine lick_vfwhm`)

The next step is to find the resolution of KAST/ESI data so that we can make HIRES data similar to KAST/ESI data. We degrade HIRES data using different resolution (FWHM), apply temporal conversion ration (CR), which we will discuss in the next step, and calculate χ^2 value between degraded HIRES data and KAST/ESI data. We wish to find the FWHM which makes χ^2 minimum. We degrade HIRES spectrum $H(\lambda)$ using 2σ truncated gaussian filter $g(x,\sigma)$, and obtain the degraded spectrum with a certain resolution FWHM, $DH(\lambda,\sigma)$:

$$DH(\lambda,\sigma) = \int_{-2\sigma}^{+2\sigma} H(\lambda - x)g(x)dx \Big/ \int_{-2\sigma}^{+2\sigma} g(x,\sigma)dx, \tag{A.4}$$

where $g(x,\sigma)$ is a gaussian filter:

$$g(x,\sigma) = \frac{1}{\sqrt{2\pi}\sigma} e^{-\frac{x^2}{2\sigma^2}}, \tag{A.5}$$

and we recall the relationship between σ and FWHM is:

$$\sigma = \frac{FWHM}{2\sqrt{2\,ln\,2}} \tag{A.6}$$

$$= 0.42466 \cdot FWHM. \tag{A.7}$$

Likewise, we can calculate degraded HIRES 1σ error $\delta DH(\lambda,\sigma)$ from HIRES 1σ error array $\delta H(\lambda)$ as follows:

$$\delta DH(\lambda,\sigma) = \left(\int_{-2\sigma}^{+2\sigma} \frac{g(x)}{\delta H^2(\lambda - x)} dx \Big/ \int_{-2\sigma}^{+2\sigma} g(x,\sigma)dx \right)^{-\frac{1}{2}} \tag{A.8}$$

Then we rebin degraded HIRES $DH(\lambda,\sigma)$ (Figure A.7) into KAST/ESI pixels and obtain degraded and rebinned HIRES spectrum $h(\lambda,\sigma)$:

$$h(\lambda,\sigma) = \int_{\lambda-\frac{\Delta\lambda}{2}}^{\lambda+\frac{\Delta\lambda}{2}} \frac{DH(\lambda,\sigma)}{\delta DH^2(\lambda,\sigma)} dx \Big/ \int_{\lambda-\frac{\Delta\lambda}{2}}^{\lambda+\frac{\Delta\lambda}{2}} \frac{1}{\delta DH^2(\lambda,\sigma)} dx, \tag{A.9}$$

where $\Delta\lambda$ is the size of the rebinning pixel, and we can calculate 1σ error in the following way:

$$\delta h(\lambda,\sigma) = \left(\int_{\lambda-\frac{\Delta\lambda}{2}}^{\lambda+\frac{\Delta\lambda}{2}} \frac{1}{\delta DH^2(\lambda,\sigma)} dx \Big/ \int_{\lambda-\frac{\Delta\lambda}{2}}^{\lambda+\frac{\Delta\lambda}{2}} dx. \right)^{-\frac{1}{2}} \tag{A.10}$$

Then we can calculate the reduced χ^2 value for a resolution FWHM:

$$\chi^2(\sigma) = \frac{1}{N-1}\sum_{i=1}^{N}\frac{(f(\lambda_i) - h(\lambda_i,\sigma))^2}{\delta f(\lambda_i)^2}, \tag{A.11}$$

where N is the total number of pixels in an echelle order, and $\delta f(\lambda_i)$ is a 1σ error of the KAST/ESI data. Here we assume the error from the HIRES data is negligible ($\delta h(\lambda) << \delta f(\lambda)$)when we degrade it. In Figure A.5, we plot FWHM vs. χ^2. We can find the χ^2 minimum from the parabola and that x-value is the resolution we are looking for. When S/N is low, the χ^2 parabola is not in a good shape, and we find it difficult to find FWHM. But we can extrapolate or interpolate from the neighboring echelle orders. We show Echelle Order vs. FWHM in Figure A.6. In this figure, the echelle order is numbered from blue to red wavelength. We hope the resolution is uniform throughout the KAST spectrum, but in practice, the resolution could be non-uniform. This is because we optimize the focus of KAST spectrograph at a certain wavelength, and possibly the edges of the spectrum is slightly out of focus which lowers the resolution. We can barely see the trend in Figure A.6, and the resolution is highest in the middle, but since the change is not so significant, we just take the average of FWHM points. Since the HIRES has its own resolution $\mathrm{FWHM}_{HIRES} \sim 8km/s$, the resolution of KAST, FWHM_{KAST}, can be calculated in a quadrature form using above measured FWHM:

$$FWHM_{KAST} = \sqrt{FWHM^2 + FWHM^2_{HIRES}}. \tag{A.12}$$

In our example, we estimate $FWHM = 254.8km/s$ and $FWHM_{KAST} = 254.9$ km/s with measurement error of $\pm 19.8km/s$.

Step 3: Calculating the Conversion Ratio (§4.7.3, `subroutine get_cr`)

Now, we are ready to compare the KAST data with the degraded HIRES data. We calculate what we call conversion ratio (CR) which transfers the flux information from KAST/ESI to HIRES. We define CR as degraded hires spectrum divided by KAST/ESI spectrum:

$$CR(\lambda) = \frac{h(\lambda)}{f(\lambda)}, \tag{A.13}$$

and the error can be calculated using Gauss' error propagation law:

$$\delta CR(\lambda) = \sqrt{\frac{1}{h^2(\lambda)}\delta h^2(\lambda) + \left(\frac{h(\lambda)}{f(\lambda)}\right)^2 \delta f^2(\lambda)} \tag{A.14}$$

In Figure A.8 (left panel), we plot the raw CR in 2D which is similar to the original CCD image and the wavelength goes from the bottom left to the top right. In the right panel, we plot the same 2D CR image but normalized near the center using the average of ± 15 % of pixels from the center of the echelle order. In normalized 2D plot, we can see more detailed and complexed structures of CR. We wish to remove spiky CR features which is not real and find underlying smooth CR function. The spiky features appear at the wavelengths of high column density absorption lines because both the denominator and the numerator of CR gets close to zero, and it does not represent underlying CR. To remove spikes, we perform 2σ rejection using 3rd order chebyshev polynomial fit (Figure A.9). Thus, it is useful to have the CR error, and we can see the S/N of CR is getting higher with wavelength and poor at the edges of echelle orders and wavelengths where we have absorption lines in A.10. In Figure A.11, we show the 2σ rejected CR in 2D. We mask 2σ rejected pixels.

Step 4: Smoothing the Conversion Ratio (§4.7.4, `subroutine smooth_cr`)

Now, we wish to find a smooth function which represents CR. In chapter 4, we used 1D fit to each echelle order, but we can take the advantage of neighboring echelle orders since they are similar and help us to avoid erroneous CR fit. We use Chebyshev polynomials to the 2D surface and find the best fit by minimizing χ^2 via singular value decomposition technique:

$$\chi^2 = \sum_{j=1}^{N}\sum_{i=1}^{M} \frac{(CR(\lambda_j, i) - Chebyshev(\lambda_j, i))^2}{\delta CR^2(\lambda_j, i)}, \tag{A.15}$$

where λ_j is the wavelength, i is the echelle order, N is the total number of pixels, m is the order of echelle, M is the total number of echelle orders, $CR(\lambda_j, i)$ is a 2σ rejected CR, $Chebyshev(\lambda_j, i)$ is a 5th order chebyshev polynomial fit, and $\delta CR(\lambda_j, i)$ is the 1σ CR error.

Failed Example : On the course of code development, we tried to use gaussian filter for smoothing. But it did not give us satisfactory result. We can obtain smoothed CR, $SCR(\lambda, i)$:

$$SCR(\lambda, i) = \int_{-2\sigma_x}^{+2\sigma_x} \int_{-2\sigma_y}^{+2\sigma_y} CR(\lambda - x, i - y) g(x) g(y) dx dy \Big/ \int_{-2\sigma_x}^{+2\sigma_x} g(x) dx \int_{-2\sigma_y}^{+2\sigma_y} g(y) dy, \tag{A.16}$$

where g(x) and g(y) are gaussian filter as before, σ_x corresponds to a resolution in 1σ. We define σ_y as:

$$\sigma_y = \frac{\sigma_x}{\Delta\lambda}, \tag{A.17}$$

where $\Delta\lambda$ is the pixel size. Gaussian filter has a disadvantage. It degrades CR and destroys real CR features. We show gaussian smoothed CR in Figure A.13. We could reproduce the similar CR features as smooth function fit. However, if we compare it with Figure A.12, we notice that the CR features are degraded and the height of CR, which is real, is reduced by several percent which is unacceptable. Thus, we abandoned gaussian smoothing method.

Step 5: Applying the Conversion Ratio (§4.7.5, `subroutine xtest_fluxhires`)
Now, we are ready to apply smoothed CR to the HIRES data. We have found 2D smooth function, but we are missing smoothed CR at edges of the echelle orders. As we can see in Figure A.12, every echelle order starts and ends in a different horizontal pixel position, a few pixels are missed, but we do not want to lose these pixels. Therefore, we extrapolate at the edges. In Figure A.14, we show the extrapolated CR smooth function in 1D. Finally, we can obtain flux calibrated HIRES spectrum $FH(\lambda, i)$ (Figure A.15):

$$FH(\lambda) = \frac{H(\lambda)}{Chebyshev(\lambda)}, \tag{A.18}$$

where $H(\lambda)$ is HIRES data (MAKEE's output), and $Chebyshev(\lambda)$ is the smooth function for CR. We apply the same formula to the error array $\delta H(\lambda)$ so that we can keep the same S/N, and we obtain the flux calibrated error array, $\delta FH(\lambda)$. In Figure A.16 and A.17, we show the spectra of the echelle order overlapping region.

Step 6: Calculating the Mean Spectrum (§4.8, `subroutine xgetmeanflux`)

We have multiple exposures on the same object. We flux calibrate each exposure individually, namely, we repeat **Step 3-5** for each exposure, and find slightly different CRs, but we should have similar flux calibrated HIRES data $FH(\lambda, k)$ where k stands for $k$the exposure frame out of n exposures. We wish to obtain the mean spectrum, $\mu(\lambda)$. We take the weighted mean:

$$\mu(\lambda) = \sum_{k=1}^{n} \frac{FH(\lambda,k)}{\delta FH^2(\lambda,k)} \Big/ \sum_{k=1}^{n} \frac{1}{\delta FH^2(\lambda,k)}, \tag{A.19}$$

and the weighted error:

$$\delta\mu(\lambda) = \left(1/\sum_{k=1}^{n} \frac{1}{\delta FH^2(\lambda,k)}\right)^{-\frac{1}{2}}. \tag{A.20}$$

We do not divide $\delta\mu(\lambda)$ by $\sqrt{n}$ to get the error on the mean because we found that the error on the mean is too small to represent 1σ error of the data. We also tried to use simple standard deviation from multiple exposures, but the error gets too big and dominated by low S/N data. Therefore, we concluded that simple weighted mean and error is a good representation of the data.

In Figure A.18, we show the mean flux calibrated spectrum and its 1σ error. Using the mean flux calibrated spectrum $\mu(\lambda)$ and its weighted error $\delta\mu(\lambda)$, we can calculate the chi^2 value for an exposure k:

$$\chi^2(k) = \frac{1}{N-1} \sum_{i=1}^{N} \frac{(FH(\lambda_i,k) - \mu(\lambda_i))^2}{\delta\mu(\lambda_i)^2}, \tag{A.21}$$

where k stands for kth exposure, and i for an pixel in an echelle order N is the total number of pixels in an order. In Figure A.19, we test χ^2 distribution of the 7 exposures we used. This test is for MAKEE's error array rather than our flux calibration since we keep S/N and do not change the relative relationship between flux and error array. If we understand the error correctly, the χ^2 distribution should follow:

$$f_n(\chi^2) = \frac{1}{2^{\frac{n}{2}}\Gamma\left(\frac{n}{2}\right)} \left(\chi^2\right)^{\frac{n}{2}-1} e^{-\frac{\chi^2}{2}}, \tag{A.22}$$

where n is the degree of freedom and Γ is a Γ function. We plot both observed χ^2 distribution and the expected χ^2 distribution in Figure A.19. In general, they agree quite well, but in red wavelength, the observed χ^2 value is a bit smaller than expected, meaning our error is a bit bigger than expected. In an echelle order which has our main Lyα absorber, the observed χ^2 distribution is distorted. It implies that the observed error is too small. Probably, the size of the error at the bottom of absorption where we have zero flux is too small.

Step 7: Combine Echelle Orders (§4.8, `subroutine xtestmergeorders`)

The last step is to merge echelle orders and obtain 1D spectrum. We take weighted mean and error when we have overlaps which happens at the edge of echelle orders. In overlap region, we have 2 spectra at the same wavelength λ_i. Suppose we have $f_{blue}(\lambda_i)$ and $f_{red}(\lambda_i)$ for flux and $\sigma_{blue}(\lambda_i)$ and $\sigma_{red}(\lambda_i)$ for error. The merged spectrum $f(\lambda_i)$ should be:

$$f(\lambda_i) = \sigma^2(\lambda_i) \left(\frac{f_{blue}(\lambda_i)}{\sigma^2_{blue}(\lambda_i)} + \frac{f_{red}(\lambda_i)}{\sigma^2_{red}(\lambda_i)} \right), \tag{A.23}$$

where the weighted error σ_{λ_i} is :

$$\sigma(\lambda_i) = \sqrt{\frac{\sigma^2_{blue}(\lambda_i)\, \sigma^2_{red}(\lambda_i)}{\sigma^2_{blue}(\lambda_i) + \sigma^2_{red}(\lambda_i)}}. \tag{A.24}$$

We introduce the following statistics to assess the goodness of the order merging. First we introduce reduced χ^2-like statistics:

$$\chi^2 = \frac{1}{N-1} \sum_{i=1}^{N} \frac{\left(f_{blue}(\lambda_i) - f_{red}(\lambda_i)\right)^2}{\sigma^2_{blue}(\lambda_i) + \sigma^2_{red}(\lambda_i)}, \tag{A.25}$$

where N is the total number of overlapping pixels. If everything goes well, we expect to have the above reduced χ^2 to be close to unity. In Figure A.20, we show 1D flux calibrated mean spectrum with echelle orders in colors. In this particular example, our reduced χ^2 value is 1.31 which is not bad. However, this is not real χ^2, and as we have seen in the previous section, sometimes error array is not that accurate, we introduce another simple and practical statistics:

$$\Delta = \left| 1.0 - \frac{1}{N} \sum_{i=1}^{N} \frac{f_{blue}(\lambda_i)}{f_{red}(\lambda_i)} \right|, \tag{A.26}$$

where N is the number of pixels whose S/N of both $f_{blue}(\lambda_i)$ and $f_{red}(\lambda_i)$ are greater than 3 in the wavelength overlapping region. Δ simply represents the average absolute disagreement of the flux level in fraction. In our example, $\Delta = 0.0067$, meaning 0.67% averaged offset over 11722 pixels which we can claim that they are in a good agreement.

Finally, we obtain 1D flux calibrated mean spectrum (Figure A.10). The code creates 2 FITS files (flux and error) and an ascii file. The ascii file has 4 columns. The first column is wavelength, the second is flux, the third is error and fourth column is Tom Barlow's MAKEE's ID, j, for the wavelength (Equation A.1).

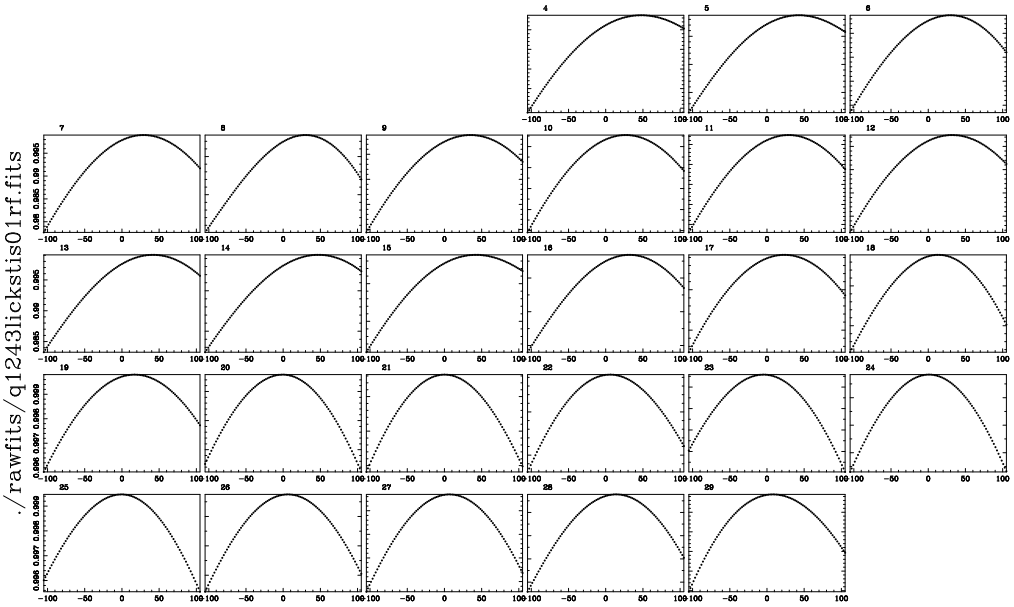

Figure A.1: Measuring KAST data wavelength shift using HIRES data. Each box corresponds to an echelle order, and the wavelength increases from top left to the bottom right. The x-axis is the number of shifted HIRES pixel n, and the y-axis is the cross-correlation value $c(n)$. The parabola should peak at n_{max} where both spectra match in wavelength. In this example, we see +40 HIRES pixel offset at the blue end of the KAST spectrum. (The name of output postscript file from the flux calibration code is '10_KAST_shift_vs_crosscorr.ps' and is shown hereafter in the parentheses in figure captions)

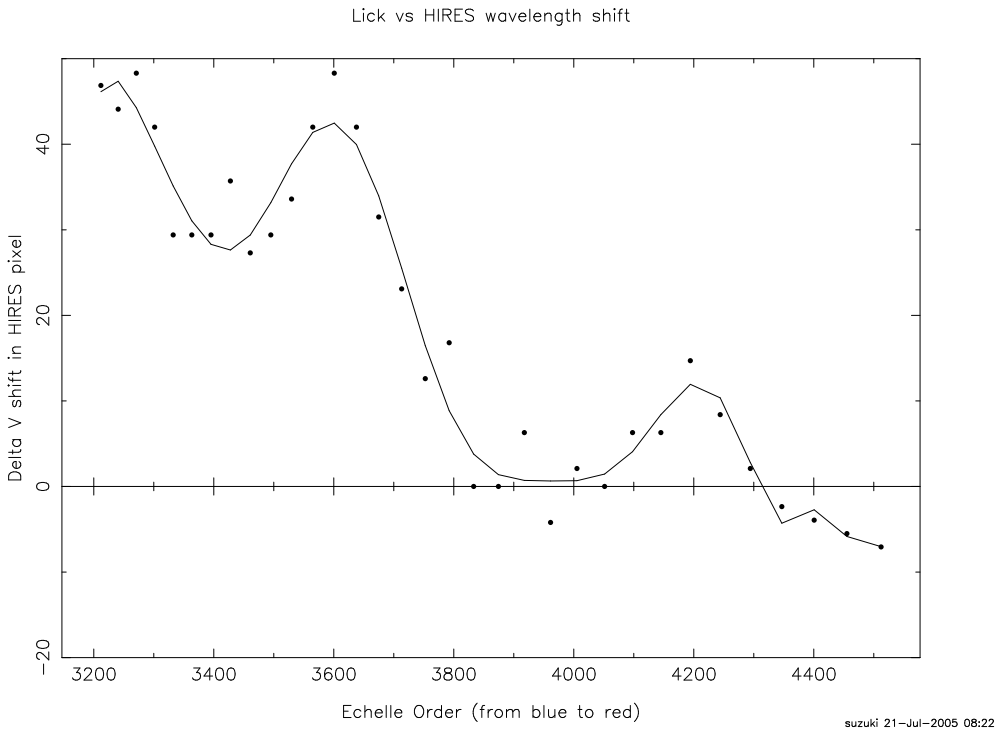

Figure A.2: Measured Kast data wavelength shift. Each point corresponds to an echelle order. We plot the central wavelength of the echelle order vs. measured shift in HIRES pixel n. We fit chebyshev polynomials to the data points, and apply it to the KAST/ESI spectrum to correct the wavelength shift. (12_KASTwavelengthshift_fitted_EchelleOrder_vs_v.ps)

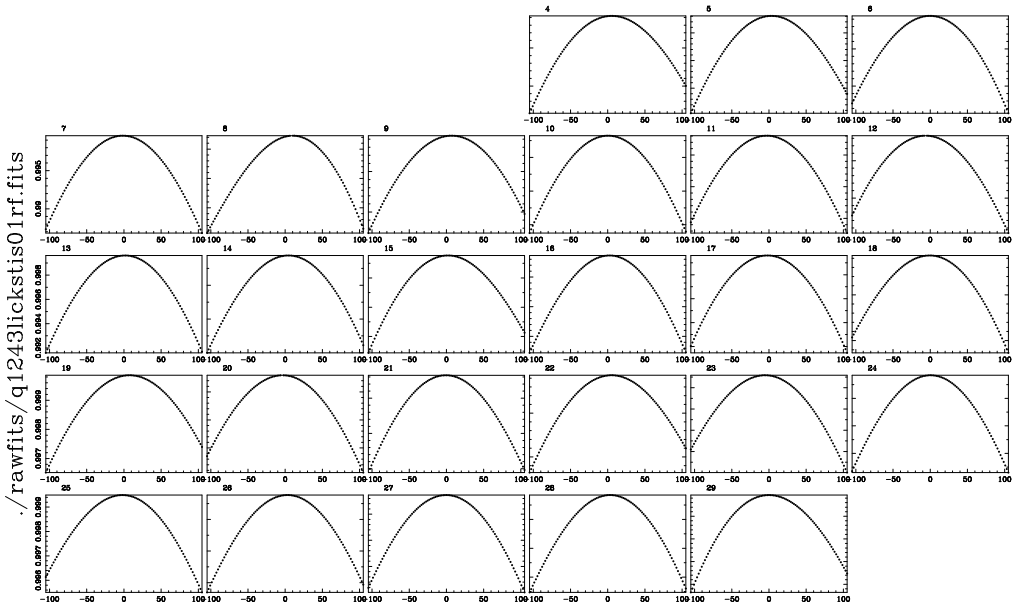

Figure A.3: Same as A.1 but the with wavelength corrected KAST data. The cross-correlation parabola $c(n)$ peaks at n_{max}=0, meaning KAST/ESI wavelength well matches to the HIRES data. (13_KASTcheckshifted_shift_vs_crosscorr.ps)

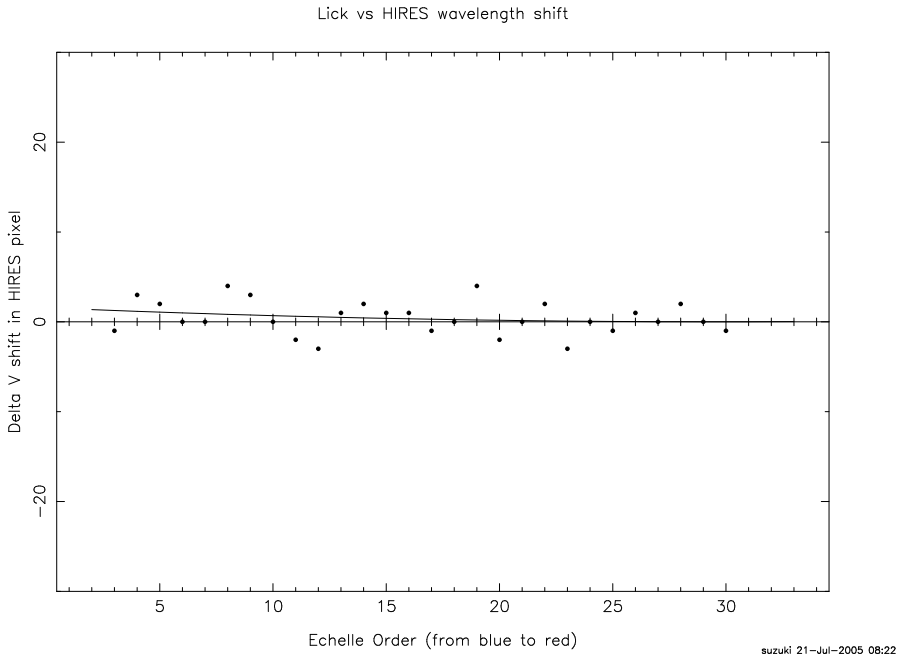

Figure A.4: Same as Figure A.2 but with the wavelength corrected KAST data. The wavelength shifts are properly corrected and the data points are fluctuating around zero. (14_KASTcheckshifted_EchelleOrder_vs_v.ps)

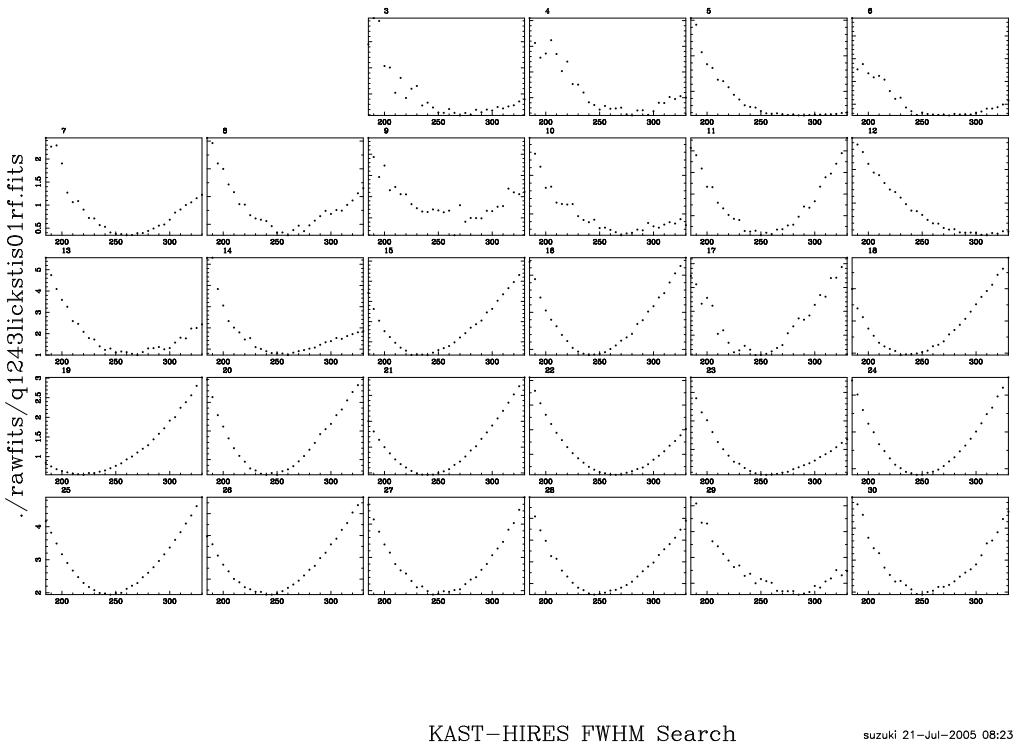

Figure A.5: Measuring KAST data resolution. Each box corresponds to an echelle order, and the wavelength increases from top left to the bottom right. The x-axis is the FWHM in km/s, and the y-axis is the reduced χ^2 value. The parabola should have the minimum when the resolution matches to the KAST data. The parabola in the blue echelle orders is not in a good shape because of the low S/N of the KAST data. (20_KASTfwhmsearch_fwhm_vs_chisq.ps)

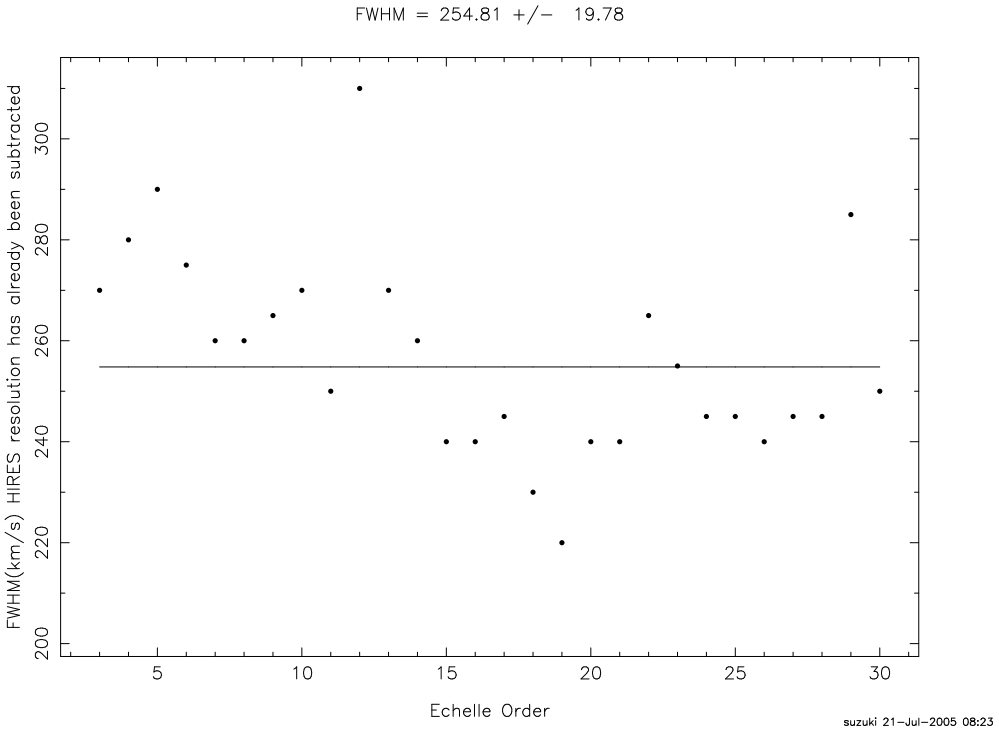

Figure A.6: Measured Kast resolution in km/s. Each point corresponds to an echelle order. In this figure, we count the echelle order from the shortest wavelength. We can barely see the trend that the resolution slightly changes with wavelength. (21_KASTfwhmserch_EchelleOrder_vs_fwhm.ps)

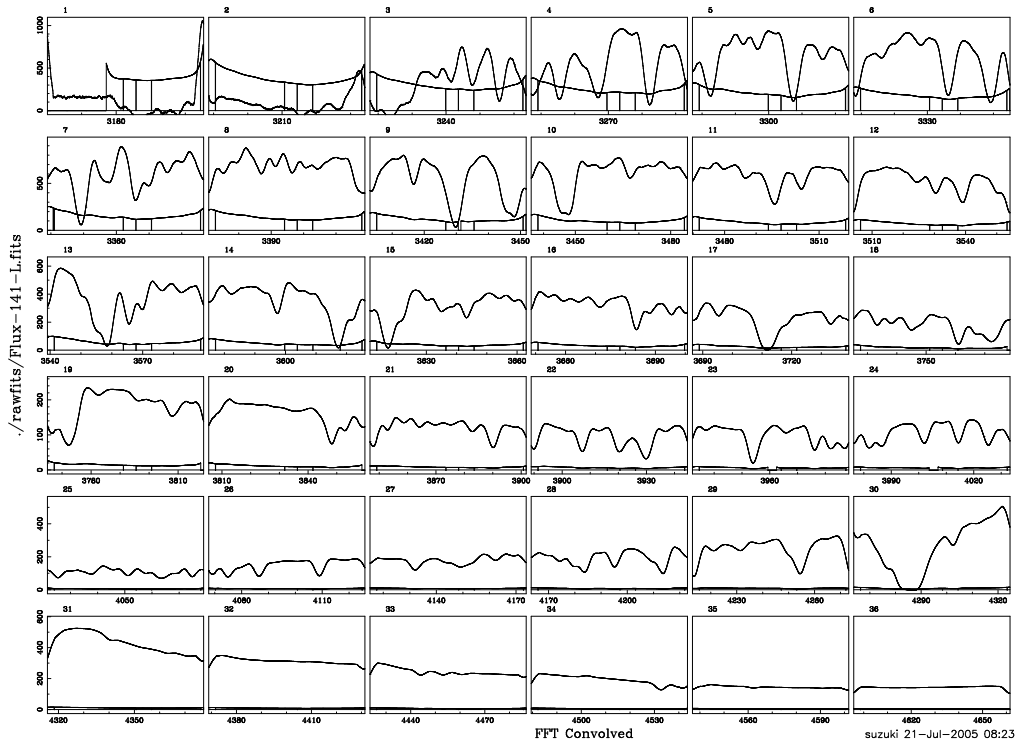

Figure A.7: Degraded HIRES spectrum without rebinning: We use FFT and convolve with gaussian with FWHM$_{KAST}$=254.9 km/s. We use this gaussian convolved spectrum for the cross-correlation calculation and resolution search. (30_1dFFTconvolved_F142.ps)

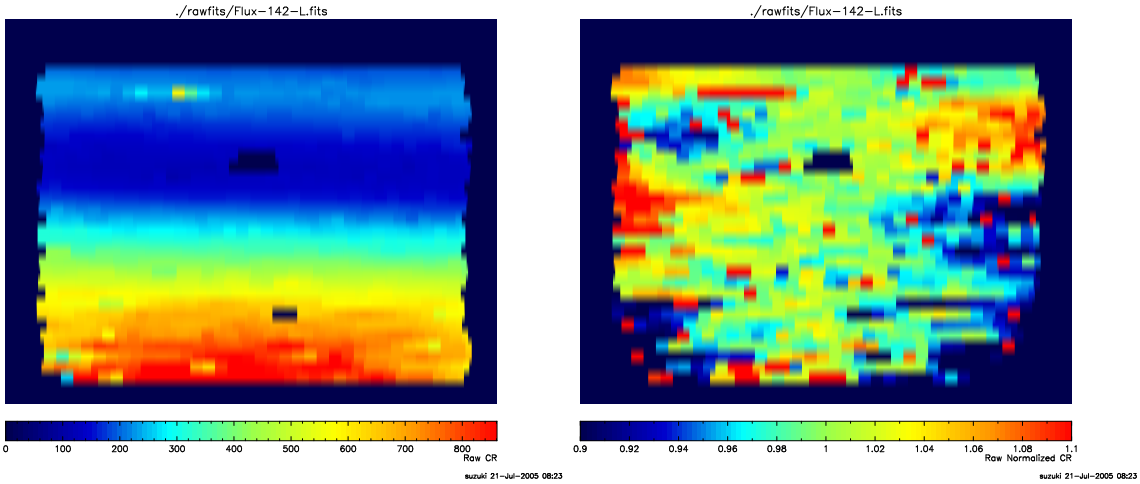

Figure A.8: **Left:** 2D Raw Conversion Ratio. With this projection, we can simulate the CCD image before we extract the data. The wavelength goes from the left bottom to the top right just like original CCD image. The pixel size corresponds to the KAST binning. (32a_2dCRraw_F142.ps) **Right:** Same as left panel but normalized near the center of each echelle order by taking the average of ± 15% of the pixels from the center. We can clearly see the the rapid relative change in CR in en echelle order. (32b_2dNCRraw_F142.ps)

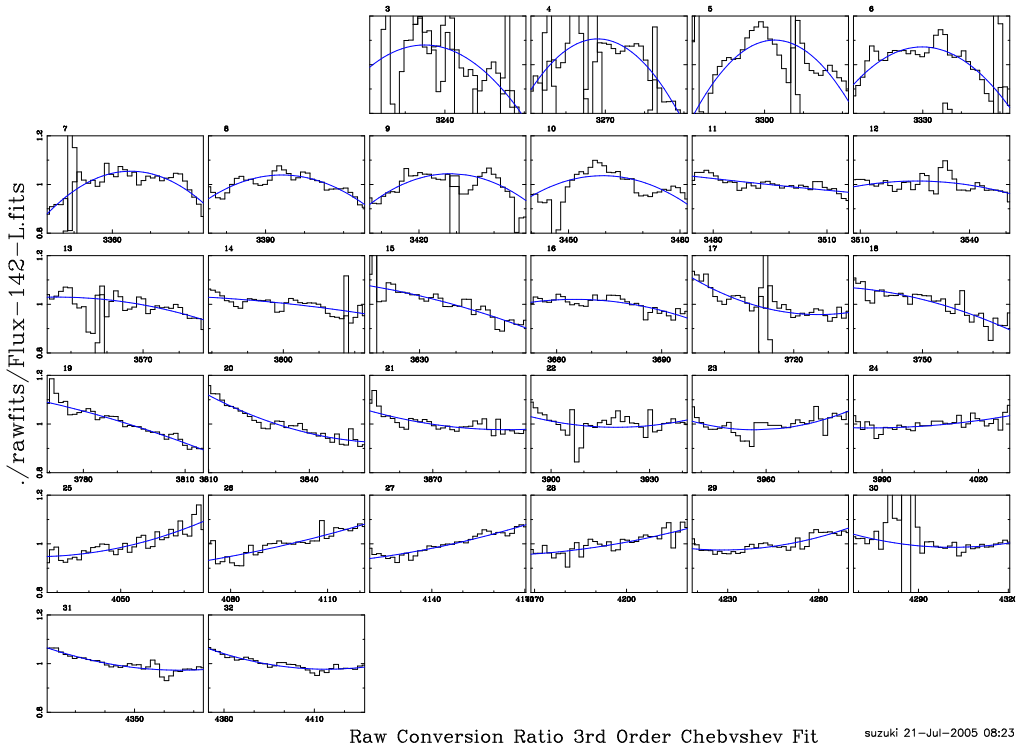

Figure A.9: Raw Conversion Ratio (histgrams) with a 3rd order chebyshev polinomial fit (smooth curve). A small box corresponds to an echelle order, and the wavelength goes from top left to bottom right. Spiky features seen in the bluest orders are from error array. CR changes with wavelength, however, the neighboring echelle orders have similar CR in shape. (31_1dCRraw_F142.ps)

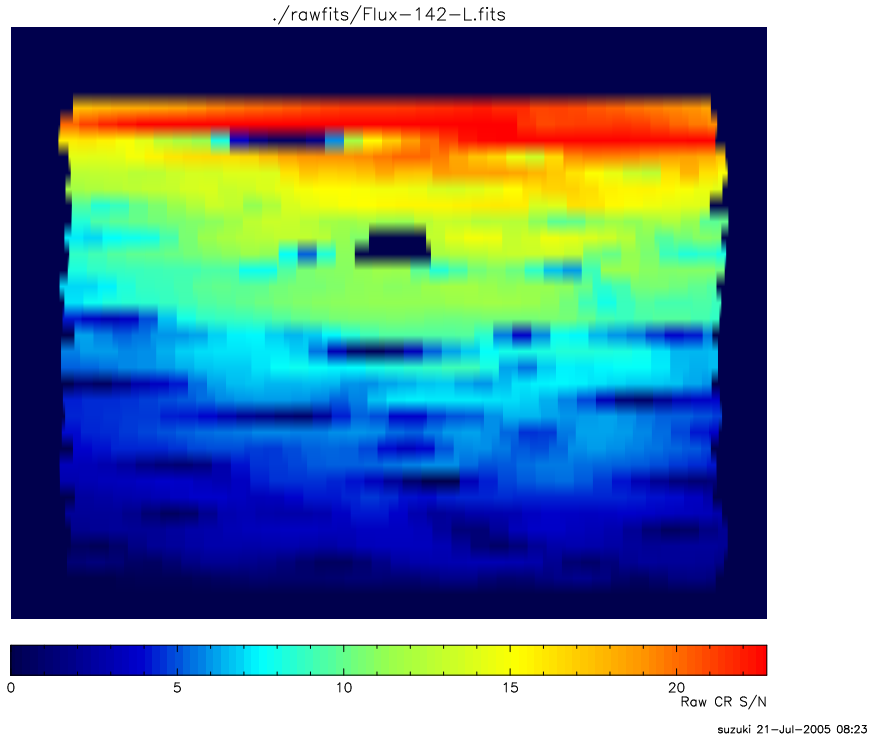

Figure A.10: S/N of the CR in 2D projection. The wavelength goes from the bottom left to the top right. S/N is getting higher with wavelength, but poor at the edges of each echelle orders and where we have absorption lines. (34_2dCR_SNR_F142.ps)

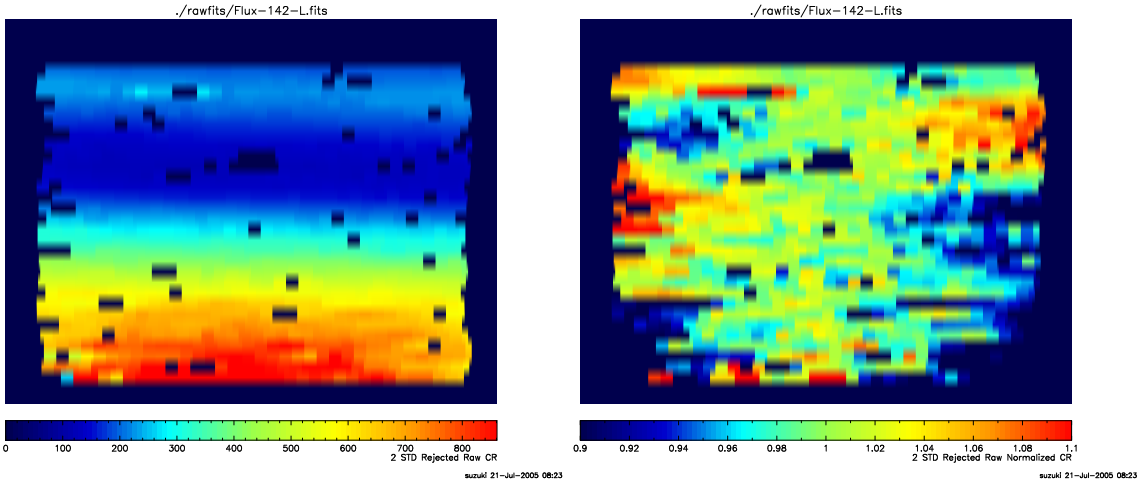

Figure A.11: **Left:** Same as Figure A.8 but we removed CR pixels with 2σ off from the 3rd order chebyshev fit. We mask 2σ rejected pixels. (35a_2dCRstdrejected_F142.ps) **Right:** Same as left panel but normalized near the center of each echelle order. (35b_2dNCRstdrejected_F142.ps)

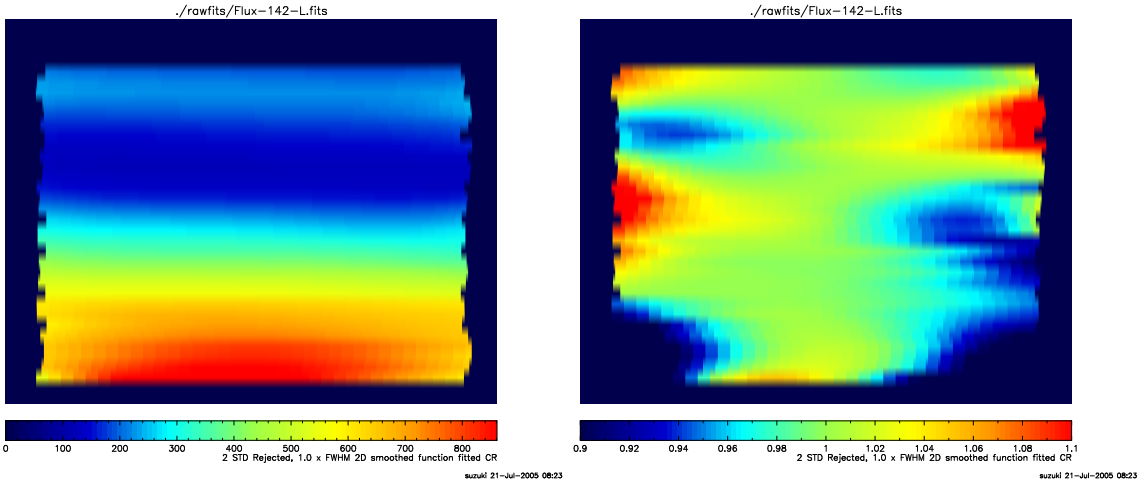

Figure A.12: **Left:** Same as Figure A.8 but smooth function fitted CR. We chose order Chebyshev polynomials. (37a_2dCRsmoothed_F142.ps) **Right:** Same as left panel but normalized near the center. (37b_2dNCRsmoothed_F142.ps)

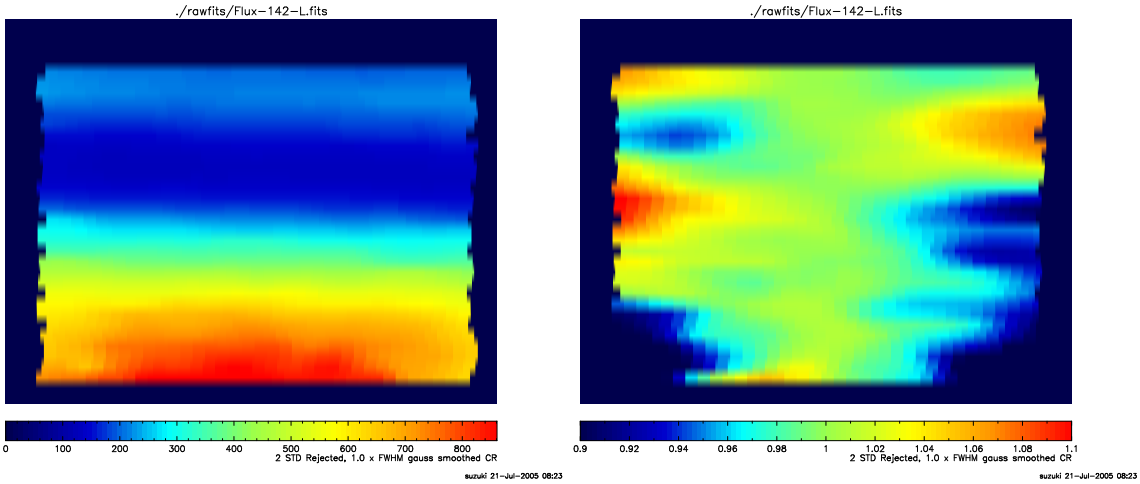

Figure A.13: **Left:** Same as Figure A.12 but smoothed by a gaussian filter. (99a_2dCRsmoothedbygaussian_F142.ps) **Right:** Same as left panel but normalized near the center. Compared to Figure A.12, gaussian smoothing degrades CR features and reduce the height of CR peaks by several percent which is unacceptable for our calibration. (99b_2dNCRsmoothedbygaussian_F142.ps)

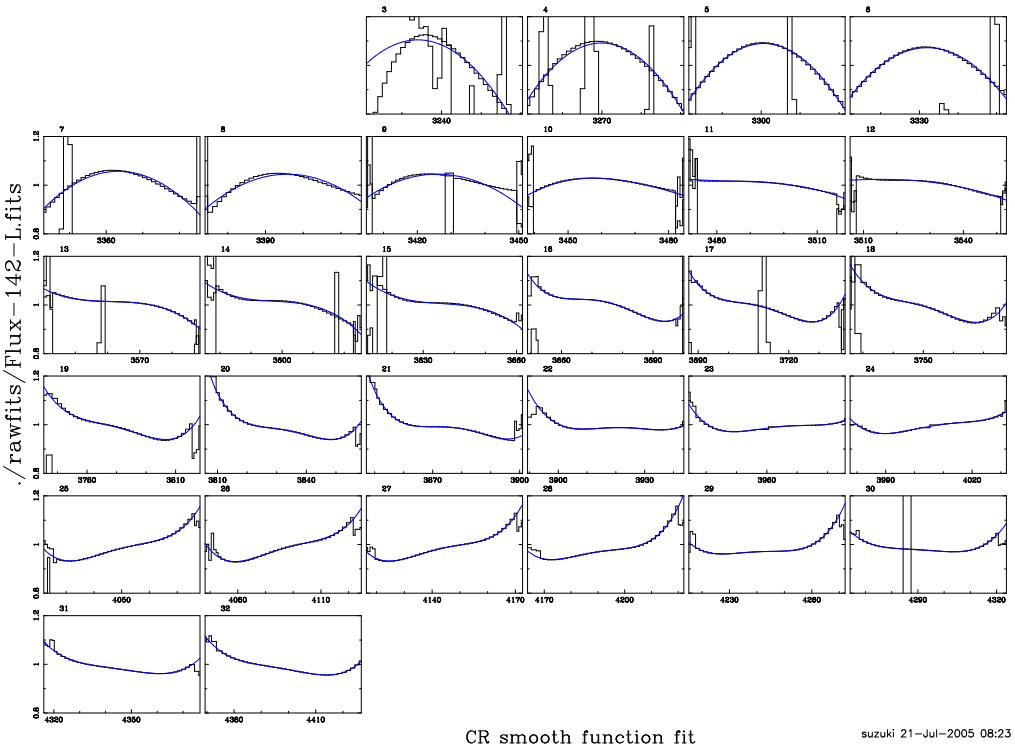

Figure A.14: 2D smooth fit conversion ratio. Smooth line in blue is smoothed fit with extrapolation to the edges. (36_1dCRsmoothed_F142.ps)

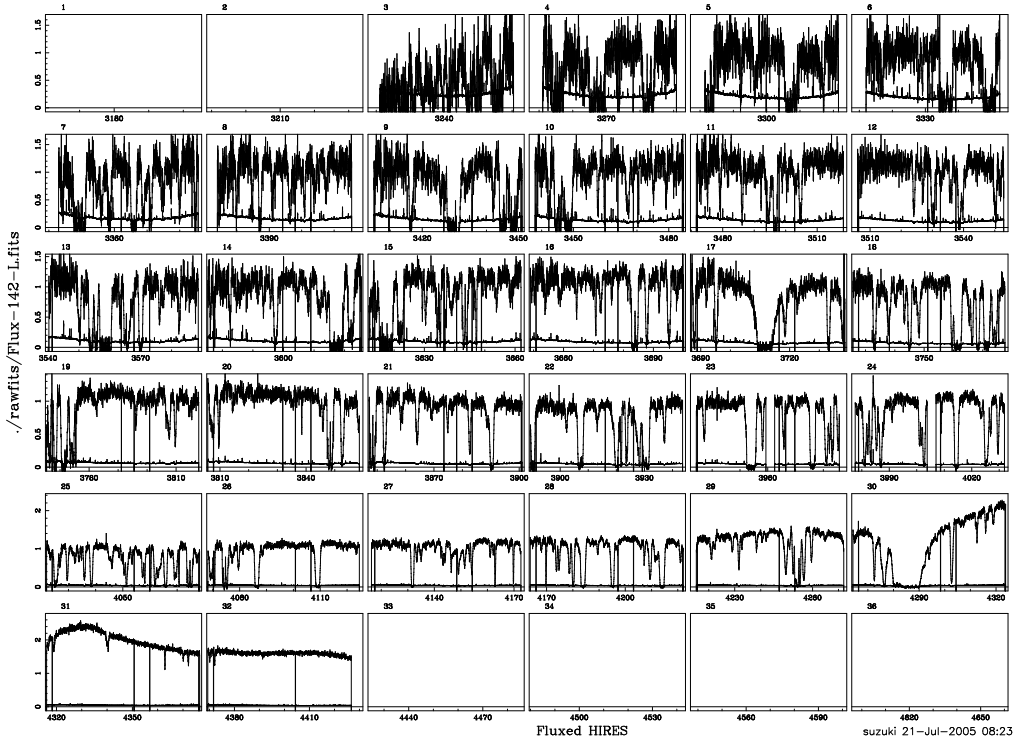

Figure A.15: Flux calibrated HIRES data from the smooth Chebyshev polynomials curve fitted CR. Each small box corresponds to each echelle order, and the wavelength goes from the top left to the bottom right. We do not flux calibrate the wavelengths below the Lyman limit because the flux goes to zero and we cannot find CR. (50_1dFluxedHIRES_F142.ps)

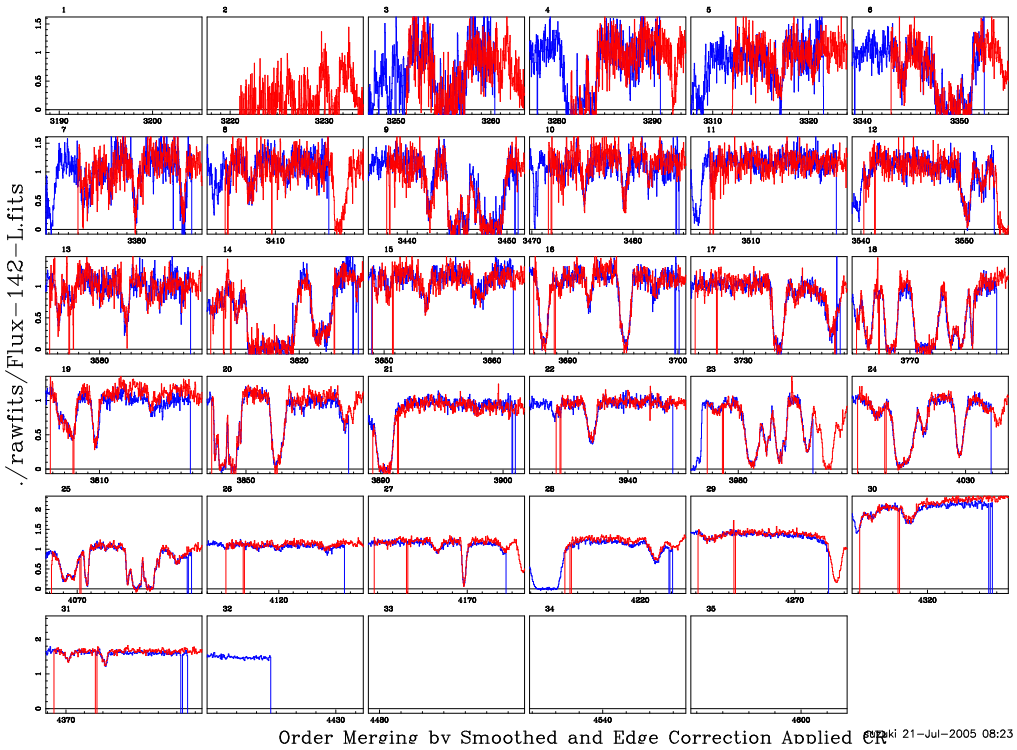

Figure A.16: Echelle orders' overlaps: We show the flux calibrated data with zoomed up echelle order overlapping regions. The blue color represents data from the bluer echelle order and red color represents data from redder order. If we succeed to flux calibrate, the blue and red spectrum should overlap exactly. (40_1dOrderJoint_F142.ps)

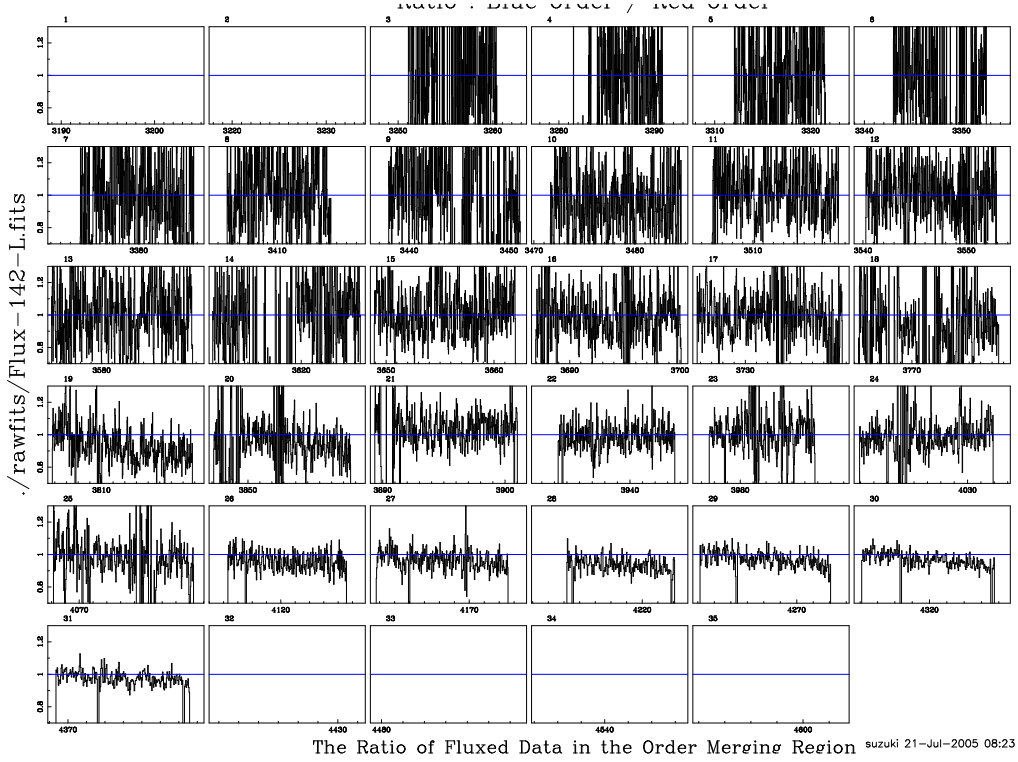

Figure A.17: Same as Figure A.16 but we are taking ratios of overlapping region. The ratios should be close to one, and they get noisy when they have absorption lines. In this particular exposure, we have good ratios in the middle of spectrum but we have a systematic tilt towards red wavelength. (41_1dOrderJointRatio_F142.ps)

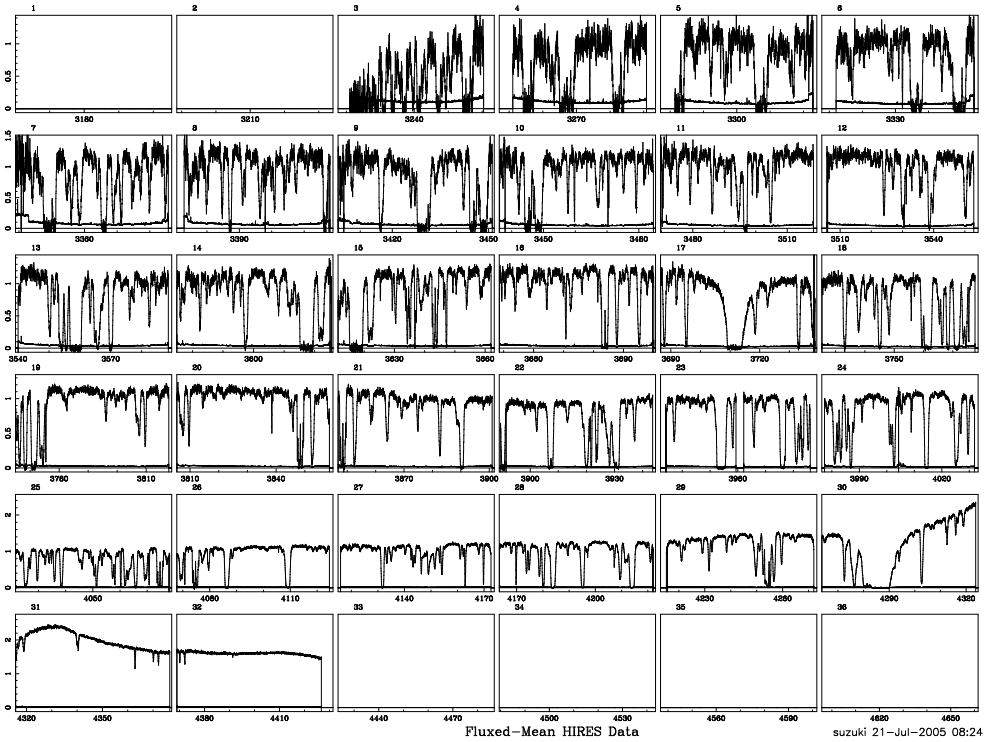

Figure A.18: Flux calibrated mean spectrum. We take the weighted sum of 7 exposures. Small box corresponds to an echelle order, and the wavelength goes from the top left to the bottom left. We flux calibrate each exposure individually. (70_Mean-HIRES_by_EchelleOrders.ps)

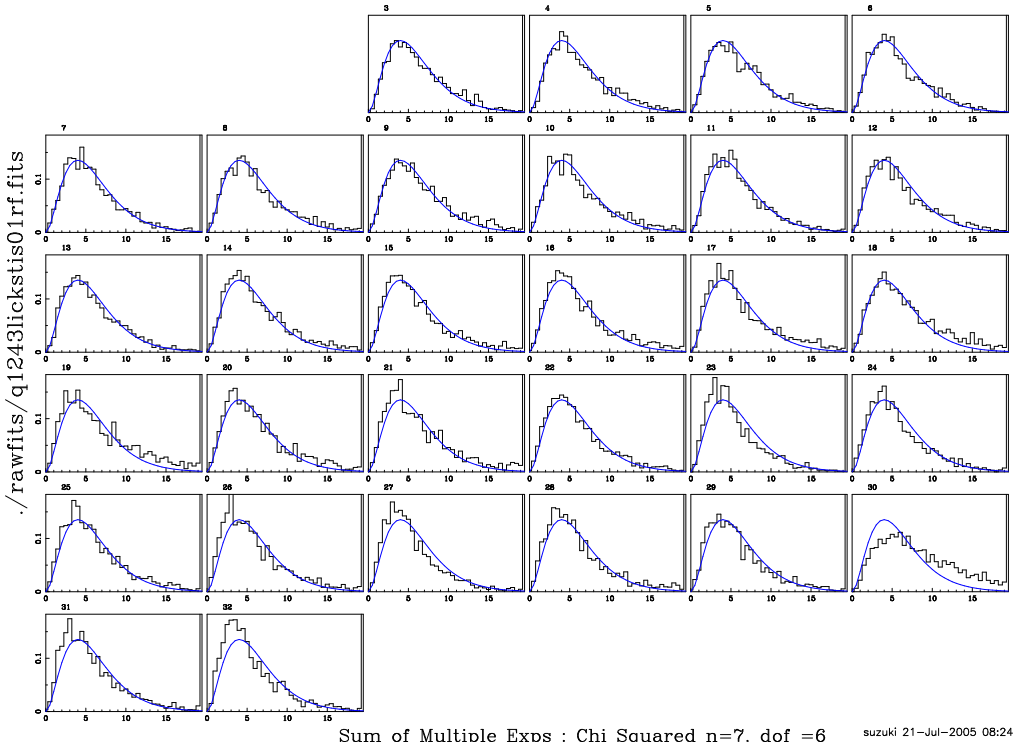

Figure A.19: χ^2 distribution of 7 exposures. When we take the weighted mean from 7 exposures, we also calculate the weighed error. Using both weighted mean and error, we can calculate individual pixels χ^2 value and check if they behave as we expected. x-axis is the χ^2 and y-axis is the normalized frequency. The blue curve is the expected χ^2 distribution (The degree of freedom is 6). Each small box corresponds to an echelle order. In general, the observed distribution and expected distribution matches quite well. However, in red wavelength, the observed χ^2 is a bit smaller than expected. It implies the size of error is a bit bigger than expected. In echelle order 30, the observed distribution is distorted. In this order, we have our main Lyα absorber, and probably, the size of error at the bottom of absorber which has zero flux is too small. (60_ChiSqStatistics.ps)

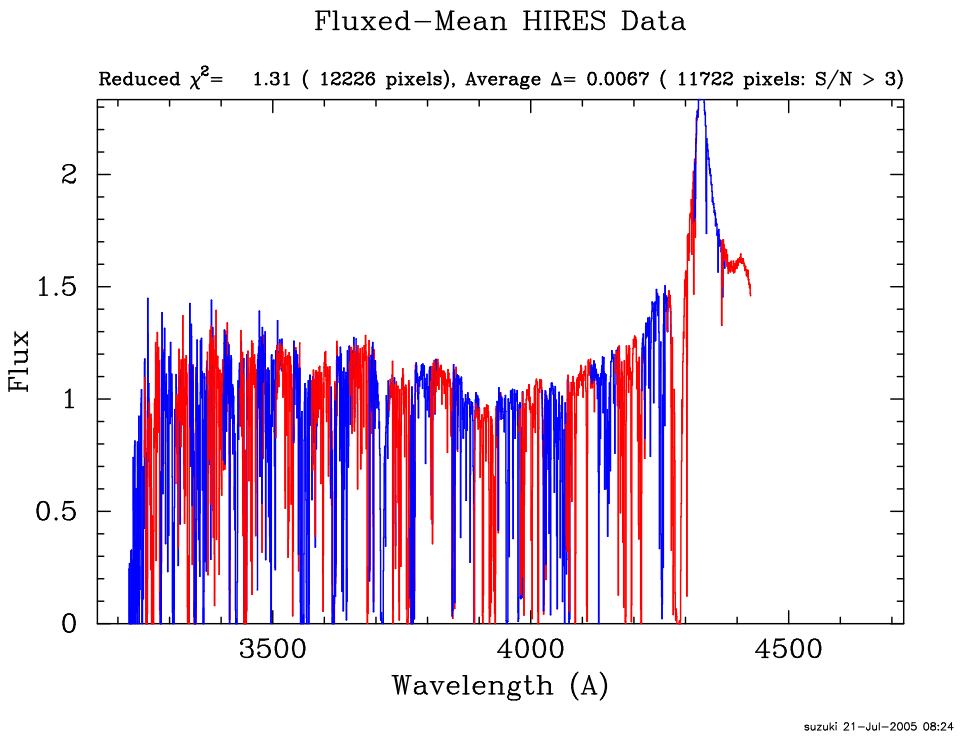

Figure A.20: 1D Flux calibrated mean spectrum with echelle orders in colors. Even echelle orders are colored in red, and odd orders are in blue. We can see the scale of echelle orders how they merge. There is no obvious disagreement. (71_Fluxed-HIRES_1d_ordermergingcheck.ps)

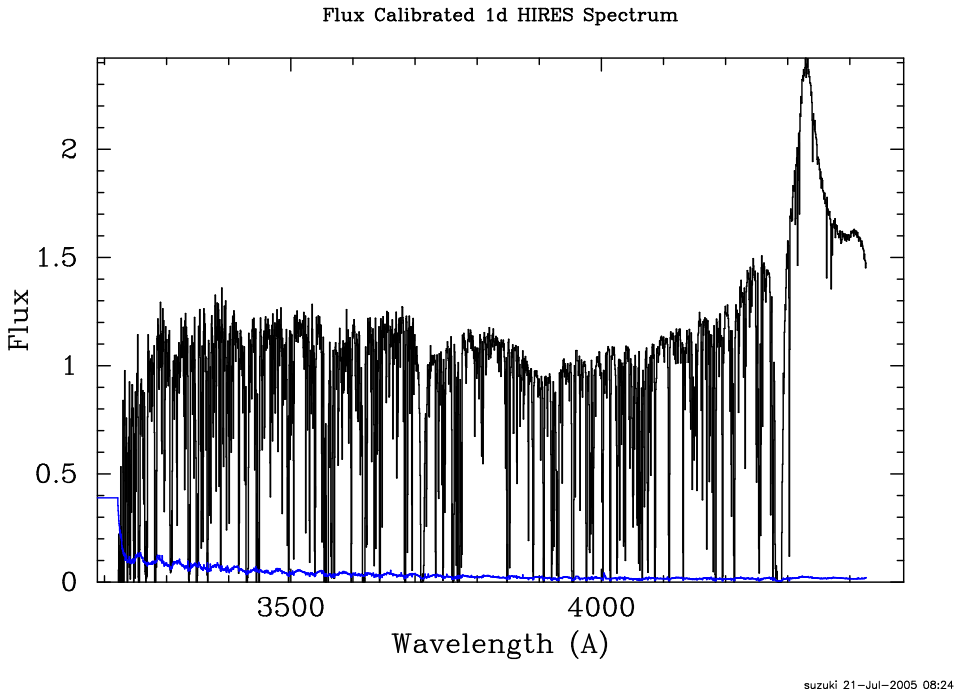

Figure A.21: 1D Flux calibrated mean spectrum. This is the final product. The code produces FITS files (flux and 1σ error) and ascii file. (72_Fluxed-HIRES_1d.ps)

A.3 Flux Calibration with ESI

We use the same code for the flux calibration from KAST and ESI data. The input file is different. We need to modify default pixel size, resolution and ESI file names. The code runs just like KAST fluxing:

```
>cd cvs/fluxtools/q1243
>../nsbin/fluxhires_with_kast inputfile_esi
```

It would create a new directory, called "fluxed_data_esi", and all of the new files are stored in that directory. The "inputfile_esi" should look like as follows:

```
CC HIRES Fluxing using KAST data

            reference='esi'

CC Quasar's Properties:
              lylimit=3215.0    ! Ly Limit(abs) Wavelength (A)
           lyemission=4330.0    ! Ly alpha Emission Wavelength (A)

CC Kast Data Properties:
           db_lickvpix=14.7d0    ! Kast Data Pixel Size (km/s)
         defaultvfwhm=58.0       ! Starting Default Kast FWHM (km/s)

CC Input ESI Spectrum
       orglickfluxname='./rawfits/q1243esif.fits'
        orglickerrname='./rawfits/q1243esie.fits'

CC Input  : A List of HIRES Spectra
         hiresfluxlist='./rawfits/q1243hiresflux.list'
          hireserrlist='./rawfits/q1243hireserr.list'
```

```
CC Output : Velocity Corrected/Shifted Kast Spectrum
          lickfluxname='./rawfits/q1243esirf.fits'
           lickerrname='./rawfits/q1243esire.fits'

cc Output : Flux Calibrated 1D Spectrum
       fluxed_1d_ascii='./q1243_esifluxed_v69.dat'
       fluxed_1d_fitsf='./q1243_esi_v69f.fits'
       fluxed_1d_fitse='./q1243_esi_v69e.fits'
```

In this section, we briefly summarize the result of flux calibration with ESI data. We would not repeat discussing the algorithm, but we show the results which are different from calibration with KAST.

Step 1 & 2 : Matching Wavelength and Resolution

Based on our experience in chapter 4, we know the wavelength shift and the resolution of ESI is uniform. Therefore, we skip measuring these and simply apply the values used in chapter 4 to ESI data. If we wish to repeat the measurement, we need to modify the relevant subroutines (lick_crosscorr,lick_vfwhm) for ESI data.

Step 3 : Calculating the Conversion Ratio

Since the resolution of ESI is higher and the pixel size of ESI (11.5 - 14.7 km/s) is smaller than KAST data ($\sim$ 107.1 km/s), we can obtain CR in higher resolution. However, the wavelength of ESI starts from 4000Åby design, and we cannot calibrate spectrum below 4000Å. We show 2D raw CR in Figure A.22 and 1D raw CR in Figure A.23. S/N of CR per pixel (Figure A.24) is not so different from what we have with KAST data, but the number of pixels are far greater than that of KAST, so we can expect we can find underlying smooth CR in better precision. We perform 2σ rejection using 3rd order chebyshev polynomial fit before we do smooth function fitting (Figure A.25).

Step 4 & 5 : Smoothing and Apply the CR

We can find high resolution CR from ESI data. Once again, 2D chebyshev polynomial fit (Figure A.26) works better than gaussian filter (Figure A.27).

Step 6 & 7 : Calculate the Mean and Combine Echelle Orders

Same as flux calibration with KAST.

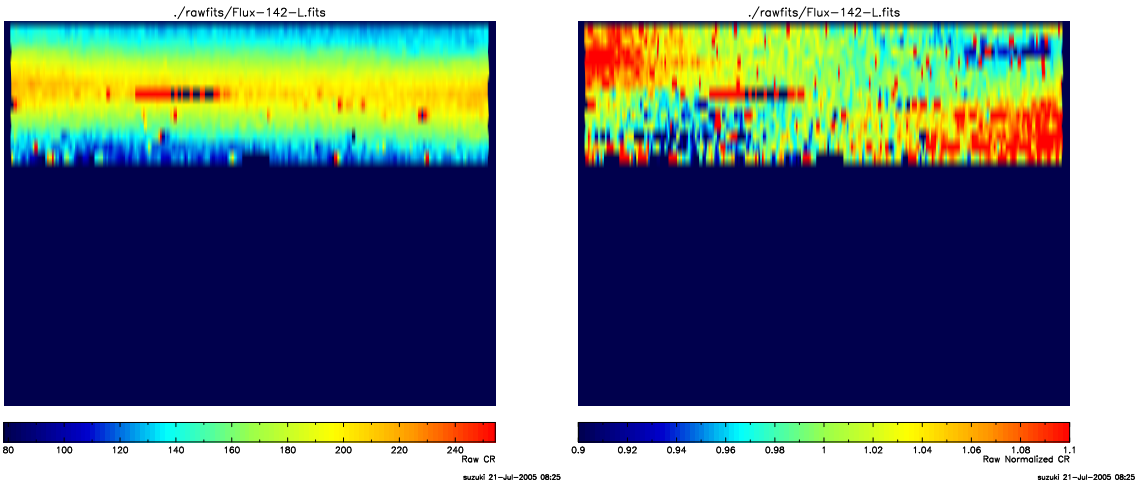

Figure A.22: **Left:** 2D Raw Conversion Ratio from ESI data. With this projection, we can simulate the CCD image before we extract the data. The wavelength goes from the left bottom to the top right just like original CCD image. ESI wavelength starts from 4000 Å, and we do not have data below 4000 Å. The pixel size corresponds to the ESI binning. (32a_2dCRraw_F142.ps) **Right:** Same as left panel but normalized near the center of each echelle order by taking the average of ± 15% of the pixels from the center. We can clearly see the the rapid relative change in CR in en echelle order. (32b_2dNCRraw_F142.ps)

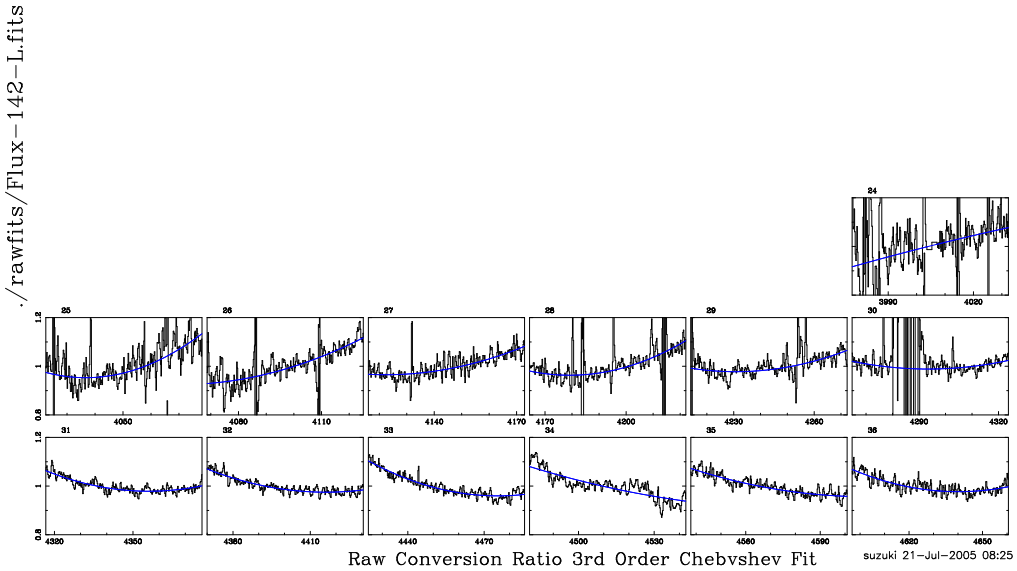

Figure A.23: Raw Conversion Ratio (histograms) with a 3rd order chebyshev polynomial fit (smooth curve). A small box corresponds to an echelle order, and the wavelength goes from top left to bottom right. CR changes with wavelength, however, the neighboring echelle orders have similar CR in shape. (31_1dCRraw_F142.ps)

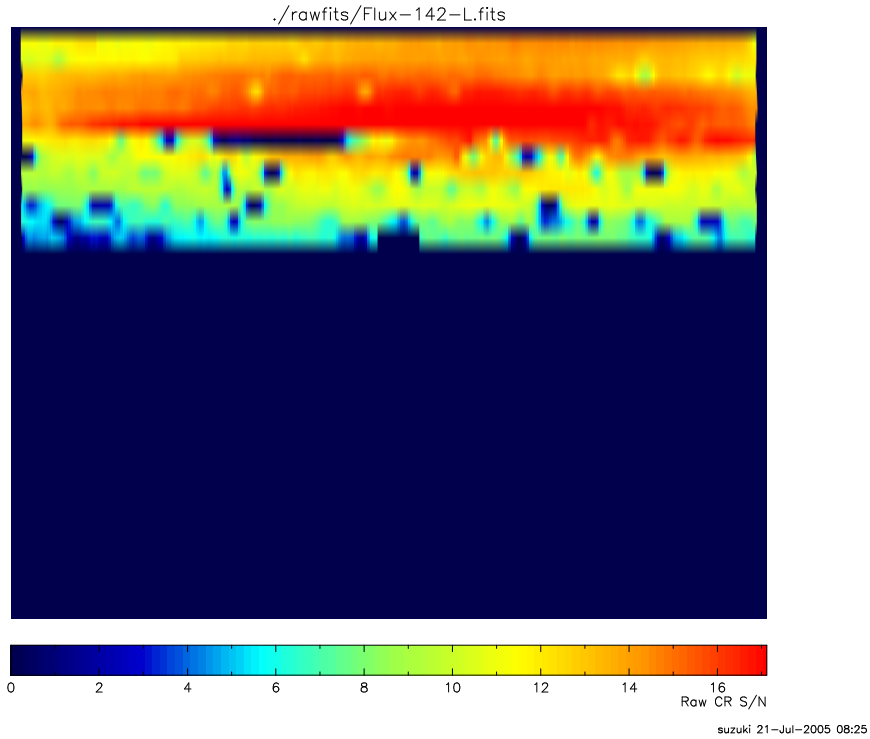

Figure A.24: S/N of the CR in 2D projection. The wavelength goes from the bottom left to the top right. S/N is getting higher with wavelength, but poor at the edges of each echelle orders and where we have absorption lines. (34_2dCR_SNR_F142.ps)

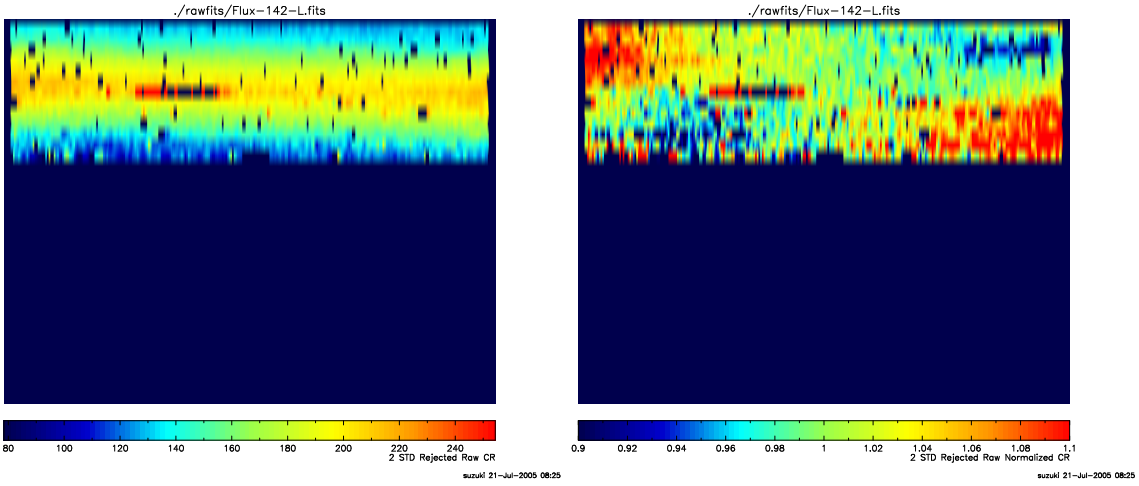

Figure A.25: **Left:** Same as Figure A.22 but we removed CR pixels with 2σ off from the 3rd order chebyshev fit. We mask 2σ rejected pixels. (35a_2dCRstdrejected_F142.ps) **Right:** Same as left panel but normalized near the center of each echelle order. (35b_2dNCRstdrejected_F142.ps)

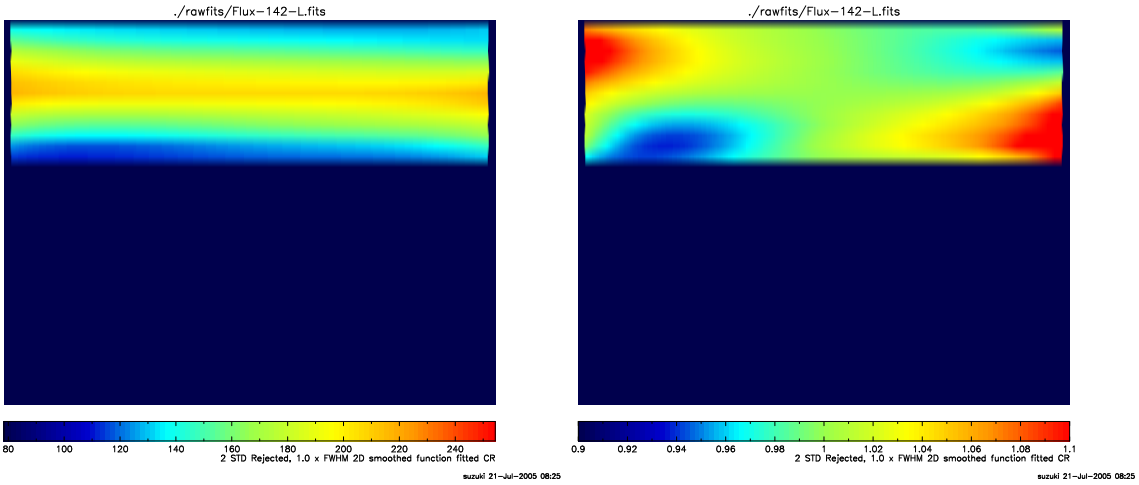

Figure A.26: **Left:** Same as Figure A.22 but smooth function fitted CR. We chose order Chebyshev polynomials. (37a_2dCRsmoothed_F142.ps) **Right:** Same as left panel but normalized near the center. (37b_2dNCRsmoothed_F142.ps)

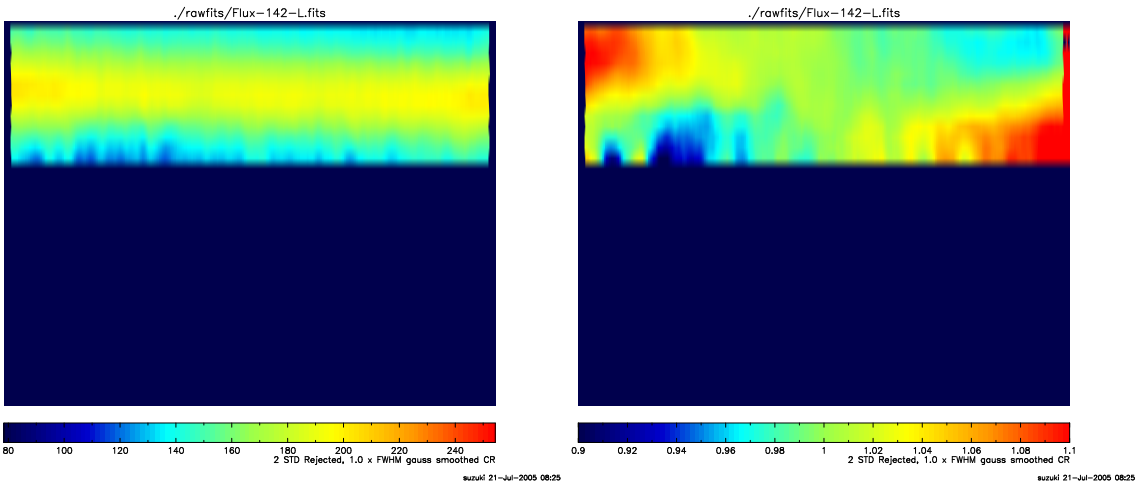

Figure A.27: **Left:** Same as Figure A.26 but smoothed by a gaussian filter. (99a_2dCRsmoothedbygaussian_F142.ps) **Right:** Same as left panel but normalized near the center. Compared to Figure A.26, gaussian smoothing degrades CR features and reduce the height of CR peaks by several percent which is unacceptable for our calibration. Also, false features propagate to the neighboring orders. (99b_2dNCRsmoothedbygaussian_F142.ps)

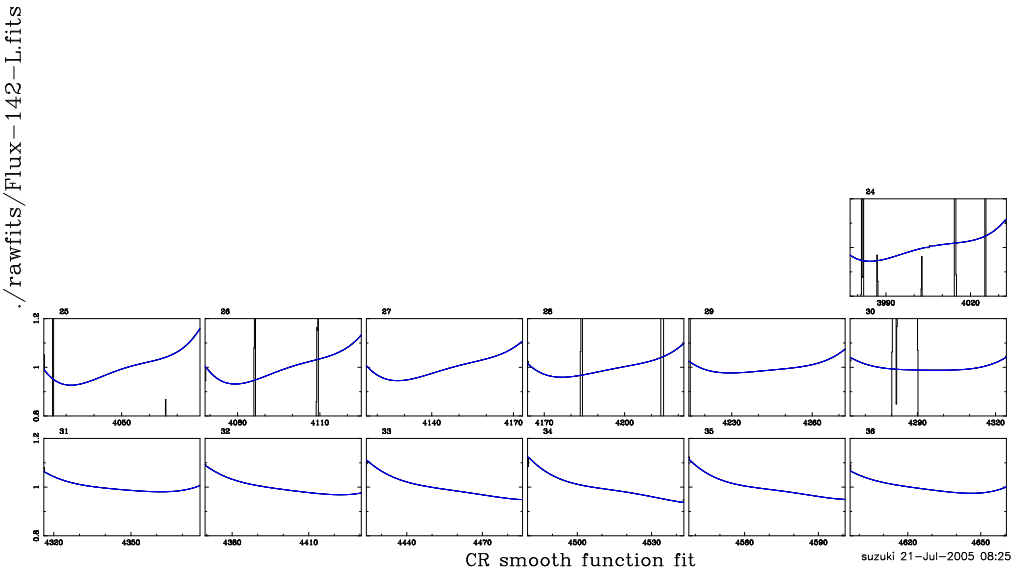

Figure A.28: 2D smoothed fit conversion ratio. Smooth line in blue is smoothed fit with extrapolation to the edges. (36_1dCRsmoothed_F142.ps)

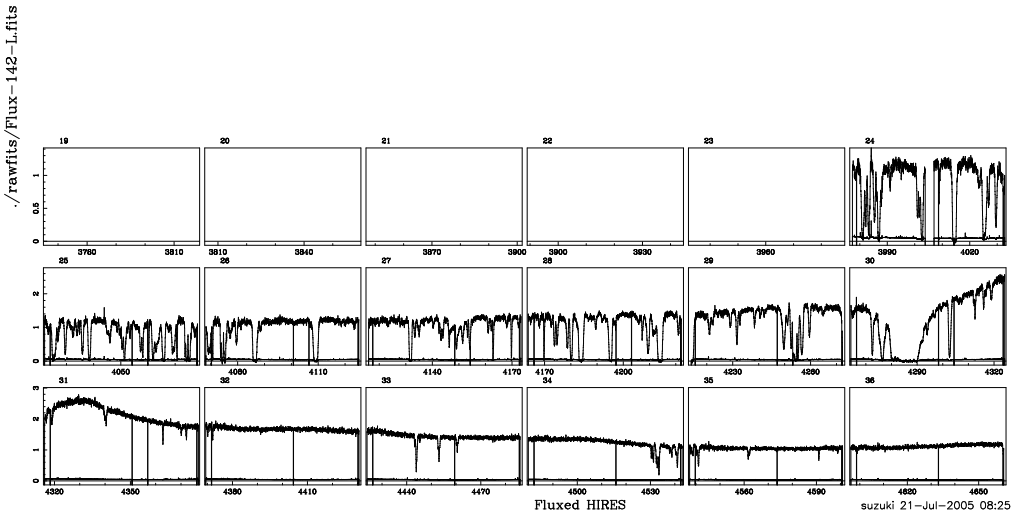

Figure A.29: Smooth Chebyshev fit applied HIRES data. Each small box corresponds to each echelle order, and the wavelength goes from the top left to the bottom right. We do not flux calibrate the wavelengths below the Lyman limit because the flux goes to zero and we cannot find CR. (50_1dFluxedHIRES_F142.ps)

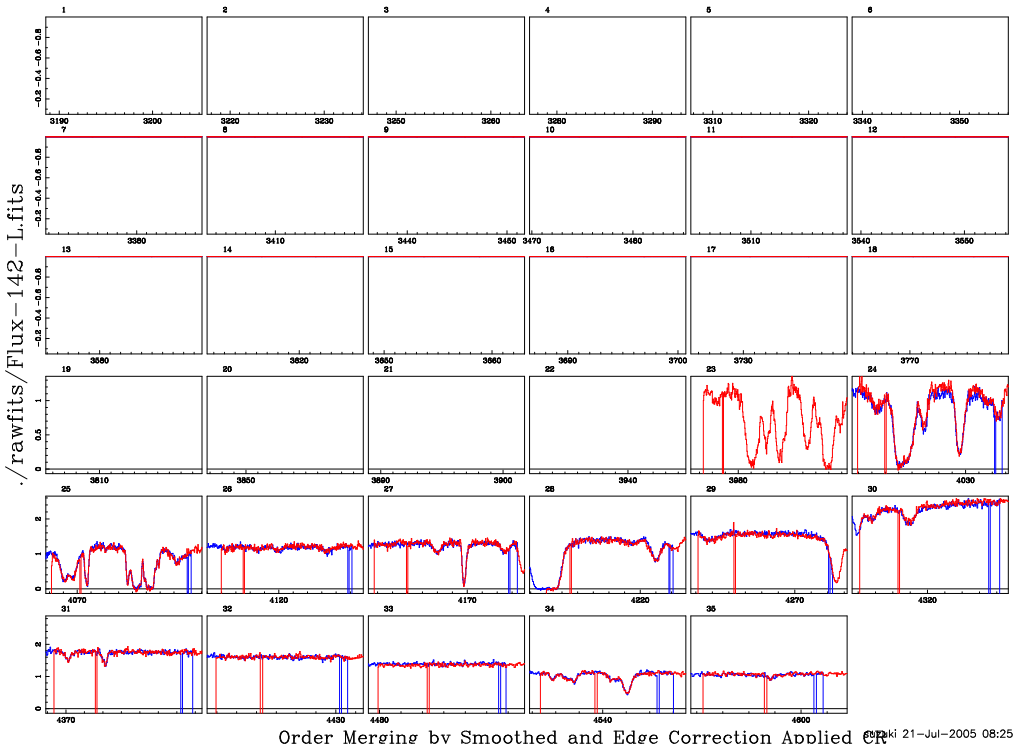

Figure A.30: Echelle orders overlap in wavelength, and we show flux calibrated data with zoomed up echelle order overlapping region. The blue color represents data from the bluer echelle order and red color represents data from redder order. If we succeed to flux calibrate, the blue and red spectrum should overlap in flux. (40_1dOrderJoint_F142.ps)

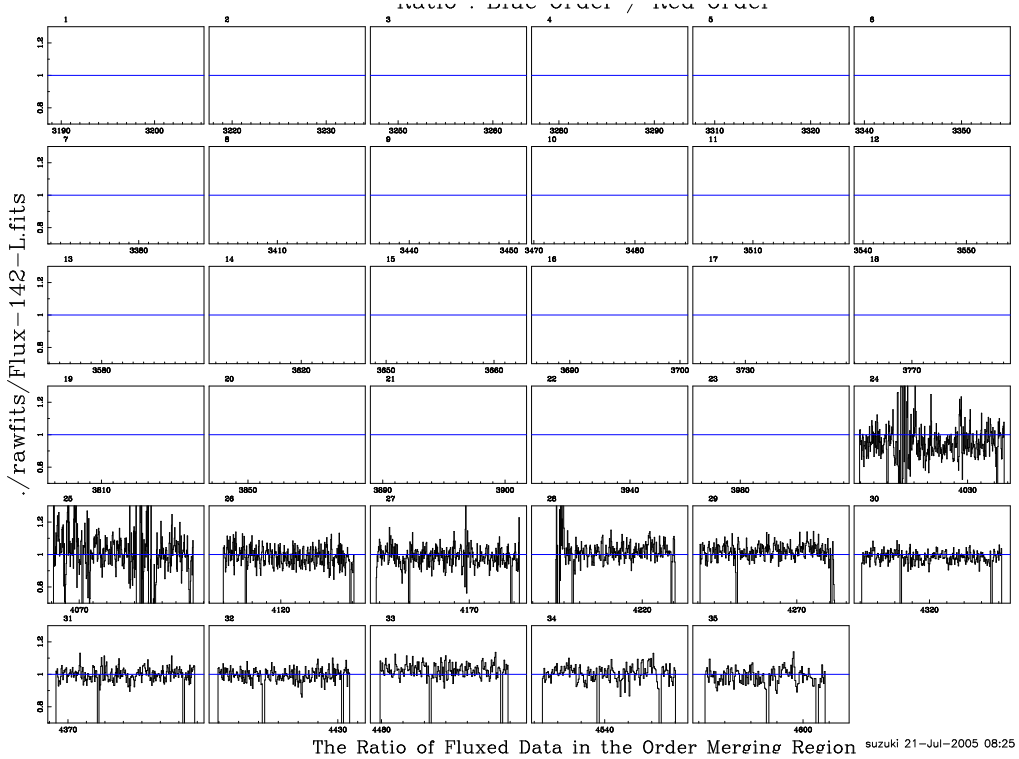

Figure A.31: Same as Figure A.30 but we are taking ratios of overlapping region. The ratios should be close to one, and they get noisy when they have absorption lines. In this particular example, ESI can do better job than KAST in Figure A.17 (41_1dOrderJointRatio_F142.ps).

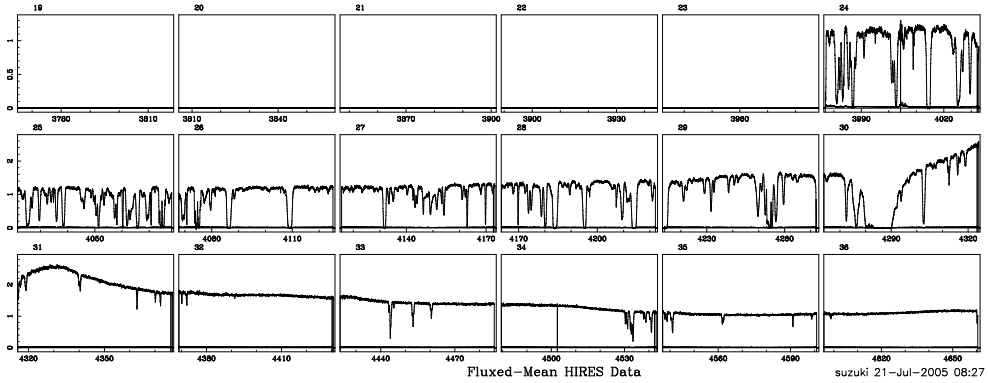

Figure A.32: Flux calibrated mean spectrum. ESI spectrum starts from 4000 Å. We take the weighted sum of 7 exposures. Small box corresponds to an echelle order, and the wavelength goes from the top left to the bottom left. We flux calibrate each exposure individually. (70_Mean-HIRES_by_EchelleOrders.ps)

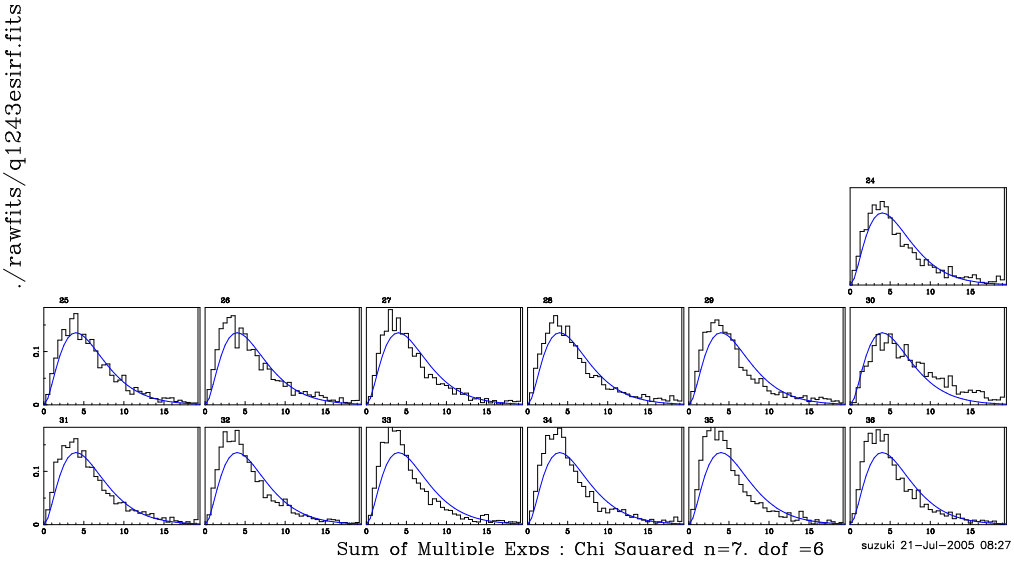

Figure A.33: Same as Figure A.19. χ^2 distribution of 7 exposures. In general, the observed distribution and expected distribution matches quite well. However, the observed χ^2 is a bit smaller than expected. It implies the size of error is a bit bigger than expected. In echelle order 30, the observed distribution is distorted. In this order, we have our main Lyα absorber, and probably, the size of error at the bottom of absorber which has zero flux is too small. (60_ChiSqStatistics.ps)

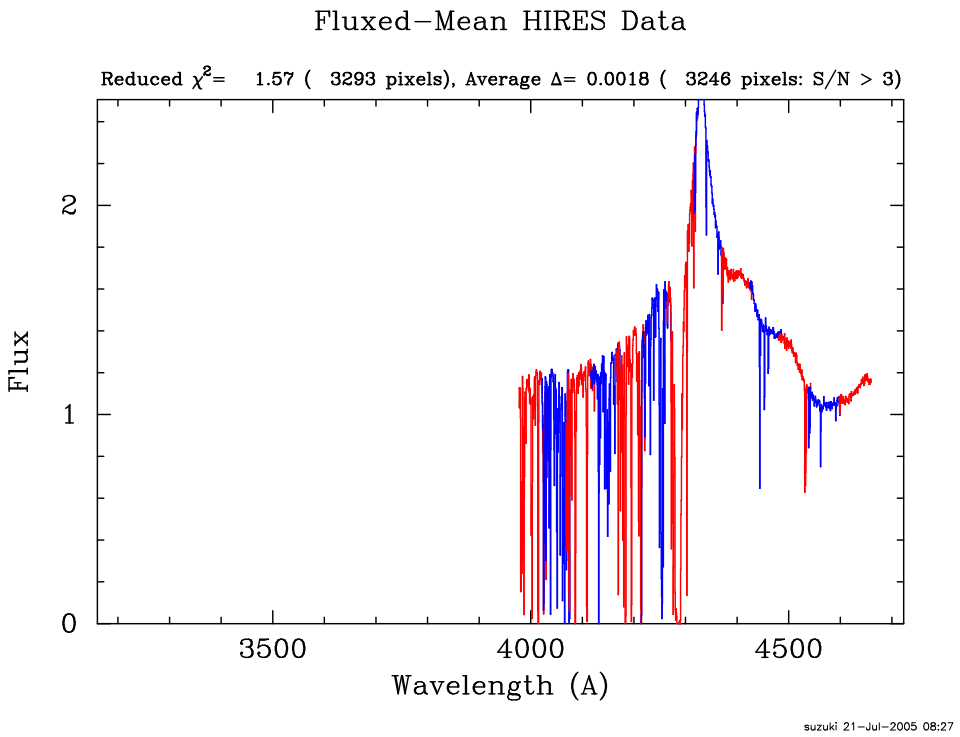

Figure A.34: 1D Flux calibrated mean spectrum with echelle orders in colors. Even echelle orders are colored in red, and odd orders are in blue. We can see the scale of echelle orders how they merge. There is no obvious disagreement. (71_Fluxed-HIRES_1d_ordermergingcheck.ps)

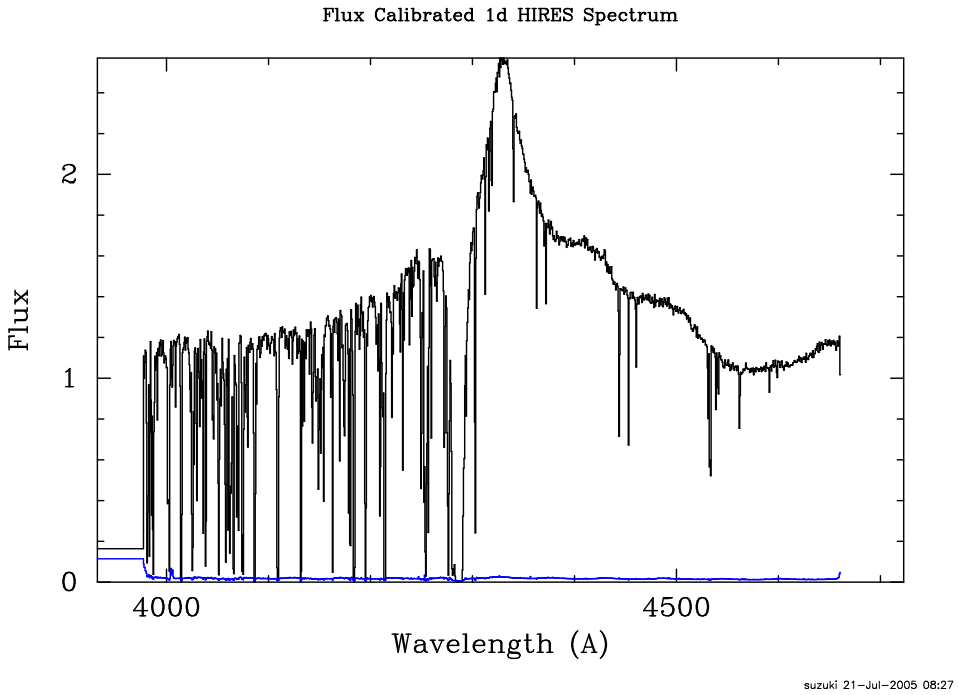

Figure A.35: 1D Flux calibrated mean spectrum. This is the final product. The code produces FITS files (flux and 1σ error) and ascii file. (72_Fluxed-HIRES_1d.ps)

A.4 Flux Calibration with HIRES Standard Star

We use simple flux calibration method here. It has been said that the standard calibration method, which transfers flux information from the standard star spectrum to the quasar spectrum, does not work on the HIRES data for the reasons discussed in chapter 4. However, I found that the standard method sometimes works well, although it does not always guarantee us any good results. We cannot predict in which occasion it works. We must explore the combinations of exposures of the standard star and quasars. One of the key elements of the successful flux calibration is the high resolution standard star spectrum from which we find the response. We use full resolution model standard star G191-B2B here to perform flux calibration.

To run the code for our example, we need to be in the directory **cvs/fluxtools/q1243** and type:

```
>cd cvs/fluxtools/q1243
>../nsbin/fluxhires inputfile_hires
```

The input file looks like as follows:

```
CC HIRES Fluxing

               qsoname= 'Q1243+3047'
              starname= 'G191B2B'

CC Quasar's Properties:
              lylimit=3215.0    ! Ly Limit(abs) Wavelength (A)
           lyemission=4330.0    ! Ly alpha Emission Wavelength (A)

CC Input  : A List of HIRES Spectra
         hiresfluxlist='./rawfits/q1243hiresflux.list'
          hireserrlist='./rawfits/q1243hireserr.list'
```

```
CC Input  : Standard Star Data
              starmodel= "/home/suzuki/DH/database/g191modelhires.dat"
          hiresstarflux="./rawfits/Flux-137-L.fits"
           hiresstarerr="./rawfits/Err-137-L.fits"

cc Output : Flux Calibrated 1D Spectrum
        fluxed_1d_ascii='./q1243_hiresfluxed_v70.dat'
        fluxed_1d_fitsf='./q1243_hires_v70f.fits'
        fluxed_1d_fitse='./q1243_hires_v70e.fits'
```

The calibration process is simple, and the order of process is different from what we have for the calibration with KAST/ESI data. We go through the following five steps:

Step 1: Calculating the Ratios between Exposures (`subroutine a_tilt_directratio`)

Step 2: Calculating the Mean Spectrum (`subroutine xgetmeanflux`)

Step 3: Calculating the Response (`subroutine getresponse`)

Step 4: Fitting and Applying the Response (`subroutine a_hiresfluxing`)

Step 5: Combine Echelle Orders (`subroutine xtestmergeorders`)

The above steps **Step 3 & 5** are the same as KAST/ESI flux calibration. In this section, we describe the steps which are unique to the flux calibration with HIRES standard star.

A.4.1 Algorithms and Subroutines

Step 1: Calculating the Ratios between Exposures (`subroutine a_tilt_directratio`)

First, we normalize the multiple exposures to the reference exposure and calculate the mean spectrum before we perform the flux calibration. We can reduce the procedure to flux calibrate each exposure. We can justify this procedure because we

found that the ratios between quasar exposures in an echelle order is a constant and flat as is shown in Figure A.36. However, in a global scale, the ratio is changing at the blue end (Figure A.37). This is probably because of the atmospheric extinction. Although we apply atmospheric extinction correction, it could differ from the real extinction we observe. Using these ratios, we can normalize the rest of exposures to be like the reference frame.

Step 2: Calculating the Mean Spectrum (`subroutine xgetmeanflux`)
Same as the flux calibration with KAST/ESI. We take weighted mean of multiple exposures. We show χ^2 statistics of the seven exposures in Figure A.38. It is interesting to note that the deviation from the χ^2 distribution is different in blue and red end. In blue end, we probably underestimate the size of errors while in red end, we overestimate the error.

Step 3: Calculating the Response (`subroutine getresponse`)
We calculate the response function which transfers CCD counts into physical unit. We use the model standard star G191-B2B from Bohlin et al. (2001), and we define the response as :

$$Response = \frac{CCDCounts}{ModelSpectrum}. \tag{A.27}$$

Step 4: Fitting and Applying the Response (`subroutine a_hiresfluxing`)
We fit 10th order Chebyshev polynomial to the raw response. We show the raw response and smooth curve fit in Figure A.39, and show the same response in 2D image in Figures A.40 and A.41 where left panel shows the raw response and the right panel shows the normalized response. Now we know what we have seen in the calibration with KAST/ESI is real. There are rapid change in response. The raw response shows that the response is similar to the neighboring orders, but keeps changing, and the normalized response shows that the relative response changes rapidly in an echelle order. Also, we can conclude the gaussian filter that we attempted to use in Figures A.13 and A.27 deforms the response and not good enough

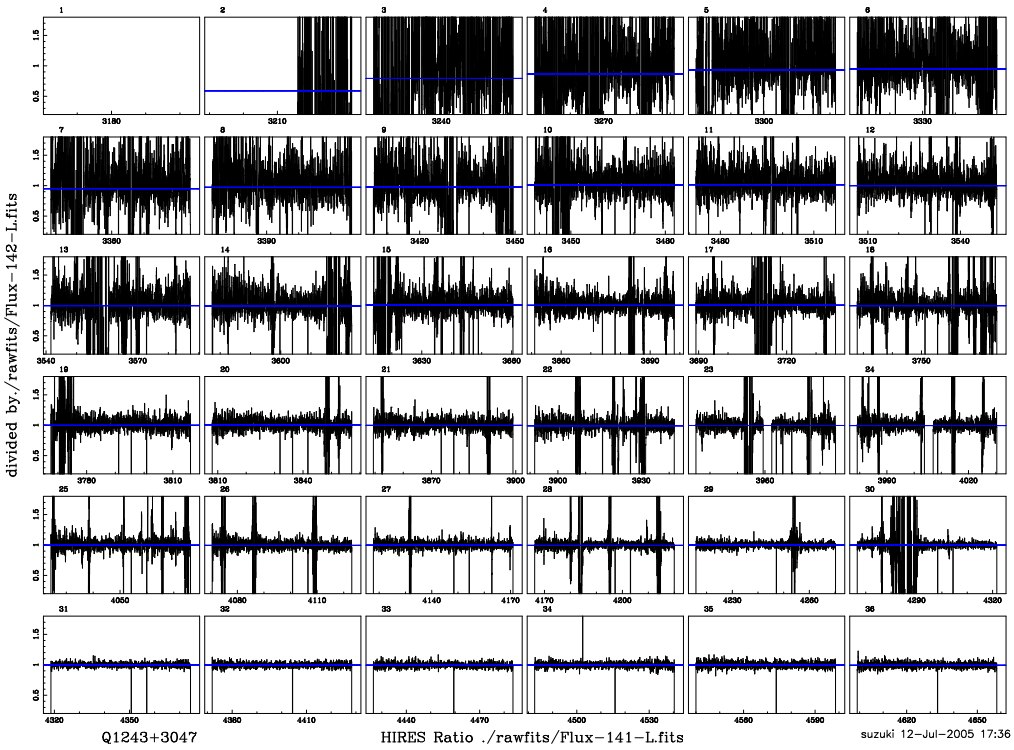

Figure A.36: Ratio of two HIRES quasar exposures. We have not calibrated flux yet. These are MAKEE's direct output (Flux-141-L.fits and Flux-142-L.fits). An exposure File-141 is divided by the reference File-142. Small box corresponds to an echelle order, and the wavelength goes from the top left to the bottom right. The ratios are flat within an echelle order. (10_HIRESratio_F141.ps)

to calibrate HIRES data. Once we have fitted response, we can apply it to the HIRES data, and we will have flux calibrated data.

Step 5: Combine Echelle Orders (`subroutine xtestmergeorders`)

The last step is to combine echelle orders and generate 1D flux calibrated spectrum. Echelle orders join quite well, and we show the results in Figures A.44, A.45, and A.46.

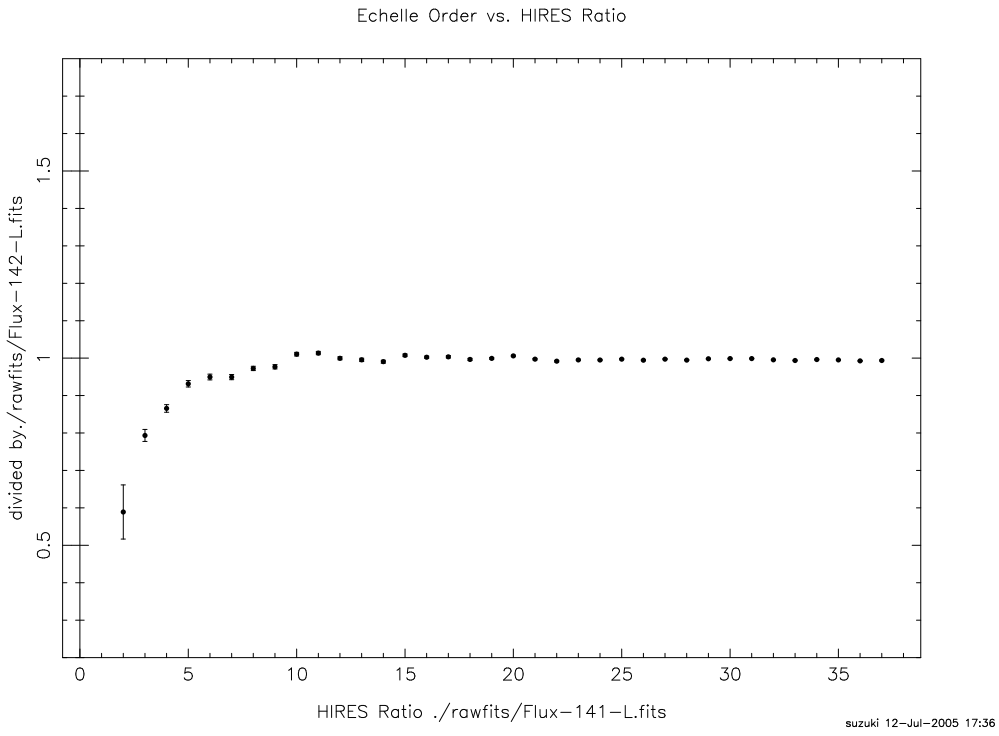

Figure A.37: Echelle order vs. Ratio of two HIRES quasar exposures. Echelle order is numbered from blue to red. The ratio drops at the blue end. This is probably due to inaccurate extinction correction. The ratio is flat within an echcelle order, but it changes gradually at the blue end. We use this calculated ratio to normalize an exposure. (11_Order_vs_Ratio_F141.ps)

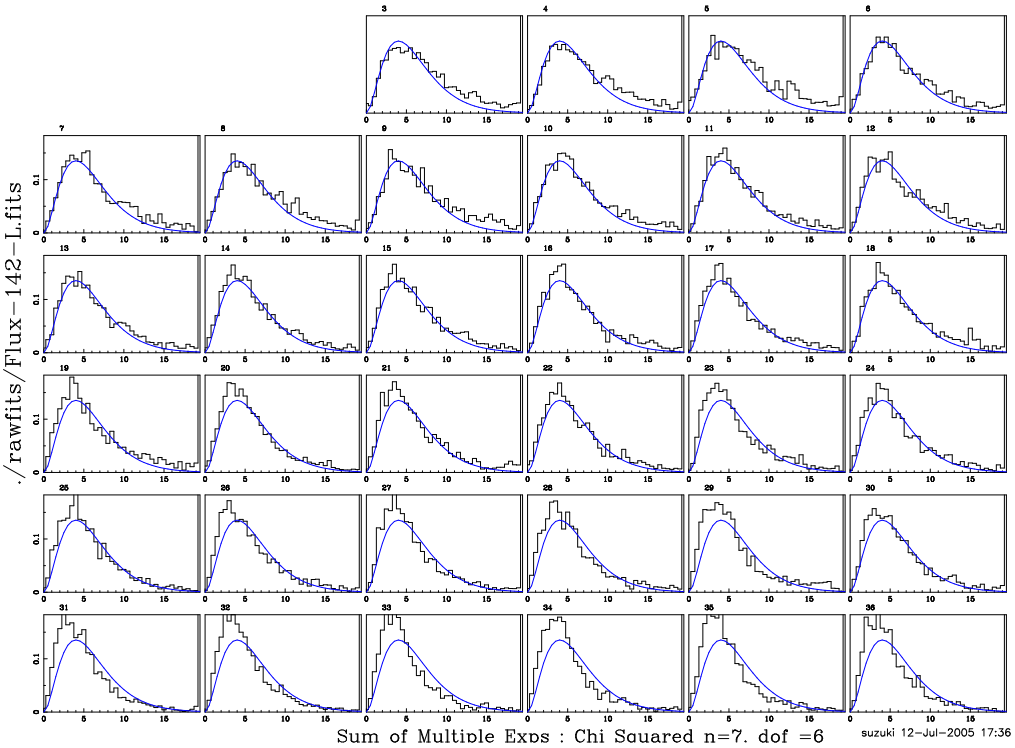

Figure A.38: Same as Figure A.19, A.33 but with without flux calibration. We normalized 7 exposures, and took weighted mean and this is the χ^2 distribution of 7 exposures. Interestingly, the deviation from the expected value implies that the we may under estimate 1σ error in blue and overestimate in red. (60_ChiSqStatistics.ps)

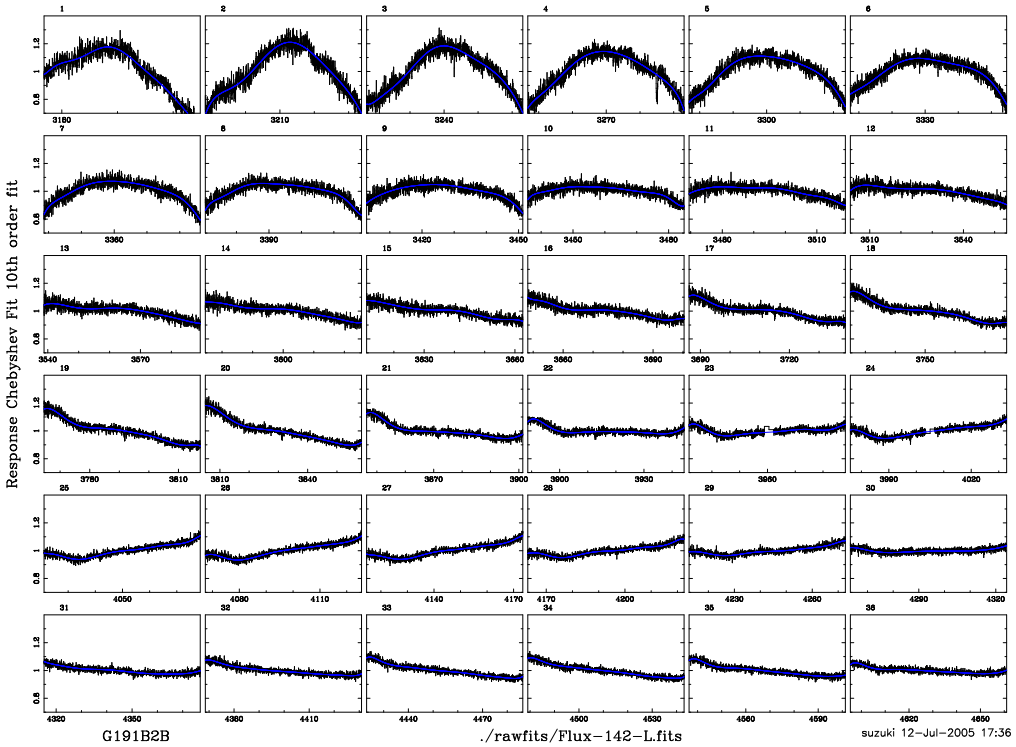

Figure A.39: Raw Response and 10th order Chebyshev polynomial fit. Small box corresponds to an echelle order. The response is normalized near the center of each echelle order for viewing purpose. (31_1dCRraw_F142.ps)

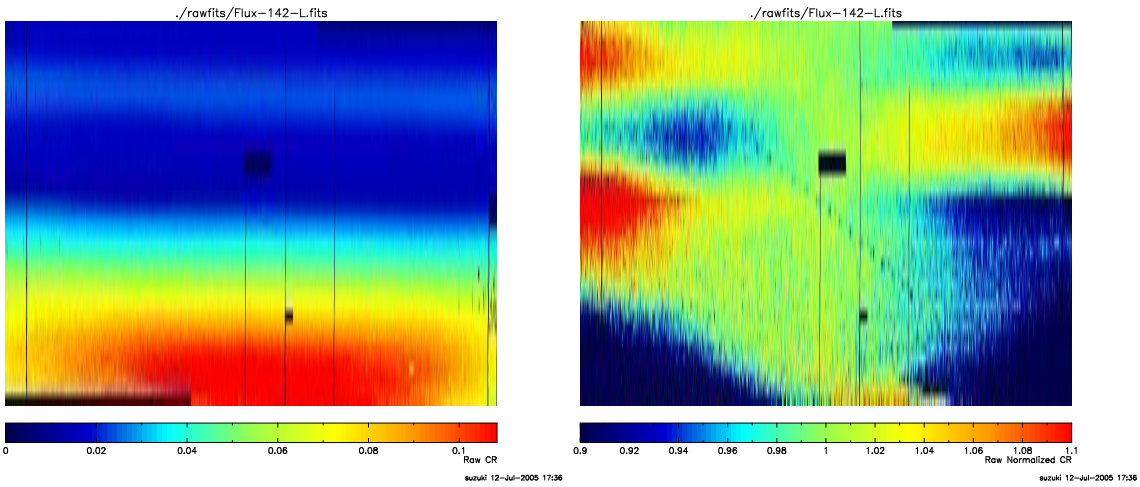

Figure A.40: **Left:** 2D raw response. The hole in the center is an ink spot. Thin black line is a dead CCD column. The pixels are in 2.1 km/s HIRES pixel size. (32a_2dCRraw_F142.ps) **Right:** Same as left panel but normalized near the center of each echelle order by taking the average of ± 15% of the pixels from the center. We can clearly see the the rapid relative change in CR in en echelle order. (32b_2dNCRraw_F142.ps)

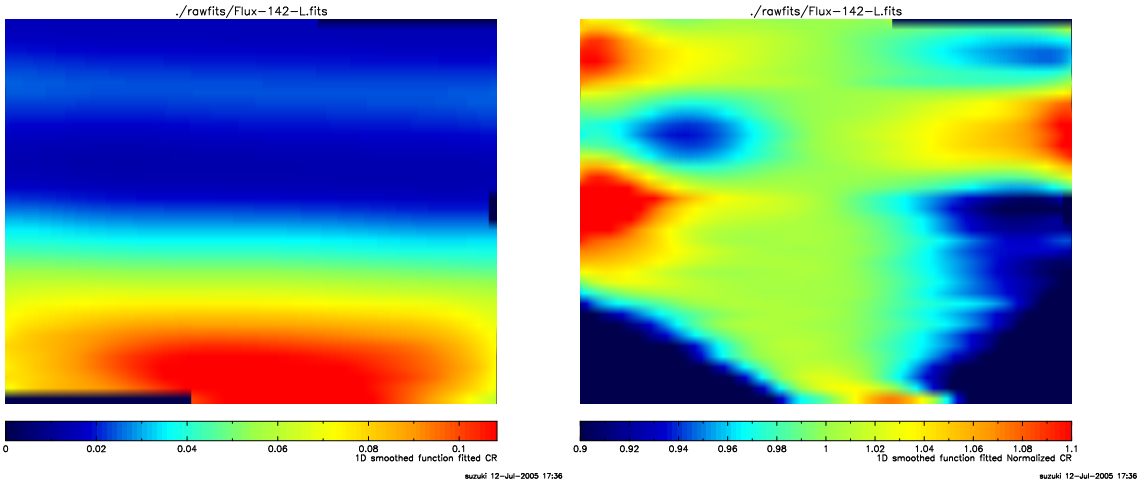

Figure A.41: **Left:** Response with 10th order chebyshev polynomial fit. This is not 2D fit but each echelle order is fitted by 10th order chebyshev polynomials. (37a_2dCRsmoothed_F142.ps) **Right:** Same as left panel but normalized near the center of each echelle order by taking the average of $\pm$ 15% of the pixels from the center. We can clearly see the the rapid relative change in response in en echelle order. What we have seen in Figure A.12 was real and we can conclude gaussian filter used in Figure A.13 is not good enough. (37b_2dNCRsmoothed_F142.ps)

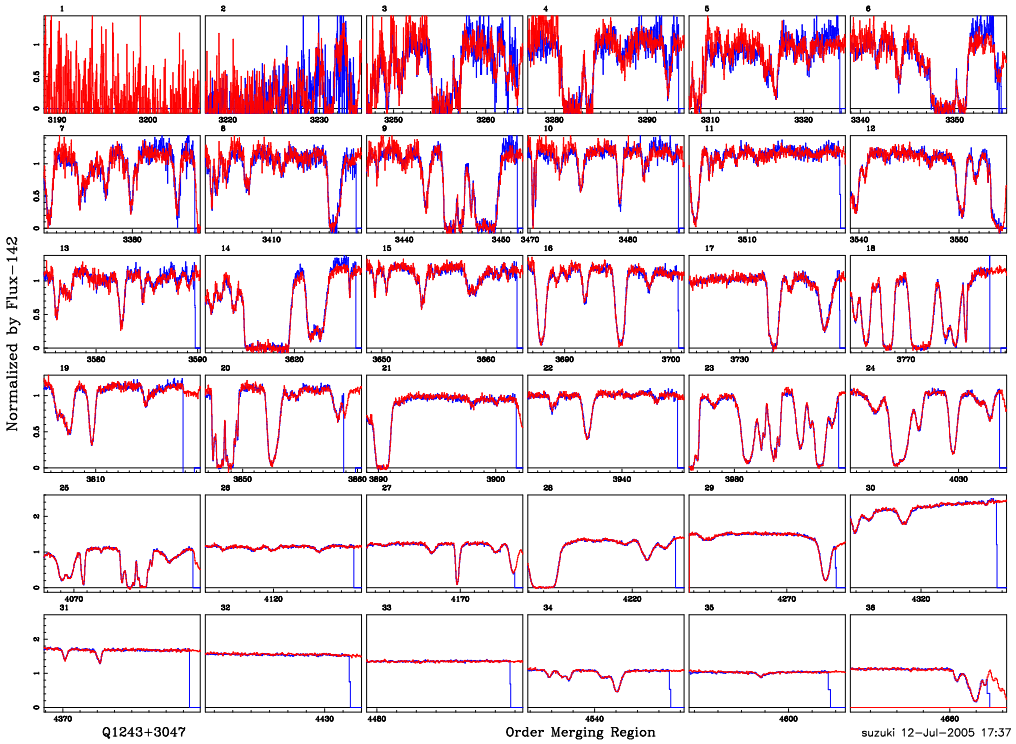

Figure A.42: Echelle orders' overlaps. The blue color represents data from the bluer echelle order and red color represents data from redder order. If we succeed to flux calibrate, the blue and red spectrum should overlap exactly. (40_1dOrderJoint.ps)

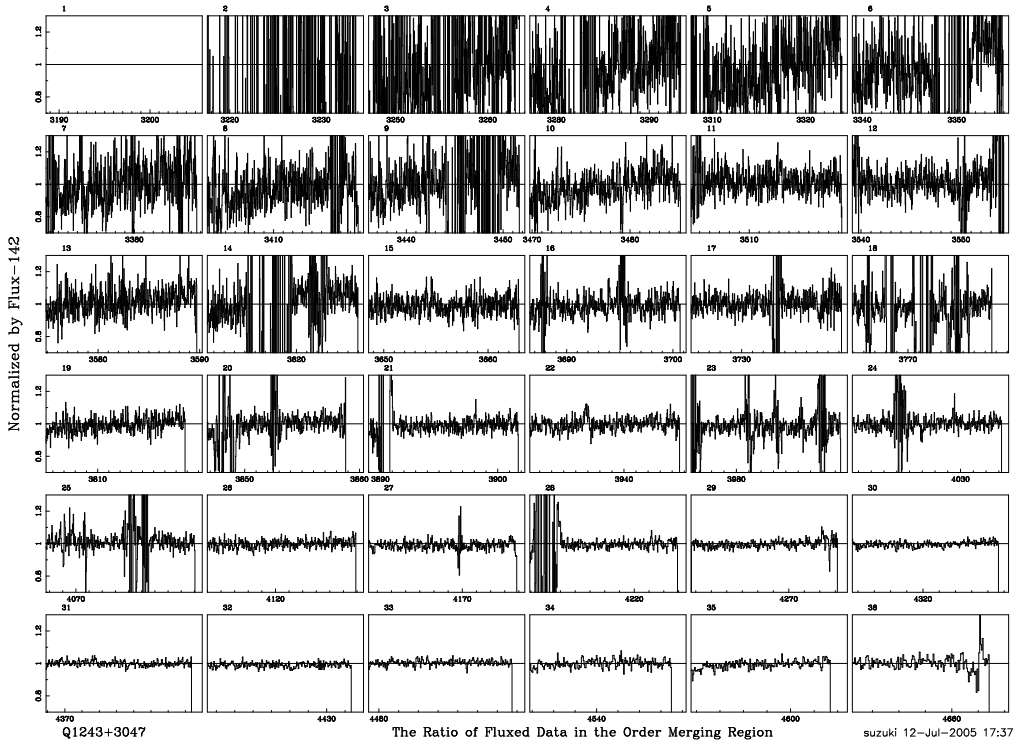

Figure A.43: Same as Figure A.42 but we are taking ratios of overlapping regions. The ratios should be close to one, and we have a good result on this example. (41_1dOrderJointRatio.ps)

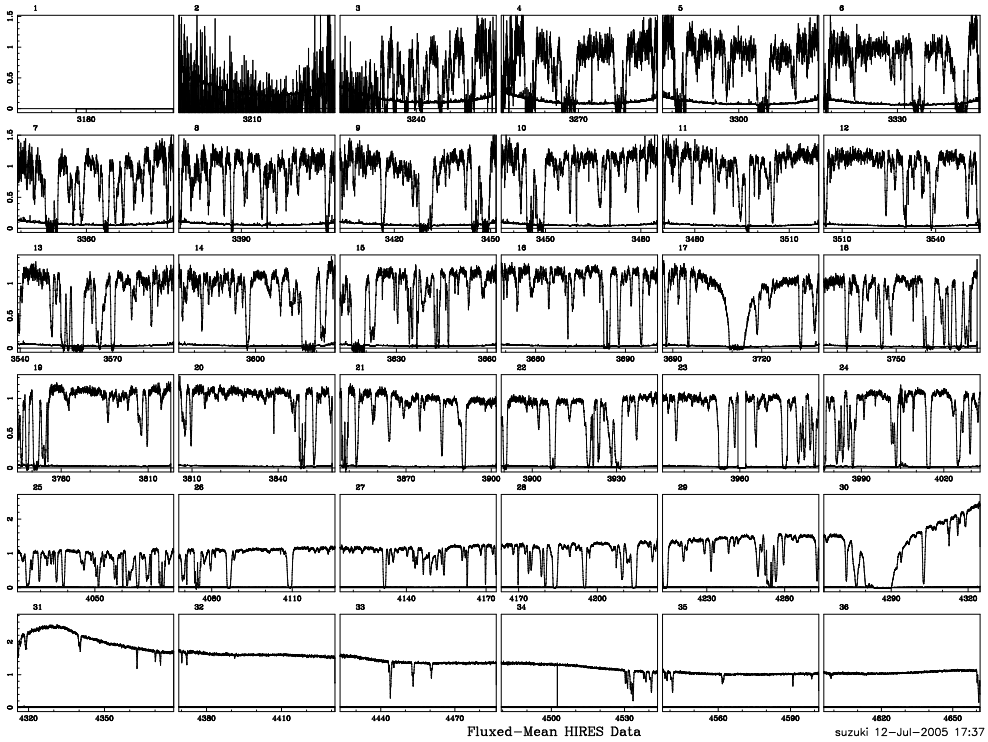

Figure A.44: Flux calibrated mean spectrum using high resolution model standard star. We took the weighted sum of 7 exposures. Small box corresponds to an echelle order, and the wavelength goes from the top left to the bottom left. (70_Mean-HIRES_by_EchelleOrders.ps)

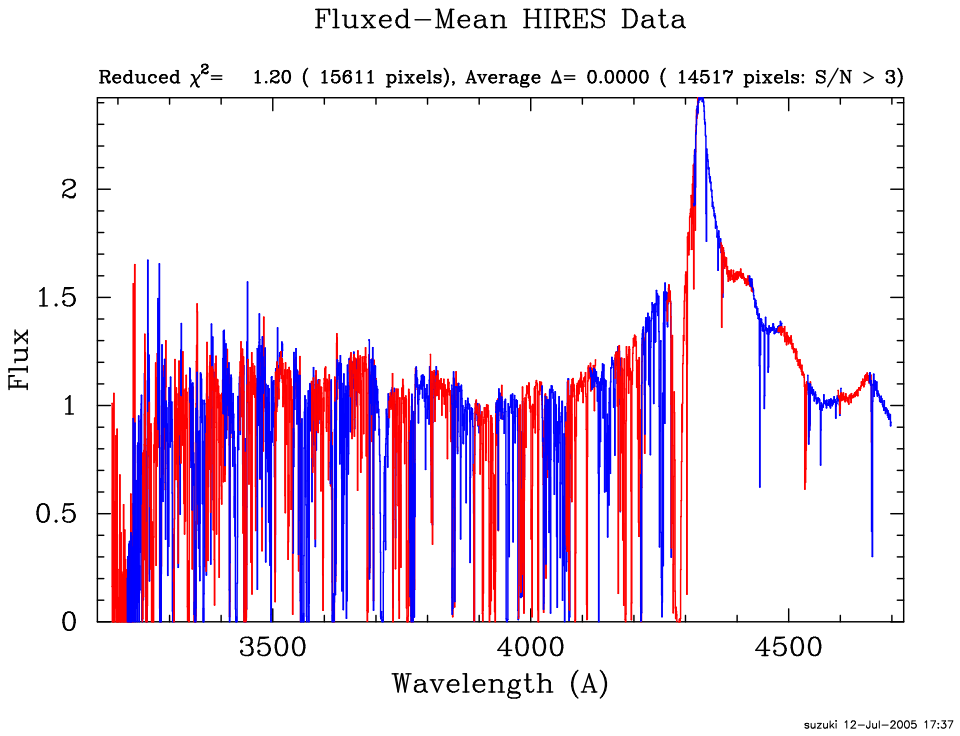

Figure A.45: 1D Flux calibrated mean spectrum with echelle orders in colors. Even echelle orders are colored in red, and odd orders are in blue. We can check the scale of echelle orders how they merge. (71_Fluxed-HIRES_1d_ordermergingcheck.ps)

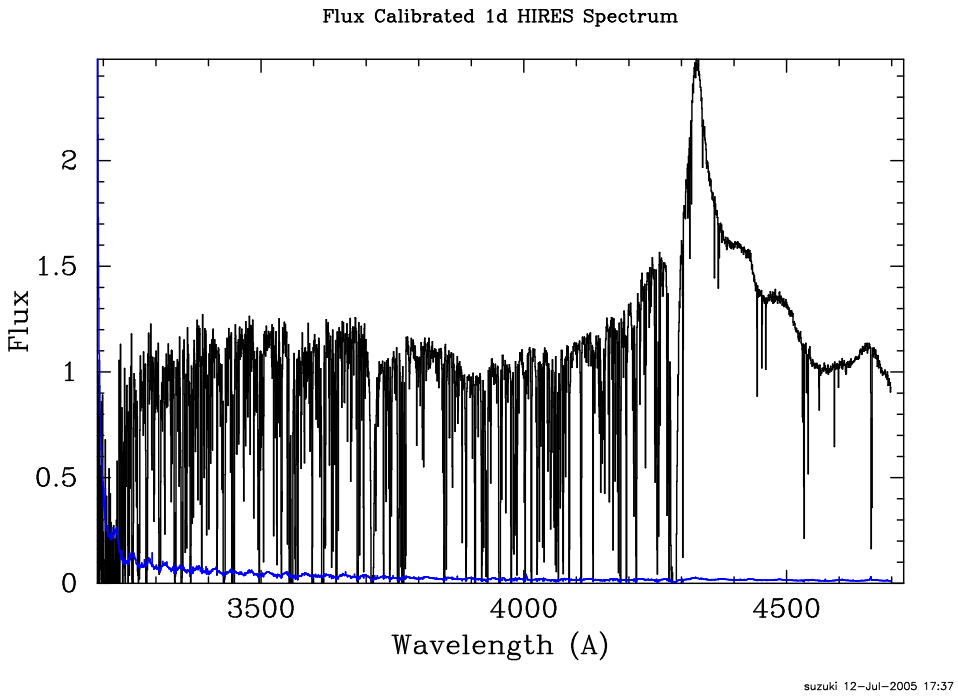

Figure A.46: 1D Flux calibrated mean spectrum using high resolution model standard star spectrum. Bumps seen in the spectrum are real emission lines. (72_Fluxed-HIRES_1d.ps)

Appendix B

High Resolution Standard Star Spectrum

B.1 Abstract

We present high resolution (FWHM=8km/s, 0.05 Å) and flux calibrated standard star spectra that are calibrated to better than 1% in absolute flux units. We calibrate 4 hot stars which are featureless and relatively easy to calibrate, and we can use them in a "flux ladder" to calibrate other objects. The calibrated flux standards will be made widely available to the community. This work is not directly related to stellar physics or our QSO absorption lines studies, but will serve any field of astronomy which requires high accuracy in flux calibration.

B.2 Introduction

The combination of large aperture telescopes and high resolution spectrographs has dramatically improved nearly every facet of astronomy. In the last decade, a number of 8-10m class telescopes have been constructed, each having a moderate to high resolution spectrographs with resolutions in the range of FWHM=0.05–0.1 Å (Table B.2).

Table B.1. Telescopes & Spectrographs

Telescope	Spectrograph	Year	R	FWHM (km/s)	Wavelength Range (Å)
KeckI	HIRES	1994	67,000	8	3200-10000
HST	STIS	1997	110,000	6	1150-10300
VLT	UVES	1999	110,000	6	3200-10500
Subaru	HDS	1999	160,000	4	3200-10000
Gemini	HROS	2002	150,000	4	4000-10000
Magellan	MIKE	2002	65,000	8	3200-10000

Flux calibration is important for precise measurements when we cannot see the unabsorbed continuum level, as with M stars or the Lyα forest in QSOs. However, flux calibration of the spectra these instruments produce is quite difficulty. The difficulty arises because the response function, particularly for echelles, can change rapidly on the scale of a few Å, and currently available standard stars do not have enough resolution to determine the response function on scales less than approximately 10 Å.

In Table B.2, we list the most commonly used sources for flux standards, and note in particular the lack of high resolution spectra (Hayes, 1970; Stone & Baldwin, 1983; Massey et al., 1988; Oke, 1990; Jacoby et al., 1984) These sources are unsuitable for work at high resolution, since they contain broad absorption features which prevent the interpolation of the sampled spectra to higher resolution.

Bohlin et al. (2001) released HST STIS spectra which have FWHM=2Å in resolution, but they still do not satisfy our needs. The size of these broad absorption lines (e.g. Balmer lines) are sometimes comparable to the wavelength coverage of an echelle order. An example of such a broad absorption feature from our HIRES data, together with the best available spectrophotometric flux standard for the same star, is shown in Figure B.1. The community needs spectrophotometric standard stars which resolve these lines.

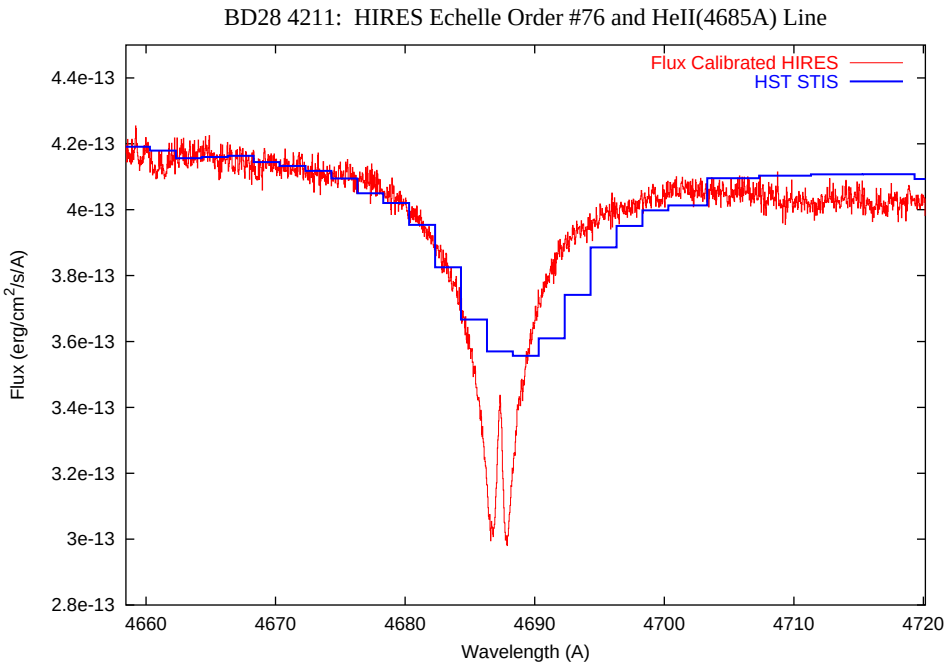

Figure B.1: The HeII λ4685 Å absorption feature in the spectrum of BD+28 4211. We show data from one order of the Keck HIRES spectrograph, and the best publicly available standard data (Bohlin et al., 2001) for the same star. Both HIRES and STIS spectra are in vacuum wavelength. We believe HIRES has more accurate wavelengths and flux. We used a response we obtained from another observed standard star, G191B2B, and its model spectrum. If we were to use this STIS standard spectra, we could introduce 5% errors in this region.

Table B.2. Popular Flux Standards

Paper	Year	Stars	Telescope	FWHM (Å)	Wavelength Range (Å)
Oke	1964	12	Palomar(5m)	50	3390–10800
Hayes	1970	12	Lick Crossley(0.9m)	30–45	3200–10870
Oke & Schild	1970	1	Palomar(5m)	100–400	3300–10800
Oke	1974	38	Palomar(5m)	20–80	3200–10500
Oke & Gunn	1983	6	Palomar(5m)	40	3080–12000
Jacoby *et al.*	1984	161	Kitt Peak(0.9m)	4.5	3510–7427
Stone & Baldwin	1983	18	CTIO(1.5m)	40–80	3200–8370
Massey *et al.*	1988	25	Kitt Peak(2.1m)	7–14	3200–8100
Oke	1990	25	Palomar(5m)	7–13	3200–9200

B.3 Data

B.3.1 Stars

We flux calibrate the four hot starts in Table B.3. These four stars are chosen for three reasons. First, they have smooth and nearly featureless spectra which make our flux calibration easier. Second, they are often used as flux standards and they all have the best optical calibrations of any stars, by Bohlin et al. (2001). Third, we have multiple exposures of each of these stars, including 70 of G191-B2B. We are aware that none of these stars is ideal, since they have all have lines in the blue – UV region, and G191-B2B is a binary, but they are among the simplest spectra that have been regularly used for spectrophotometry.

B.3.2 HIRES

We use high resolution echelle spectrograph (HIRES) on 10m Keck-I telescope which has a resolution of 8 km/s. HIRES divides a spectrum into 30-40 echelle orders, and originally it was not designed to be able to calibrate flux.

Table B.3. Primary Hot Standard Stars

Name	RA(J2000)	DEC(J2000)	V	Sp. Type
G191B2B	05 05 30.6	+52 49 54	11.78	DAO
Feige 34	10 39 36.7	+43 06 10	11.18	DO
BD28 4211	21 51 11.1	+28 51 52	10.51	Op
Feige 110	23 19 58.4	–05 09 56	11.82	DOp

B.4 Flux Calibration Method

We use the method described in §A.4. Before we flux calibrate the spectrum, we need to extract the spectrum from the 2D CCD image. We will use the normal software to extract the 1D spectrum from the HIRES CCD output. This software called MAKEE was written by Tom Barlow and has been used for many years with success. This software does a good job of removing cosmic ray hits and the usual flat field division. We have examined the ability of this software to extract a constant proportion of the flux at all wavelengths in a spectrum. We have some evidence that this is not perfect and may need improving. MAKEE also applies the mean extinction correction for Mauna Kea. Most temporal variations from this mean are smooth functions of wavelength and readily corrected later. Unfortunately the variations in the Ozone is strong at < 3400 Å(Schachter, 1991), and it will be hard to completely remove from the observed spectrum since we lack relevant calibrations. MAKEE subtracts the sky spectrum, and we will check the relevant wavelengths. We will convert the spectra to the heliocentric rest frame. At this point the remaining flux calibration errors change slowly across each order.

Once extraction is done, we generate response spectra using a model scpectrum G191B2B. We apply these responses to the other star spectra. As we have discussed in §A.4, it does not always succeed, but sometimes it does. As of today, we do not have a good prediction in what condition the flux calibration succeeds. But,

based on our experience, if the echelle order merges well, the global flux calibration is very likely to succeed. Therefore, the statistics which we introduced in §A.4 such as χ^2 and Δ are good indicators of the quality of flux calibration. We look for the best combination of the response and the observed star spectrum which produces well flux calibrated spectrum. We choose the flux calibrated data which gives the smallest χ^2 and Δ . Then we normalize the rest of the same star spectra to be like the best calibrated spectrum and sum them up.

B.5 Results

In Table B.4, we show the observation log of the first four flux calibrated high resolution spectra. We need to have a pair of standard stars to calibrate flux. Once we have a set of flux calibrated standard star spectra, we can apply them as a "flux calibration ladder", and we can iterate until they converge within the size of errors. The first iteration of the flux calibration is shown in Figure B.2 - B.5. Echelle orders overlap well, and they are reasonably well flux calibrated. The best Δ value is less than 1% . We can iterate the process and find the smallest Δ or χ^2 and normalize the rest of the exposures. We expect that we can achieve high S/N shown in Table B.5.

The high resolution flux calibrated spectrum is more reliable than STIS data in wavelength accuracy and relative flux values, although the absolute flux value relies on the STIS data itself since we use the STIS spectrum for absolute normalization. However, we believe our HIRES standard star spectrum is more reliable than the STIS spectrum. In Figure B.6, we show the comparison of the HIRES flux calibrated data with STIS spectrum on the same standard star BD28 4211. The STIS spectrum has an abrupt change in flux which is very unnatural while the HIRES has a smooth spectrum. We also found that the tiny spikes seen in the BD28 4211 are real OV and NV emission lines (Figure B.7). They are probably from the hot gas surrounds the white dwarf.

Table B.4. First FLux Calibrated Standard Stars

Name	Date	File ID	Exp (sec)	Response Star	Date	File ID	Exp (sec)	χ^2	Δ
G191B2B	1999 Mar 9	230	300	Feige 34	1999 Mar 9	240	300	0.9759	0.0040
Feige 34	1999 Mar 9	240	300	G191B2B[a]	1999 Mar 9	230	300	1.3242	0.0037
BD28 4211	1998 Oct 27	204	300	G191B2B[a]	1998 Oct 27	216	300	3.5519	0.0096
Feige 110	1998 Dec 14	273	300	Feige 34	1998 Dec 13	151	200	0.9908	0.0012

[a]Response is generated from G191B2B model spectrum (Bohlin, 2000)

Note. — The flux calibration ladder stars from these four standard stars. First, we use G191B2B model spectrum, we flux calibrate Feige 34 & BD28 4211. Then can flux calibrate G191B2B and Feige 110 using Feige 34.

Table B.5. Expected Results

Name	S/N (3200 Å)	S/N (5000 Å)	Exposure	Achievable S/N at 3200
G191B2B	N/A	N/A	14,970s(4.2hrs)	700
Feige 34	30	100	7,650s(2.1hrs)	500
BD28 4211	100	150	9,410s(2.6hrs)	500
Feige 110	N/A	N/A	1,800s(0.5hr)	250

B.6 Future Prospective

If we can iterate the flux calibration process and make a composite spectrum, we can obtain very high S/N spectrum. The templates of the ozone features seen below 3400 Å and atmospheric absorption lines (A & B band) would be useful for those who perform precise measurements. The high precision measurements demand accurate calibration. The accurate calibration starts from the standard star. This work will become the basis of all of the high resolution spectroscopy studies.

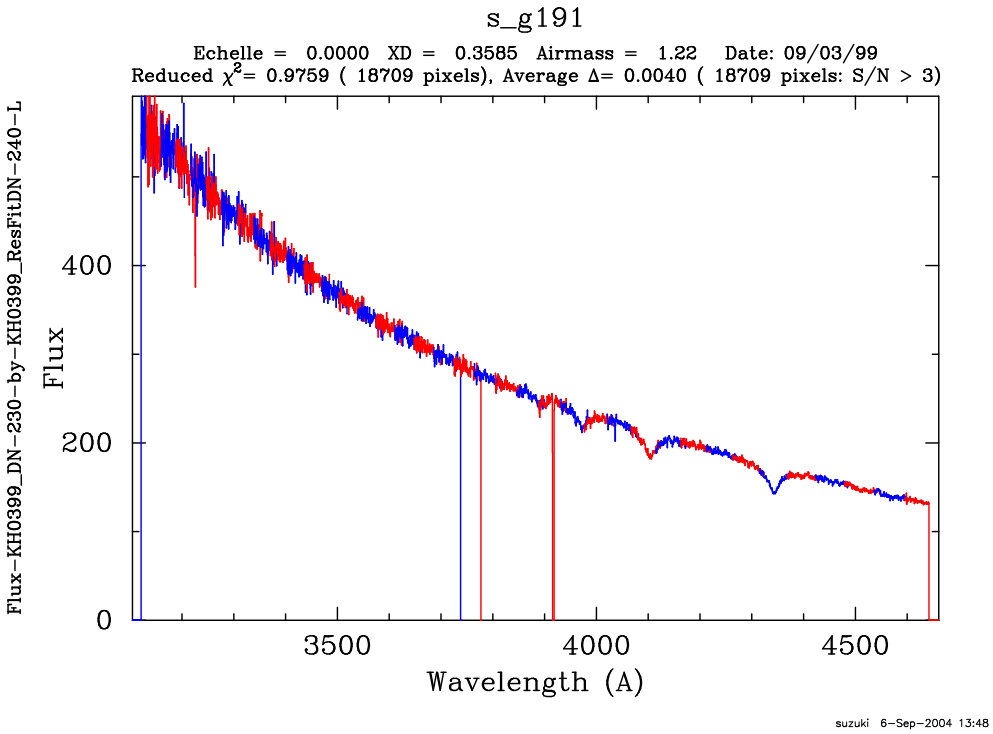

Figure B.2: Flux calibrated high resolution G191B2B HIRES spectrum. A color represents the size of an echelle order.

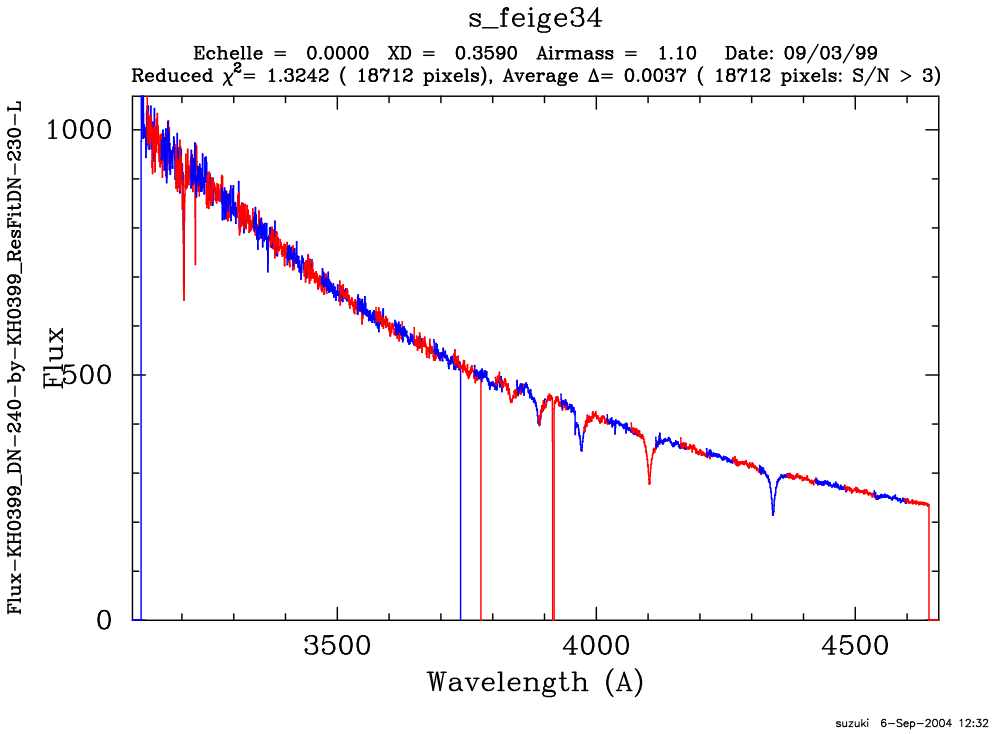

Figure B.3: Flux calibrated high resolution Feige 34 HIRES spectrum. A color represents the size of an echelle order.

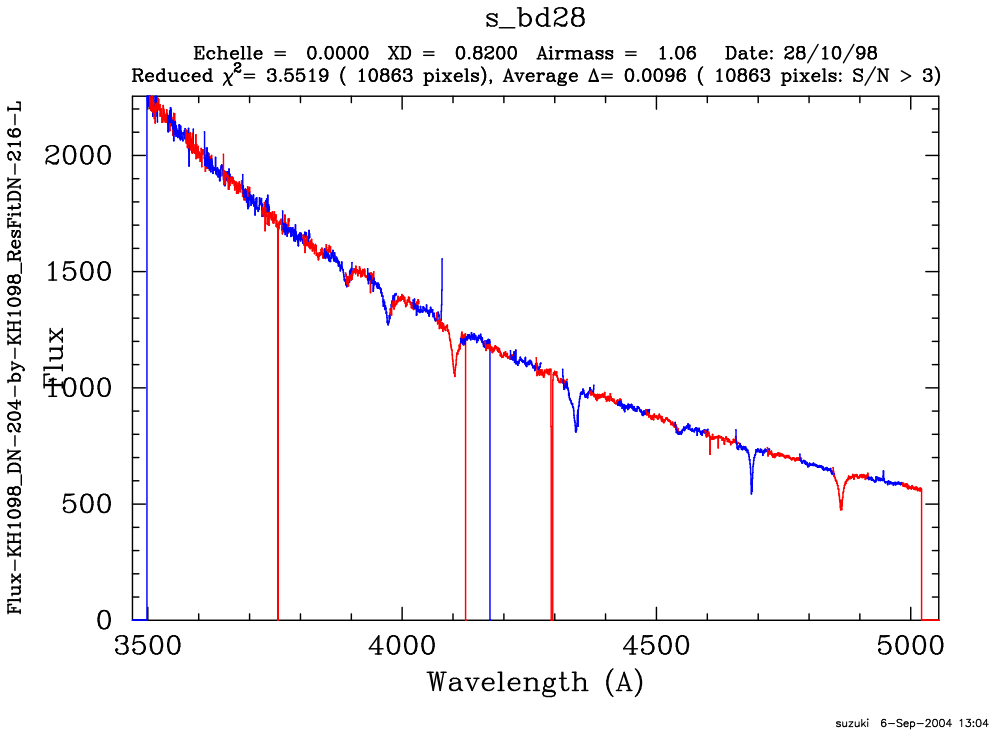

Figure B.4: Flux calibrated high resolution BD28 4211 HIRES spectrum. A color represents the size of an echelle order.

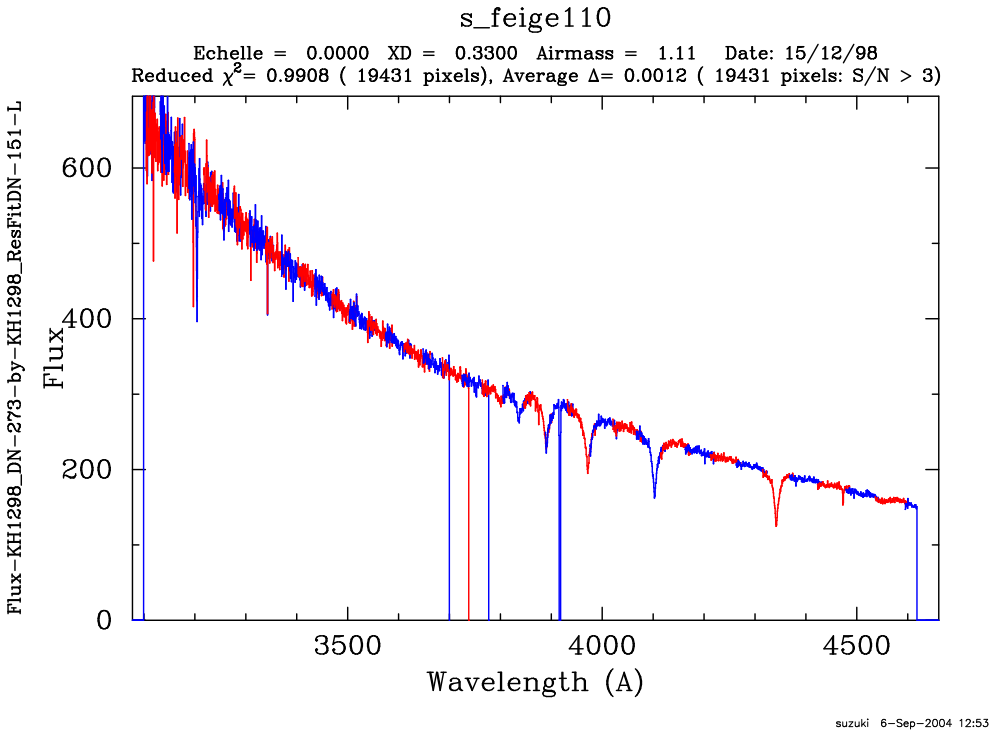

Figure B.5: Flux calibrated high resolution Feige 110 HIRES spectrum. A color represents the size of an echelle order.

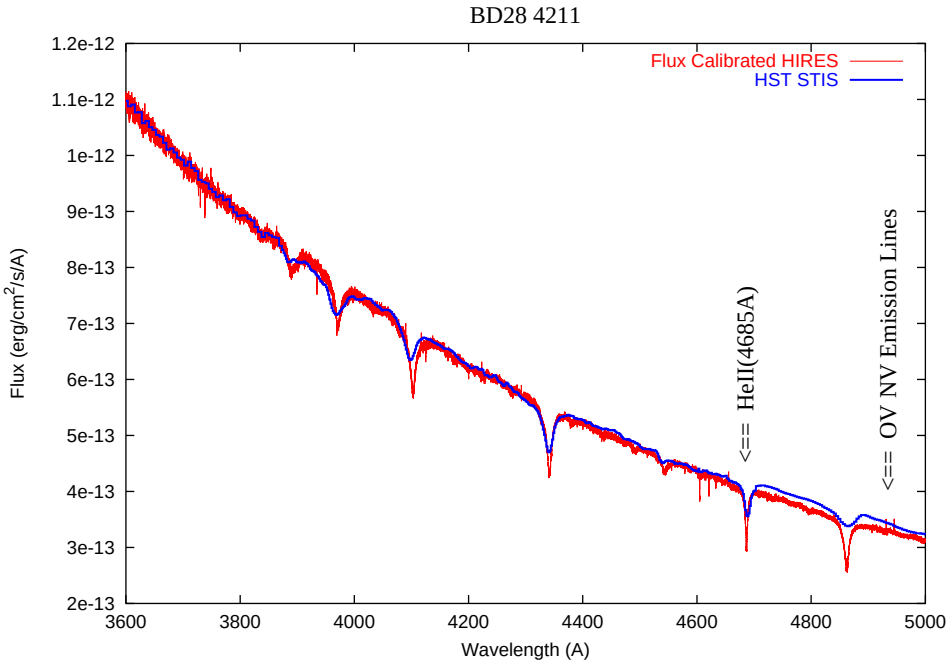

Figure B.6: Flux calibrated high resolution BD28 4211 HIRES spectrum (red) and STIS spectrum (blue). The STIS data has an abrupt change in flux around 4700 Å which is very unnatural. The tiny spikes seen around 4940 Å are real emission lines.

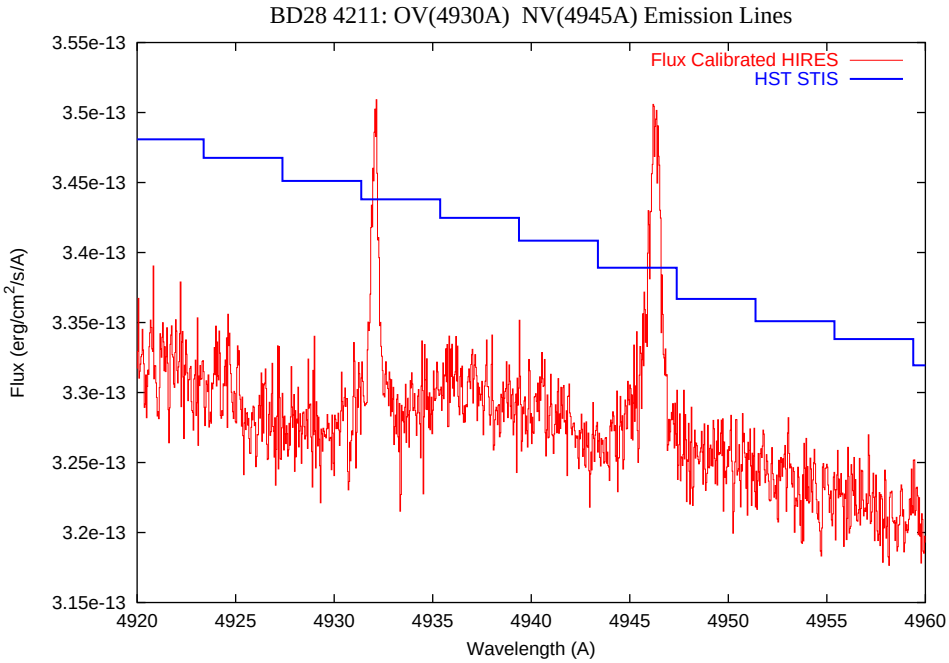

Figure B.7: Flux calibrated high resolution BD28 4211 HIRES spectrum (red) and STIS spectrum (blue). The spikes seen around 4940 Å are real emission lines: OV(4930Å) and NV(4945Å) lines. The HIRES spectrum shows their emission profiles. Probably, the white dwarf BD28 4211 is surrounded by a very hot gas and these emission lines are originated from this hot gas.

Bibliography

Abazajian, K. N. 2003, Astroparticle Physics, 19, 303

Allende Prieto, C., Lambert, D. L., & Asplund, M. 2001, ApJL, 556, L63

Alpher, R. A., Bethe, H., & Gamow, G. 1948, Physical Review, 73, 803

Aoki, W. 2002, http://www.subarutelescope.org/Observing/Instruments/HDS/index.html

Bahcall, J. N., Bergeron, J., Boksenberg, A., Hartig, G. F., Jannuzi, B. T., Kirhakos, S., Sargent, W. L. W., Savage, B. D., Schneider, D. P., Turnshek, D. A., Weymann, R. J., & Wolfe, A. M. 1993, ApJS, 87, 1

—. 1996, ApJ, 457, 19

Bahcall, J. N., Kirhakos, S., Saxe, D. H., & Schneider, D. P. 1997, ApJ, 479, 642

Baldwin, J. A. 1977, ApJ, 214, 679

Bania, T. M., Rood, R. T., & Balser, D. S. 2002, Nature, 415, 54

Barlow, T. A. & Sargent, W. L. W. 1997, AJ, 113, 136

Bechtold, J., Dobrzycki, A., Wilden, B., Morita, M., Scott, J., Dobrzycka, D., Tran, K., & Aldcroft, T. L. 2002, ApJS, 140, 143

Becker, R. H., Fan, X., White, R. L., Strauss, M. A., Narayanan, V. K., Lupton, R. H., Gunn, J. E., Annis, J., Bahcall, N. A., Brinkmann, J., Connolly, A. J., Csabai, I., Czarapata, P. C., Doi, M., Heckman, T. M., Hennessy, G. S., Ivezić,

Ž., Knapp, G. R., Lamb, D. Q., McKay, T. A., Munn, J. A., Nash, T., Nichol, R., Pier, J. R., Richards, G. T., Schneider, D. P., Stoughton, C., Szalay, A. S., Thakar, A. R., & York, D. G. 2001, AJ, 122, 2850

Bernardi, M., Sheth, R. K., SubbaRao, M., Richards, G. T., Burles, S., Connolly, A. J., Frieman, J., Nichol, R., Schaye, J., Schneider, D. P., Vanden Berk, D. E., York, D. G., Brinkmann, J., & Lamb, D. Q. 2003, AJ, 125, 32

Bigelow, B. C. & Nelson, J. E. 1998, in Proc. SPIE Vol. 3355, p. 164-174, Optical Astronomical Instrumentation, Sandro D'Odorico; Ed., Vol. 3355, 164–174

Bohlin, R. C. 2000, AJ, 120, 437

Bohlin, R. C., Dickinson, M. E., & Calzetti, D. 2001, AJ, 122, 2118

Bolton, J. S., Haehnelt, M. G., Viel, M., & Springel, V. 2004, MNRAS *submitted* (astro-ph/0411072)

Boroson, T. A. 2002, ApJ, 565, 78

Boroson, T. A. & Green, R. F. 1992, ApJS, 80, 109

Bruzual A., G. & Charlot, S. 1993, ApJ, 405, 538

Burki, G., Rufener, F., Burnet, M., Richard, C., Blecha, A., & Bratschi, P. 1995, A&AS, 112, 383

Burles, S. 1997, Ph.D. Thesis (UCSD)

Burles, S., Nollett, K. M., & Turner, M. S. 2001, ApJL, 552, L1

Burles, S. & Tytler, D. 1998a, ApJ, 499, 699

—. 1998b, ApJ, 507, 732

Burstein, D. & Heiles, C. 1982, AJ, 87, 1165

Cabanac, R. A., de Lapparent, V., & Hickson, P. 2002, A&A, 389, 1090

Cardelli, J. A., Clayton, G. C., & Mathis, J. S. 1989, ApJ, 345, 245

Carswell, R. F., Whelan, J. A. J., Smith, M. G., Boksenberg, A., & Tytler, D. 1982, MNRAS, 198, 91

Cen, R. 2003, ApJ, 591, 12

Clayton, M. 1996, http://starlink.rl.ac.uk/star/docs/sg9.htx/sg9.html

Connolly, A. J., Szalay, A. S., Bershady, M. A., Kinney, A. L., & Calzetti, D. 1995, AJ, 110, 1071

Copi, C. J., Olive, K. A., & Schramm, D. N. 1998, Proceedings of the National Academy of Science, 95, 2758

Croft, R. A. C., Hernquist, L., Springel, V., Westover, M., & White, M. 2002a, ApJ, 580, 634

Croft, R. A. C., Weinberg, D. H., Bolte, M., Burles, S., Hernquist, L., Katz, N., Kirkman, D., & Tytler, D. 2002b, ApJ, 581, 20

Cyburt, R. H., Fields, B. D., & Olive, K. A. 2003, Physics Letters B, 567, 227

Dekker, H., D'Odorico, S., Kaufer, A., Delabre, B., & Kotzlowski, H. 2000, in Proc. SPIE Vol. 4008, p. 534-545, Optical and IR Telescope Instrumentation and Detectors, Masanori Iye; Alan F. Moorwood; Eds., Vol. 4008, 534–545

di Bari, P. & Foot, R. 2001, Physical Review D, 63, 043008

Diego, F., Charalambous, A., Fish, A. C., & Walker, D. D. 1990, in Instrumentation in astronomy VII; Proceedings of the Meeting, Tucson, AZ, Feb. 13-17, 1990 (A91-29601 11-35). Bellingham, WA, Society of Photo-Optical Instrumentation Engineers, 1990, p. 562-576. Anglo-Australian Observatory-supported research., Vol. 1235, 562–576

Djorgovski, S. G., Castro, S., Stern, D., & Mahabal, A. A. 2001, ApJL, 560, L5

Dolgov, A. D. 2002, Physics Reports, 370, 333

Dolgov, A. D. & Pagel, B. E. J. 1999, New Astronomy, 4, 223

Efstathiou, G. 2002, MNRAS, 332, 193

Elvis, M., Wilkes, B. J., McDowell, J. C., Green, R. F., Bechtold, J., Willner, S. P., Oey, M. S., Polomski, E., & Cutri, R. 1994, ApJS, 95, 1

Epps, H. W. & Miller, J. S. 1998, in Proc. SPIE Vol. 3355, p. 48-58, Optical Astronomical Instrumentation, Sandro D'Odorico; Ed., Vol. 3355, 48–58

Epstein, R. I., Lattimer, J. M., & Schramm, D. N. 1976, Nature, 263, 198

Esposito, S., Mangano, G., Miele, G., & Pisanti, O. 2000a, Nuclear Physics B Proceedings Supplements, 85, 292

Esposito, S., Miele, G., Pastor, S., Peloso, M., & Pisanti, O. 2000b, Nuclear Physics B, 590, 539

Everett, M. E. & Wagner, R. M. 1995, PASP, 107, 1059

Famiano, M. A., Boyd, R. N., & Kajino, T. 2002, ApJ, 576, 89

Fan, X., Narayanan, V. K., Lupton, R. H., Strauss, M. A., Knapp, G. R., Becker, R. H., White, R. L., Pentericci, L., Leggett, S. K., Haiman, Z., Gunn, J. E., Ivezić, Ž., Schneider, D. P., Anderson, S. F., Brinkmann, J., Bahcall, N. A., Connolly, A. J., Csabai, I., Doi, M., Fukugita, M., Geballe, T., Grebel, E. K., Harbeck, D., Hennessy, G., Lamb, D. Q., Miknaitis, G., Munn, J. A., Nichol, R., Okamura, S., Pier, J. R., Prada, F., Richards, G. T., Szalay, A., & York, D. G. 2001, AJ, 122, 2833

Fan, X., Strauss, M. A., Schneider, D. P., Becker, R. H., White, R. L., Haiman, Z., Gregg, M., Pentericci, L., Grebel, E. K., Narayanan, V. K., Loh, Y., Richards, G. T., Gunn, J. E., Lupton, R. H., Knapp, G. R., Ivezić, Ž., Brandt, W. N., Collinge, M., Hao, L., Harbeck, D., Prada, F., Schaye, J., Strateva, I., Zakamska,

N., Anderson, S., Brinkmann, J., Bahcall, N. A., Lamb, D. Q., Okamura, S., Szalay, A., & York, D. G. 2003, AJ, 125, 1649

Fields, B. D., Olive, K. A., Silk, J., Cassé, M., & Vangioni-Flam, E. 2001, ApJ, 563, 653

Fitzpatrick, E. L. 1999, PASP, 111, 63

Francis, P. J., Hewett, P. C., Foltz, C. B., & Chaffee, F. H. 1992, ApJ, 398, 476

Fukuda, Y., Hayakawa, T., Ichihara, E., Inoue, K., Ishihara, K., Ishino, H., Itow, Y., Kajita, T., Kameda, J., Kasuga, S., Kobayashi, K., Kobayashi, Y., Koshio, Y., Miura, M., Nakahata, M., Nakayama, S., Okada, A., Okumura, K., Sakurai, N., Shiozawa, M., Suzuki, Y., Takeuchi, Y., Totsuka, Y., Yamada, S., Earl, M., Habig, A., Kearns, E., Messier, M. D., Scholberg, K., Stone, J. L., Sulak, L. R., Walter, C. W., Goldhaber, M., Barszczxak, T., Casper, D., Gajewski, W., Halverson, P. G., Hsu, J., Kropp, W. R., Price, L. R., Reines, F., Smy, M., Sobel, H. W., Vagins, M. R., Ganezer, K. S., Keig, W. E., Ellsworth, R. W., Tasaka, S., Flanagan, J. W., Kibayashi, A., Learned, J. G., Matsuno, S., Stenger, V. J., Takemori, D., Ishii, T., Kanzaki, J., Kobayashi, T., Mine, S., Nakamura, K., Nishikawa, K., Oyama, Y., Sakai, A., Sakuda, M., Sasaki, O., Echigo, S., Kohama, M., Suzuki, A. T., Haines, T. J., Blaufuss, E., Kim, B. K., Sanford, R., Svoboda, R., Chen, M. L., Conner, Z., Goodman, J. A., Sullivan, G. W., Hill, J., Jung, C. K., Martens, K., Mauger, C., McGrew, C., Sharkey, E., Viren, B., Yanagisawa, C., Doki, W., Miyano, K., Okazawa, H., Saji, C., Takahata, M., Nagashima, Y., Takita, M., Yamaguchi, T., Yoshida, M., Kim, S. B., Etoh, M., Fujita, K., Hasegawa, A., Hasegawa, T., Hatakeyama, S., Iwamoto, T., Koga, M., Maruyama, T., Ogawa, H., Shirai, J., Suzuki, A., Tsushima, F., Koshiba, M., Nemoto, M., Nishijima, K., Futagami, T., Hayato, Y., Kanaya, Y., Kaneyuki, K., Watanabe, Y., Kielczewska, D., Doyle, R. A., George, J. S., Stachyra, A. L., Wai, L. L., Wilkes, R. J., & Young, K. K. 1998, Physical Review Letters, 81, 1562

Fuller, G. M. & Shi, X. 1997, ApJL, 487, L25

Galli, D., Palla, F., Ferrini, F., & Penco, U. 1995, ApJ, 443, 536

Green, P. J., Aldcroft, T. L., Mathur, S., Wilkes, B. J., & Elvis, M. 2001, ApJ, 558, 109

Gunn, J. E. & Peterson, B. A. 1965, ApJ, 142, 1633

Haardt, F. & Madau, P. 2001, in Clusters of galaxies and the high redshift universe observed in X-rays, Recent results of XMM-Newton and Chandra, XXXVIth Rencontres de Moriond, XXIst Moriond Astrophysics Meeting, March 10-17, 2001, Savoie France. Edited by D.M. Neumann & J.T.T. Van

Hagen, H.-J., Engels, D., & Reimers, D. 1999, A&AS, 134, 483

Hayashi, C. 1950, Progress of Theoretical Physics, 5, 224

Hayes, D. S. 1970, ApJ, 159, 165

Hewett, P. C., Foltz, C. B., & Chaffee, F. H. 1995, AJ, 109, 1498

—. 2001, AJ, 122, 518

Hui, L., Haiman, Z., Zaldarriaga, M., & Alexander, T. 2002, ApJ, 564, 525

Hui, L., Stebbins, A., & Burles, S. 1999, ApJL, 511, L5

Izotov, Y. I. & Thuan, T. X. 1998, ApJ, 500, 188

—. 2004, ApJ, 602, 200

Jacoby, G. H., Hunter, D. A., & Christian, C. A. 1984, ApJS, 56, 257

Jannuzi, B. T., Bahcall, J. N., Bergeron, J., Boksenberg, A., Hartig, G. F., Kirhakos, S., Sargent, W. L. W., Savage, B. D., Schneider, D. P., Turnshek, D. A., Weymann, R. J., & Wolfe, A. M. 1998, ApJS, 118, 1

Jannuzi, B. T., Hartig, G. F., Kirhakos, S., Sargent, W. L. W., Turnshek, D. A., Weymann, R. J., Bahcall, J. N., Bergeron, J., Boksenberg, A., Savage, B. D., Schneider, D. P., & Wolfe, A. M. 1996, ApJL, 470, L11

Jedamzik, K. 2002, Planet. Space Sci., 50, 1239

Jedamzik, K. & Fuller, G. M. 1997, ApJ, 483, 560

Jena, T., Norman, M. L., Tytler, D., Kirkman, D., Suzuki, N., Chapman, A., Melis, C., Paschos, P., O'Shea, B., So, G., Lubin, D., Lin, W., Reimers, D., Janknecht, E., & Fechner, C. 2005, MNRAS, 361, 70

Kainulainen, K., Kurki-Suonio, H., & Sihvola, E. 1999, Physical Review D, 59, 83505

Kanbur, S. M., Iono, D., Tanvir, N. R., & Hendry, M. A. 2002, MNRAS, 329, 126

Kaplinghat, M. & Turner, M. S. 2001, Physical Review Letters, 86, 385

Karhunen, H. 1947, Ann. Acad. Sci. Fenn. A., 1, 37

Kendall, M. G. 1980, Multivariate Analysis (London: Griffin)

Kennefick, J. D., Djorgovski, S. G., & de Carvalho, R. R. 1995, AJ, 110, 2553

Kim, T., Hu, E. M., Cowie, L. L., & Songaila, A. 1997, AJ, 114, 1

Kim, T.-S., Cristiani, S., & D'Odorico, S. 2001, A&A, 373, 757

Kirkman, D. & Tytler, D. 1997, ApJ, 484, 672

Kirkman, D., Tytler, D., Burles, S., Lubin, D., & O'Meara, J. M. 2000, ApJ, 529, 655

Kirkman, D., Tytler, D., Suzuki, N., O'Meara, J. M., & Lubin, D. 2003, ApJS, 149, 1

Kneller, J. P. & Steigman, G. 2003, Physical Review D, 67, 063501

Kolb, E. W. & Turner, M. S. 1990, The Early Universe (Frontiers in Physics, Reading, MA: Addison-Wesley, 1988, 1990)

Kurki-Suonio, H. 2000, in IAU Symposium, Vol. 198, 25

Levshakov, S., Tytler, D., & Burles, S. 1999, in Early Universe: Cosmological Problems and Instrumental Techniques, proceedings of the Gamov Memorial Intern. Conf. St. Petersburg, Aug 23-28

Levshakov, S. A., Kegel, W. H., & Takahara, F. 1998, ApJL, 499, L1

Liske, J. & Williger, G. M. 2001, MNRAS, 328, 653

Loeb, A. & Barkana, R. 2001, ARA&A, 39, 19

Loève, M. 1948, Processus Stochastiques et Mouvement Brownien (Paris, Hermann)

Lopez, R. E. & Turner, M. S. 1999, Physical Review D, 59, 103502

Lubowich, D. A., Pasachoff, J. M., Balonek, T. J., Millar, T. J., Tremonti, C., Roberts, H., & Galloway, R. P. 2000, Nature, 405, 1025

Madau, P. 1995, ApJ, 441, 18

Madau, P., Ferguson, H. C., Dickinson, M. E., Giavalisco, M., Steidel, C. C., & Fruchter, A. 1996, MNRAS, 283, 1388

Madau, P., Haardt, F., & Rees, M. J. 1999, ApJ, 514, 648

Malkan, M. A. 1983, ApJ, 268, 582

Malkan, M. A. & Sargent, W. L. W. 1982, ApJ, 254, 22

Massey, P., Strobel, K., Barnes, J. V., & Anderson, E. 1988, ApJ, 328, 315

Massey, P., Valdes, F., & Barnes, J. 1992, http://iraf.noao.edu/docs/spectra.html

McDonald, P. 2003, ApJ, 585, 34

McDonald, P. & Miralda-Escudé, J. 2001, ApJL, 549, L11

McDonald, P., Seljak, U., Burles, S., Schlegel, D. J., Weinberg, D. H., Shih, D., Schaye, J., Schneider, D. P., Brinkmann, J., Brunner, R. J., & Fukugita, M. 2004, ApJsubmitted, astro-ph/0405013

McLean, I. S., Becklin, E. E., Bendiksen, O., Brims, G., Canfield, J., Figer, D. F., Graham, J. R., Hare, J., Lacayanga, F., Larkin, J. E., Larson, S. B., Levenson, N., Magnone, N., Teplitz, H., & Wong, W. 1998, in Proc. SPIE Vol. 3354, p. 566-578, Infrared Astronomical Instrumentation, Albert M. Fowler; Ed., Vol. 3354, 566

Meiksin, A. & White, M. 2004, MNRAS, eprint arXiv:astro-ph/0205387, 350, 1107

Moos, H. W., Sembach, K. R., Vidal-Madjar, A., York, D. G., Friedman, S. D., Hébrard, G., Kruk, J. W., Lehner, N., Lemoine, M., Sonneborn, G., Wood, B. E., Ake, T. B., André, M., Blair, W. P., Chayer, P., Gry, C., Dupree, A. K., Ferlet, R., Feldman, P. D., Green, J. C., Howk, J. C., Hutchings, J. B., Jenkins, E. B., Linsky, J. L., Murphy, E. M., Oegerle, W. R., Oliveira, C., Roth, K., Sahnow, D. J., Savage, B. D., Shull, J. M., Tripp, T. M., Weiler, E. J., Welsh, B. Y., Wilkinson, E., & Woodgate, B. E. 2002, ApJS, 140, 3

Morton, D. C. 1991, ApJS, 77, 119

Noguchi, K., Ando, H., Izumiura, H., Kawanomoto, S., Tanaka, W., & Aoki, W. 1998, in Proc. SPIE Vol. 3355, p. 354-362, Optical Astronomical Instrumentation, Sandro D'Odorico; Ed., Vol. 3355, 354–362

Oke, J. B. 1964, ApJ, 140, 689

—. 1974, ApJS, 27, 21

—. 1990, AJ, 99, 1621

Oke, J. B. & Gunn, J. E. 1983, ApJ, 266, 713

Oke, J. B. & Korycansky, D. G. 1982, ApJ, 255, 11

Oke, J. B. & Schild, R. E. 1970, ApJ, 161, 1015

Olive, K. A. & Skillman, E. D. 2001, New Astronomy, Volume 6, Issue 3, p. 119-150., 6, 119

Olive, K. A., Steigman, G., & Skillman, E. D. 1997, ApJ, 483, 788

Oliveira, C. M., Hébrard, G., Howk, J. C., Kruk, J. W., Chayer, P., & Moos, H. W. 2003, ApJ, 587, 235

O'Meara, J. M., Tytler, D., Kirkman, D., Suzuki, N., Prochaska, J. X., Lubin, D., & Wolfe, A. M. 2001, ApJ, 552, 718

Ostriker, J. P. & Tinsley, B. M. 1975, ApJL, 201, L51

Pagel, B. E. J. 2000, Physics Reports, 333, 433

Paschos, P. & Norman, M. L. 2005, ApJ (submitted, astro-ph/0412244)

Peebles, P. J. E. 1966, ApJ, 146, 542

Pei, Y. C. 1995, ApJ, 438, 623

Peimbert, A., Peimbert, M., & Luridiana, V. 2002, ApJ, 565, 668

Perlmutter, S., Aldering, G., Goldhaber, G., Knop, R. A., Nugent, P., Castro, P. G., Deustua, S., Fabbro, S., Goobar, A., Groom, D. E., Hook, I. M., Kim, A. G., Kim, M. Y., Lee, J. C., Nunes, N. J., Pain, R., Pennypacker, C. R., Quimby, R., Lidman, C., Ellis, R. S., Irwin, M., McMahon, R. G., Ruiz-Lapuente, P., Walton, N., Schaefer, B., Boyle, B. J., Filippenko, A. V., Matheson, T., Fruchter, A. S., Panagia, N., Newberg, H. J. M., Couch, W. J., & The Supernova Cosmology Project. 1999, ApJ, 517, 565

Pettini, M. & Bowen, D. V. 2001, ApJ, 560, 41

Pinsonneault, M. H., Steigman, G., Walker, T. P., & Narayanan, V. K. 2002, ApJ, 574, 398

Prantzos, N. 1996, A&A, 310, 106

Prantzos, N. & Ishimaru, Y. 2001, A&A, 376, 751

Prantzos, N. & Silk, J. 1998, ApJ, 507, 229

Press, W. H., Rybicki, G. B., & Schneider, D. P. 1993, ApJ, 414, 64

Press, W. H., Teukolsky, S. A., Vetterling, W. T., & Flannery, B. P. 1992, Numerical Recipes in FORTRAN (Cambridge: University Press, 2nd ed.)

Prochaska, J. X. & Wolfe, A. M. 1997, ApJ, 474, 140

Pruet, J., Guiles, S., & Fuller, G. M. 2002, ApJ, 580, 368

Rauch, M. 1998, ARA&A, 36, 267

Rauch, M., Miralda-Escude, J., Sargent, W. L. W., Barlow, T. A., Weinberg, D. H., Hernquist, L., Katz, N., Cen, R., & Ostriker, J. P. 1997, ApJ, 489, 7

Ryan, S. G., Beers, T. C., Olive, K. A., Fields, B. D., & Norris, J. E. 2000, ApJL, 530, L57

Ryan, S. G., Norris, J. E., & Beers, T. C. 1999, ApJ, 523, 654

Sakurai, J. J. 1985, Modern Quantum Mechanics (Addison Wesley, M.A., edited by Tuan, San Fu)

Sanders, D. B., Phinney, E. S., Neugebauer, G., Soifer, B. T., & Matthews, K. 1989, ApJ, 347, 29

Sanders, D. B., Soifer, B. T., Elias, J. H., Madore, B. F., Matthews, K., Neugebauer, G., & Scoville, N. Z. 1988, ApJ, 325, 74

Sanduleak, N. & Pesch, P. 1984, ApJS, 55, 517

Sargent, W. L. W., Boksenberg, A., & Steidel, C. C. 1988, ApJS, 68, 539

Schachter, J. 1991, PASP, 103, 457

Schaye, J., Aguirre, A., Kim, T.-S., Theuns, T., Rauch, M., & Sargent, W. L. W. 2003, ApJ, 596, 768

Schneider, D. P., Schmidt, M., & Gunn, J. E. 1991, AJ, 101, 2004

Schramm, D. N. & Turner, M. S. 1998, Reviews of Modern Physics, 70, 303

Schramm, D. N. & Wagoner, R. V. 1977, Annual Review of Nuclear and Particle Science, 27, 37

Schroeder, D. J. 1987, Astronomical Optics (San Diego: Academic Press, 1987)

Scott, J., Bechtold, J., Morita, M., Dobrzycki, A., & Kulkarni, V. P. 2002, ApJ, 571, 665

Scott, J. E., Kriss, G. A., Brotherton, M., Green, R. F., Hutchings, J., Shull, J. M., & Zheng, W. 2004, ApJ, 615, 135

Seljak, U., McDonald, P., & Makarov, A. 2003, MNRAS, 342, L79

Shang, Z., Brotherton, M. S., Green, R. F., Kriss, G. A., Scott, J., Quijano, J. K., Blaes, O., Hubeny, I., Hutchings, J., Kaiser, M. E., Koratkar, A., Oegerle, W., & Zheng, W. 2005, ApJ, 619, 41

Shang, Z., Wills, B. J., Robinson, E. L., Wills, D., Laor, A., Xie, B., & Yuan, J. 2003, ApJ, 586, 52

Sheinis, A. I., Miller, J. S., Bolte, M., & Sutin, B. M. 2000, in Proc. SPIE Vol. 4008, p. 522-533, Optical and IR Telescope Instrumentation and Detectors, Masanori Iye; Alan F. Moorwood; Eds., Vol. 4008, 522–533

Sonneborn, G., Tripp, T. M., Ferlet, R., Jenkins, E. B., Sofia, U. J., Vidal-Madjar, A., & Woźniak, P. R. 2000, ApJ, 545, 277

Spergel, D. N., Verde, L., Peiris, H. V., Komatsu, E., Nolta, M. R., Bennett, C. L., Halpern, M., Hinshaw, G., Jarosik, N., Kogut, A., Limon, M., Meyer, S. S., Page,

L., Tucker, G. S., Weiland, J. L., Wollack, E., & Wright, E. L. 2003, ApJS, 148, 175

Spinrad, H., Stern, D., Bunker, A., Dey, A., Lanzetta, K., Yahil, A., Pascarelle, S., & Fernández-Soto, A. 1998, AJ, 116, 2617

Steidel, C. C., Pettini, M., & Adelberger, K. L. 2001, ApJ, 546, 665

Steidel, C. C. & Sargent, W. L. W. 1987, ApJ, 313, 171

Steigman, G. 2002, Fortschritte der Physik, vol. 50, Issue 5, pp.562-568, 50, 562

Steigman, G. & Tosi, M. 1992, ApJ, 401, 150

Stone, R. P. S. & Baldwin, J. A. 1983, MNRAS, 204, 347

Stoughton, C., Lupton, R. H., Bernardi, M., Blanton, M. R., Burles, S., Castander, F. J., Connolly, A. J., Eisenstein, D. J., Frieman, J. A., Hennessy, G. S., Hindsley, R. B., Ivezić, Ž., Kent, S., Kunszt, P. Z., Lee, B. C., Meiksin, A., Munn, J. A., Newberg, H. J., Nichol, R. C., Nicinski, T., Pier, J. R., Richards, G. T., Richmond, M. W., Schlegel, D. J., Smith, J. A., Strauss, M. A., SubbaRao, M., Szalay, A. S., Thakar, A. R., Tucker, D. L., Vanden Berk, D. E., Yanny, B., Adelman, J. K., Anderson, J. E., Anderson, S. F., Annis, J., Bahcall, N. A., Bakken, J. A., Bartelmann, M., Bastian, S., Bauer, A., Berman, E., Böhringer, H., Boroski, W. N., Bracker, S., Briegel, C., Briggs, J. W., Brinkmann, J., Brunner, R., Carey, L., Carr, M. A., Chen, B., Christian, D., Colestock, P. L., Crocker, J. H., Csabai, I., Czarapata, P. C., Dalcanton, J., Davidsen, A. F., Davis, J. E., Dehnen, W., Dodelson, S., Doi, M., Dombeck, T., Donahue, M., Ellman, N., Elms, B. R., Evans, M. L., Eyer, L., Fan, X., Federwitz, G. R., Friedman, S., Fukugita, M., Gal, R., Gillespie, B., Glazebrook, K., Gray, J., Grebel, E. K., Greenawalt, B., Greene, G., Gunn, J. E., de Haas, E., Haiman, Z., Haldeman, M., Hall, P. B., Hamabe, M., Hansen, B., Harris, F. H., Harris, H., Harvanek, M., Hawley, S. L., Hayes, J. J. E., Heckman, T. M., Helmi, A., Henden, A., Hogan, C. J., Hogg, D. W.,

Holmgren, D. J., Holtzman, J., Huang, C., Hull, C., Ichikawa, S., Ichikawa, T., Johnston, D. E., Kauffmann, G., Kim, R. S. J., Kimball, T., Kinney, E., Klaene, M., Kleinman, S. J., Klypin, A., Knapp, G. R., Korienek, J., Krolik, J., Kron, R. G., Krzesiński, J., Lamb, D. Q., Leger, R. F., Limmongkol, S., Lindenmeyer, C., Long, D. C., Loomis, C., Loveday, J., MacKinnon, B., Mannery, E. J., Mantsch, P. M., Margon, B., McGehee, P., McKay, T. A., McLean, B., Menou, K., Merelli, A., Mo, H. J., Monet, D. G., Nakamura, O., Narayanan, V. K., Nash, T., Neilsen, E. H., Newman, P. R., Nitta, A., Odenkirchen, M., Okada, N., Okamura, S., Ostriker, J. P., Owen, R., Pauls, A. G., Peoples, J., Peterson, R. S., Petravick, D., Pope, A., Pordes, R., Postman, M., Prosapio, A., Quinn, T. R., Rechenmacher, R., Rivetta, C. H., Rix, H., Rockosi, C. M., Rosner, R., Ruthmansdorfer, K., Sandford, D., Schneider, D. P., Scranton, R., Sekiguchi, M., Sergey, G., Sheth, R., Shimasaku, K., Smee, S., Snedden, S. A., Stebbins, A., Stubbs, C., Szapudi, I., Szkody, P., Szokoly, G. P., Tabachnik, S., Tsvetanov, Z., Uomoto, A., Vogeley, M. S., Voges, W., Waddell, P., Walterbos, R., Wang, S., Watanabe, M., Weinberg, D. H., White, R. L., White, S. D. M., Wilhite, B., Wolfe, D., Yasuda, N., York, D. G., Zehavi, I., & Zheng, W. 2002, AJ, 123, 485

Sun, W. & Malkan, M. A. 1989, ApJ, 346, 68

Suzuki, N., Tytler, D., Kirkman, D., O'Meara, J. M., & Lubin, D. 2003, PASP, 115, 1050

—. 2005, ApJ, 618, 592

Telfer, R. C., Zheng, W., Kriss, G. A., & Davidsen, A. F. 2002, ApJ, 565, 773

Thuan, T. X. & Izotov, Y. I. 2002, Space Science Reviews, v. 100, Issue 1/4, p. 263-276 (2002)., 100, 263

Tinsley, B. M. 1974, ApJ, 192, 629

—. 1980, Fundamentals of Cosmic Physics, 5, 287

Tull, R. G. 1998, in Proc. SPIE Vol. 3355, p. 387-398, Optical Astronomical Instrumentation, Sandro D'Odorico; Ed., Vol. 3355, 387–398

Tytler, D. & Burles, S. 1997, in Origin of matter and evolution of galaxies in the universe '96. Proceedings of an international conference held in Atami, Japan, 18-20 January 1996, Singapore: World Scientific, —c1997, edited by T. Kajino, Y. Yoshii, and S. Kubono, p. 37., 37

Tytler, D., Fan, X.-M., & Burles, S. 1996, Nature, 381, 207

Tytler, D., Kirkman, D., O'Meara, J., Suzuki, N., Orin, A., Lubin, D., Paschos, P., Jena, T., Lin, W.-C., & Norman, M. 2004, ApJ, astro-ph/0403688, 617, 1

Tytler, D., Kirkman, D., O'Meara, J. M., Suzuki, N., Orin, A., Lubin, D., Paschos, P., Jena, T., Lin, W., Norman, M. L., & Meiksin, A. 2004a, ApJ, 617, 1

Tytler, D., O'Meara, J. M., Suzuki, N., Kirkman, D., Lubin, D., & Orin, A. 2004b, AJ, 128, 1058

Vanden Berk, D. E., Richards, G. T., Bauer, A., Strauss, M. A., Schneider, D. P., Heckman, T. M., York, D. G., Hall, P. B., Fan, X., Knapp, G. R., Anderson, S. F., Annis, J., Bahcall, N. A., Bernardi, M., Briggs, J. W., Brinkmann, J., Brunner, R., Burles, S., Carey, L., Castander, F. J., Connolly, A. J., Crocker, J. H., Csabai, I. ., Doi, M., Finkbeiner, D., Friedman, S., Frieman, J. A., Fukugita, M., Gunn, J. E., Hennessy, G. S., Ivezić, Ž., Kent, S., Kunszt, P. Z., Lamb, D. Q., Leger, R. F., Long, D. C., Loveday, J., Lupton, R. H., Meiksin, A., Merelli, A., Munn, J. A., Newberg, H. J., Newcomb, M., Nichol, R. C., Owen, R., Pier, J. R., Pope, A., Rockosi, C. M., Schlegel, D. J., Siegmund, W. A., Smee, S., Snir, Y., Stoughton, C., Stubbs, C., SubbaRao, M., Szalay, A. S., Szokoly, G. P., Tremonti, C., Uomoto, A., Waddell, P., Yanny, B., & Zheng, W. 2001, AJ, 122, 549

Vangioni-Flam, E., Coc, A., & Cassé, M. 2000, A&A, 360, 15

Vangioni-Flam, E., Olive, K. A., & Prantzos, N. 1994, ApJ, 427, 618

Vidal-Madjar, A., Lemoine, M., Ferlet, R., Hebrard, G., Koester, D., Audouze, J., Casse, M., Vangioni-Flam, E., & Webb, J. 1998, A&A, 338, 694

Vogt, S. S. 1987, PASP, 99, 1214

Vogt, S. S., Allen, S. L., Bigelow, B. C., Bresee, L., Brown, B., Cantrall, T., Conrad, A., Couture, M., Delaney, C., Epps, H. W., Hilyard, D., Hilyard, D. F., Horn, E., Jern, N., Kanto, D., Keane, M. J., Kibrick, R. I., Lewis, J. W., Osborne, J., Pardeilhan, G. H., Pfister, T., Ricketts, T., Robinson, L. B., Stover, R. J., Tucker, D., Ward, J., & Wei, M. Z. 1994a, in Proc. SPIE Instrumentation in Astronomy VIII, David L. Crawford; Eric R. Craine; Eds., Volume 2198, p. 362, Vol. 2198, 362

Vogt, S. S., Allen, S. L., Bigelow, B. C., Bresee, L., Brown, B., Cantrall, T., Conrad, A., & Couture, M. *et al.* 1994b, in Proc. SPIE Instrumentation in Astronomy VIII, David L. Crawford; Eric R. Craine; Eds., Volume 2198, p. 362, Vol. 2198, 362

Wagoner, R. V. 1973, ApJ, 179, 343

Wagoner, R. V., Fowler, W. A., & Hoyle, F. 1967, ApJ, 148, 3

Webb, J. K. 1987, Ph.D. thesis, University of Cambridge

White, R. L., Becker, R. H., Fan, X., & Strauss, M. A. 2003, astroph/0303476

Whitmire, S. E. & Scherrer, R. J. 2000, Physical Review D, 61, 083508

Whitney, C. A. 1983, A&AS, 51, 443

Willmarth, D. & Barnes, J. 1994, http://iraf.noao.edu/docs/spectra.html

Wills, B. J., Thompson, K. L., Han, M., Netzer, H., Wills, D., Baldwin, J. A., Ferland, G. J., Browne, I. W. A., & Brotherton, M. S. 1995, ApJ, 447, 139

Wolfe, A. M. & Prochaska, J. X. 2000, ApJ, 545, 591

Yip, C. W., Connolly, A. J., Vanden Berk, D. E., Ma, Z., Frieman, J. A., SubbaRao, M., Szalay, A. S., Richards, G. T., Hall, P. B., Schneider, D. P., Hopkins, A. M., Trump, J., & Brinkmann, J. 2004, AJ, 128, 2603

York, D. G., Adelman, J., Anderson, J. E., Anderson, S. F., Annis, J., Bahcall, N. A., Bakken, J. A., Barkhouser, R., Bastian, S., Berman, E., Boroski, W. N., Bracker, S., Briegel, C., Briggs, J. W., Brinkmann, J., Brunner, R., Burles, S., Carey, L., Carr, M. A., Castander, F. J., Chen, B., Colestock, P. L., Connolly, A. J., Crocker, J. H., Csabai, I., Czarapata, P. C., Davis, J. E., Doi, M., Dombeck, T., Eisenstein, D., Ellman, N., Elms, B. R., Evans, M. L., Fan, X., Federwitz, G. R., Fiscelli, L., Friedman, S., Frieman, J. A., Fukugita, M., Gillespie, B., Gunn, J. E., Gurbani, V. K., de Haas, E., Haldeman, M., Harris, F. H., Hayes, J., Heckman, T. M., Hennessy, G. S., Hindsley, R. B., Holm, S., Holmgren, D. J., Huang, C., Hull, C., Husby, D., Ichikawa, S., Ichikawa, T., Ivezić, Ž., Kent, S., Kim, R. S. J., Kinney, E., Klaene, M., Kleinman, A. N., Kleinman, S., Knapp, G. R., Korienek, J., Kron, R. G., Kunszt, P. Z., Lamb, D. Q., Lee, B., Leger, R. F., Limmongkol, S., Lindenmeyer, C., Long, D. C., Loomis, C., Loveday, J., Lucinio, R., Lupton, R. H., MacKinnon, B., Mannery, E. J., Mantsch, P. M., Margon, B., McGehee, P., McKay, T. A., Meiksin, A., Merelli, A., Monet, D. G., Munn, J. A., Narayanan, V. K., Nash, T., Neilsen, E., Neswold, R., Newberg, H. J., Nichol, R. C., Nicinski, T., Nonino, M., Okada, N., Okamura, S., Ostriker, J. P., Owen, R., Pauls, A. G., Peoples, J., Peterson, R. L., Petravick, D., Pier, J. R., Pope, A., Pordes, R., Prosapio, A., Rechenmacher, R., Quinn, T. R., Richards, G. T., Richmond, M. W., Rivetta, C. H., Rockosi, C. M., Ruthmansdorfer, K., Sandford, D., Schlegel, D. J., Schneider, D. P., Sekiguchi, M., Sergey, G., Shimasaku, K., Siegmund, W. A., Smee, S., Smith, J. A., Snedden, S., Stone, R., Stoughton, C., Strauss, M. A., Stubbs, C., SubbaRao, M., Szalay, A. S., Szapudi, I., Szokoly, G. P., Thakar, A. R., Tremonti, C., Tucker, D. L., Uomoto, A., Vanden Berk, D., Vogeley, M. S., Waddell, P., Wang, S., Watanabe, M., Weinberg, D. H., Yanny,

B., & Yasuda, N. 2000, AJ, 120, 1579

Zheng, W., Kriss, G. A., Telfer, R. C., Grimes, J. P., & Davidsen, A. F. 1997, ApJ, 475, 469

Zuo, L. & Lu, L. 1993, ApJ, 418, 601